Rheinland-Pfälzische
Technische Universität
Kaiserslautern
Landau

Riemannian shape optimization of thin elastic shells using isogeometric analysis

Vom Fachbereich Mathematik der Rheinland-Pfälzischen Technischen Universität Kaiserslautern-Landau genehmigte

DISSERTATION

von

Rozan Irsyadulfawaz Rosandi

zur Verleihung des akademischen Grades

„Doktor der Naturwissenschaften“
(*Doctor rerum naturalium*, Dr. rer. nat.)

1. Gutachter: Prof. Dr. Bernd Simeon (RPTU Kaiserslautern-Landau)
2. Gutachter: Prof. Dr. Volker Schulz (Universität Trier)

Datum der Disputation: 17. Juli 2025

DE-386

Abstract

In this thesis, we consider the optimal shape design of thin elastic shells based on a model of Koiter's type, whose shape can be described by a surface embedded in three-dimensional Euclidean space. We regard the set of unparametrized embeddings of the surface as an infinite-dimensional Riemannian shape manifold and perform numerical optimization in this setting using the Riemannian shape gradient. Non-uniform rational B-splines (NURBS) are employed to discretize the shell and numerically solve the equations that govern its mechanical behavior via isogeometric finite element analysis (IGA). The aim is to develop and implement new numerical methods for solving shape optimization problems constrained by partial differential equations (PDEs) that take the inherent geometric structure of shape spaces into account and make use of the integration of finite element analysis (FEA) with technologies from computer-aided design (CAD). In contrast to existing methods based on the Riemannian framework, we investigate the use of geodesic retractions instead of linear updates on shape spaces of planar curves and surfaces for the gradient descent method. We demonstrate our proposed approach and numerical methods mainly on the computation of minimal surfaces, the compliance minimization of thin elastic shell structures under static load and fixed area constraint, as well as the identification of parameters for a model of Earth's lithosphere in the context of geoscientific applications.

Zusammenfassung

In dieser Arbeit wird die Formoptimierung von dünnen elastischen Koiter-Schalen behandelt, dessen Form durch eine in den dreidimensionalen euklidischen Raum eingebettete Fläche beschrieben werden kann. Wir betrachten die Menge aller nichtparametrisierten Einbettungen der Fläche als eine unendlichdimensionale Riemann'sche Formmannigfaltigkeit und führen in diesem Rahmen unter Verwendung des Riemann'schen Formgradients eine numerische Formoptimierung durch. Nicht-uniforme rationale B-splines (NURBS) werden eingesetzt, um die Schale anhand von isogeometrischer Analysis (IGA) zu diskretisieren und die partiellen Differentialgleichungen (PDEs), die das mechanische Verhalten des Festkörpers festlegen, numerisch zu lösen. Das Ziel ist es, neuartige numerische Verfahren für die PDE-beschränkte Optimierung von Formen zu entwickeln und zu implementieren, die die inhärente geometrische Struktur von Riemann'schen Formräumen in Betracht ziehen. Dabei werden Technologien aus dem rechnerunterstütztem Konstruieren (CAD) mit der Finite-Elemente-Analysis (FEA) integriert. Im Gegensatz zu bestehenden Methoden, die auf dem Riemann'schen Modell basieren, wird die Verwendung einer geodätischen Retraktion statt einer linearen Iterationsvorschrift für das Gradientenverfahren auf Formräumen von ebenen Kurven und Flächen untersucht. Der vorgeschlagene Ansatz wird insbesondere auf die Berechnung von Minimalflächen und die Minimierung der Nachgiebigkeit von dünnen elastischen Schalen unter statischer Belastung und mit festem Flächeninhalt angewandt. Darüber hinaus werden im geowissenschaftlichen Anwendungsbereich Parameter in einem mathematischen Modell für die Lithosphäre der Erde geschätzt.

Acknowledgements

First and foremost, I express my sincere gratitude to my advisor Prof. Dr. Bernd Simeon for the guidance throughout my doctoral studies. Thank you for giving me the freedom to research to my heart's content, for letting me develop my own academic independence, and for providing me with full support whenever it was needed. I have been inspired by your kindness, your professionality, the way you teach and present yourself, as well as the numerous anecdotes, historical remarks, and personal experiences that you have shared.

Thank you to my fellow colleagues Jeremias Arf and Henry Jäger as well as former ones who are affiliated with the Differential-Algebraic Systems and Numerical Analysis Group: Clarissa Arioli, Benjamin Bauer, Urs Baumgart, Felix Dietrich, Simon Gottschalk, Elise Grosjean, Jonathan Jahnke, Diana Manvelyan, Steffen Plunder, and Alexander Shamanskiy for the engaging discussions and helpful advice, especially at the start of my PhD journey. It has been a pleasure getting through our math studies together with you from the very beginning, Jeremias, and thank you for organizing the occasional hiking tours and board game evenings, Ben. Moreover, I would also like to thank the staff at the Department of Mathematics and Fraunhofer ITWM, as well as the people who have enabled me to study under the Felix Klein scholarship.

I am very grateful to all the people whom I met along the way at conferences and with whom I had fruitful discussions or just a pleasurable time during the events. Thank you to Ronny Bergmann for igniting my interest in differential geometry, Florian Beiser for introducing me to the summer school on shape and topology optimization, and Daniela Fußeder for the groundwork on isogeometric shape optimization. Furthermore, I have also gained a lot of knowledge from a certain online math community and would like to express my gratitude to the acquaintances that I have made there.

I also thank my previous roommates Stephan and Niklas for the great time that we had together, as well as the weekly Mao group with Dennis and Simon. Thanks to all my peers and friends during these times, especially Niko for the hospitality every Christmas, Sarah for the best gift that a mathematician can wish for, Michi for getting me into doing regular physical exercises, as well as Liam, Max, Erik, David, Marvin, Nicolas, Viny, Raihan, Ochi, Matthias, and many others for the lunches, dinners, and time that we shared together.

My deepest gratitude goes to both of my parents for everything that they have done for me. Thank you for your unwavering support, for your genuine understanding, for providing me with so many vital opportunities in my life, and for making me the person that I am today. I am truly happy and proud to be your son. Not to be forgotten is my big, younger brother Arofa with whom I have spent a great chunk of my childhood and who shares the same passion for similar and not-so-similar hobbies as me. I am glad that we still have the opportunity to hang out during our studies in Kaiserslautern.

Words cannot fully describe how much I appreciate my lovely wife Nisa. This thesis would not have been possible without her constant support. Thank you for the immense patience, for always listening to my doubts and giving me encouragement, for taking care of a lot of things in our lives, for reminding me to take a break whenever it is needed, and for your all-embracing love. I also express my gratitude to my parents- and sisters-in-laws as well as other family members and friends back in Indonesia for their support from far away.

Last but not least, thank you to all the excellent researchers out there in the world who, just by me reading and studying their work, have inspired me throughout the years.

Contents

List of acronyms and abbreviations

ALM	augmented Lagrangian method
ANDES	assumed natural deviatoric strain
(L-)BFGS	(limited-memory) Broyden–Fletcher–Goldfarb–Shanno
BVP	boundary value problem
CAD	computer-aided design
CCSA	conservative convex separable approximation
DG	discontinuous Galerkin
DKT	discrete Kirchhoff triangle
EG	Euclidean gradient
FDM	finite difference method
FDTO	first discretize–then optimize
FEA	finite element analysis
FEM	finite element method
FOTD	first optimize–then discretize
FSDT	first-order shear deformation theory
FSI	fluid–structure interaction
GR	geodesic retraction
HHJ	Hellan–Herrmann–Johnson
IDA	implicit differential-algebraic
IGA	isogeometric analysis
IGM	isogeometric (finite element) method
IPM	interior-point method
IVP	initial value problem
KKT	Karush–Kuhn–Tucker
LDDMM	large deformation diffeomorphic mapping method
LERP	linear interpolation
LF	limit of Fréchet spaces
LR	linear retraction
MMA	method of moving asymptotes
NURBS	non-uniform rational basis spline
ODE	ordinary differential equation
PDE	partial differential equation
QN	quasi-Newton
RF	rotation-free
RG	Riemannian gradient
SD	steepest descent
SIMP	solid isotropic material with penalization
SOP	shape optimization problem
SQP	sequential quadratic programming
SRNF	square root normal field
SRVF	square root velocity field
(LC)TVS	(locally convex) topological vector space
VAMOS	vertex-assigned morphing of optimal shape

1 Introduction

Shape optimization is concerned with finding an optimal design for the shape of an entity within a set of admissible designs to achieve a certain objective. In contrast to conventional problems in mathematical optimization, the design variables involve shapes. Shape is a rather intuitive notion that nevertheless has several possible interpretations and requires a precise mathematical definition. There are numerous applications of shape optimization in industrial design, which generally aim at reducing the manufacturing costs and improving the performance of products by modifying their shape [185, 47, 10].

A prevalent example is given by structural shape optimization in mechanical, vehicle, and civil engineering, where the objective is to design components with a reasonable amount of structural integrity to withstand existing loads under normal operational conditions [201, 137, 122]. This can be accomplished by minimizing the compliance of the component, which corresponds to maximizing its stiffness. Some additional constraints may be imposed on the geometry, such as prescribing a desired volume or—for the wrench in Figure 1—a minimum width and length to keep the tool usable. Other common use cases include the design of compliant mechanisms [247, 136, 287], aerodynamic shape optimization [141, 228, 176] (see Figure 2 for an illustration), acoustic shape optimization [62, 262, 98], optimization of fluid flow channels [93, 44], optimization of electric machines [106], image segmentation [65, 130], interface identification [233, 244, 237], and mathematical visualization [285, 284].

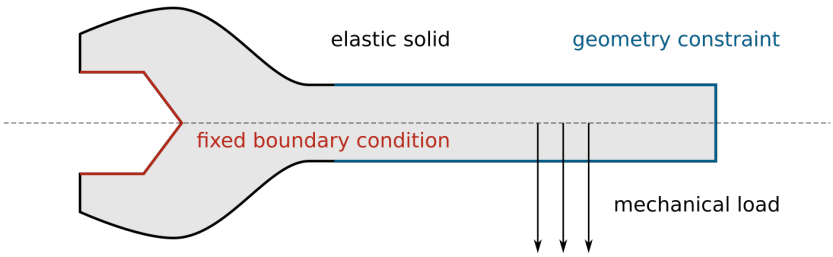

Figure 1: Shape optimization of a wrench. Compliance minimization aims to reduce the strain on the object when a load consistent with the boundary conditions is applied.

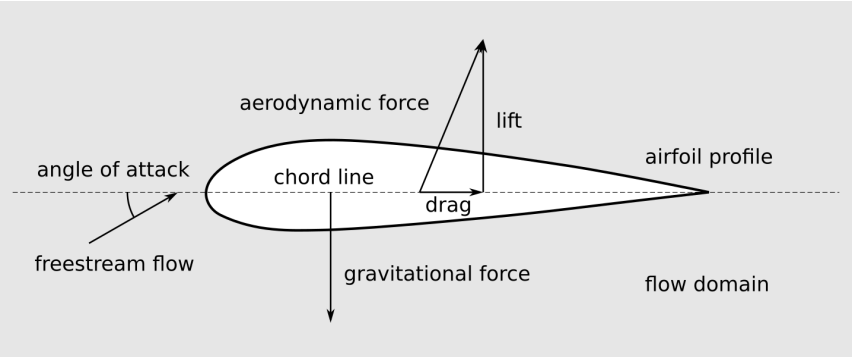

Figure 2: Shape optimization of an airfoil. The objective function and constraints may involve aerodynamic forces experienced by the aircraft, e.g., one can strive to minimize the drag while trying to maintain a minimum amount of lift required to fly.

Many problems do not only involve shapes but also partial differential equations (PDEs) that describe the behavior of some physical system related to the problem. In most cases, the domain of the governing equations depends on the shape, which adds a complexity that has to be addressed in the solution framework and optimization process. Techniques from optimal control theory and optimization with PDE constraints [131, 260], such as the adjoint state method, can be adapted to shape optimization problems—with the caveat that the design space may no longer be a subset of some linear space. A suitable choice has to be made for the design space to provide useful mathematical models of shape [278]. In any case, shape optimization deals with inherently infinite-dimensional problems due to the seemingly countless ways that one can perturb and modify shapes.

Framework for PDE constrained shape optimization

Several frameworks have been developed for shape optimization over the past decades, many of which are heuristic-driven, owing to the need of pragmatic solutions to relevant industrial problems [47]. In general, one distinguishes between two approaches for handling infinite-dimensional problems numerically. The first one is the *first optimize–then discretize* (FOTD) approach, where the optimality conditions are considered in the infinite-dimensional setting. Discretization is done to approximate the design and state variables numerically. In the second approach, i.e., *first discretize–then optimize* (FDTO), a finite-dimensional representation of the problem is considered a priori and optimality conditions are posed on some subset of the Euclidean space. The FOTD approach attempts a careful investigation and discretization of the underlying infinite-dimensional problem, while the FDTO approach relies on powerful existing methods for numerical optimization in the finite-dimensional setting and ad hoc preconditioning schemes.

This thesis follows the FOTD approach, in particular the Riemannian framework for PDE constrained shape optimization proposed by Schulz et al. [232, 234] based on the shape spaces introduced by Michor and Mumford [182]. Riemannian shape spaces have been initially studied for simple closed curves in the Euclidean plane. They have been generalized to immersed submanifolds of some ambient Riemannian manifold [181, 27, 28], especially to surfaces in three-dimensional Euclidean space, where almost local and Sobolev-type Riemannian metrics have been considered. Inner metrics of this kind, along with outer metrics induced by the diffeomorphism group of the ambient space, have been commonly used for statistical shape analysis with applications in the broad field of visual computing, e.g., Beg et al. [33], Srivastava et al. [255], Bauer et al. [29, 30, 31, 32], Hartman et al. [121]. The Steklov–Poincaré Riemannian metric, which is an inner metric derived from an outer metric, has been proposed for efficient PDE constrained shape optimization by Schulz et al. [235], and successfully applied to interface optimization as well as problems in fluid mechanics [231, 43, 209], when the shape is given by the boundary of a domain on which the shape derivative can be evaluated.

Scope, research projects, and contributions

The problems considered in this thesis are shell and plate problems in solid mechanics. In particular, we discuss the compliance minimization of thin elastic shell structures [221] and the identification of parameters for a model of Earth's lithosphere [222]. The latter is a standard optimization problem with PDE constraints based on classical plate theory, where the domain does not change and the design variables are simply given by scalar fields. The former, on the other hand, is a shape optimization problem where the design space consists of embeddings of a surface in three-dimensional Euclidean space. The main

research project is to apply the Riemannian framework to the shell optimization problem and use discretization methods from isogeometric finite element analysis [138] to compute numerical approximations of solutions to the problem. To the best of our knowledge, this has not been attempted before, prior to the work of Rosandi and Simeon [221].

A retraction based on pointwise linear extrapolation is commonly used to update the shapes using either a Riemannian gradient descent method or a quasi-Newton method. This is efficient to implement and execute, since the theoretically correct way requires a numerical solution to the geodesic equation in each optimization step, which is prohibitively expensive for large-scale problems. A first-order approximation to the geodesic path has been shown to be sufficient for optimization purposes [2]. Nevertheless, we are inclined to investigate whether using a geodesic retraction offers any significant improvements over the simplest retraction, especially because the geodesic equation corresponds to the Hamiltonian flow associated with the Riemannian metric [183], i.e., there are conserved quantities that might be beneficial for the shape updates. The conservation of reparametrization momentum, in particular, has a potential for preserving the mesh quality during the optimization process and may allow for larger step sizes to be taken in the first few descent steps.

Apart from the above contributions, the author of this thesis has dealt with the relation of inverse problems to a particular regularization technique used for shape optimization.

Sensitivity filtering and smoothing techniques

Most solution methods from the engineering community are based on the FDTO approach using, e.g., nodal variables [161], spline representations [56], and subdivision surfaces [71]. In node-based shape optimization, a mesh is generated for the geometry and a subset of vertex coordinates is chosen as independent design variables. It is straightforward to implement and among the earliest methods for numerical shape optimization [161]. Shape sensitivities are usually computed using finite differences or finite element discretizations. A major drawback of this approach, however, is that information on the connectivity of nodes and the inherent geometry of the original shape is lost during the transition from the continuous to the discrete setting, which often causes poor design updates and numerical instabilities, leading to mesh entanglement and mesh-dependent results. For this reason, various sensitivity filtering and smoothing techniques have been developed to regularize the problem. See, e.g., Pironneau [208], Sigmund and Maute [249], and Bletzinger [46].

Filtering can be done either explicitly or implicitly [134]. The latter requires the solution of an elliptic PDE and is also known as implicit fairing in the computer graphics community [87], motivated by implicit integration of the diffusion equation and the curvature flow to remove rough features and noises from irregular meshes. In the mathematical community, it is referred to as Sobolev smoothing or Sobolev preconditioning [193, 213, 151, 214, 192], which corresponds to a higher-order gradient flow [22, 21, 94, 236]. This technique and point of view are compatible with the Riemannian framework for shape optimization, where the gradient is associated with a Sobolev-type Riemannian metric.

The idea of using explicit filtering to deal with checkerboard patterns and mesh-dependent results in structural topology optimization stems from Sigmund [246, 245, 249]. Motivated by its effectiveness, the vertex morphing method has been developed for node-based shape optimization by Bletzinger et al. [134, 46, 15, 109, 229]. One of the first research projects conducted by the author of this thesis is the investigation of the vertex morphing method from a mathematical point of view. A connection with Tikhonov regularization in the case of a linear least squares problem has been established and published as a poster in [220].

Isogeometric finite element discretization

Isogeometric analysis (IGA) is a computational paradigm for solving PDEs that employs the same shape functions used to describe the domain of the problem to construct finite element numerical approximations of solutions to the problem. It allows the integration of finite element analysis (FEA) with technologies from computer-aided design (CAD). The concept of IGA has first been presented in the seminal work by Hughes et al. [138] in 2005. Standard references on the subject include Cottrell et al. [79], Buffa and Sangalli [60], Lyche et al. [170], Jüttler and Simeon [145], and van Brummelen et al. [263].

B-splines and non-uniform rational B-splines (NURBS) are conventionally used for the shape functions in IGA. One advantage of using them for shell and plate problems is the simple construction of C^1 isogeometric spline spaces on a single patch to discretize the equations with less degrees of freedom than standard C^1 finite element methods [153]. For multi-patch geometries, which are commonplace for problems of practical relevance, it is not a trivial task to preserve the C^1 continuity along patch interfaces. Significant effort on this matter has been undertaken over the past 15 years by, e.g., Kiendl et al. [154], Apostolatos et al. [17], Dornisch et al. [92], Kapl et al. [147], Collin et al. [73], Chan et al. [64], Schuß et al. [238], Coradello et al. [77], Farahat et al. [102]. A recent progress is due to Bracco et al. [54], where the challenge is additionally combined with adaptive local refinement.

We employ isogeometric discretization methods to compute numerical approximations of solutions to the state equation involved in the shape optimization problem that are then used to obtain descent directions for the optimization process. The implementation of the algorithms in MATLAB relies on the GeoPDEs package for IGA [268], extended by a self-written package for Riemannian shape optimization to compute the shape sensitivities and perform numerical optimization. A pre-release version of the software has been uploaded to

`https://github.com/rozanxt/shellopt` [219].

Isogeometric analysis of Earth's lithosphere

In addition to the compliance minimization problem, we consider the numerical simulation of shells and plates in the context of isostasy to showcase the capabilities of IGA in solving higher-order problems in geoscientific applications. Earth's lithosphere is modeled as a thin elastic shell or plate floating on the asthenosphere and subject to topographic loads. We use the computational methods to predict the deformation of the lithosphere in isostatic equilibrium using information on the topography of Earth's surface and demonstrate our approach on selected geographic locations. The results have been published in [222].

For Europe, the computed lithospheric depression is compared with available Mohorovičić depth data. This also serves as a basis for identifying parameters of the model, such as the effective elastic thickness of the lithosphere, the rock density, and the topographic load that are most plausible to explain the observed depths. An iterative method based on PDE constrained optimization is used for parameter identification as opposed to the commonly used direct inversion of spectral measures [155].

An example of simulating the entire lithosphere of the Earth as a spherical shell has also been considered, where multi-patch IGA has been employed. It provides an alternative to spherical harmonics for solving PDEs on a spherical domain. The code used for the numerical simulations is available at

`https://github.com/rozanxt/igalith` [218].

Outline of the dissertation

The main objective of this thesis is two-fold. First, we want to provide a comprehensive mathematical framework for PDE constrained shape optimization using geodesic paths with a focus on H^1 Sobolev–Riemannian metrics. Second is the numerical implementation and analysis of methods for solving shape optimization problems related to thin elastic shells and surfaces in general based on computational tools from IGA.

The document is structured as follows:

- Section 2 introduces some background material—mainly the mathematical concepts required for the topics discussed in subsequent sections—and sets up the notation used throughout the thesis.
- Section 3 starts with a mathematical description of three-dimensional elasticity and proceeds with a derivation of the equilibrium equations for thin elastic shells and plates. A simple model of Earth's lithosphere in isostatic equilibrium is discussed at the end of the section.
- Section 4 presents existing mathematical frameworks for shape spaces and delves into infinite-dimensional Riemannian geometry in order to derive the geodesic equation for Sobolev-type Riemannian metrics.
- Section 5 discusses shape optimization constrained by PDEs in the context of Riemannian shape spaces. A summary of methods for numerical optimization is given, and relevant shape sensitivities for the problems in question are derived.
- Section 6 provides the tools required for the numerical discretization of the problems using isogeometric finite element analysis. Furthermore, implementation details for the shape optimization procedures are discussed.
- Section 7 presents selected problems and numerical results related to the geodesic equation on shape spaces of planar curves and surfaces, shape optimization without PDE constraints, compliance minimization of thin elastic shells, and simulations of Earth's lithosphere with parameter identification.
- A conclusion and an outlook on future research work are given in Section 8.

We end the introductory section by citing David Mumford—a Fields Medalist who, aside from his contributions to algebraic geometry, is also known for his research in vision and pattern theory:

> *"Shapes are the ultimate non-linear sort of thing."*
> — David Mumford, 1974

Thus, the next appropriate setting for the analysis of shapes arises from infinite-dimensional differential geometry, and sophisticated numerical methods for shape optimization can be developed by investigating the inherent structure of shape spaces.

2 Preliminaries

The necessary prerequisites are grouped into the following subjects: basic definitions and notation, including notions of differentiation between topological vector spaces (Section 2.1), function spaces and integrals with a focus on those that are relevant for shape analysis and differential equations as well as geometric transformations that preserve the regularity of domains and functions (Section 2.2), concepts from differential geometry, such as manifolds, bundles, and tensors (Section 2.3), followed by the special case of surfaces in Euclidean space (Section 2.4). We begin with the general mathematical symbols used in this thesis.

2.1 Basic definitions and notation

2.1.1 Sets, numbers, and matrices

Let $\mathscr{P}(M)$ denote the power set of an arbitrary set M, i.e., the set of all subsets of M. For a mapping between two sets $f\colon M \to N$, the restriction of f to a subset S of M is denoted by $f|_S$. We write $S \subset M$ instead of $S \subseteq M$ if S is a proper subset of M. The disjoint union of two sets M and N is written as $M \uplus N$ instead of $M \cup N$ to indicate that $M \cap N = \varnothing$.

The set of natural numbers is denoted by $\mathbb{N}_0$ if it contains zero, and $\mathbb{N}$ otherwise. Let $\mathbb{Z}$ denote the set of integers, $\mathbb{Q}$ the set of rational numbers, $\mathbb{R}$ the set of real numbers, and $\mathbb{C}$ the set of complex numbers with the usual operations and inclusions. We write $\mathbb{K} \in \{\mathbb{R}, \mathbb{C}\}$ for either the set of real or complex numbers and $\overline{\mathbb{R}} = \mathbb{R} \uplus \{-\infty, \infty\}$ for the set of extended real numbers. Round and square brackets are used to denote real intervals. The absolute value is written as $|\cdot|$, where $\cdot$ is a placeholder for a variable in a function. We use the symbol $\simeq$ for isomorphism and $\approx$ for approximate equality.

For $m, n \in \mathbb{N}$, let $\mathbb{K}^n$ denote the n-dimensional real or complex coordinate space and $\mathbb{K}^{m\times n}$ the set of matrices of size $m \times n$ with entries in $\mathbb{K}$. A matrix $A \in \mathbb{K}^{m\times n}$ is an array of real or complex numbers

$$A = \begin{pmatrix} A_{11} & \dots & A_{1n} \\ \vdots & \ddots & \vdots \\ A_{m1} & \dots & A_{mn} \end{pmatrix}, \tag{2.1}$$

which can also be written compactly as $A = (A_{ij})_{i,j=1}^{m,n}$, where $A_{ij} \in \mathbb{K}$ for $i = 1, \dots, m$ and $j = 1, \dots, n$. Its transpose $A^\mathsf{T} \in \mathbb{K}^{n\times m}$ and conjugate transpose $A^\mathsf{H} \in \mathbb{K}^{n\times m}$ are given by

$$A^\mathsf{T} = \begin{pmatrix} A_{11} & \dots & A_{m1} \\ \vdots & \ddots & \vdots \\ A_{1n} & \dots & A_{mn} \end{pmatrix}, \quad A^\mathsf{H} = \overline{A^\mathsf{T}} = \begin{pmatrix} \overline{A_{11}} & \dots & \overline{A_{m1}} \\ \vdots & \ddots & \vdots \\ \overline{A_{1n}} & \dots & \overline{A_{mn}} \end{pmatrix}, \tag{2.2}$$

where $\overline{\cdot}$ denotes complex conjugation. We write $a = (a_1, \dots, a_n) \in M^n$ for an n-tuple of elements $a_1, \dots, a_n$ in some set M and identify $\mathbb{K}^n$ with the set of column vectors $\mathbb{K}^{1\times n}$.

Consider a property that can be satisfied by a mapping $f\colon M \to N$ at points in the domain M, e.g., continuity of a mapping between topological spaces. We say that the property is satisfied on a subset S of M if it is satisfied at all points in S. If it is satisfied on the whole domain, then f is said to satisfy that property.

2.1.2 Topological vector spaces

In this thesis, we only consider real vector spaces, i.e., vector spaces over the field of real numbers. A topological vector space (TVS) is a vector space endowed with a topology that

makes vector addition and scalar multiplication continuous. We assume that the topological vector spaces considered in this thesis are Hausdorff and locally convex, i.e., distinct points can be separated by (open) neighborhoods and every neighborhood of the origin contains an absolutely convex neighborhood of the origin. More information on topological vector spaces can be found in the literature, e.g., Grothendieck [116] and Rudin [225]. We mostly consider Fréchet, Banach, and Hilbert spaces as well as other mathematical constructions that are based on them, e.g., functions, manifolds, and bundles.

Recall that a metric space (X, dist) is a topological space whose topology is induced by a metric, i.e., a distance function, via open balls. If every Cauchy sequence of points in X converges to an element of X, then X is said to be a complete metric space. Note that we identify an algebraic structure with its underlying set if the operations are clear from the context. For some positive real number $r > 0$ and $x \in X$, let

$$\mathrm{B}_r(x) = \big\{ y \in X \;\big|\; \operatorname{dist}(x, y) < r \big\} \tag{2.3}$$

denote the open ball in X with radius r that is centered at x and

$$\overline{\mathrm{B}_r(x)} = \big\{ y \in X \;\big|\; \operatorname{dist}(x, y) \leq r \big\} \tag{2.4}$$

its topological closure, i.e., the closed ball in X with the same radius and center.

A Fréchet space X is a (Hausdorff and locally convex) topological vector space (LCTVS) that is completely metrizable, i.e., its topology can be induced by a translation-invariant metric that turns X into a complete metric space. Equivalently, the metric topology is induced by a countable family of semi-norms.

A Banach space $(X, \| \cdot \|)$ is a normed vector space that is complete with respect to the induced metric. It is a Fréchet space, where the translation-invariant metric is given by

$$\operatorname{dist}(x, y) = \|x - y\|, \quad x, y \in X. \tag{2.5}$$

A Hilbert space $(X, \langle \cdot\,, \cdot \rangle)$ is a Banach space whose norm is induced by an inner product. An example of a finite-dimensional Hilbert space is given by the real coordinate space $\mathbb{R}^n$ endowed with the standard dot product

$$\langle x, y \rangle = x \cdot y = \sum_{i=1}^{n} x_i y_i, \quad x, y \in \mathbb{R}^n, \tag{2.6}$$

which induces the Euclidean norm

$$\|x\| = \sqrt{\langle x, x \rangle}, \quad x \in \mathbb{R}^n. \tag{2.7}$$

Any two norms on a finite-dimensional vector space are equivalent and the induced topology is called the Euclidean topology. The n-dimensional hyper-sphere in $\mathbb{R}^{n+1}$ is denoted by

$$\mathbb{S}_n = \big\{ x \in \mathbb{R}^{n+1} \;\big|\; \|x\| = 1 \big\}. \tag{2.8}$$

For topological vector spaces X and Y, let $\mathrm{L}(X; Y)$ denote the space of continuous linear functions from X to Y. If $X_1, \ldots, X_k$ are topological vector spaces, then the space of continuous k-linear functions is denoted by $\mathrm{L}(X_1, \ldots, X_k; Y)$. The dual vector space X^* is defined as the space of continuous linear functionals on X, i.e., $X^* = \mathrm{L}(X; \mathbb{R})$. We also write $\langle \alpha, x \rangle = \alpha(x)$ for the duality pairing, where $\alpha \in X^*$ and $x \in X$.

2.1.3 Differentiable functions

The notions of differentiation introduced in this section for functions between topological vector spaces can be found in Ambrosetti and Prodi [12] and Lang [160].

Definition 2.1 (Gateaux derivative)

Let X, Y be topological vector spaces and $f\colon S \subseteq X \to Y$ be a function from an open subset S of X to Y. The (directional) derivative of f at $x \in S$ in the direction of $v \in X$ is defined as

$$\delta f(x, v) = \frac{\mathrm{d}}{\mathrm{d}t} f(x + tv)\bigg|_{t=0} = \lim_{t \to 0} \frac{f(x + tv) - f(x)}{t}. \tag{2.9}$$

If the limit exists, then f is said to be (directionally) differentiable at x in the direction of v. The first variation of f at x refers to the function $v \mapsto \delta f(x, v)$, which is defined on the set of all directions in X for which the derivative exists. We say that f is Gateaux differentiable at x if $\delta f(x, v)$ exists for all directions $v \in X$. If f is Gateaux differentiable on S, then the function $\delta f\colon S \times X \to Y$ is called the Gateaux derivative of f on S. We say that f is continuously differentiable at x if it is Gateaux differentiable on some open neighborhood of x and δf is continuous on its domain. Higher-order Gateaux derivatives are obtained inductively via repeated differentiation, i.e., the Gateaux derivative of order $r \in \mathbb{N}$ is given by

$$\delta^r f\colon S \times \underbrace{X \times \cdots \times X}_{r \text{ times}} \to Y, \quad (x, v_1, \ldots, v_r) \mapsto \frac{\mathrm{d}}{\mathrm{d}t} \delta^{r-1} f(x + tv_r, v_1, \ldots, v_{r-1})\bigg|_{t=0}, \tag{2.10}$$

where $\delta^0 f = f$. The function f is said to be r-times continuously differentiable (or of class C^r) at x if there is an open neighborhood of x on which $\delta^r f$ exists and is continuous. It is called infinitely differentiable or smooth at x if it is of class C^∞ at x, i.e., f is of class C^r at x for all $r \in \mathbb{N}_0$. The class C^0 at x corresponds to f being continuous at x.

Definition 2.2 (Fréchet derivative)

If X and Y are Fréchet spaces, then continuous differentiability of f at $x_0 \in S$ implies that the first variation $\delta f(x_0, \cdot)\colon X \to Y$ is continuous and linear [120, Lemma 3.3.1]. In this case, we write

$$f'(x_0) = \delta f(x_0, \cdot) \tag{2.11}$$

for the continuous linear function in $\mathrm{L}(X; Y)$ and call it the Fréchet derivative of f at x_0. Furthermore, for all functions $\rho\colon U \subseteq X \to Y$ from a neighborhood U of the origin in X to Y with $x_0 + U \subseteq S$ that satisfy

$$f(x) = f(x_0) + f'(x_0)(x - x_0) + \rho(x - x_0) \tag{2.12}$$

for all $x \in x_0 + U$, we have that ρ is tangent to the origin, i.e., given a neighborhood of W of the origin in Y, there is a neighborhood V of the origin in X such that

$$\rho(tV) \subseteq o(t)W \tag{2.13}$$

for all $t \in (-\varepsilon, \varepsilon)$ with $\varepsilon > 0$, where $o\colon (-\varepsilon, \varepsilon) \to \mathbb{R}$ is a function that satisfies

$$\lim_{t \to 0} o(t)/t = 0. \tag{2.14}$$

If the above condition is fulfilled for some continuous linear function $f'(x_0) \in \mathrm{L}(X; Y)$, then $f'(x_0)$ is uniquely determined by the first variation $\delta f(x_0, \cdot)$. In this case, f is said to be Fréchet differentiable at x_0 with Fréchet derivative $f'(x_0)$.

Remark 2.3

For functions between normed vector spaces $(X, \|\cdot\|_X)$ and $(Y, \|\cdot\|_Y)$, the condition that ρ is tangent to the origin is given by

$$\lim_{h\to 0} \frac{\|\rho(h)\|_Y}{\|h\|_X} = 0, \tag{2.15}$$

which leads to the usual definition of total differentiability [160, Chapter 1, Section 3].

Definition 2.4 (Partial derivatives)

Let $f\colon W \subseteq X \times Y \to Z$ be a function from an open subset W of the product $X \times Y$ of Fréchet spaces to a Fréchet space Z. The partial (Fréchet) derivative of F at $(x_0, y_0) \in W$ with respect to the first variable corresponds to the (Fréchet) derivative of the function $x \mapsto f(x, y_0)$ at x_0. We write $\partial_1 f(x_0, y_0)$ or $\partial_x f(x_0, y_0)$ for the partial derivative of f at (x_0, y_0) with respect to the first variable x. Similarly, partial derivatives with respect to other variables can be defined.

2.1.4 Multi-variable differential calculus

Let $f\colon \Omega \subseteq \mathbb{R}^n \to \mathbb{R}^m$ be a vector-valued function of several variables defined on an open subset Ω of $\mathbb{R}^n$. In this setting, Fréchet differentiability corresponds to the notion of total differentiability, while Gateaux differentiability is associated with partial differentiability. Let $\partial_j f^i(x)$ denote the partial derivative of the i-th component of f with respect to the j-th variable at some point $x \in \Omega$, i.e.,

$$\partial_j f^i(x) = \frac{\partial f^i}{\partial x^j}(x) = \lim_{t\to 0} \frac{f^i(x + te_j) - f^i(x)}{t}, \tag{2.16}$$

where f^i denotes the i-th component of the function f and e_j the j-th standard basis vector in $\mathbb{R}^n$ for $i = 1, \ldots, m$ and $j = 1, \ldots, n$. If all partial derivatives exist, then the Jacobian matrix of f at x is given by the $m \times n$ matrix

$$\mathrm{J}_f(x) = \big(\partial_j f^i(x)\big)_{i,j=1}^{m,n} = \begin{pmatrix} \partial_1 f^1(x) & \cdots & \partial_n f^1(x) \\ \vdots & \ddots & \vdots \\ \partial_1 f^m(x) & \cdots & \partial_n f^m(x) \end{pmatrix}. \tag{2.17}$$

Let f be a real-valued function, i.e., $m = 1$, that is partially differentiable up to order r. When equality of mixed partial derivatives holds, we can use the multi-index notation to refer to higher-order partial derivatives. We write

$$\partial^\alpha f = \partial_1^{\alpha_1} \cdots \partial_n^{\alpha_n} f \tag{2.18}$$

for the multi-index $\alpha = (\alpha_1, \ldots, \alpha_n) \in \mathbb{N}_0^n$ with $|\alpha| \leq r$ and $r \in \mathbb{N}_0$, where the sum of all components is denoted by $|\alpha| = \alpha_1 + \cdots + \alpha_n$. If all partial derivatives are continuous, then f is r-times continuously differentiable. If f is twice continuously differentiable, then the Hessian matrix of f at x is given by the symmetric $n \times n$ matrix

$$\mathrm{H}_f(x) = \big(\partial_i \partial_j f(x)\big)_{i,j=1}^{n,n} = \begin{pmatrix} \partial_1 \partial_1 f(x) & \cdots & \partial_1 \partial_n f(x) \\ \vdots & \ddots & \vdots \\ \partial_n \partial_1 f(x) & \cdots & \partial_n \partial_n f(x) \end{pmatrix}. \tag{2.19}$$

2.2 Function spaces and integrals

In this section, we introduce the function spaces that are relevant for shape analysis and differential equations as well as the integral notation that is used in this thesis. We refer to, e.g., Evans [100], Folland [103], Adams and Fournier [3], Atkinson and Han [20], Brezis [58], and Alt [11] for a general treatment of functional analysis and the topics discussed.

2.2.1 Continuously differentiable functions

Definition 2.5 (Continuously differentiable functions)

Let Ω be a bounded and open subset of $\mathbb{R}^n$ with boundary $\partial\Omega$ and closure $\overline{\Omega}$. For $r \in \mathbb{N}_0$, a function $f\colon \Omega \to \mathbb{R}$ is said to be r-times continuously differentiable on $\overline{\Omega}$ if it is r-times continuously differentiable on Ω and $\partial^\alpha f$ can be continuously extended to $\overline{\Omega}$ for $|\alpha| \leq r$. The space of r-times continuously differentiable functions on $\overline{\Omega}$ is denoted by $\mathrm{C}^r(\overline{\Omega})$. For $r = 0$, we obtain the space of continuous functions on $\overline{\Omega}$, which is also denoted by $\mathrm{C}(\overline{\Omega})$.

Since the image of compact sets under continuous functions is compact, every $\partial^\alpha f$ is a bounded function if $f \in \mathrm{C}^r(\overline{\Omega})$. Endowed with the C^r norm

$$\|f\|_{\mathrm{C}^r(\overline{\Omega})} = \sum_{|\alpha|\leq r} \|\partial^\alpha f\|_\infty, \quad f \in \mathrm{C}^r(\overline{\Omega}), \tag{2.20}$$

where the supremum norm of a bounded function $f\colon \overline{\Omega} \to \mathbb{R}$ is given by

$$\|f\|_\infty = \sup_{x\in\overline{\Omega}} |f(x)|, \tag{2.21}$$

the pair $(\mathrm{C}^r(\overline{\Omega}), \|\cdot\|_{\mathrm{C}^r(\overline{\Omega})})$ becomes a Banach space.

A stronger notion of continuity is given by the Hölder condition

$$|f(x) - f(y)| \leq C\,|x-y|^\gamma \quad \forall\, x, y \in \overline{\Omega}, \tag{2.22}$$

where C is some non-negative real constant and $0 < \gamma \leq 1$. Functions that satisfy (2.22) are called Hölder continuous with exponent γ and coefficient

$$[f]_{\mathrm{C}^{0,\gamma}(\overline{\Omega})} = \sup_{\substack{x,y\in\overline{\Omega}\\ x\neq y}} \frac{|f(x)-f(y)|}{|x-y|^\gamma}. \tag{2.23}$$

Definition 2.6 (Hölder spaces)

For $r \in \mathbb{N}_0$ and $0 < \gamma \leq 1$, we define the Hölder spaces on $\overline{\Omega}$ as

$$\mathrm{C}^{r,\gamma}(\overline{\Omega}) = \left\{ f \in \mathrm{C}^r(\overline{\Omega}) \,\middle|\, \forall\, \alpha \in \mathbb{N}_0^n \text{ with } |\alpha| = r : [\partial^\alpha f]_{\mathrm{C}^{0,\gamma}(\overline{\Omega})} < \infty \right\} \tag{2.24}$$

and identify the case $\gamma = 0$ with $\mathrm{C}^r(\overline{\Omega})$. We can equip $\mathrm{C}^{r,\gamma}(\overline{\Omega})$ with the $\mathrm{C}^{r,\gamma}$ norm

$$\|f\|_{\mathrm{C}^{r,\gamma}(\overline{\Omega})} = \sum_{|\alpha|\leq r} \|\partial^\alpha f\|_\infty + \sum_{|\alpha|=r} [\partial^\alpha f]_{\mathrm{C}^{0,\gamma}(\overline{\Omega})}, \quad f \in \mathrm{C}^{r,\gamma}(\overline{\Omega}), \tag{2.25}$$

such that $(\mathrm{C}^{r,\gamma}(\overline{\Omega}), \|\cdot\|_{\mathrm{C}^{r,\gamma}(\overline{\Omega})})$ is a Banach space for $\gamma > 0$. Note that the space of Lipschitz continuous functions on $\overline{\Omega}$ corresponds to $\mathrm{C}^{0,1}(\overline{\Omega})$ with $r = 0$ and $\gamma = 1$. For the case of vector-valued functions, we write $\mathrm{C}^{r,\gamma}(\overline{\Omega}, Y)$, where Y is a Banach space.

Next, we consider the case $r = \infty$, i.e., smooth functions that are infinitely differentiable. They play a significant role in the setting of smooth shape spaces (see Section 4.2).

Definition 2.7 (Smooth functions)
The space of smooth functions on $\overline{\Omega}$ is defined as the intersection

$$\mathrm{C}^\infty(\overline{\Omega}) = \bigcap_{r \in \mathbb{N}_0} \mathrm{C}^r(\overline{\Omega}). \tag{2.26}$$

Note that $\mathrm{C}^\infty(\overline{\Omega})$ is no longer a Banach space. However, it is a Fréchet space when endowed with the countable family of (semi-)norms given by

$$\|f\|_{\mathrm{C}^r} = \sum_{|\alpha| \leq r} \|\partial^\alpha f\|_\infty, \quad r \in \mathbb{N}_0, \tag{2.27}$$

for $f \in \mathrm{C}^\infty(\overline{\Omega})$.

In the following, let Ω be an open subset of $\mathbb{R}^n$, which is not necessarily bounded. The above function spaces can also be constructed for functions defined on Ω. However, some additional structures might not exist after. Note that the function space $\mathrm{C}^r(\Omega)$, endowed with another kind of family of (semi-)norms, is still a Fréchet space for $r \in \mathbb{N}_0 \cup \{\infty\}$.

Definition 2.8 (Compact support)
A function $f \colon \Omega \to \mathbb{R}$ is said to have compact support if its closed support given by

$$\operatorname{supp}(f) = \overline{\{x \in \Omega \mid f(x) \neq 0\}} \tag{2.28}$$

is a compact subset of Ω. Let $\mathrm{C}^r_\mathrm{c}(\Omega)$ denote the subspace of all functions in $\mathrm{C}^r(\Omega)$ that have compact support, where $r \in \mathbb{N}_0 \cup \{\infty\}$.

Even if $\overline{\Omega}$ is not compact, the C^r norm can be defined for such functions, provided that $r < \infty$. We have that $(\mathrm{C}^r_\mathrm{c}(\Omega), \|\cdot\|_{\mathrm{C}^r(\Omega)})$ is a Banach space for $r < \infty$. The case $r = \infty$ is important for defining weak and distributional derivatives when the function space is endowed with the canonical LF topology, which stands for the limit of Fréchet spaces.

Weak derivatives generalize the concept of derivatives to integrable functions that are not assumed to be differentiable in the classical sense. In order to define them, it is essential to introduce integration on measure spaces first.

2.2.2 Lebesgue spaces

Let (Ω, Σ, μ) be a measure space with underlying set Ω, σ-algebra $\Sigma \subseteq \mathscr{P}(\Omega)$, and measure $\mu \colon \Sigma \to [0, \infty]$. A subset S of Ω is called μ-measurable if it is an element of Σ. A function $f \colon S \to \overline{\mathbb{R}}$ is said to be μ-measurable if the pre-image of any open subset of $\overline{\mathbb{R}}$ under f is μ-measurable. We write

$$\int_S f \,\mathrm{d}\mu = \int_S f(x) \,\mathrm{d}\mu(x) = \int_S f(x) \,\mathrm{d}x \tag{2.29}$$

for the Lebesgue integral of a μ-measurable function $f \colon S \to \overline{\mathbb{R}}$ over a μ-measurable subset $S \subseteq \Omega$ and use the notation $\mathrm{d}x$ instead of $\mathrm{d}\mu(x)$ if the measure μ is clear from the context. Properties of the integral and more information on measure and integration theory can be found in many resources, e.g., Folland [103] and Schilling [227].

Definition 2.9 (Lebesgue spaces)

Let (Ω, Σ, μ) be a measure space. We define the function spaces

$$\begin{aligned} \mathscr{L}^p(\Omega) &= \left\{ f\colon \Omega \to \overline{\mathbb{R}} \ \mu\text{-measurable} \,\middle|\, \int_\Omega |f|^p \,\mathrm{d}\mu < \infty \right\}, \quad 1 \le p < \infty, \\ \mathscr{L}^\infty(\Omega) &= \left\{ f\colon \Omega \to \overline{\mathbb{R}} \ \mu\text{-measurable} \,\middle|\, \operatorname*{ess\,sup}_{x\in\Omega} |f(x)| < \infty \right\}, \end{aligned} \tag{2.30}$$

where the essential supremum of some μ-measurable function $f\colon \Omega \to \overline{\mathbb{R}}$ is given by

$$\operatorname*{ess\,sup}_{x\in\Omega} |f(x)| = \inf \left\{ \sup_{x\in\Omega\setminus N} |f(x)| \,\middle|\, N \in \Sigma,\, \mu(N) = 0 \right\}. \tag{2.31}$$

The Lebesgue space $\mathrm{L}^p(\Omega)$ is the quotient space of $\mathscr{L}^p(\Omega)$ by the equivalence relation

$$f \sim g \quad \Leftrightarrow \quad f = g \quad \mu\text{-a.e.}, \tag{2.32}$$

i.e., $\mathrm{L}^p(\Omega) = \mathscr{L}^p(\Omega)/\!\sim$. Endowed with the L^p (Lebesgue) norms

$$\begin{aligned} \|f\|_{\mathrm{L}^p(\Omega)} &= \left(\int_\Omega |f|^p \,\mathrm{d}\mu \right)^{\frac{1}{p}}, \quad 1 \le p < \infty, \\ \|f\|_{\mathrm{L}^\infty(\Omega)} &= \operatorname*{ess\,sup}_{x\in\Omega} |f(x)|, \end{aligned} \tag{2.33}$$

Lebesgue spaces are Banach spaces. For $p = 2$, we can define the inner product

$$\langle f, g \rangle_{\mathrm{L}^2(\Omega)} = \int_\Omega f g \,\mathrm{d}\mu, \quad f, g \in \mathrm{L}^2(\Omega), \tag{2.34}$$

on $\mathrm{L}^2(\Omega)$. With respect to this inner product, $(\mathrm{L}^2(\Omega), \langle \,\cdot\,, \,\cdot\, \rangle_{\mathrm{L}^2(\Omega)})$ is a Hilbert space with the same topology as $(\mathrm{L}^2(\Omega), \|\cdot\|_{\mathrm{L}^2(\Omega)})$. Functions in $\mathrm{L}^2(\Omega)$ are called square integrable. If (Ω, Σ, μ) is a topological measure space, we define the space of locally integrable functions on Ω as

$$\mathrm{L}^1_{\mathrm{loc}}(\Omega) = \left\{ f\colon \Omega \to \overline{\mathbb{R}} \ \mu\text{-measurable} \,\middle|\, \forall\, K \subseteq \Omega \text{ compact} : f|_K \in \mathrm{L}^1(K) \right\}. \tag{2.35}$$

Weak derivatives lie in this space as described in the next part.

2.2.3 Sobolev spaces

Let Ω be an open subset of $\mathbb{R}^n$. In this thesis, we consider the topological measure space $(\Omega, \mathscr{B}(\Omega), \lambda)$ for subsets of the Euclidean space, where $\mathscr{B}(\Omega)$ denotes the Borel σ-algebra and λ the Lebesgue measure on $\mathscr{B}(\Omega)$.

Definition 2.10 (Weak derivatives)

The weak α-th (partial) derivative of a locally integrable function $f \in \mathrm{L}^1_{\mathrm{loc}}(\Omega)$ is given by the locally integrable function $g \in \mathrm{L}^1_{\mathrm{loc}}(\Omega)$ that satisfies

$$\int_\Omega f\, \partial^\alpha \varphi \,\mathrm{d}\lambda = (-1)^{|\alpha|} \int_\Omega g\, \varphi \,\mathrm{d}\lambda \quad \forall\, \varphi \in \mathrm{C}^\infty_{\mathrm{c}}(\Omega), \tag{2.36}$$

where $\alpha \in \mathbb{N}_0^n$ is a multi-index. If such a function exists, then it is uniquely determined, and we write $\partial^\alpha f = g$. If the weak α-th derivative of f exists for all $\alpha \in \mathbb{N}_0^n$ with $|\alpha| \le r$, then f is said to be r-times weakly differentiable. The space of r-times weakly differentiable functions on Ω is denoted by $\mathrm{W}^{r,1}_{\mathrm{loc}}(\Omega)$.

Note that if $f \in \mathrm{C}^r(\Omega)$ is r-times continuously differentiable in the classical sense and has locally integrable partial derivatives, i.e., $\partial^\alpha f \in \mathrm{L}^1_{\mathrm{loc}}(\Omega)$ for $|\alpha| \leq r$, then weak derivatives of f exist and coincide with classical derivatives.

Definition 2.11 (Sobolev spaces)

For $r \in \mathbb{N}_0$ and $1 \leq p \leq \infty$, we define the Sobolev spaces on Ω as

$$\mathrm{W}^{r,p}(\Omega) = \Big\{ f \in \mathrm{W}^{r,1}_{\mathrm{loc}}(\Omega) \;\Big|\; \forall\, \alpha \in \mathbb{N}_0^n \text{ with } |\alpha| \leq r \colon \partial^\alpha f \in \mathrm{L}^p(\Omega) \Big\}. \tag{2.37}$$

Endowed with the $\mathrm{W}^{r,p}$ (Sobolev) norms

$$\begin{aligned} \|f\|_{\mathrm{W}^{r,p}(\Omega)} &= \left(\sum_{|\alpha| \leq r} \|\partial^\alpha f\|^p_{\mathrm{L}^p(\Omega)} \right)^{\frac{1}{p}}, \quad 1 \leq p < \infty, \\ \|f\|_{\mathrm{W}^{r,\infty}(\Omega)} &= \max_{|\alpha| \leq r} \|\partial^\alpha f\|_{\mathrm{L}^\infty(\Omega)}, \end{aligned} \tag{2.38}$$

Sobolev spaces are Banach spaces. For $p = 2$, the Sobolev space $\mathrm{H}^r(\Omega) = \mathrm{W}^{r,2}(\Omega)$ is a Hilbert space with inner product

$$\langle f, g \rangle_{\mathrm{H}^r(\Omega)} = \sum_{|\alpha| \leq r} \langle \partial^\alpha f, \partial^\alpha g \rangle_{\mathrm{L}^2(\Omega)}, \quad f, g \in \mathrm{H}^r(\Omega). \tag{2.39}$$

The H^r norm in (2.38) is induced by this inner product. Moreover, a semi-norm is defined on $\mathrm{W}^{r,p}(\Omega)$ by

$$\begin{aligned} |f|_{\mathrm{W}^{r,p}(\Omega)} &= \left(\sum_{|\alpha| = r} \|\partial^\alpha f\|^p_{\mathrm{L}^p(\Omega)} \right)^{\frac{1}{p}}, \quad 1 \leq p < \infty, \\ |f|_{\mathrm{W}^{r,\infty}(\Omega)} &= \max_{|\alpha| = r} \|\partial^\alpha f\|_{\mathrm{L}^\infty(\Omega)}. \end{aligned} \tag{2.40}$$

According to the Meyers–Serrin theorem [178], the function space $\mathrm{C}^\infty(\Omega) \cap \mathrm{W}^{r,p}(\Omega)$ is a dense subspace of $\mathrm{W}^{r,p}(\Omega)$ for $1 \leq p < \infty$. This characterization is also commonly used for the space of Sobolev functions that are vanishing at the boundary, which is defined as the completion of $\mathrm{C}^\infty_{\mathrm{c}}(\Omega)$ in $\mathrm{W}^{r,p}(\Omega)$ with respect to the $\mathrm{W}^{r,p}$ norm, i.e.,

$$\mathrm{W}^{r,p}_0(\Omega) = \Big\{ f \in \mathrm{W}^{r,p}(\Omega) \;\Big|\; \exists\, (f_i)_{i \in \mathbb{N}} \subset \mathrm{C}^\infty_{\mathrm{c}}(\Omega) : \lim_{i \to \infty} \|f_i - f\|_{\mathrm{W}^{r,p}(\Omega)} = 0 \Big\}, \tag{2.41}$$

for $1 \leq p < \infty$. It is a closed subspace of $\mathrm{W}^{r,p}(\Omega)$. We write $\mathrm{H}^r_0(\Omega)$ for $\mathrm{W}^{r,2}_0(\Omega)$.

2.2.4 Types of regular domains

Some important results on Sobolev spaces hold if the domain Ω of the function space is bounded with a "sufficiently regular" boundary $\partial\Omega$. Existence and regularity of solutions to differential equations also often depend on the regularity of $\partial\Omega$. In the following, we specify what is meant by a regular domain and state the different kinds of regularity for bounded domains. Note that the term "domain" refers to connected and open subsets of the Euclidean space.

Definition 2.12 (Regular domains)

Let $\Omega \subset \mathbb{R}^n$ be a bounded domain, i.e., a bounded, connected, and open subset of $\mathbb{R}^n$, with

boundary $\partial\Omega$ and closure $\overline{\Omega}$. For $r \in \mathbb{N}_0$ and $0 \leq \gamma \leq 1$, we say that Ω is a regular $\mathrm{C}^{r,\gamma}$ domain if for all $s \in \partial\Omega$, there is a radius $\delta > 0$, a local coordinate chart $y\colon \mathrm{B}_\delta^n(s) \to \mathrm{B}_\delta^n(0)$ with $y(x) = Q(x-s)$ for an orthogonal matrix $Q \in \mathbb{R}^{n\times n}$, and a function $g \in \mathrm{C}^{r,\gamma}(\overline{\mathrm{B}_\delta^{n-1}(0)})$ such that

$$\Omega \cap \mathrm{B}_\delta^n(s) = \Big\{ x \in \mathrm{B}_\delta^n(s) \;\Big|\; y_n(x) < g\big(y_1(x), \dots, y_{n-1}(x)\big) \Big\}, \tag{2.42}$$

where $\mathrm{B}_\delta^n(x)$ denotes an open ball in $\mathbb{R}^n$. A regular $\mathrm{C}^{0,1}$ domain is referred to as a Lipschitz domain or a domain with Lipschitz boundary. If $g \in \mathrm{C}^\infty(\overline{\mathrm{B}_\delta^{n-1}(0)})$, we call Ω a domain with smooth boundary.

The property (2.42) states that $\partial\Omega$ can be locally expressed as the graph of $\mathrm{C}^{r,\gamma}$ functions. Note that if Ω is a Lipschitz domain, then the outward-pointing unit normal to $\partial\Omega$ exists almost everywhere. Furthermore, the trace operator can be defined [20, Theorem 6.3.10], which extends the notion of the restriction to the boundary to functions in $\mathrm{W}^{1,p}(\Omega)$ for $1 \leq p < \infty$. We write $f|_{\partial\Omega} \in \mathrm{L}^p(\partial\Omega)$ for the trace or restriction of $f \in \mathrm{W}^{1,p}(\Omega)$ to $\partial\Omega$.

2.2.5 Geometric transformations

Geometric transformations can be used to express functions defined on some initial domain with respect to another, compatible one. When working with integrals, we have to ensure that the transformed functions are still integrable and regular in the same fashion as the original ones, so that problems resulting from a domain transformation are equivalent to the original problems posed on the initial domain. In the following, we discuss conditions on geometric transformations that establish the equivalence.

First, we state a corollary of a more general theorem in Varberg [264] regarding the change of variables formula for integrals:

Proposition 2.13 (Change of variables)

Let $\varphi\colon \Omega \to \mathbb{R}^n$ be Lipschitz continuous on an open subset Ω of $\mathbb{R}^n$. If the mapping φ is injective on some subset of Ω whose complement in Ω has measure zero, then

$$\int_{\varphi(S)} f(y)\,\mathrm{d}y = \int_S f(\varphi(x))|\det \mathrm{J}_\varphi(x)|\,\mathrm{d}x \tag{2.43}$$

holds for every measurable subset S of Ω and $f \in \mathrm{L}^1(\varphi(S))$.

Proof. We refer to [264, Corollary 2]. □

We consider two relevant classes of geometric transformations that preserve the regularity of functions: bi-Lipschitz transformations and diffeomorphisms with bounded derivatives.

Proposition 2.14 (Bi-Lipschitz transformations)

Let $\varphi\colon \Omega_0 \to \Omega$ be a bi-Lipschitz transformation between two bounded domains in $\mathbb{R}^n$, i.e.,

$$\varphi \text{ is invertible with } \varphi \in \mathrm{C}^{0,1}(\overline{\Omega}_0, \mathbb{R}^n) \text{ and } \varphi^{-1} \in \mathrm{C}^{0,1}(\overline{\Omega}, \mathbb{R}^n). \tag{2.44}$$

Then the Lebesgue space $\mathrm{L}^p(\Omega)$ is transformed boundedly to $\mathrm{L}^p(\Omega_0)$ via the composition operator associated with φ, i.e., for $f \in \mathrm{L}^p(\Omega)$, we have $(f \circ \varphi) \in \mathrm{L}^p(\Omega_0)$, for $1 \leq p < \infty$. This also holds for functions in $\mathrm{W}^{1,p}(\Omega)$.

Proof. A proof can be found in [195, Lemma 3.1 and 3.2, p. 60]. □

A stronger result holds for diffeomorphisms with bounded derivatives. In this case, the domains are not required to be bounded. The order of differentiability is preserved and the case $p = \infty$ is also included.

Proposition 2.15 (Diffeomorphisms with bounded derivatives)
For $r \geq 1$, let $\varphi\colon \Omega_0 \to \Omega$ be a C^r diffeomorphism with bounded derivatives, i.e.,

$$\varphi \text{ is invertible with } \varphi \in \mathrm{C}^r(\overline{\Omega}_0, \mathbb{R}^n) \text{ and } \varphi^{-1} \in \mathrm{C}^r(\overline{\Omega}, \mathbb{R}^n), \tag{2.45}$$

and there are some constants $0 < c < C$ such that for all $x \in \Omega_0$, we have that

$$c \leq |\det \mathrm{J}_\varphi(x)| \leq C. \tag{2.46}$$

Then the Sobolev space $\mathrm{W}^{r,p}(\Omega)$ is transformed boundedly to $\mathrm{W}^{r,p}(\Omega_0)$ via the composition operator associated with φ, i.e., if $f \in \mathrm{W}^{r,p}(\Omega)$, then $(f \circ \varphi) \in \mathrm{W}^{r,p}(\Omega_0)$, for $1 \leq p \leq \infty$. Furthermore, the composition operator

$$\varphi^*\colon \mathrm{W}^{r,p}(\Omega) \to \mathrm{W}^{r,p}(\Omega_0), \quad f \mapsto (f \circ \varphi), \tag{2.47}$$

has a bounded inverse and the following chain rule holds for the first weak derivatives:

$$\partial_i(f \circ \varphi) = \sum_{j=1}^{n} (\partial_j f \circ \varphi)\, \partial_i \varphi^j, \quad i = 1, \dots, n. \tag{2.48}$$

Proof. We refer to [3, Theorem 3.41] for the claim regarding the composition operator and [11, Section 2.26] for the chain rule. □

We use the term "pullback" for the operator φ^* and "pushforward" for the derivative of φ, which is also denoted by $\varphi_* = \delta\varphi$. If f is an integrable function on Ω, then the pullback of f by φ is given by its image under φ^*, i.e.,

$$\hat{f} = \varphi^*(f) = f \circ \varphi. \tag{2.49}$$

Geometric transformations can thus pull back quantities defined on the domain Ω to the initial domain Ω_0 and push forward tangent vectors from Ω_0 to Ω. In the next section, we discuss this terminology in the setting of differentiable manifolds with more details.

2.3 Manifolds, bundles, and tensors

This section introduces the necessary concepts and language from differential geometry that are used throughout this thesis. We mostly follow the approach in Kriegl and Michor [159] and Lang [160], since we are also dealing with infinite-dimensional manifolds. Other main references include do Carmo [89], Marsden and Hughes [174], Jänich [144], O'Neill [202], Michor [180], Lee [162], Tu [261], and Lee [163].

2.3.1 Differentiable manifolds

Definition 2.16 (Charts)

Let M be a set and X be a topological vector space. An X-valued chart on M is a bijection $x\colon U \to V$ from a subset U of M to an open subset V of X. We write (U, x) instead of x for the chart to emphasize its domain of definition. A chart that contains some point $p \in M$ (or some subset of M) is said to be a chart around that point (or the subset of M, respectively).

Definition 2.17 (Atlases)

Let M be a set, $r \in \mathbb{N}_0 \cup \{\infty\}$, and $\mathcal{A}$ be an index set.

a) A family of charts $(U_\alpha, x_\alpha)_{\alpha\in\mathcal{A}}$ on M with respective values in $(X_\alpha)_{\alpha\in\mathcal{A}}$ is called a C^r atlas on M with values in $(X_\alpha)_{\alpha\in\mathcal{A}}$ if the following conditions are satisfied:

(i) The domains of definition constitute a cover of M, i.e., $M = \bigcup_{\alpha\in\mathcal{A}} U_\alpha$.

(ii) Subsets of the form $x_\alpha(U_\alpha \cap U_\beta)$ for $\alpha, \beta \in \mathcal{A}$ are open in X_α.

(iii) For $\alpha, \beta \in \mathcal{A}$ with non-empty intersection $U_\alpha \cap U_\beta$, the transition mapping

$$x_\beta \circ x_\alpha^{-1} \colon x_\alpha(U_\alpha \cap U_\beta) \to x_\beta(U_\alpha \cap U_\beta) \tag{2.50}$$

is a C^r diffeomorphism.

b) Two C^r atlases on M are C^r compatible if their union is a C^r atlas on M.

c) A C^r structure on M is an equivalence class of C^r atlases on M by C^r compatibility. It can be represented by a maximal C^r atlas, which is the union of all C^r atlases in the equivalence class and contains every C^r atlas compatible to it.

d) The topology induced by a C^r structure is given by the coarsest topology on M that makes all charts in the maximal C^r atlas continuous. It is the final topology with respect to inverses of the charts and referred to as the C^r manifold topology.

Definition 2.18 (Manifolds)

A C^r manifold modeled on $(X_\alpha)_{\alpha\in\mathcal{A}}$ is a topological space whose topology is induced by a C^r structure with values in the model spaces $(X_\alpha)_{\alpha\in\mathcal{A}}$. When charts on a C^r manifold are discussed, we assume that they are contained in the C^r structure of the manifold, i.e., in the maximal C^r atlas. A C^∞ manifold is also called a smooth manifold.

Remark 2.19

Every C^1 manifold is C^1 diffeomorphic to a C^∞ manifold [132, 180], so it suffices to treat smooth manifolds (in the finite-dimensional case). Note that not every C^0 manifold admits a C^1 structure. In this thesis, the term "manifold" is used to refer to a smooth manifold. For manifolds with boundary, we refer to the standard references on differential geometry.

Remark 2.20 (Model spaces)

Let M be a manifold modeled on $(X_\alpha)_{\alpha\in\mathcal{A}}$.

a) If the model spaces are Fréchet spaces, then M is called a Fréchet manifold.

b) If the model spaces are Banach spaces, then M is called a Banach manifold.

c) If the model spaces are Hilbert spaces, then M is called a Hilbert manifold.

d) If the model spaces are finite-dimensional of the same dimension $m \in \mathbb{N}_0$, then M is called an m-dimensional manifold. In this case, each model space can be identified with the real coordinate space $\mathbb{R}^m$.

Remark 2.21 (Local coordinate chart)

Points in a finite-dimensional manifold can locally be expressed in terms of finitely many coordinates once a chart around them has been chosen. The local coordinates of a point $p \in M$ in a manifold of dimension m with respect to some chart (U, x) around p are given by the components of $x(p) = (x^1(p), \ldots, x^m(p))$.

2.3.2 Mappings between manifolds

Let $f\colon M \to N$ be a mapping between manifolds. Its representation in local coordinates with respect to a chart (U, x) on M and a chart (V, y) on N with $f(U) \subseteq V$ is given by the composite mapping

$$y \circ f \circ x^{-1}\colon x(U) \to y(V). \tag{2.51}$$

Mappings between manifolds are characterized by their representation in local coordinates. Properties of the representation can be transferred to the mapping if they are independent of the choice of charts. A mapping between manifolds is of class C^r at some point $p \in M$ if its representation $y \circ f \circ x^{-1}$ is of class C^r at $x(p)$ for every choice of charts (U, x) around p and (V, y) around $f(p)$ with $f(U) \subseteq V$. In this particular case, if f is of class C^r with respect to some representation, then it is of class C^r with respect to all of them, so it suffices to check the property for a single representation. We say that f is a C^r mapping if it is of class C^r at every point of M, or equivalently, if its representation is of class C^r for some choice of atlas. Let $\mathrm{C}^r(M, N)$ denote the space of C^r mappings from M to N and $\mathrm{C}^r(M)$ the space of C^r scalar fields on M, i.e., real-valued C^r functions on M. The space of germs of C^r scalar fields at p, denoted by $\mathrm{C}^r_p(M)$, refers to the algebra of equivalence classes of C^r scalar fields on M that coincide on a neighborhood of p.

2.3.3 Tangent vectors and derivations

Let M be a manifold and $p \in M$.

a) A tangent vector of M at p is an equivalence class of (smooth) paths in M passing through p at 0. Two such paths γ and δ are said to be (tangentially) equivalent if for every chart (U, x) around p, we have that $(x \circ \gamma)'(0) = (x \circ \delta)'(0)$. The set of all tangent vectors of M at p constitutes the tangent space T_pM, which is a vector space isomorphic to the model space of the manifold.

b) A tangent vector $v \in \mathrm{T}_pM$ induces a derivation on $\mathrm{C}^\infty_p(M)$ through the mapping

$$v\colon \mathrm{C}^\infty_p(M) \to \mathbb{R}, \quad [h]_p \mapsto (h \circ \gamma)'(0), \tag{2.52}$$

where γ is a representative path corresponding to v. We write D_pM for the vector space of derivations on $\mathrm{C}^\infty_p(M)$, which consists of (bounded) linear mappings that satisfy the product rule. If M is finite-dimensional, then D_pM can be identified with T_pM and both have the same dimension as M, i.e., derivations on $\mathrm{C}^\infty_p(M)$ are in one-to-one correspondence with tangent vectors of M at p. Otherwise, we regard T_pM as a vector subspace of D_pM.

c) The tangent bundle of M is the vector bundle of tangent spaces of M given by

$$\mathrm{T}M = \coprod_{p \in M} \mathrm{T}_pM = \big\{(p, v) \,\big|\, p \in M,\, v \in \mathrm{T}_pM\big\}. \tag{2.53}$$

It is the total space of a vector bundle with base space M and bundle projection $\pi_M\colon \mathrm{T}M \to M$, $(p, v) \mapsto p$. Similarly, the bundle of derivations on $\mathrm{C}^\infty(M)$ is given by the vector bundle

$$\mathrm{D}M = \coprod_{p \in M} \mathrm{D}_pM = \big\{(p, v) \,\big|\, p \in M,\, v \in \mathrm{D}_pM\big\}. \tag{2.54}$$

If M is finite-dimensional, then $\mathrm{D}M$ can be identified with the tangent bundle $\mathrm{T}M$ and both constitute a manifold with twice the dimension of M. Otherwise, we regard $\mathrm{T}M$ as a vector subbundle of $\mathrm{D}M$.

2.3.4 Differentials and tangent mappings

A differentiable mapping $f\colon M \to N$ between manifolds induces a linear mapping for each $p \in M$ via

$$\mathrm{D}_p f\colon \mathrm{D}_p M \to \mathrm{D}_{f(p)} N, \quad v \mapsto f_*(p)v, \tag{2.55}$$

called the differential of f at p, where $f_*(p)v$ is the pushforward of v by f at p given by

$$(f_*(p)v)[h]_{f(p)} = v(f^*(p)h) = v[h \circ f]_p \tag{2.56}$$

for $[h]_{f(p)} \in \mathrm{C}^\infty_{f(p)}(N)$ and $f^*(p)h = [h \circ f]_p \in \mathrm{C}^\infty_p(M)$ is the pullback of h by f at p. This yields a fiberwise linear bundle mapping

$$\mathrm{D}f\colon \mathrm{D}M \to \mathrm{D}N, \quad (p, v) \mapsto (f(p), f_*(p)v). \tag{2.57}$$

We write $\mathrm{D}f(p) = \mathrm{D}_p f$ for the restriction of $\mathrm{D}f$ to $\mathrm{D}_p M$ and $\mathrm{D}f(p)[v] = \mathrm{D}_p f(v) \in \mathrm{D}_{f(p)} N$ for $(p, v) \in \mathrm{D}M$.

The restriction of $\mathrm{D}f$ to the tangent bundle $\mathrm{T}f\colon \mathrm{T}M \to \mathrm{T}N$ is referred to as the tangent mapping of f. If $f \in \mathrm{C}^1(M, E)$ for some topological vector space E over $\mathbb{R}$, then we can identify $\mathrm{D}E$ with $E \times \mathrm{D}_0 E$ and consider the projection onto the second component

$$\mathrm{d}f\colon \mathrm{D}M \to \mathrm{D}_0 E, \quad (p, v) \mapsto f_*(p)v, \tag{2.58}$$

as the (total) derivative of f. It restricts to a fiberwise linear mapping $\mathrm{d}f\colon \mathrm{T}M \to E$. For $f \in \mathrm{C}^1(M)$, we have $\mathrm{d}f\colon \mathrm{D}M \to \mathbb{R}$ with $\mathrm{d}f(p, v) = v[f]_p$. We also write $\mathrm{d}f(p) = \mathrm{d}_p f$ for the restriction of $\mathrm{d}f$ to $\mathrm{D}_p M$ and $\mathrm{d}f(p)[v] = \mathrm{d}_p f(v) \in \mathrm{D}_0 E$ for $(p, v) \in \mathrm{D}M$.

2.3.5 Immersions and submersions

Let $f \in \mathrm{C}^1(M, N)$ be a continuously differentiable mapping between manifolds and $p \in M$.

a) If M and N are finite-dimensional, then the rank of f at p is defined as the rank of its derivative at p.

b) If $\mathrm{D}f(p)$ is injective, then f is called an immersion at p. A C^r immersion is a C^r mapping between manifolds that is an immersion at every point of its domain. We write $\mathrm{Imm}_{\mathrm{C}^r}(M, N)$ for the space of C^r immersions of M in N. Note that, in the finite-dimensional case, being an immersion is equivalent to the having constant rank equal to the dimension of its domain.

c) If $\mathrm{D}f(p)$ is surjective, then f is called a submersion at p. A C^r submersion is a C^r mapping between manifolds that is a submersion at every point of its domain. We write $\mathrm{Sub}_{\mathrm{C}^r}(M, N)$ for the space of C^r submersions of M in N. Note that, in the finite-dimensional case, being a submersion is equivalent to having constant rank equal to the dimension of its codomain.

d) A C^r diffeomorphism refers to a bijective C^r mapping with C^r inverse. We write $\mathrm{Diff}_{\mathrm{C}^r}(M, N)$ for the space of C^r diffeomorphisms from M to N and $\mathrm{Diff}_{\mathrm{C}^r}(M)$ as a shorthand for $\mathrm{Diff}_{\mathrm{C}^r}(M, M)$.

e) A C^r embedding refers to an injective C^r immersion that is a C^r diffeomorphism onto its image. We write $\mathrm{Emb}_{\mathrm{C}^r}(M, N)$ for the space of C^r embeddings of M in N.

If there is a C^1 diffeomorphism between finite-dimensional manifolds, then there is a C^∞ diffeomorphism between them [132, 180].

2.3.6 Bundles and sections

In the following, we consider bundles and sections in the category of smooth manifolds.

Let $\pi\colon E \to B$ be a surjective mapping between manifolds. If π satisfies the local product property (or local triviality condition) that, for each $b \in B$, there is an open neighborhood $U \subseteq B$ of b and a diffeomorphism $\varphi\colon \pi^{-1}(U) \to U \times X_b$ with $\pi = \mathrm{pr}_1 \circ \varphi$, i.e., the following diagram commutes:

$$\begin{array}{ccc} \pi^{-1}(U) & \xrightarrow{\varphi} & U \times X_b, \\ {\scriptstyle\pi}\big\downarrow & \swarrow_{\mathrm{pr}_1} & \\ U & & \end{array}$$

where X_b is a manifold and $\mathrm{pr}_1\colon U \times X_b \to U$ is the projection onto the first factor, then (E, B, π) is called a fiber bundle with total space E, base space B, and bundle projection π. A diffeomorphism with the above property is referred to as a bundle chart (or local trivialization) of the fiber bundle and the corresponding open neighborhood is called a trivializing neighborhood. The preimage $E_b = \pi^{-1}(\{b\})$ is diffeomorphic to X_b for all $b \in B$ and is called the fiber over b.

A section of a fiber bundle (E, B, π) is a mapping $s\colon B \to E$ that is a right inverse of the bundle projection, i.e., $\pi \circ s = \mathrm{id}_B$, where id_B denotes the identity mapping on B. The space of sections of the fiber bundle is denoted by $\Gamma(E)$.

Let $f\colon A \to B$ be a mapping between manifolds. The pullback of a fiber bundle (E, B, π) by f is defined as the fiber bundle $(f^*E, A, f^*\pi)$ with total space

$$f^*E = \big\{(a, e) \in A \times E \;\big|\; \pi(e) = f(a)\big\}, \tag{2.59}$$

base space A, and bundle projection $f^*\pi\colon f^*E \to A$, $(a, e) \mapsto a$. The projection onto the second factor yields a bundle mapping $\mathrm{pr}_2\colon f^*E \to E$ such that the following diagram commutes:

$$\begin{array}{ccc} f^*E & \xrightarrow{\mathrm{pr}_2} & E \\ {\scriptstyle f^*\pi}\big\downarrow & & \big\downarrow{\scriptstyle\pi} \\ A & \xrightarrow{f} & B. \end{array}$$

Sections of the pullback bundle f^*E are referred to as sections of E over f and can be identified with mappings $s\colon A \to E$ that satisfy $\pi \circ s = f$. We write

$$\Gamma_f(E) = \big\{s\colon A \to E \;\big|\; \pi \circ s = f\big\} \simeq \Gamma(f^*E) \tag{2.60}$$

for the space of sections of E over f. If $f|_D\colon D \subseteq A \to B$ is the restriction of f to an open subset D of A, then we write $\Gamma_f(D, E) = \Gamma_{f|_D}(E) \simeq \Gamma((f|_D)^*E)$. In particular, if $A = B$, f is the identity mapping id_B, and $\iota_D = (\mathrm{id}_B)|_D$ is its restriction to an open subset D of B, i.e., the inclusion mapping of D in B, we have that

$$\Gamma(D, E) = \Gamma_{\mathrm{id}_B}(D, E) = \Gamma_{\iota_D}(E) \simeq \Gamma((\iota_D)^*E) \simeq \Gamma(E|_D), \tag{2.61}$$

where $E|_D = \pi^{-1}(D)$ is the total space and $\pi_D = \pi|_{\pi^{-1}(D)}$ is the bundle projection of the fiber bundle $(E|_D, D, \pi_D)$ with base space D, called the restriction of (E, B, π) to D.

Let (E, B, π_E) and (F, B, π_F) be fiber bundles over the same base space. Then $E \times F$ is the total space of a (product) fiber bundle over $B \times B$ with bundle projection

$$(\pi_E \times \pi_F)\colon E \times F \to B \times B, \quad (v, w) \mapsto (\pi_E(v), \pi_F(w)). \tag{2.62}$$

The fiber product (or Whitney sum) of E and F is defined as the pullback of

$$(E \times F, B \times B, \pi_E \times \pi_F) \tag{2.63}$$

by the diagonal mapping $\delta\colon B \to B \times B$, $b \mapsto (b, b)$. Its total space can be identified with

$$E \times_B F \simeq \big\{(v, w) \in E \times F \;\big|\; \pi_E(v) = \pi_F(w)\big\}. \tag{2.64}$$

Similarly, we can define the fiber product of finitely many fiber bundles.

A fiber bundle (E, B, π) is called a vector bundle if each fiber E_b is modeled on a topological vector space X_b, i.e., E_b is given a topological vector space structure such that the restriction of each bundle chart

$$\varphi_b\colon E_b \to \{b\} \times X_b \simeq X_b \tag{2.65}$$

around $b \in B$ is a continuous linear isomorphism between E_b and the model space X_b. A vector bundle is a topological vector space and a $\mathrm{C}^\infty(M)$-module under fiberwise vector addition and scalar multiplication. If the model spaces are finite-dimensional of the same dimension $k \in \mathbb{N}_0$, then M is said to be a vector bundle of rank k.

The dual vector bundle is defined as the vector bundle (E^*, B, π^*) with total space

$$E^* = \big\{(b, w) \;\big|\; b \in B,\, w \in E_b^*\big\}, \tag{2.66}$$

base space B, and bundle projection $\pi^*\colon E^* \to B$, $(b, w) \mapsto b$. For the space of sections of E^*, there is a canonical isomorphism of $\mathrm{C}^\infty(B)$-modules

$$\Gamma(E^*) \simeq \Gamma(E)^*. \tag{2.67}$$

See, e.g., Conlon [74, Theorem 7.5.4]. For more information on fiber bundles, we also refer to Husemoller [139].

2.3.7 Tensor product spaces

Let V and W be vector spaces. The tensor product $\otimes$ and the tensor product space $V \otimes W$ are characterized by the universal property that, for any bilinear function $f\colon V \times W \to Z$ to a vector space Z, there is a unique linear function $\tilde{f}\colon V \otimes W \to Z$ such that

$$\tilde{f}(v \otimes w) = f(v, w) \tag{2.68}$$

for all $v \in V$ and $w \in W$, i.e., the following diagram commutes:

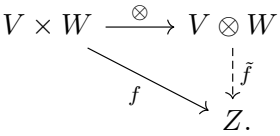

The tensor product is associative and commutative in the sense that

$$(V \otimes W) \otimes Z \simeq V \otimes (W \otimes Z), \quad V \otimes W \simeq W \otimes V \tag{2.69}$$

for vector spaces V, W, and Z, where $\simeq$ denotes a (linear) isomorphic relation.

The space of linear functions $\mathrm{L}(V \otimes W; Z)$ can be identified with the space of bilinear functions $\mathrm{L}(V, W; Z)$ via the (natural) linear isomorphism

$$\mathrm{L}(V \otimes W; Z) \to \mathrm{L}(V, W; Z), \quad \tilde{f} \mapsto \Big((v, w) \mapsto \tilde{f}(v \otimes w)\Big), \tag{2.70}$$

and its inverse

$$\mathrm{L}(V,W;Z) \to \mathrm{L}(V\otimes W;Z), \quad f \mapsto \Big((v\otimes w)\mapsto f(v,w)\Big). \tag{2.71}$$

The latter is obtained from the universal property of tensor products. For $f \in \mathrm{L}(V,W;Z)$, there is a unique $\tilde{f} \in \mathrm{L}(V\otimes W;Z)$ such that $\tilde{f}(v\otimes w) = f(v,w)$ for all $v \in V$ and $w \in W$. The abuse of notation $(v\otimes w)\mapsto f(v,w)$ refers to the linear form $u \mapsto \tilde{f}(u)$.

We have that $\mathbb{R}\otimes V \simeq V$ via the linear isomorphism $\mathbb{R}\otimes V \to V$ defined by

$$(r\otimes v)\mapsto rv. \tag{2.72}$$

There is also linear isomorphism $V \to \mathrm{L}(\mathbb{R};V)$ with

$$v \mapsto \Big(r \mapsto rv\Big). \tag{2.73}$$

Furthermore, a linear injection $V^*\otimes W \to \mathrm{L}(V;W)$ is given by

$$(\alpha\otimes w)\mapsto \Big(v\mapsto \alpha(v)w\Big). \tag{2.74}$$

It is a linear isomorphism in the finite-dimensional case, i.e., $V^*\otimes W \simeq \mathrm{L}(V;W)$, but not surjective in general.

There are linear injections $V^*\otimes W^* \to \mathrm{L}(V;W^*) \to (V\otimes W)^*$ given by the functions

$$(\alpha\otimes\beta)\mapsto \Big(v\mapsto \alpha(v)\beta\Big)\mapsto \Big((v\otimes w)\mapsto \alpha(v)\beta(w)\Big). \tag{2.75}$$

Similarly, there is a linear injection

$$W_1\otimes\cdots\otimes W_r\otimes V_1^*\otimes\cdots\otimes V_s^* \to \mathrm{L}(W_1^*,\dots,W_s^*,V_1,\dots,V_s;\mathbb{R}) \tag{2.76}$$

given by the function

$$\begin{aligned}&(w_1\otimes\cdots\otimes w_r\otimes\alpha_1\otimes\cdots\otimes\alpha_s)\\ &\qquad\mapsto \Big((\beta_1,\dots,\beta_r,v_1,\dots,v_s)\mapsto \beta_1(w_1)\cdots\beta_r(w_r)\alpha_1(v_1)\cdots\alpha_s(v_s)\Big).\end{aligned} \tag{2.77}$$

A tensor of type (r,s) over V is an element of the tensor product space

$$\mathrm{T}^{r,s}(V) = \underbrace{V\otimes\cdots\otimes V}_{r\text{ times}}\otimes\underbrace{V^*\otimes\cdots\otimes V^*}_{s\text{ times}}. \tag{2.78}$$

It induces a multilinear form

$$T\colon \underbrace{V^*\times\cdots\times V^*}_{r\text{ times}}\times\underbrace{V\times\cdots\times V}_{s\text{ times}}\to\mathbb{R}, \tag{2.79}$$

according to the linear injections above. If V is finite-dimensional of dimension n, then the components of T with respect to an ordered basis $(e_1,\dots,e_n)$ and its dual $(e^1,\dots,e^n)$ with $e^i(e_j)=\delta^i{}_j$ for $i,j\in\{1,\dots,n\}$ are given by

$$T^{i_1,\dots,i_r}{}_{j_1,\dots,j_s} = T(e^{i_1},\dots,e^{i_r},e_{j_1},\dots,e_{j_s}) \tag{2.80}$$

for $i_1,\dots,i_r,j_1,\dots,j_s\in\{1,\dots,n\}$. We also write

$$T = T^{i_1,\dots,i_r}{}_{j_1,\dots,j_s}\,(e_{i_1}\otimes\cdots\otimes e_{i_r}\otimes e^{j_1}\otimes\cdots\otimes e^{j_s}). \tag{2.81}$$

In general, a tensor refers to an element of some tensor product space.

2.3.8 Tensor bundles and fields

Let (E, B, π_E) and (F, B, π_F) be vector bundles over the same base space. The tensor product bundle $(E \otimes_B F, B, \pi_{E\otimes_B F})$ is defined as the vector bundle with total space

$$E \otimes_B F = \coprod_{b\in B} E_b \otimes F_b = \big\{(b, u) \,\big|\, b \in B,\, u \in E_b \otimes F_b\big\}, \tag{2.82}$$

base space B, and bundle projection $\pi_{E\otimes_B F}\colon E \otimes_B F \to B$, $(b, u) \mapsto b$. Similarly, we can define tensor product bundles of finitely many vector bundles over the same base space.

For the space of sections of $E \otimes_B F$, there is a canonical isomorphism of $\mathrm{C}^\infty(B)$-modules

$$\Gamma(E \otimes_B F) \simeq \Gamma(E) \otimes_{\mathrm{C}^\infty(B)} \Gamma(F). \tag{2.83}$$

See, e.g., Conlon [74, Theorem 7.5.5].

Let (E, B, π) be a vector bundle. The (fiberwise) tensor product of r copies of E and s copies of E^* constitutes a tensor bundle

$$\mathrm{T}^{r,s}(E) = \underbrace{E \otimes_B \cdots \otimes_B E}_{r \text{ times}} \otimes_B \underbrace{E^* \otimes_B \cdots \otimes_B E^*}_{s \text{ times}} \tag{2.84}$$

of type (r, s) over E with contravariant rank r and covariant rank s. A tensor field of type (r, s) over E is a section of $\mathrm{T}^{r,s}(E)$. It induces a fiberwise multilinear form

$$T\colon \underbrace{E^* \times_B \cdots \times_B E^*}_{r \text{ times}} \times_B \underbrace{E \times_B \cdots \times_B E}_{s \text{ times}} \to \mathbb{R}. \tag{2.85}$$

If E has rank n, then the components of T with respect to some local frame $(e_1, \dots, e_n)$ and the corresponding dual frame $(e^1, \dots, e^n)$ with $e^i(e_j) = \delta^i{}_j$ for $i, j \in \{1, \dots, n\}$ are given by

$$T^{i_1,\dots,i_r}{}_{j_1,\dots,j_s} = T(e^{i_1}, \dots, e^{i_r}, e_{j_1}, \dots, e_{j_s}) \in \mathrm{C}^\infty(B) \tag{2.86}$$

for $i_1, \dots, i_r, j_1, \dots, j_s \in \{1, \dots, n\}$. We can write

$$T = T^{i_1,\dots,i_r}{}_{j_1,\dots,j_s}\, (e_{i_1} \otimes \cdots \otimes e_{i_r} \otimes e^{j_1} \otimes \cdots \otimes e^{j_s}) \in \Gamma(\mathrm{T}^{r,s}(E)). \tag{2.87}$$

Let M be an m-dimensional manifold. The tangent bundle $\mathrm{T}M$ is a vector bundle with twice the dimension of M. We define the cotangent bundle of M as the dual vector bundle of $\mathrm{T}M$, i.e.,

$$\mathrm{T}^*M = \coprod_{p\in M} \mathrm{T}^*_pM = \big\{(p, w) \,\big|\, p \in M,\, w \in \mathrm{T}^*_pM\big\}, \tag{2.88}$$

where $\mathrm{T}^*_pM = (\mathrm{T}_pM)^* = \mathrm{L}(\mathrm{T}_pM; \mathbb{R})$ denotes the dual vector space of T_pM for $p \in M$.

A tensor field of type (r, s) on M is a section of the tensor bundle $\mathrm{T}^{r,s}M = \mathrm{T}^{r,s}(\mathrm{T}M)$ over the tangent bundle of M. A scalar field corresponds to a tensor field of type $(0, 0)$, a vector field is associated with a tensor field of type $(1, 0)$, and a covector field is a tensor field of type $(0, 1)$. For more information on tensor fields, we refer to Marsden and Hughes [174, Section 1.4].

2.3.9 Connections and covariant derivatives

Definition 2.22 (Linear connection)

Let (E, B, π) be a vector bundle. A linear connection on E is an $\mathbb{R}$-bilinear function

$$\nabla\colon \Gamma(\mathrm{T}B) \times \Gamma(E) \to \Gamma(E) \tag{2.89}$$

such that, for all $X \in \Gamma(\mathrm{T}B)$, $Y \in \Gamma(E)$, and $f \in \mathrm{C}^\infty(B)$, the following conditions hold:

a) $\nabla(fX, Y) = f\nabla(X, Y)$, ($\mathrm{C}^\infty(B)$-linearity in the first argument)

b) $\nabla(X, fY) = (Xf)Y + f\,\nabla(X, Y)$. (Leibniz rule in the second argument)

Instead of $\nabla(X, Y)$, we write $\nabla_X Y$ for the resulting section of E and call it the covariant derivative of Y with respect to X.

Definition 2.23 (Affine connection)

An affine connection on a manifold M is a linear connection on the tangent bundle $\mathrm{T}M$. We refer to the pair (M, ∇) as an affine manifold.

Definition 2.24 (Covariant derivative of tensor fields)

Let $X \in \Gamma(\mathrm{T}M)$ be a vector field, $\alpha \in \Gamma(\mathrm{T}^*M)$ be a covector field, and $T \in \Gamma(\mathrm{T}^{r,s}M)$ be a tensor field.

a) The covariant derivative of α with respect to X is given by the covector field $\nabla_X\alpha \in \Gamma(\mathrm{T}^*M)$ with

$$\nabla_X\alpha(Y) = X(\alpha(Y)) - \alpha(\nabla_X Y) \tag{2.90}$$

for all $Y \in \Gamma(\mathrm{T}M)$.

b) The covariant derivative of T with respect to X is given by the tensor field $\nabla_X T \in \Gamma(\mathrm{T}^{r,s}M)$ with

$$\begin{aligned}\nabla_X T(\alpha_1, \dots, \alpha_r, Y_1, \dots, Y_s) = {} & X(T(\alpha_1, \dots, \alpha_r, Y_1, \dots, Y_s)) \\ & - T(\nabla_X\alpha_1, \alpha_2, \dots, \alpha_r, Y_1, \dots, Y_s) \\ & - \dots \\ & - T(\alpha_1, \dots, \alpha_{r-1}, \nabla_X\alpha_r, Y_1, \dots, Y_s) \\ & - T(\alpha_1, \dots, \alpha_r, \nabla_X Y_1, Y_2, \dots, Y_s) \\ & - \dots \\ & - T(\alpha_1, \dots, \alpha_r, Y_1, \dots, Y_{s-1}, \nabla_X Y_s)\end{aligned} \tag{2.91}$$

for all $\alpha_1, \dots, \alpha_r \in \Gamma(\mathrm{T}^*M)$ and $Y_1, \dots, Y_s \in \Gamma(\mathrm{T}M)$.

c) The (total) covariant derivative of T is given by the tensor field $\nabla T \in \Gamma(\mathrm{T}^{r,s+1}M)$ with

$$\nabla T(\alpha_1, \dots, \alpha_r, Y_1, \dots, Y_s, X) = \nabla_X T(\alpha_1, \dots, \alpha_r, Y_1, \dots, Y_s) \tag{2.92}$$

for all $\alpha_1, \dots, \alpha_r \in \Gamma(\mathrm{T}^*M)$ and $Y_1, \dots, Y_s \in \Gamma(\mathrm{T}M)$. Note that the nabla operator can be seen as a differential operator

$$\nabla\colon \Gamma(\mathrm{T}^{r,s}M) \to \Gamma(\mathrm{T}^{r,s+1}M), \quad T \mapsto \nabla T, \tag{2.93}$$

that raises the covariant rank of tensor fields. This also explains the term "covariant derivative".

Remark 2.25 (Extension to vector-valued tensor fields)

Let (E, M, π) be a vector bundle. The covariant derivative can be extended to E-valued tensor fields on M, i.e., $\nabla\colon \Gamma(E \otimes_M \mathrm{T}^{r,s}M) \to \Gamma(E \otimes_M \mathrm{T}^{r,s+1}M)$.

Remark 2.26 (Tensor field associated with a vector field)

Let $X, Y \in \Gamma(\mathrm{T}M)$ be vector fields and $T \in \Gamma(\mathrm{T}^{1,0}M)$ be a tensor field associated with Y, i.e., $T(\alpha) = \alpha(Y)$ for all $\alpha \in \Gamma(\mathrm{T}^*M)$. Then the covariant derivative $\nabla_X T$ is associated with the covariant derivative $\nabla_X Y$ since

$$\nabla_X T(\alpha) = X(T(\alpha)) - T(\nabla_X \alpha) = X(\alpha(Y)) - \nabla_X \alpha(Y) = \alpha(\nabla_X Y) \tag{2.94}$$

for all $\alpha \in \Gamma(\mathrm{T}^*M)$.

Remark 2.27 (Lie bracket of vector fields)

For $X, Y \in \Gamma(\mathrm{T}M)$, the Lie bracket of vector fields $[\,\cdot\,,\,\cdot\,]\colon \Gamma(\mathrm{T}M) \times \Gamma(\mathrm{T}M) \to \Gamma(\mathrm{T}M)$ is defined as

$$[X, Y] = XY - YX, \tag{2.95}$$

where $(XY)f = X(Yf) \in \mathrm{C}^\infty(M)$ for $f \in \mathrm{C}^\infty(M)$. It is an anti-symmetric $\mathbb{R}$-bilinear operator and satisfies the Jacobi identity

$$[X, [Y, Z]] + [Z, [X, Y]] + [Y, [Z, X]] = 0 \tag{2.96}$$

for $X, Y, Z \in \Gamma(\mathrm{T}M)$, which turns $\Gamma(\mathrm{T}M)$ into a Lie algebra. We refer to $\mathcal{L}_X Y = [X, Y]$ as the Lie derivative of Y along X. The Lie derivative can be realized as the transport of Y along the flow, i.e., a collection of integral paths, generated by X (see, e.g., Marsden and Hughes [174]) and extends to tensor fields $T \in \Gamma(\mathrm{T}^{r,s}M)$ instead of Y.

Remark 2.28 (Torsion and Riemann curvature tensor)

There are two fundamental tensors associated with an affine connection ∇ on M. The first one is the torsion tensor $\mathrm{Tor}\colon \Gamma(\mathrm{T}M) \times \Gamma(\mathrm{T}M) \to \Gamma(\mathrm{T}M)$ defined by

$$\mathrm{Tor}(X, Y) = \nabla_X Y - \nabla_Y X - [X, Y], \tag{2.97}$$

for $X, Y \in \Gamma(\mathrm{T}M)$. The affine connection ∇ is called torsion-free if $\mathrm{Tor}(X, Y) = 0$, i.e.,

$$[X, Y] = \nabla_X Y - \nabla_Y X \tag{2.98}$$

for all $X, Y \in \Gamma(\mathrm{T}M)$. The second one is the Riemann curvature tensor $\mathrm{Rie}\colon \Gamma(\mathrm{T}M) \times \Gamma(\mathrm{T}M) \times \Gamma(\mathrm{T}M) \to \Gamma(\mathrm{T}M)$ given by

$$\mathrm{Rie}(X, Y)Z = \nabla_X \nabla_Y Z - \nabla_Y \nabla_X Z - \nabla_{[X,Y]} Z, \tag{2.99}$$

for $X, Y, Z \in \Gamma(\mathrm{T}M)$, which is a measure for the failure of second covariant derivatives to commute. For more information, we refer to standard references on Riemannian geometry, e.g., do Carmo [90], Petersen [206], Jost [143], and Lee [164].

Remark 2.29 (Ehresmann connection)

Let (E, N, π) be a vector bundle. A vector subbundle of the tangent bundle $\mathrm{T}E$ is given by the fiberwise kernel of the tangent mapping $\mathrm{T}\pi\colon \mathrm{T}E \to \mathrm{T}N$, which is referred to as the vertical bundle $\mathrm{V}E = \ker(\mathrm{T}\pi)$ of $\mathrm{T}E$. The vertical lift is given by the isomorphism

$$\mathrm{vl}\colon E \times_N E \to \mathrm{V}E, \quad (v, w) \mapsto (\gamma(0), \dot\gamma(0)) = \left(v, \frac{\mathrm{d}}{\mathrm{d}t}(v + tw)\bigg|_{t=0}\right), \tag{2.100}$$

where $\gamma\colon \mathbb{R} \to E$, $t \mapsto v + tw$ is a vertical path in E. The vertical projection $\mathrm{vp}\colon \mathrm{V}E \to E$, $(v, w) \mapsto \mathrm{pr}_2(\mathrm{vl}^{-1}(v, w))$ refers to the projection of the inverse of the vertical lift onto the second factor.

An Ehresmann connection on E is a choice of horizontal bundle $\mathrm{H}E$ of $\mathrm{T}E$ such that

$$\mathrm{T}E = \mathrm{V}E \oplus_E \mathrm{H}E, \tag{2.101}$$

where $\oplus_E$ denotes the fiberwise direct product. It can be equivalently described by the kernel $\mathrm{H}E = \ker(\Phi)$ of a connection form $\Phi\colon \mathrm{T}E \to \mathrm{V}E$. The corresponding connector is given by the projection $K\colon \mathrm{T}E \to E$, $(v, w) \mapsto \mathrm{vp}(\Phi(v, w))$. The mapping

$$(\pi_E, \mathrm{T}\pi)\colon \mathrm{T}E \to E \times_N \mathrm{T}N, \tag{2.102}$$

restricted to a horizontal bundle $\mathrm{H}E$, is an isomorphism. Its inverse $\mathrm{hl}\colon E \times_N \mathrm{T}N \to \mathrm{H}E$ is referred to as the horizontal lift.

Remark 2.30 (Covariant derivative of sections over smooth mappings)

Let $f\colon M \to N$ be a smooth mapping, $X \in \Gamma(\mathrm{T}M)$ be a vector field, and $s \in \Gamma(f^*E)$ be a section over f. Given an Ehresmann connection on E, the covariant derivative of s with respect to X is defined as the section

$$\nabla_X s = K \circ \mathrm{T}s \circ X \in \Gamma(f^*E) \tag{2.103}$$

over f. It induces a linear connection $\nabla\colon \Gamma(\mathrm{T}M) \times \Gamma(f^*E) \to \Gamma(f^*E)$, which reduces to the usual notion of an affine connection $\nabla\colon \Gamma(\mathrm{T}N) \times \Gamma(\mathrm{T}N) \to \Gamma(\mathrm{T}N)$ for $E = \mathrm{T}N$ and $f = \mathrm{id}_N$. If $s \in \Gamma(E)$ is a section and $Y \in \Gamma(\mathrm{T}N)$ is f-related to X, i.e., $\mathrm{T}f \circ X = Y \circ f$, then

$$\nabla_X(s \circ f) = K \circ \mathrm{T}(s \circ f) \circ X = K \circ \mathrm{T}s \circ \mathrm{T}f \circ X = K \circ \mathrm{T}s \circ Y \circ f = \nabla_Y s \circ f. \tag{2.104}$$

This is also called the chain rule for covariant derivatives. For more information on the covariant derivative in this regard, we refer to Michor [180, Section 19.12, Section 22.9].

Remark 2.31 (Parallel transport)

A vector field $s \in \Gamma(f^*\mathrm{T}N)$ over a smooth mapping $f\colon M \to N$ between manifolds is called parallel over f if it is covariantly constant, i.e., $\nabla s = 0$. If $M = [a, b]$ is an interval, then f is a path in N and a linear ODE can be obtained in local coordinates to which a unique solution exists in the finite-dimensional case if an initial condition is given, according to the Picard–Lindelöf theorem. The parallel transport along f is defined as

$$\mathrm{T}_{f(a),f(b)}\colon \mathrm{T}_{f(a)}N \to \mathrm{T}_{f(b)}N, \quad v \mapsto s_v(b), \tag{2.105}$$

where $s_v \in \Gamma(f^*\mathrm{T}N)$ is the unique parallel vector field along f satisfying $s_v(a) = v$.

2.3.10 Riemannian metrics and associated tensors

Definition 2.32 (Riemannian vector bundle)

Let (E, B, π) be a vector bundle. A Riemannian bundle metric on E is a smooth section g of the tensor bundle $\mathrm{T}^{0,2}(E)$ such that $g_b\colon E_b \times E_b \to \mathbb{R}$ is an inner product on E_b for all $b \in B$. A Riemannian vector bundle (E, B, π, g) refers to a vector bundle endowed with a Riemannian bundle metric.

Definition 2.33 (Riemannian manifold)

A pair (M, g) consisting of a manifold M and a Riemannian bundle metric g on the tangent bundle $\mathrm{T}M$ is called a Riemannian manifold. We refer to g as a Riemannian metric on M.

Remark 2.34 (Musical isomorphisms)

A Riemannian metric induces a bundle mapping $\flat\colon \mathrm{T}M \to \mathrm{T}^*M$ via

$$v \mapsto \Big(w \mapsto g(v, w)\Big), \tag{2.106}$$

which is invertible in the finite-dimensional setting with inverse mapping $\sharp = \flat^{-1}\colon \mathrm{T}^*M \to \mathrm{T}M$. We refer to $\flat$ and $\sharp$ as canonical or musical isomorphisms due to the use of musical symbols and the resulting operation of lowering and raising indices of tensor components. For $v \in \mathrm{T}M$ and $\alpha \in \mathrm{T}^*M$, we write $v^\flat = \flat(v)$ and $\alpha^\sharp = \sharp(\alpha)$ for the associated covector and vector, respectively.

Remark 2.35 (Raising and lowering indices)

Let (M, g) be a Riemannian manifold of dimension m. In local coordinates, we can express $v = v^i e_i$ and $\alpha = \alpha_i e^i$ as linear combinations, where $(e_1, \dots, e_m)$ is an ordered local basis and $(e^1, \dots, e^m)$ is the corresponding dual basis. Components of the associated covector $v^\flat = v_i e^i$ and vector $\alpha^\sharp = \alpha^i e_i$ are related to the original components via

$$v_i = g_{ij} v^j, \quad \alpha^i = g^{ij} \alpha_j, \tag{2.107}$$

using the Einstein summation convention for $i, j = 1, \dots, m$ with the metric and inverse metric tensor components

$$g_{ij} = g(e_i, e_j), \quad g^{ij} = (g_{ij})^{-1}. \tag{2.108}$$

This can be extended to tensors and tensor fields by specifying which indices should be lowered or raised and considering a local and dual frame on M.

Remark 2.36 (Tensor product metric)

For the inverse metric tensor $g^{-1}\colon \mathrm{T}^*M \times_M \mathrm{T}^*M \to \mathbb{R}$ defined by

$$g^{-1}(\alpha, \beta) = g(\alpha^\sharp, \beta^\sharp) = \alpha(\beta^\sharp) = \beta(\alpha^\sharp), \tag{2.109}$$

we have that $g^{-1}(e^i, e^j) = g^{ij}$ for $i, j = 1, \dots, m$. The tensor product metric

$$g^{r,s} = \underbrace{g \otimes \cdots \otimes g}_{r \text{ times}} \otimes \underbrace{g^{-1} \otimes \cdots \otimes g^{-1}}_{s \text{ times}}\colon \mathrm{T}^{r,s}M \times_M \mathrm{T}^{r,s}M \to \mathbb{R} \tag{2.110}$$

given by

$$\begin{aligned}(v_1 \otimes \cdots \otimes v_r \otimes \alpha_1 \otimes \cdots \otimes \alpha_s, w_1 \otimes \cdots \otimes w_r \otimes \beta_1 \otimes \cdots \otimes \beta_s)& \\ \mapsto g(v_1, w_1) \cdots g(v_r, w_r) g^{-1}(\alpha_1, \beta_1) \cdots g^{-1}(\alpha_s, \beta_s),&\end{aligned} \tag{2.111}$$

extends g to a Riemannian bundle metric on $\mathrm{T}^{r,s}M$.

Remark 2.37 (Trace of tensor fields)

By restricting ourselves to the right-most contravariant and covariant index, we can define the musical isomorphisms

$$\begin{aligned}\flat\colon \Gamma(\mathrm{T}^{r+1,s}M) \to \Gamma(\mathrm{T}^{r,s+1}M), \quad T \mapsto Tg,& \\ \sharp\colon \Gamma(\mathrm{T}^{r,s+1}M) \to \Gamma(\mathrm{T}^{r+1,s}M), \quad T \mapsto Tg^{-1}.&\end{aligned} \tag{2.112}$$

This convention also allows us to define the following traces for tensor fields:

$$\begin{aligned} \mathrm{tr}_g &\colon \Gamma(\mathrm{T}^{r+2,s}M) \to \Gamma(\mathrm{T}^{r,s}M), \quad T \mapsto \mathrm{tr}(T^\flat), \\ \mathrm{tr}^g &\colon \Gamma(\mathrm{T}^{r,s+2}M) \to \Gamma(\mathrm{T}^{r,s}M), \quad T \mapsto \mathrm{tr}(T^\sharp), \end{aligned} \tag{2.113}$$

where $\mathrm{tr}\colon \Gamma(\mathrm{T}^{r+1,s+1}M) \to \Gamma(\mathrm{T}^{r,s}M)$ is the tensor contraction of the right-most contravariant index with the right-most covariant index. Note that

$$\begin{aligned} \mathrm{tr}_g(A) &= \mathrm{tr}(Ag) = \mathrm{tr}(gA), \\ \mathrm{tr}^g(B) &= \mathrm{tr}(Bg^{-1}) = \mathrm{tr}(g^{-1}B), \end{aligned} \tag{2.114}$$

for $A \in \Gamma(\mathrm{T}^{2,0}M)$ and $B \in \Gamma(\mathrm{T}^{0,2}M)$.

Remark 2.38 (Differential operators)

Let ∇ be an affine connection on M. The gradient of a tensor field $T \in \Gamma(\mathrm{T}^{r,s}M)$ is given by the tensor field

$$\mathrm{grad}\, T = (\nabla T)^\sharp \in \Gamma(\mathrm{T}^{r+1,s}M) \tag{2.115}$$

associated with the covariant derivative. It defines a differential operator

$$\mathrm{grad}\colon \Gamma(\mathrm{T}^{r,s}M) \to \Gamma(\mathrm{T}^{r+1,s}M). \tag{2.116}$$

On the other hand, the divergence operator

$$\mathrm{div}\colon \Gamma(\mathrm{T}^{r+1,s}M) \to \Gamma(\mathrm{T}^{r,s}M) \tag{2.117}$$

maps a tensor field $T \in \Gamma(\mathrm{T}^{r+1,s}M)$ to the trace of the covariant derivative, i.e.,

$$\mathrm{div}(T) = \mathrm{tr}(\nabla T) \in \Gamma(\mathrm{T}^{r,s}M). \tag{2.118}$$

Composition of both operators yields the Laplace–Beltrami operator with

$$\mathrm{div}(\mathrm{grad}\, T) = \mathrm{tr}(\nabla(\nabla T)^\sharp) = \mathrm{tr}^g(\nabla^2 T) \tag{2.119}$$

for $T \in \Gamma(\mathrm{T}^{r,s}M)$. Note that $(\nabla T)^\sharp = \nabla T^\sharp$ holds for $T \in \Gamma(\mathrm{T}^{r,s+1}M)$. In this thesis, we mainly use another notion of the Laplace operator introduced in Section 2.3.14 for which we reserve the symbol Δ. The above operations can be extended to E-valued tensor fields in $\Gamma(E \otimes_M \mathrm{T}^{r,s}M)$, where E is the total space of a vector bundle over M.

Remark 2.39 (Levi-Civita connection)

An affine connection is said to be compatible with the Riemannian metric if

$$X(g(Y,Z)) = g(\nabla_X Y, Z) + g(Y, \nabla_X Z) \tag{2.120}$$

for all $X, Y, Z \in \Gamma(\mathrm{T}M)$. In this case, the affine connection is called a metric connection.

The Riemannian metric is covariantly constant with respect to a metric connection, i.e., $\nabla g = 0$, since the relation

$$\nabla_X g(Y,Z) = X(g(Y,Z)) - g(\nabla_X Y, Z) + g(Y, \nabla_X Z) = 0 \tag{2.121}$$

holds for all $X, Y, Z \in \Gamma(\mathrm{T}M)$. A covariantly constant tensor field is also called a parallel tensor field.

In a finite-dimensional Riemannian manifold, there is a unique affine connection, called the Levi-Civita connection, that is torsion-free and compatible with the Riemannian metric. This is known as the fundamental theorem of Riemannian geometry [164, Theorem 5.4].

2.3.11 Geodesics in Riemannian manifolds

Let (M, g) be a (path-)connected Riemannian manifold. A distance function on M can be introduced via the Riemannian metric g. We assume that M is finite-dimensional in this section, but the concepts can be transferred to the infinite-dimensional setting, which is required for geodesic paths in shape spaces (see Section 4.4).

Definition 2.40 (Riemannian distance)

The Riemannian distance on M is defined as $\operatorname{dist}\colon M \times M \to [0, \infty)$ with

$$\operatorname{dist}(p_1, p_2) = \inf\big\{L(\gamma) \,\big|\, \gamma\colon [a, b] \to M \text{ piecewise smooth}, \gamma(a) = p_1, \gamma(b) = p_2\big\}, \quad (2.122)$$

for $p_1, p_2 \in M$, where the length functional is given by

$$L(\gamma) = \int_a^b \|\dot{\gamma}(t)\|_{\gamma(t)} \,\mathrm{d}t \quad (2.123)$$

and the norm $\|\cdot\|_p\colon \mathrm{T}_pM \to [0, \infty)$ is induced by the Riemannian metric, i.e.,

$$\|v\|_p = \sqrt{g_p(v, v)} \quad (2.124)$$

for $p \in M$ and $v \in \mathrm{T}_pM$. Here, $\dot{\gamma}\colon [a, b] \to \mathrm{T}M$ denotes the velocity vector field over γ defined by

$$\dot{\gamma}(t_0) = \mathrm{T}\gamma(\partial_t(t_0)) \quad (2.125)$$

and $\partial_t\colon [a, b] \to \mathrm{T}[a, b]$ is the standard basis vector field on $[a, b] \subseteq \mathbb{R}$ given by

$$\partial_t(t_0)[h]_{t_0} = \partial_t h(t_0) = \lim_{t \to 0} \frac{h(t_0 + t) - h(t_0)}{t} \quad (2.126)$$

for $t_0 \in [a, b]$ and $[h]_{t_0} \in \mathrm{C}^\infty_{t_0}([a, b])$. Differentiability at an end point is either understood as a one-sided limit or in the sense that the path can be extended to a smooth mapping on an open neighborhood of $[a, b]$ in $\mathbb{R}$.

The Riemannian distance is a distance function that induces the same topology as the original manifold topology [184, Theorem 5.3.8]. Similar to the length functional, one can define the energy functional on the space of piecewise smooth curves $\gamma\colon [a, b] \to M$ by

$$E(\gamma) = \frac{1}{2} \int_a^b \|\dot{\gamma}(t)\|^2_{\gamma(t)} \,\mathrm{d}t. \quad (2.127)$$

Stationary points of the energy functional minimize the length locally and have constant speed. They can also be characterized as paths whose velocity vectors are parallel with respect to the Levi-Civita connection. See, e.g., Lee [164] for more information.

Definition 2.41 (Geodesics)

A geodesic is a smooth path $\gamma\colon [a, b] \to M$ satisfying the geodesic equation

$$\nabla_{\partial_t} \dot{\gamma} = 0. \quad (2.128)$$

The geodesic equation yields an ODE in local coordinates, which is of second order and not necessarily linear, in contrast to the parallel transport in Remark 2.31. Unique solutions to (2.128) still exist locally, but global existence cannot be guaranteed.

Definition 2.42 (Riemannian exponential and logarithmic mapping)

Let $p \in M$ and $\mathrm{S}_pM \subseteq \mathrm{T}_pM$ denote the set of all tangent vectors $v \in \mathrm{T}_pM$ for which a unique solution $\gamma_{p,v}\colon [0,1] \to M$ to the geodesic equation (2.128) with the initial conditions $\gamma_{p,v}(0) = p$, $\dot{\gamma}_{p,v}(0) = v$, and constant speed exists. The (Riemannian) exponential mapping at p is then defined as

$$\exp_p\colon \mathrm{S}_pM \to M, \quad v \mapsto \gamma_{p,v}(1). \tag{2.129}$$

A Riemannian manifold is called geodesically complete if the exponential mapping $\exp_p$ can be defined on the entire tangent space, i.e., $\mathrm{S}_pM = \mathrm{T}_pM$, for all $p \in M$. In this case, the exponential mapping is a bundle mapping $\exp\colon \mathrm{T}M \to \mathrm{M}$ given by

$$\exp(p, v) = \exp_p(v). \tag{2.130}$$

The exponential mapping at p is a local diffeomorphism, i.e., it can be restricted to an open neighborhood $\mathrm{U}_pM \subseteq \mathrm{S}_pM$ of the origin such that $\exp_p|_{\mathrm{U}_pM}$ is a diffeomorphism. We can define the (Riemannian) logarithmic mapping at p as the inverse mapping

$$\log_p = (\exp_p|_{\mathrm{B}_{\iota(p)}(0)})^{-1}\colon \exp_p(\mathrm{B}_{\iota(p)}(0_p)) \to \mathrm{B}_{\iota(p)}(0_p), \tag{2.131}$$

where $\iota(p) = \sup\{\delta > 0 \mid \exp_p \text{ is injective on } \mathrm{B}_\delta(0_p)\}$ denotes the injectivity radius of M at p and $\mathrm{B}_\delta(0_p) = \{v \in \mathrm{T}_pM \mid \|v\|_p < \delta\}$ is an open ball in the tangent space with radius $\delta > 0$ and center $0_p \in \mathrm{T}_pM$ corresponding to the norm induced by the Riemannian metric. We write $\log(p, q) = \log_p(q)$ for q in the open geodesic ball $\exp_p(\mathrm{B}_{\iota(p)}(0_p)) \subseteq M$.

2.3.12 Integration on Riemannian manifolds

Let M be an oriented manifold of dimension m and $\omega \in \Omega^m_{\mathrm{c}}(M)$ be a compactly supported differential m-form on M. Taking a smooth partition of unity $(\rho_\alpha)_{\alpha\in\mathcal{A}}$ on M subordinate to some positively oriented atlas $(U_\alpha, x_\alpha)_{\alpha\in\mathcal{A}}$ on M, representing the differential m-form

$$\omega = f_\alpha \,\mathrm{d}x^1_\alpha \wedge \cdots \wedge \mathrm{d}x^m_\alpha, \quad \alpha \in \mathcal{A}, \tag{2.132}$$

with respect to each chart, and summing up the weighted integrals obtained from pullback yields a well-defined quantity

$$\int_M \omega = \sum_{\alpha\in\mathcal{A}} \int_{x_\alpha(U_\alpha)} (x_\alpha^{-1})^*(\rho_\alpha f_\alpha)\,\mathrm{d}\lambda \tag{2.133}$$

that is independent of the chosen partition of unity [162, Chapter 9]. Common properties of this integral can be found in standard references, e.g., Spivak [254], Jänich [144], Lee [162] and Lee [163]. If M is not oriented, we can take the integral of a density function on M instead [144, Chapter 5].

In the following, we summarize some important tools from the theory of integration on manifolds. The first one is the change of variables formula for integrals.

Proposition 2.43 (Change of variables)

Let $\varphi\colon M \to N$ be an orientation-preserving diffeomorphism between oriented manifolds of dimension m and $\omega \in \Omega^m_{\mathrm{c}}(\varphi(M))$ be a compactly supported differential m-form on $\varphi(M)$. Then

$$\int_M \varphi^*\omega = \int_{\varphi(M)} \omega. \tag{2.134}$$

Proposition 2.44 (Stokes' theorem)

Let M be an oriented manifold of dimension m with piecewise smooth boundary ∂M and $\omega \in \Omega_c^m(M)$ be a compactly supported differential $(m-1)$-form. Then

$$\int_M \mathrm{d}\omega = \int_{\partial M} \iota^* \omega, \tag{2.135}$$

where ∂M is endowed with the orientation induced by M and $\iota\colon \partial M \to M$ is the inclusion mapping.

Definition 2.45 (Volume form and density)

Let (M, g) be an oriented Riemannian manifold. The volume form on M is given by

$$\mathrm{vol}(g) = \sqrt{\det(g)}\, \mathrm{d}x^1 \wedge \cdots \wedge \mathrm{d}x^m \tag{2.136}$$

in local coordinates. The oriented volume of M is defined as

$$\mathrm{Vol}(M) = \int_M \mathrm{vol}(g). \tag{2.137}$$

For a Riemannian manifold (M, g), which is not necessarily oriented, the volume density is similarly defined by

$$|\mathrm{vol}(g)| = \sqrt{\det(g)}\, \mathrm{d}x^1 \otimes \cdots \otimes \mathrm{d}x^m \tag{2.138}$$

in local coordinates. The volume of a Riemannian manifold M is defined as

$$|\mathrm{Vol}(M)| = \int_M |\mathrm{vol}(g)|. \tag{2.139}$$

2.3.13 Sobolev spaces of Riemannian vector bundles

Definition 2.46 (Metrics on tensor fields)

Let (M, g) be a Riemannian manifold. The metric $G^{r,s}$ on $\Gamma(\mathrm{T}^{r,s}M)$ is defined by

$$G^{r,s}(X, Y) = \int_M g^{r,s}(X, Y)\, \mathrm{vol}(g) \tag{2.140}$$

for tensor fields $X, Y \in \Gamma(\mathrm{T}^{r,s}M)$. If $(E, M, \pi, \bar{g})$ is a Riemannian vector bundle, then the metric $\bar{G}^{r,s}$ on $\Gamma(E \otimes_M \mathrm{T}^{r,s}M)$ is defined by

$$\bar{G}^{r,s}(X, Y) = \int_M (\bar{g} \otimes g^{r,s})(X, Y)\, \mathrm{vol}(g) \tag{2.141}$$

for E-valued tensor fields $X, Y \in \Gamma(E \otimes_M \mathrm{T}^{r,s}M)$.

Definition 2.47 (Sobolev spaces of Riemannian vector bundles)

Let (M, g) be a Riemannian manifold and $(E, M, \pi, \bar{g})$ be a Riemannian vector bundle. The Levi-Civita connections ∇^g and $\nabla^{\bar{g}}$ induce metric connections ∇ on tensor bundles $E \otimes_M \mathrm{T}^{r,s}M$ via the tensor product connection. The Sobolev space $\mathrm{H}^s(E)$ of order $s \in \mathbb{N}_0$ is defined as the completion of the space of smooth sections $\Gamma(E)$ with respect to the Sobolev norm

$$\|u\|^2_{\mathrm{H}^s(E)} = \sum_{j=0}^{s} \bar{G}^{0,j}(\nabla^j u, \nabla^j u), \quad u \in \Gamma(E). \tag{2.142}$$

The resulting topology does not depend on the choice of the Riemannian metrics and the metric connections if M is compact [27, Section 6.6].

Definition 2.48 (Sobolev spaces of vector fields over immersions)

Let $\xi\colon M \to N$ be a smooth immersion of a manifold M in a Riemannian manifold N with Riemannian metric $\bar{g}$. We endow M with the pullback Riemannian metric g induced by ξ. The Sobolev space of H^s vector fields over ξ is then defined as $\mathrm{H}^s(\xi^*\mathrm{T}N)$.

For more information on Sobolev spaces on Riemannian manifolds, we refer to Eichhorn [95, 96] and Hebey [126].

2.3.14 Bochner–Laplace operator

Let (M, g) be a Riemannian manifold. The Laplace operator considered in this thesis is the Bochner–Laplace operator defined in terms of the adjoint of the covariant derivative. Recall that the covariant derivative can be regarded as a mapping $\nabla\colon \Gamma(\mathrm{T}^{r,s}M) \to \Gamma(\mathrm{T}^{r,s+1}M)$, which raises the covariant rank of tensor fields by one.

Definition 2.49 (Adjoint of the covariant derivative)

The adjoint operator of the covariant derivative $\nabla\colon \Gamma(\mathrm{T}^{r,s}M) \to \Gamma(\mathrm{T}^{r,s+1}M)$ is defined as the mapping $\nabla^*\colon \Gamma(\mathrm{T}^{r,s+1}M) \to \Gamma(\mathrm{T}^{r,s}M)$ that satisfies

$$G^{r,s}(A, \nabla^* B) = G^{r,s+1}(\nabla A, B) \tag{2.143}$$

for all $A \in \Gamma(\mathrm{T}^{r,s}M)$ and $B \in \Gamma(\mathrm{T}^{r,s+1}M)$.

Lemma 2.50

For $B \in \Gamma(\mathrm{T}^{r,s+1}M)$, we have that

$$\nabla^* B = -\operatorname{tr}^g(\nabla B) = -\operatorname{div}(B^\sharp). \tag{2.144}$$

Proof. A proof is given in [27, Section 3.10]. □

Definition 2.51 (Bochner–Laplace operator)

The Bochner–Laplace operator $\Delta\colon \Gamma(\mathrm{T}^{r,s}M) \to \Gamma(\mathrm{T}^{r,s}M)$ is defined by

$$\Delta A = \nabla^*(\nabla A) \tag{2.145}$$

for $A \in \Gamma(\mathrm{T}^{r,s}M)$.

Remark 2.52

Note that the Bochner–Laplace operator is defined for all tensor fields on M and differs from the commonly used Laplace–Beltrami operator by a sign, since

$$\Delta A = -\operatorname{tr}^g(\nabla^2 A) = -\operatorname{div}(\operatorname{grad} A) \tag{2.146}$$

for $A \in \Gamma(\mathrm{T}^{r,s}M)$ by Lemma 2.50. Another generalization of the Laplace operator is given by the Hodge–Laplace operator $\tilde{\Delta}\colon \Omega^s(M) \to \Omega^s(M)$ for differential forms with

$$\tilde{\Delta} = \mathrm{d}\mathrm{d}^* + \mathrm{d}^*\mathrm{d}, \tag{2.147}$$

which is related to the Bochner–Laplace operator by the Weitzenböck identity [40]. Here, $\mathrm{d}^*\colon \Omega^{s+1}(M) \to \Omega^s(M)$ denotes the adjoint of the exterior derivative $\mathrm{d}\colon \Omega^s(M) \to \Omega^{s+1}(M)$ characterized by

$$G^{0,s}(\alpha, \mathrm{d}^*\beta) = G^{0,s+1}(\mathrm{d}\alpha, \beta) \tag{2.148}$$

for all $\alpha \in \Omega^s(M)$ and $\beta \in \Omega^{s+1}(M)$.

Remark 2.53

By definition, we have that

$$G^{r,s}(\Delta A, B) = G^{r,s+1}(\nabla A, \nabla B) \tag{2.149}$$

for $A, B \in \Gamma(\mathrm{T}^{r,s}M)$. The Bochner–Laplace operator can also be constructed in a similar way for E-valued tensor fields in $\Gamma(E \otimes_M \mathrm{T}^{r,s}M)$ using the respective covariant derivative and the bundle metric $\bar{G}^{r,s}$, where $(E, M, \pi, \bar{g})$ is a Riemannian vector bundle.

2.4 Differential geometry of surfaces

In this section, we provide the necessary tools required for computations involving surfaces in three-dimensional Euclidean space or, more generally, Riemannian submanifolds in the finite-dimensional case. For more information, see, e.g., do Carmo [89] and Michor [180].

2.4.1 Immersed Riemannian submanifolds

Definition 2.54 (Pullback metric)

Let $(N, \bar{g})$ be a Riemannian manifold of dimension n and M be a manifold of dimension $m \leq n$. An immersion $\xi \in \mathrm{Imm}(M, N)$ induces a Riemannian metric g on M, called the pullback metric or first fundamental form, via $g = \xi^* \bar{g}$, i.e.

$$g(X, Y) = \bar{g}(\mathrm{T}\xi \circ X, \mathrm{T}\xi \circ Y) \tag{2.150}$$

for $X, Y \in \Gamma(\mathrm{T}M)$, which turns (M, g) into a Riemannian manifold. We refer to (M, ξ) as an immersed Riemannian submanifold if it is endowed with the pullback metric.

Definition 2.55 (Tangent and normal bundle)

Let $p \in M$. Since ξ is an immersion, the tangent space T_pM can be identified with the subspace $\mathrm{T}_p\xi(\mathrm{T}_pM) \subseteq \mathrm{T}_{\xi(p)}N$ of the ambient tangent space. The normal subspace of M in N at p is then defined as

$$\mathrm{N}_pM = (\mathrm{T}_p\xi(\mathrm{T}_pM))^\perp = \big\{ w \in \mathrm{T}_{\xi(p)}N \,\big|\, \forall\, v \in \mathrm{T}_pM : \bar{g}_p(\mathrm{T}_p\xi(v), w) = 0 \big\}. \tag{2.151}$$

We can thus write $\mathrm{T}_{\xi(p)}N = \mathrm{T}_p\xi(\mathrm{T}_pM) \oplus \mathrm{N}_pM$. The normal subspaces of M in N form a normal bundle $\mathrm{N}M = \coprod_{p \in M} \mathrm{N}_pM$ in the usual way. We use the superscripts $\parallel$ and $\perp$ to refer to the tangential and normal part of vector fields over ξ, respectively.

Definition 2.56 (Second fundamental form)

The covariant derivative $\nabla_X(\mathrm{T}\xi \circ Y)$ can be written in terms of its tangential and normal part, i.e.,

$$\nabla_X(\mathrm{T}\xi \circ Y) = (\nabla_X(\mathrm{T}\xi \circ Y))^\parallel + (\nabla_X(\mathrm{T}\xi \circ Y))^\perp. \tag{2.152}$$

The vector-valued second fundamental form is a symmetric $(0,2)$-tensor field $\vec{h} \colon \mathrm{T}M \times_M \mathrm{T}M \to \mathrm{N}M$, which maps (X, Y) to the normal part of $\nabla_X(\mathrm{T}\xi \circ Y)$ given by

$$\vec{h}(X, Y) = (\nabla_X(\mathrm{T}\xi \circ Y))^\perp = \nabla_X(\mathrm{T}\xi \circ Y) - \mathrm{T}\xi \circ \nabla_X Y. \tag{2.153}$$

If M is an oriented hyper-surface (immersed submanifold of codimension 1), we can define the scalar-valued second fundamental form $h \colon \mathrm{T}M \times_M \mathrm{T}M \to \mathbb{R}$ via the normal component of $\vec{h}(X, Y)$, i.e.,

$$h(X, Y) = \bar{g}(n, \vec{h}(X, Y)) = \bar{g}(n, \nabla_X(\mathrm{T}\xi \circ Y)) = -\bar{g}(\nabla_X n, \mathrm{T}\xi \circ Y), \tag{2.154}$$

where $n \in \Gamma(\mathrm{N}M)$ is the unit normal vector field on M. The last equality follows from

$$\bar{g}(\nabla_X n, \mathrm{T}\xi \circ Y) + \bar{g}(n, \nabla_X(\mathrm{T}\xi \circ Y)) = X(\bar{g}(n, \mathrm{T}\xi \circ Y)) = 0. \tag{2.155}$$

The shape operator refers to the associated Weingarten mapping $\mathcal{S}\colon \mathrm{T}M \to \mathrm{T}M$, which is characterized by

$$\bar{g}(\mathrm{T}\xi \circ \mathcal{S} \circ X, \mathrm{T}\xi \circ Y) = g(\mathcal{S} \circ X, Y) = h(X, Y) = \bar{g}(-\nabla_X n, \mathrm{T}\xi \circ Y), \tag{2.156}$$

thus $\mathrm{T}\xi \circ \mathcal{S} \circ X = -\nabla_X n = -\nabla n \circ X$. We write $\kappa = \mathrm{tr}(\mathcal{S}) = \mathrm{tr}(g^{-1}h)$ for the trace of the shape operator, which is also given by the sum of principal curvatures, i.e., the eigenvalues of $\mathcal{S}$. For the vector-valued case, $\vec{\kappa} = \mathrm{tr}^g(\vec{h}) \in \Gamma(\mathrm{N}M)$ is a section of the normal bundle.

2.4.2 Surfaces in three-dimensional Euclidean space

A surface is a two-dimensional manifold. Given an immersion $\xi \in \mathrm{Imm}(M, \mathbb{E}^3)$ of a surface in three-dimensional Euclidean space, we endow the surface M with the Riemannian metric induced by the Euclidean metric $\langle \cdot\,, \cdot \rangle$ in $\mathbb{E}^3$. The resulting pullback metric is called the first fundamental form and denoted by the roman numeral

$$\mathrm{I}\colon \mathrm{T}M \times_M \mathrm{T}M \to \mathbb{R}, \quad (p, v, w) \mapsto \langle \xi_*(p)v, \xi_*(p)w \rangle. \tag{2.157}$$

For an oriented surface M, the unit normal vector field $n\colon M \to \mathbb{S}_2$ is given by the Gauss mapping, which assigns a unit vector $n(p) \in \mathbb{S}_2$ orthogonal to the tangent plane of M in $\mathbb{E}^3$ (and consistent with the orientation of M) to each point $p \in M$. In local coordinates, the unit normal vector field reads

$$n = \frac{\partial_1\gamma \times \partial_2\gamma}{\|\partial_1\gamma \times \partial_2\gamma\|}, \tag{2.158}$$

where $\gamma\colon D \to \mathbb{E}^3$ is a parametrization of the surface on an open subset $D \subseteq \mathbb{R}^2$ and $\|\cdot\|$ denotes the Euclidean norm. The shape operator refers to the Weingarten mapping

$$\mathcal{S}\colon \mathrm{T}M \to \mathrm{T}M, \quad (p, v) \mapsto \mathcal{S}_p(v), \tag{2.159}$$

where $\mathcal{S}_p(v)$ is the element of T_pM that corresponds to the negative of $\nabla_v n(p)$.

The eigenvalues κ_1 and κ_2 of the shape operator (as a fiberwise linear mapping) are called the principal curvatures of M. Its mean

$$H = \frac{1}{2}(\kappa_1 + \kappa_2) \tag{2.160}$$

is called the mean curvature of M and its product is the Gaussian curvature

$$K = \kappa_1\kappa_2, \tag{2.161}$$

which is an intrinsic property of the surface according to the Theorema Egregium of Gauss. The minimum radius of curvature refers to the quantity

$$r_{\min} = \min\left\{\frac{1}{|\kappa_1|}, \frac{1}{|\kappa_2|}\right\}, \tag{2.162}$$

which may be infinite if $\kappa_1 = \kappa_2 = 0$.

The second fundamental form is the (fiberwise) symmetric bilinear form given by

$$\mathrm{II}\colon \mathrm{T}M \times_M \mathrm{T}M \to \mathbb{R}, \quad (p, v, w) \mapsto \mathrm{I}_p(\mathcal{S}_p(v), w). \tag{2.163}$$

Its symmetry (and thus self-adjointness of the shape operator) follows from

$$\mathrm{I}(\mathcal{S}(v), w) = \langle n, \nabla_v w\rangle = \langle n, \nabla_w v + [v, w]\rangle = \mathrm{I}(v, \mathcal{S}(w)) \tag{2.164}$$

since $0 = v(\langle n, w\rangle) = \langle \nabla_v n, w\rangle + \langle n, \nabla_v w\rangle$ and the Lie bracket $[v, w] \in \mathrm{T}M$ is orthogonal to the unit normal vector.

The third fundamental form is defined as

$$\mathrm{III}\colon \mathrm{T}M \times_M \mathrm{T}M \to \mathbb{R}, \quad (p, v, w) \mapsto \mathrm{I}_p(\mathcal{S}_p(v), \mathcal{S}_p(w)) \tag{2.165}$$

and can be expressed in terms of the first and second fundamental form via

$$\mathrm{III} - 2H\,\mathrm{II} + K\,\mathrm{I} = 0, \tag{2.166}$$

where H is the mean curvature and K is the Gaussian curvature of M.

Proposition 2.57 (Steiner's formula for parallel surfaces)
Let $\gamma\colon D \to \mathbb{E}^3$ be a parametrization of an oriented smooth surface with unit normal vector field $n\colon D \to \mathbb{S}_2$ and $\tilde{\gamma}\colon D \to \mathbb{E}^3$ be a parametrization of a parallel surface given by

$$\tilde{\gamma}(\vartheta^1, \vartheta^2) = \gamma(\vartheta^1, \vartheta^2) + \zeta\, n(\vartheta^1, \vartheta^2) \tag{2.167}$$

for a sufficiently small $\zeta \in (-\varepsilon, \varepsilon)$. Then

$$\underbrace{\langle n, \partial_1\tilde{\gamma} \times \partial_2\tilde{\gamma}\rangle}_{\det(n, \partial_1\tilde{\gamma}, \partial_2\tilde{\gamma})} = (1 - 2H\zeta + K\zeta^2)\, \underbrace{\langle n, \partial_1\gamma \times \partial_2\gamma\rangle}_{\|\partial_1\gamma \times \partial_2\gamma\|}. \tag{2.168}$$

Proof. This is an exercise in [89, Section 3-5, Exercise 11]. Let $g_\alpha = \partial_\alpha\tilde{\gamma}$ and $a_\alpha = \partial_\alpha\gamma$ for $\alpha = 1, 2$. Then $g_\alpha = a_\alpha + \partial_\alpha n$. Since $\partial_\alpha n \perp n$, the partial derivatives of n can be written as

$$\partial_\alpha n = (\partial_\alpha n)^1 a_1 + (\partial_\alpha n)^2 a_2. \tag{2.169}$$

From this, it follows that

$$\begin{aligned} g_1 \times g_2 &= (a_1 + \zeta\,\partial_1 n) \times (a_2 + \zeta\,\partial_2 n) \\ &= (a_1 \times a_2) + \zeta\,(\partial_1 n \times a_2) + \zeta\,(a_1 \times \partial_2 n) + \zeta^2\,(\partial_1 n \times \partial_2 n) \\ &= (1 + \zeta\,(\partial_1 n)^1 + \zeta\,(\partial_2 n)^2 + \zeta^2\,(\partial_1 n)^1(\partial_2 n)^2 - \zeta^2\,(\partial_1 n)^2(\partial_2 n)^1)(a_1 \times a_2) \\ &= (1 - \zeta\,\mathrm{tr}(\mathcal{S}) + \zeta^2 \det(\mathcal{S}))(a_1 \times a_2) = (1 - 2H\zeta + K\zeta^2)(a_1 \times a_2). \end{aligned} \tag{2.170}$$

Thus $\langle n, g_1 \times g_2\rangle = (1 - 2H\zeta + K\zeta^2)\langle n, a_1 \times a_2\rangle = (1 - 2H\zeta + K\zeta^2)\|a_1 \times a_2\|$. □

3 Mathematical models of shell structures

In the following, we introduce some basic concepts from the theory of elasticity to formulate the mathematical models of shell structures considered in this thesis. At the end of this section, we also formulate a model of Earth's lithosphere, which is used for the numerical experiments in Section 7. For a more elaborate introduction to solid mechanics and shell structures, we refer to Marsden and Hughes [174], Ciarlet [66, 67, 68, 69], Bischoff et al. [41], Koiter [156, 157], Naghdi [189], Simo and Fox [251], Reddy [212], and Braess [55].

3.1 Three-dimensional elasticity theory

We begin with the description of deformable bodies in continuum mechanics.

3.1.1 Geometry and kinematics of bodies

Let M be a continuum body, modeled as a manifold of dimension m, and N be an ambient space—usually the Euclidean space $\mathbb{E}^3$ that represents the physical space or, more generally, a Riemannian manifold of dimension n. Elements of M are referred to as material points or particles of the body. A configuration of M in N is a mapping

$$\xi\colon M \to N, \tag{3.1}$$

which assigns a spatial point $\xi(p) \in N$ to each particle $p \in M$. We restrict ourselves to configurations that are continuously differentiable embeddings of M in N, i.e., the mapping ξ is at least a C^1 diffeomorphism onto its image. Thus, phenomena such as folding, ripping, pinching, or interpenetration of matter are excluded from the model. We write $\mathrm{Emb}(M, N)$ for the space of all admissible configurations of M in N.

A motion of M in N is a path $t \mapsto \xi_t$ in the configuration space, i.e., a continuous mapping from a time interval $I \subseteq \mathbb{R}$ to $\mathrm{Emb}(M, N)$. We write $\xi(t, p) = \xi_t(p)$ for the position of a particle $p \in M$ at time $t \in I$ and identify the motion with the mapping

$$\xi\colon I \times M \to N, \quad (t, p) \mapsto \xi(t, p). \tag{3.2}$$

The trajectory of p under the motion ξ is given by the path $t \mapsto \xi(t, p)$ in N. The material velocity of ξ refers to the vector field

$$V\colon I \times M \to \mathrm{T}N, \quad (t, p) \mapsto \partial_t \xi(t, p), \tag{3.3}$$

assuming that the trajectories are differentiable. Furthermore, the material acceleration of ξ is defined as the covariant derivative of V with respect to time, i.e.,

$$A\colon I \times M \to \mathrm{T}N, \quad (t, p) \mapsto \nabla_{\partial_t} V(t, p). \tag{3.4}$$

A C^r regular motion refers to a motion of class C^r, i.e., the associated mapping in (3.2) is of class C^r and ξ_t is a C^r embedding for all $t \in I$. We assume that the motions considered hereafter are sufficiently regular.

The material velocity can be expressed in terms of the position via the spatial velocity

$$v\colon \xi_I(M) \to \mathrm{T}N, \quad (t, x) \mapsto V(t, \xi_t^{-1}(x)), \tag{3.5}$$

where $\xi_I(M) = \coprod_{t \in I} \xi_t(M) = \{(t, x) \mid t \in I,\, x \in \xi_t(M)\} \subseteq I \times N$. Similarly, the spatial acceleration reads

$$a\colon \xi_I(M) \to \mathrm{T}N, \quad (t, x) \mapsto A(t, \xi_t^{-1}(x)). \tag{3.6}$$

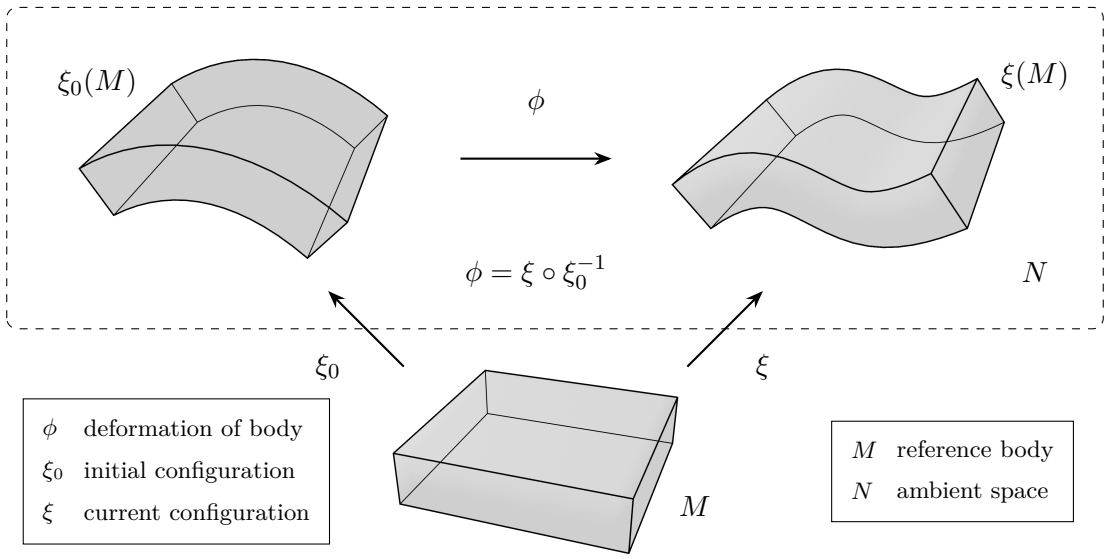

Figure 3: Deformation of a continuum body M in the ambient space N from the initial undeformed configuration ξ_0 to the current deformed configuration ξ.

Thus, we have $v(t,x) = V(t,p)$ and $a(t,x) = A(t,p)$ for the spatial point $x = \xi(t,p)$. By the chain rule for covariant derivatives in (2.104), we can express the spatial acceleration in terms of the spatial velocity:

$$a(t,x) = \nabla_{\partial_t}(v \circ \iota_p)(t) = \nabla_{(\partial_t, v)} v(t,x) = \nabla_{\partial_t} v(t,x) + \nabla_v v(t,x), \tag{3.7}$$

where $\iota_p \colon I \to \xi_I(M)$, $t \mapsto (t, \xi(t,p))$. More generally, the material (time) derivative of a tensor field T over ξ in spatial picture is given by

$$\dot{T}(t,x) = \nabla_{\partial_t} T(t,x) + \nabla_v T(t,x). \tag{3.8}$$

Thus, the relation $\dot{v} = \nabla_{\partial_t} v + \nabla_v v = a$ holds.

Let ξ_0 be an initial undeformed configuration and ξ be the current deformed configuration. The deformation of M in N from ξ_0 to ξ is described by the mapping

$$\phi \colon \xi_0(M) \to \xi(M), \quad x \mapsto (\xi \circ \xi_0^{-1})(x). \tag{3.9}$$

The deformation gradient of ϕ at $p \in M$ refers to the differential of ϕ at $\xi_0(p)$. We write

$$F(\phi) \colon \mathrm{T}\xi_0(M) \to \mathrm{T}\xi(M) \tag{3.10}$$

for both the deformation gradient and its matrix representation in local coordinates. The Jacobian determinant of ϕ is denoted by $J(\phi) = \det(F(\phi))$. The argument ϕ is omitted if the deformation is clear from the context.

Let $\bar{g}$ denote the Riemannian metric on the ambient space N. A configuration ξ induces a Riemannian metric on the body M via the pullback $g = \xi^* \bar{g}$. The pullback metric induced by the initial configuration ξ_0 is denoted by $G = \xi_0^* \bar{g}$. For a fixed initial configuration, the deformation $\phi = \xi \circ \xi_0^{-1}$ is fully characterized by ξ, so we can identify $\xi_0(M)$ with M and use the deformation gradient $F(\xi) = F(\phi)F(\xi_0) \colon \mathrm{T}M \to \mathrm{T}N$ instead.

Let $(E_1, \dots, E_m)$ be a local frame on M induced by a local coordinate chart $(\vartheta^1, \dots, \vartheta^m)$ with corresponding dual frame $(E^1, \dots, E^m)$, i.e.,

$$E_i = \frac{\partial}{\partial \vartheta^i}, \quad E^i = \mathrm{d}\vartheta^i, \quad E^i(E_j) = \delta^i{}_j, \tag{3.11}$$

for $i, j = 1, \dots, m$. Similarly, we have for $k, l = 1, \dots, n$ that

$$e_k = \frac{\partial}{\partial x^k}, \quad e^k = \mathrm{d}x^k, \quad e^k(e_l) = \delta^k{}_l, \tag{3.12}$$

where $(e_1, \dots, e_n)$ and $(e^1, \dots, e^n)$ are the local and dual frame corresponding to a local coordinate chart $(x^1, \dots, x^n)$ on N, respectively. By definition of the pullback metric, we have that

$$g = g_{ij}(E^i \otimes E^j), \quad G = G_{ij}(E^i \otimes E^j), \tag{3.13}$$

with the following components:

$$g_{ij} = g(E_i, E_j) = \bar{g}(g_i, g_j), \quad G_{ij} = G(E_i, E_j) = \bar{g}(G_i, G_j), \tag{3.14}$$

where the convected frames $(g_1, \dots, g_m)$ on $\xi(M)$ and $(G_1, \dots, G_m)$ on $\xi_0(M)$ are defined as

$$g_i = \partial_i \xi = \frac{\partial \xi^k}{\partial \vartheta^i} e_k = F^k{}_i(\xi) e_k, \quad G_i = \partial_i \xi_0 = \frac{\partial \xi_0^k}{\partial \vartheta^i} e_k = F^k{}_i(\xi_0) e_k, \tag{3.15}$$

with $k = 1, \dots, n$ and $\xi^k = x^k \circ \xi$. The deformation gradient of ξ is written as

$$F(\xi) = F^k{}_i(\xi)(e_k \otimes E^i) = (g_i \otimes E^i), \tag{3.16}$$

regarded as a two-point tensor field. When the identification of $\xi_0(M)$ with M is not made, the deformation gradient of ϕ reads $F(\phi) = (g_i \otimes G^i)$. Note that the relations $g^i(g_j) = \delta^i{}_j$ and $G^i(G_j) = \delta^i{}_j$ also hold for the dual frames that correspond to the convected frames.

A measure of local deformation of a deformable body is given by the material strain tensor

$$E = \frac{1}{2}(F^{\mathsf{T}} F - Id), \tag{3.17}$$

where $F^{\mathsf{T}} F$ is the (right Cauchy–Green) deformation tensor and Id is the identity tensor. We can lower the contravariant index of E using G to obtain the associated covariant material strain tensor

$$E^\flat = \frac{1}{2}(g - G), \tag{3.18}$$

which is expressible in terms of the difference of the metric tensors corresponding to the initial and current configuration [174, Definition 3.18, Proposition 4.13]. Since (3.18) plays a bigger role than (3.17) in constitutive theory, we omit the superscript $\flat$ and write

$$E = E_{ij}(E^i \otimes E^j), \quad E_{ij} = \frac{1}{2}(g_{ij} - G_{ij}), \tag{3.19}$$

for the (covariant) material strain tensor.

In the following, we consider the case $m = 3$ and $N = \mathbb{E}^3$ endowed with the dot product. We write $:$ for the double contraction of tensors with respect to the two innermost indices. The tangent bundle $\mathrm{T}\mathbb{E}^3$ is identified with $\mathbb{E}^3 \times \mathbb{R}^3$ in the usual way.

3.1.2 Equations of motion and constitutive relation

The equations of motion for a body follow from a set of balance laws: conservation of mass, balance of momentum, and balance of energy [174, Chapter 2]. In spatial picture, they are described by the following system of PDEs:

$$\dot{\varrho} + \varrho(\nabla \cdot v) = 0, \tag{3.20a}$$
$$\varrho \dot{v} = \nabla \cdot s + f_{\text{ext}}, \tag{3.20b}$$
$$\varrho \dot{w} = s : d - \nabla \cdot q + r_{\text{ext}}, \tag{3.20c}$$

where ϱ is the mass density, v is the spatial velocity, w is the internal energy density, s is the Cauchy stress tensor, d is the rate-of-deformation tensor, q is the heat flux vector, f_{ext} is the external force acting on the body, and r_{ext} is the external heat supply.

The difference between solid and fluid materials lies in the fact that fluids, such as liquids or gases, lack the ability to resist shear deformations. Fluids deform continuously (or flow) under applied shear forces, whereas solids can support a substantial amount of shear stress while remaining at rest. This distinction can be characterized by means of the symmetry group of the material [271]. The deformation of a solid body is usually expressed in material picture, where each individual particle of the body is tracked during the whole process. In contrast, fluid flows are usually specified in terms of the current spatial position since fluid particles might enter or leave the prescribed control volume. The former corresponds to the Lagrangian description and the latter to the Eulerian description of fields.

Elastic materials are materials that do not only resist deformation but also return to their original configuration when no external load acts on the system. Most solid materials exhibit elastic behavior for small strains. However, plastic deformation may occur when the applied load exceeds the yield strength, which results in an irreversible and permanent change of shape. We restrict ourselves to elastic deformations throughout this thesis.

The equations of motion in (3.20) are only fully determined when the dependence of stress on strain is given via some constitutive relation. In solid mechanics, the relation is usually specified in material picture in terms of the first Piola–Kirchhoff stress tensor

$$P = JsF^{-\mathsf{T}}, \tag{3.21}$$

given by the Piola transform of the Cauchy stress tensor s. The second Piola–Kirchhoff stress tensor

$$S = F^{-1}P = JF^{-1}sF^{-\mathsf{T}} \tag{3.22}$$

is also used to retain the symmetry that arises from the balance of angular momentum.

In this thesis, we mainly consider Cauchy elastic materials, where the first Piola–Kirchhoff stress tensor is a function of the deformation gradient, i.e., $P = P(F)$, or, equivalently, the second Piola–Kirchhoff stress tensor $S = S(E)$ is a function of the material strain tensor. This means that the stress at each point only depends on the current state of deformation. A special case is given by hyper-elastic materials for which there is a stored energy density function $W = W(E)$ such that $S = W'$.

The continuity equation (3.20a) is equivalent to the property that the mass

$$\int_{\xi_t(M)} \varrho(t,x)\,\mathrm{d}x = \int_M \varrho(t,\xi(t,p))J(t,p)\,\mathrm{d}p \tag{3.23}$$

is constant in time for any regular motion ξ. We define the reference mass density on M as

$$\varrho_{\mathrm{ref}}(p) = \varrho(t, \xi(t,p))J(t,p) \tag{3.24}$$

for $p \in M$, which is independent of the time variable t. Since ϱ is then already determined by ϱ_{ref} and the corresponding configuration ξ_t, we can omit the continuity equation in the Lagrangian description. Furthermore, we have no heat flux and no external heat supply in the isothermal case. Equation (3.20c) then reduces to $\varrho\dot{w} = s : d$, which is automatically satisfied when a hyper-elastic material model is assumed. Only the momentum equation (3.20b) remains in isothermal hyper-elasticity.

In material picture, Cauchy's equation of motion then reads

$$\varrho_{\mathrm{ref}} A = \nabla \cdot P + F_{\mathrm{ext}}, \tag{3.25}$$

where the external body force is now denoted by F_{ext}. Assuming a St.-Venant–Kirchhoff (linear elastic isotropic) material model, we have that

$$S = \lambda \operatorname{tr}(E) G^\sharp + 2\mu E^\sharp = K : E \tag{3.26}$$

with Lamé parameters λ and μ [174, Chapter 3, Example 5.17], which can be written in terms of the rank-4 elasticity tensor K that has the following components:

$$K^{ijkl} = \lambda G^{ij} G^{kl} + \mu(G^{ik}G^{jl} + G^{il}G^{jk}). \tag{3.27}$$

The components of S are thus given by

$$S^{ij} = K^{ijkl} E_{kl} = \lambda E^k{}_k G^{ij} + \mu(E^{ij} + E^{ji}). \tag{3.28}$$

In Voigt notation, the constitutive relation (3.26) reads

$$\begin{bmatrix} S^{11} \\ S^{22} \\ S^{33} \\ S^{23} \\ S^{13} \\ S^{12} \end{bmatrix} = \begin{bmatrix} \lambda+2\mu & \lambda & \lambda & 0 & 0 & 0 \\ \lambda & \lambda+2\mu & \lambda & 0 & 0 & 0 \\ \lambda & \lambda & \lambda+2\mu & 0 & 0 & 0 \\ 0 & 0 & 0 & \mu & 0 & 0 \\ 0 & 0 & 0 & 0 & \mu & 0 \\ 0 & 0 & 0 & 0 & 0 & \mu \end{bmatrix} \begin{bmatrix} E_{11} \\ E_{22} \\ E_{33} \\ 2E_{23} \\ 2E_{13} \\ 2E_{12} \end{bmatrix}. \tag{3.29}$$

Expressing it in terms of Young's modulus Y and Poisson's ratio ν yields

$$\begin{bmatrix} S^{11} \\ S^{22} \\ S^{33} \\ S^{23} \\ S^{13} \\ S^{12} \end{bmatrix} = \frac{Y}{(1+\nu)(1-2\nu)} \begin{bmatrix} 1-\nu & \nu & \nu & 0 & 0 & 0 \\ \nu & 1-\nu & \nu & 0 & 0 & 0 \\ \nu & \nu & 1-\nu & 0 & 0 & 0 \\ 0 & 0 & 0 & (1-2\nu)/2 & 0 & 0 \\ 0 & 0 & 0 & 0 & (1-2\nu)/2 & 0 \\ 0 & 0 & 0 & 0 & 0 & (1-2\nu)/2 \end{bmatrix} \begin{bmatrix} E_{11} \\ E_{22} \\ E_{33} \\ 2E_{23} \\ 2E_{13} \\ 2E_{12} \end{bmatrix},$$

where we substitute

$$\lambda = \frac{Y\nu}{(1+\nu)(1-2\nu)}, \quad \mu = \frac{Y}{2(1+\nu)} \tag{3.30}$$

for the Lamé parameters. St.-Venant–Kirchhoff material models are hyper-elastic with the strain energy density function

$$W = \frac{1}{2} S : E = \frac{1}{2} E : K : E = \frac{1}{2}\lambda \operatorname{tr}(E)^2 + \mu E : E. \tag{3.31}$$

3.1.3 Boundary value problem of elastostatics

Let M be a bounded, connected, three-dimensional body with piecewise smooth boundary ∂M that consists of a Dirichlet and Neumann part, i.e., $\partial M = M_{\mathrm{D}} \cup M_{\mathrm{N}}$. In the stationary case, the left-hand side of (3.25) vanishes, which leads to the boundary value problem of elastostatics: Find an admissible configuration $\xi \in \mathrm{Emb}(\overline{M}, \mathbb{E}^3)$ such that

$$-\nabla \cdot P(\xi) = F_{\mathrm{ext}} \quad \text{in } M, \tag{3.32a}$$

$$P(\xi) \cdot N = G_{\mathrm{ext}} \quad \text{on } M_{\mathrm{N}}, \tag{3.32b}$$

$$\xi = \xi_{\mathrm{fix}} \quad \text{on } M_{\mathrm{D}}, \tag{3.32c}$$

where G_{ext} is the external surface force acting on the Neumann boundary M_{N}, ξ_{fix} is the prescribed deformation on the Dirichlet boundary M_{D}, and N is the unit normal vector field defined almost everywhere on ∂M. The dependence of the fields on ξ is now written explicitly. See Figure 4 for an illustration of the domain of the boundary value problem.

The set of admissible configurations consistent with the boundary conditions is denoted by

$$\mathfrak{C} = \big\{ \xi \in \mathrm{Emb}(\overline{M}, \mathbb{E}^3) \,\big|\, \xi = \xi_{\mathrm{fix}} \text{ on } M_{\mathrm{D}} \big\}. \tag{3.33}$$

Its tangent space, i.e., the set of admissible variations at $\xi \in \mathfrak{C}$, is given by

$$\mathrm{T}_\xi \mathfrak{C} \simeq \big\{ \eta \in \mathrm{C}^1(\overline{M}, \mathbb{R}^3) \,\big|\, \eta = 0 \text{ on } M_{\mathrm{D}} \big\}. \tag{3.34}$$

The corresponding bundle of admissible variations reads

$$\mathrm{T}\mathfrak{C} = \coprod_{\xi \in \mathfrak{C}} \mathrm{T}_\xi \mathfrak{C} = \big\{ (\xi, \eta) \,\big|\, \xi \in \mathfrak{C},\, \eta \in \mathrm{T}_\xi \mathfrak{C} \big\}. \tag{3.35}$$

We occasionally write $\eta = \delta\xi$ for an admissible variation at ξ. By multiplying (3.32a) with $\eta \in \mathrm{T}_\xi \mathfrak{C}$, taking the integral over M, and applying the product rule

$$\nabla \cdot (P(\xi) \cdot \eta) = (\nabla \cdot P(\xi)) \cdot \eta + P(\xi) : F(\eta) \tag{3.36}$$

as well as the divergence theorem, we obtain the equilibrium equation

$$\int_M P(\xi) : F(\eta) \,\mathrm{dV} = \int_M F_{\mathrm{ext}} \cdot \eta \,\mathrm{dV} + \int_{M_{\mathrm{N}}} G_{\mathrm{ext}} \cdot \eta \,\mathrm{dA}. \tag{3.37}$$

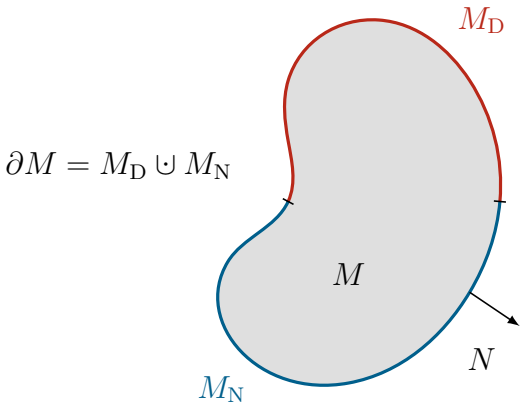

Figure 4: Domain of an elastostatic boundary value problem.

Due to the relation $P = FS$, the symmetry of the second Piola–Kirchhoff stress tensor, and the properties of the trace function, we can also write

$$P(\xi) : F(\eta) = \operatorname{tr}(S(\xi)^{\mathsf{T}} \operatorname{sym}(F(\xi)^{\mathsf{T}} F(\eta))) = S(\xi) : D(\xi, \eta), \tag{3.38}$$

where

$$D(\xi, \eta) = E'(\xi)\eta = \frac{\mathrm{d}}{\mathrm{d}t} E(\xi + t\eta)\bigg|_{t=0} = \frac{1}{2}(F(\xi)^{\mathsf{T}} F(\eta) + F(\eta)^{\mathsf{T}} F(\xi)) \tag{3.39}$$

is the material rate-of-deformation tensor, given by the symmetric part of $F(\xi)^{\mathsf{T}} F(\eta)$.

We define the fiberwise linear functional $\mathcal{R} \colon \mathrm{T}\mathfrak{C} \to \mathbb{R}$ with

$$\mathcal{R}(\xi, \eta) = \underbrace{\int_M F_{\mathrm{ext}} \cdot \eta \,\mathrm{dV} + \int_{M_{\mathrm{N}}} G_{\mathrm{ext}} \cdot \eta \,\mathrm{dA}}_{b(\eta)} - \underbrace{\int_M S(\xi) : D(\xi, \eta) \,\mathrm{dV}}_{a(\xi,\eta)}, \tag{3.40}$$

and end up with the following abstract notation for the variational formulation of the boundary value problem: Find an admissible configuration $\xi \in \mathfrak{C}$ such that

$$\mathcal{R}(\xi, \eta) = 0 \tag{3.41}$$

for all admissible variations $\eta \in \mathrm{T}_\xi \mathfrak{C}$.

For hyper-elastic materials, the above characterization is equivalent to the stationarity of the stored energy functional $\Psi \colon \mathfrak{C} \to \mathbb{R}$ with

$$\Psi(\xi) = \underbrace{\int_M F_{\mathrm{ext}} \cdot \xi \,\mathrm{dV} + \int_{M_{\mathrm{N}}} G_{\mathrm{ext}} \cdot \xi \,\mathrm{dA}}_{\Psi_{\mathrm{ext}}(\xi)} - \underbrace{\int_M W(E(\xi)) \,\mathrm{dV}}_{\Psi_{\mathrm{int}}(\xi)}, \tag{3.42}$$

where Ψ_{ext} corresponds to the mechanical work done by external forces and Ψ_{int} denotes the internal strain energy, since we have that

$$\begin{aligned}
\Psi'(\xi)\eta &= \frac{\mathrm{d}}{\mathrm{d}t} \Psi(\xi + t\eta)\bigg|_{t=0} = \frac{\mathrm{d}}{\mathrm{d}t} \Psi_{\mathrm{ext}}(\xi + t\eta)\bigg|_{t=0} - \frac{\mathrm{d}}{\mathrm{d}t} \Psi_{\mathrm{int}}(\xi + t\eta)\bigg|_{t=0} \\
&= \int_M F_{\mathrm{ext}} \cdot \mathrm{id}'(\xi)\eta \,\mathrm{dV} + \int_{M_{\mathrm{N}}} G_{\mathrm{ext}} \cdot \mathrm{id}'(\xi)\eta \,\mathrm{dA} - \int_M W'(E(\xi))E'(\xi)\eta \,\mathrm{dV} \\
&= \int_M F_{\mathrm{ext}} \cdot \eta \,\mathrm{dV} + \int_{M_{\mathrm{N}}} G_{\mathrm{ext}} \cdot \eta \,\mathrm{dA} - \int_M S(\xi) : D(\xi, \eta) \,\mathrm{dV} \\
&= \mathcal{R}(\xi, \eta).
\end{aligned} \tag{3.43}$$

Thus, $\mathcal{R}(\xi, \eta) = 0$ holds for all admissible variations $\eta \in \mathrm{T}_\xi \mathfrak{C}$ if and only if $\Psi'(\xi) = 0$. This is referred to as the principle of virtual work.

3.1.4 Linearization and displacement formulation

The variational equation in (3.41) is non-linear in the first variable. We can consider the linearization of the strain tensor at the initial undeformed configuration ξ_0 with $E(\xi_0) = 0$, i.e.,

$$E(\xi) \approx E(\xi_0) + E'(\xi_0)(\xi - \xi_0) = \delta E(\xi_0, \xi - \xi_0) = D(\xi_0, \xi - \xi_0), \tag{3.44}$$

to obtain the displacement formulation in terms of the displacement field $\xi - \xi_0 \in \mathrm{T}_{\xi_0}\mathfrak{C}$. For the partial derivative of $\mathcal{R}$ with respect to the first variable at ξ, we have that

$$\partial_1 \mathcal{R}(\xi,\eta)\zeta = -\int_M \Big(\delta E(\xi,\zeta) : K : \delta E(\xi,\eta) + S(\xi) : \delta^2 E(\xi,\eta,\zeta)\Big)\,\mathrm{dV}. \tag{3.45}$$

Linearization of the variational equation in the first variable at ξ_0 yields

$$\mathcal{R}(\xi,\eta) \approx \mathcal{R}(\xi_0,\eta) + \partial_1\mathcal{R}(\xi_0,\eta)(\xi-\xi_0) \overset{!}{=} 0. \tag{3.46}$$

With $u = \xi - \xi_0 \in \mathfrak{G}$ and $v = \eta \in \mathfrak{H}$, where we define

$$\begin{aligned} \mathfrak{G} = \mathrm{T}_{\xi_0}\mathfrak{C} &\simeq \big\{u \in \mathrm{C}^1(\overline{M},\mathbb{R}^3) \;\big|\; u = 0 \text{ on } M_\mathrm{D}\big\},\\ \mathfrak{H} = \mathrm{T}_{\xi}\mathfrak{C} &\simeq \big\{v \in \mathrm{C}^1(\overline{M},\mathbb{R}^3) \;\big|\; v = 0 \text{ on } M_\mathrm{D}\big\}, \end{aligned} \tag{3.47}$$

the above linearization results in the following equilibrium equation:

$$\int_M \Big(\delta E(\xi_0,u) : K : \delta E(\xi_0,v) + S(\xi_0) : \delta^2 E(\xi_0,v,u)\Big)\,\mathrm{dV} = \int_M F_\mathrm{ext}\cdot v\,\mathrm{dV} + \int_{M_\mathrm{N}} G_\mathrm{ext}\cdot v\,\mathrm{dA}.$$

By neglecting higher-order derivatives of the strain tensor, we obtain the displacement formulation for the linearized boundary value problem of elastostatics: Find an admissible displacement field $u \in \mathfrak{G}$ such that

$$a(u,v) = b(v) \tag{3.48}$$

for all admissible variations $v \in \mathfrak{H}$, where $a\colon \mathfrak{G}\times\mathfrak{H} \to \mathbb{R}$ is a bilinear form and $b\colon \mathfrak{H} \to \mathbb{R}$ is a linear functional given by

$$a(u,v) = \int_M \sigma(u) : \varepsilon(v)\,\mathrm{dV}, \quad b(v) = \int_M F_\mathrm{ext}\cdot v\,\mathrm{dV} + \int_{M_\mathrm{N}} G_\mathrm{ext}\cdot v\,\mathrm{dA}, \tag{3.49}$$

with the linearized stress and strain tensors

$$\sigma(u) = K : \varepsilon(u), \quad \varepsilon(u) = \delta E(\xi_0,u) = D(\xi_0,u) = \mathrm{sym}(F(\xi_0)^\mathsf{T} F(u)). \tag{3.50}$$

The corresponding linearized strain energy reads

$$\psi_\mathrm{int}\colon \mathfrak{G} \to \mathbb{R}, \quad u \mapsto \frac{1}{2}\int_M \sigma(u) : \varepsilon(u)\,\mathrm{dV}. \tag{3.51}$$

3.1.5 Weak variational formulation

Solutions to variational problems are usually found in function spaces that are weaker than the one on which the original problem is posed. Such solutions are called weak solutions, as opposed to classical solutions corresponding to the strong formulation of the problem.

For the displacement formulation of the linearized elastostatic boundary value problem, it is known that the weak variational problem is well-posed on the closed subspace

$$\mathfrak{V} = \big\{v \in \mathrm{H}^1(M,\mathbb{R}^3) \;\big|\; v = 0 \text{ on } M_\mathrm{D}\big\}, \tag{3.52}$$

i.e., there is a unique solution to the problem in $\mathfrak{V}$ that depends continuously on the data, provided that the Dirichlet boundary M_D is not of boundary measure zero. This is because, in that case, the symmetric bilinear form

$$a\colon \mathfrak{V}\times\mathfrak{V} \to \mathbb{R}, \quad (u,v) \mapsto \int_M \sigma(u) : \varepsilon(v)\,\mathrm{dV}, \tag{3.53}$$

is uniformly $\mathfrak{V}$-elliptic due to Korn's inequality [55, Chapter VI, Section 3].

For the pure Neumann problem without Dirichlet boundary conditions, additional terms or conditions have to be considered to ensure the well-posedness of the problem. For existence theorems in non-linear elasticity, we refer to Ball [25].

3.2 Reduction to lower-dimensional models

In this section, we explain how mathematical models for lower-dimensional elastic bodies, such as shells, plates, and beams, can be obtained from the three-dimensional theory. We follow the direct approach for dimensional reduction, which results in a geometrically exact model of shells [251, 281]. Our main reference is Bischoff et al. [41] from the Encyclopedia of Computational Mechanics. Further references include Ciarlet [66, 67, 68], Koiter [156], Naghdi [189], Braess [55], and Steigmann [256].

3.2.1 Shell kinematic assumptions

A shell is a three-dimensional solid whose thickness in one direction is considerably small relative to the other two directions. The mathematical model of a shell can be reduced to a two-dimensional one by considering only the mechanics on some reference surface. More formally, a shell is modeled as a fiber bundle (B, A, π), where the total space B is given by a three-dimensional body and the base space A is a surface embedded in B. Each fiber of the shell is a curve segment that is transverse to the reference surface $A \subset B$.

One typically distinguishes between thick and thin shell models. Thick shell models capture transverse shear strains in addition to membrane and bending strains, as opposed to thin shell models, where the thickness of the shell is assumed small enough, so that the effects of transverse shear deformations can be neglected. The configuration of such a thin shell is fully determined by the configuration of the reference surface in physical space, whereas the configuration of a thick shell is supplemented by a deformable vector field on the reference surface, called a director field. A surface together with a director field is referred to as a one-director Cosserat surface [114]. The concept of assigning orientations to material points as additional degrees of freedom has been proposed by the Cosserat brothers in [78].

As a rule of thumb, a shell is considered thin when the ratio between the thickness h and the minimum radius of curvature $r_{\min}$, as defined in Section 2.4.2, is small and does not exceed some threshold value, e.g.,

$$h/r_{\min} \leq 5\,\%, \tag{3.54}$$

according to Kiendl et al. [153]. A well-known and conventional model for thin elastic shells is given by the Kirchhoff–Love or Koiter shell model [156], which is confined to membrane and bending deformations. More general models for thick shells, based on first-order shear deformation theory (FSDT) akin to Reissner–Mindlin plates, have been attributed to Naghdi as a result of his work on the systematic development of shell and plate theories in [189].

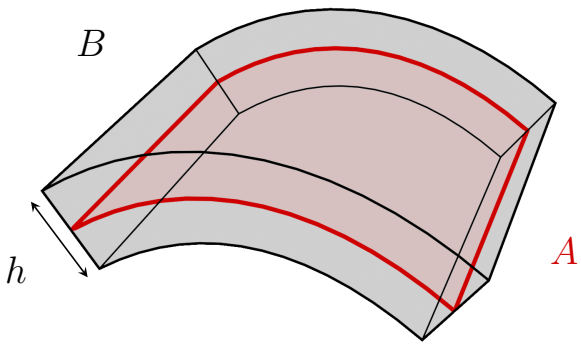

Figure 5: A shell segment of thickness h and its reference surface (red).

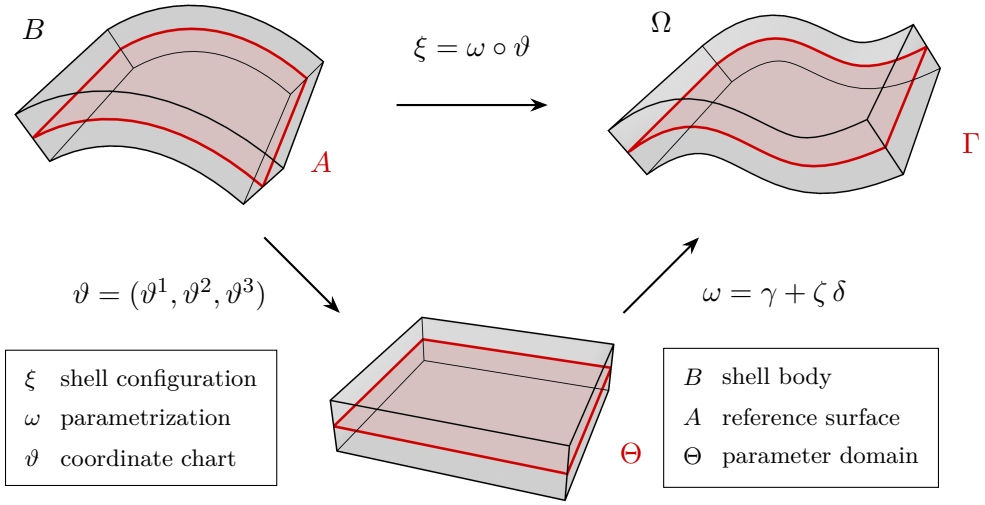

Figure 6: Parametrization of a shell segment using local curvilinear coordinates.

Let (B, A, π) be a shell. Given an admissible configuration $\xi\colon B \to \mathbb{E}^3$ of the shell body, the restriction $\xi|_A$ to the reference surface is called a surface configuration. We write $\Omega = \xi(B)$ for the image of B under ξ and $\Gamma = \xi(A)$ for the image of the surface configuration.

There are various conditions that can be imposed on configurations of a shell. In this work, we focus on the Kirchhoff–Love hypotheses for thin elastic shells and consider the following shell kinematic assumptions [168, 212]:

(A1) Mindlin hypothesis: Fibers are mapped to straight line segments that vary linearly in terms of the parameter corresponding to the transverse direction.

(A2) Kirchhoff hypothesis: Fibers are mapped to curve segments that are orthogonal to the reference surface.

(A3) Inextensibility: The length of each fiber remains constant for all configurations.

Under the Mindlin hypothesis (A1), any admissible shell configuration can be parametrized locally using curvi-linear coordinates $\vartheta = (\vartheta^1, \vartheta^2, \vartheta^3)$ by a mapping of the form

$$\omega(\vartheta^1, \vartheta^2, \vartheta^3) = \gamma(\vartheta^1, \vartheta^2) + \vartheta^3\,\delta(\vartheta^1, \vartheta^2), \tag{3.55}$$

where γ is a parametrization of the corresponding part of the surface configuration and δ is a unit director field, which coincides with the unit normal n to the surface in physical space if the Kirchhoff hypothesis (A2) is assumed. The parameter $\zeta = \vartheta^3$ corresponds to the transverse direction and ranges from a lower bound h^- to an upper bound h^+. One speaks of an inextensible Cosserat surface if the thickness $h = h^+ - h^-$ remains constant for all admissible configurations, according to (A3).

We write $\omega = \gamma + \zeta\,\delta$ for an admissible parametrization of the Cosserat surface, which is defined on the shell parameter domain

$$\Theta_{[h^-,h^+]} = \big\{(\vartheta^1, \vartheta^2, \vartheta^3) \in \mathbb{R}^3 \,\big|\, (\vartheta^1, \vartheta^2) \in \Theta,\ h^-(\vartheta^1, \vartheta^2) \leq \vartheta^3 \leq h^+(\vartheta^1, \vartheta^2)\big\}. \tag{3.56}$$

Here, $\Theta \subseteq \mathbb{R}^2$ is an open subset in two-dimensional real coordinate space corresponding to a part of the reference surface. Note that we have $h^- = -h^+$ and $h = 2h^+$ if the reference

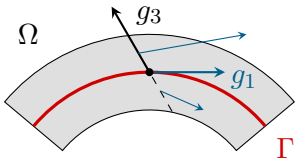

(a) Shell metric tensor g without (A2).

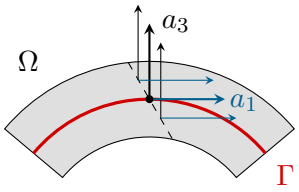

(b) Surface metric tensor a without (A2).

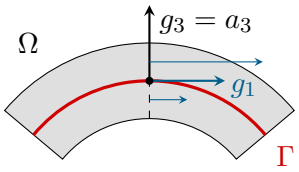

(c) Shell metric tensor g with (A2).

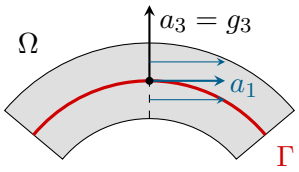

(d) Surface metric tensor a with (A2).

Figure 7: Differences between the convected frames corresponding to the shell and surface metric tensor. If the Kirchhoff hypothesis (A2) is assumed, the director $\delta = g_3$ coincides with the unit normal $n = a_3$ to the surface. Fibers are depicted using dashed lines.

surface is chosen to be the mid-surface of the shell. The thickness is said to be homogeneous if h is constant over the whole surface.

We distinguish between the shell and surface metric tensor on B induced by ξ. The shell metric tensor g is given by the pullback of the metric tensor on Ω, i.e., $g_{ij} = g_i \cdot g_j$ with $g_i = \partial_i \omega$ for $i, j = 1, 2, 3$ in local coordinates. The surface metric tensor a is given by the pullback of the metric tensor on Γ, supplemented with the unit normal vector field n, i.e., $a_{ij} = a_i \cdot a_j$ with $a_\alpha = \partial_\alpha \gamma$ for $\alpha = 1, 2$ and $a_3 = n = (a_1 \times a_2)/\|a_1 \times a_2\|$ in local coordinates. We use upper-case letters G and A to denote the corresponding tensors with respect to the initial undeformed configuration, i.e., $G_{ij} = G_i \cdot G_j$ with $G_i = \partial_i \omega_0$ as well as $A_{ij} = A_i \cdot A_j$ with $A_\alpha = \partial_\alpha \gamma_0$ and $A_3 = N = (A_1 \times A_2)/\|A_1 \times A_2\|$ in local coordinates. It should be clear from context whether A refers to the tensor or the reference surface.

The shell shifter tensor $Z = G_i \otimes A^i$ refers to the local coordinate transformation from the surface to the shell coordinate system. The fundamental assumption in the theory of thin shells is that Z is close to the identity tensor. In particular, we assume for the determinant of Z, given by Steiner's formula in Proposition 2.57, that

$$\det(Z) = \frac{\det(G_1, G_2, G_3)}{\|A_1 \times A_2\|} = (1 - 2H\zeta + K\zeta^2) \approx 1, \tag{3.57}$$

due to the small ratio in (3.54) and negligible higher-order terms in ζ. This is referred to as the thin shell assumption. We write $|\zeta| \ll 1$ when higher-order terms in ζ can be neglected due to the thin shell assumption.

3.2.2 A shell model of Koiter's type

The equilibrium equations for thin hyper-elastic shells can be derived from the principle of virtual work by expressing the strain tensor in terms of kinematic variables of the reference surface and pre-integrating along the transverse direction. In the following, we assume that the reference surface is given by the mid-surface and that the thickness is homogeneous.

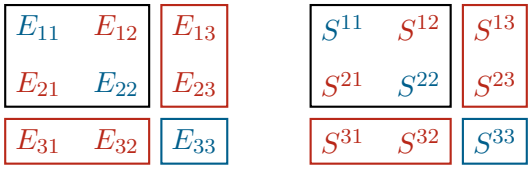

Figure 8: Nomenclature for strain and stress components. Black box: in-plane components. Colored box: transverse components. Blue: normal components. Red: shear components.

The deformation gradient of an admissible shell configuration in local coordinates reads

$$F = \begin{bmatrix} \partial_1\gamma + \zeta\,\partial_1 n & \partial_2\gamma + \zeta\,\partial_2 n & n \end{bmatrix} = \begin{bmatrix} a_1 & a_2 & n \end{bmatrix} + \zeta \begin{bmatrix} \partial_1 n & \partial_2 n & 0 \end{bmatrix} \tag{3.58}$$

under the shell kinematic assumptions. For the shell metric tensor, we have that

$$\begin{aligned} g &= \begin{bmatrix} a_1\cdot a_1 & a_1\cdot a_2 & a_1\cdot n \\ a_2\cdot a_1 & a_2\cdot a_2 & a_2\cdot n \\ n\cdot a_1 & n\cdot a_2 & n\cdot n \end{bmatrix} + 2\zeta \begin{bmatrix} \partial_1 n\cdot a_1 & \partial_1 n\cdot a_2 & 0 \\ \partial_2 n\cdot a_1 & \partial_2 n\cdot a_2 & 0 \\ 0 & 0 & 0 \end{bmatrix} + \zeta^2 \begin{bmatrix} \partial_1 n\cdot \partial_1 n & \partial_1 n\cdot \partial_2 n & 0 \\ \partial_2 n\cdot \partial_1 n & \partial_2 n\cdot \partial_2 n & 0 \\ 0 & 0 & 0 \end{bmatrix} \\ &= \begin{bmatrix} a_{11} & a_{12} & 0 \\ a_{21} & a_{22} & 0 \\ 0 & 0 & 1 \end{bmatrix} - 2\zeta \begin{bmatrix} b_{11} & b_{12} & 0 \\ b_{21} & b_{22} & 0 \\ 0 & 0 & 0 \end{bmatrix} + \zeta^2 \begin{bmatrix} c_{11} & c_{12} & 0 \\ c_{21} & c_{22} & 0 \\ 0 & 0 & 0 \end{bmatrix}. \end{aligned} \tag{3.59}$$

From (3.59), we see that the material strain tensor (3.18) has no transverse components. Thus, we can define the in-plane strain tensor with respect to the surface metric by

$$\bar{E} = E_{\alpha\beta}(A^\alpha \otimes A^\beta) = \frac{1}{2}(a - A) - 2\zeta\frac{1}{2}(b - B) + \zeta^2\frac{1}{2}(c - C), \tag{3.60}$$

which can be written in terms of the first, second, and third fundamental form with respect to the current and initial undeformed configuration .

The inextensibility condition (A3) implies that transverse normal strains are zero, i.e.,

$$E_{33} = 0, \tag{3.61}$$

which is an artificial constraint that is incompatible with the zero transverse normal stress condition (conventionally used to model thin plates and membranes in planar elasticity) and leads to an over-stiff behavior of the shell model. To mitigate this problem, we allow non-zero transverse normal strains and impose the following condition instead:

$$S^{33} = 0. \tag{3.62}$$

This corresponds to static condensation of transverse normal strains [41, Section 4.4.5].

The above condition (3.62), together with the constitutive relation (3.29), yields

$$S^3{}_3 = S^{3i}G_{i3} = \lambda\,\mathrm{tr}(E) + 2\mu E^3{}_3 = \lambda(E^1{}_1 + E^2{}_2) + (\lambda + 2\mu)E^3{}_3 = 0, \tag{3.63}$$

thus

$$E^3{}_3 = -\frac{\lambda}{\lambda + 2\mu}(E^1{}_1 + E^2{}_2), \tag{3.64}$$

which leads to

$$\lambda\,\mathrm{tr}(E) = -2\mu E^3{}_3 = \bar{\lambda}(E^1{}_1 + E^2{}_2) \tag{3.65}$$

with the modified Lamé parameter

$$\bar{\lambda} = \frac{2\mu\lambda}{\lambda + 2\mu} = \frac{Y\nu}{1-\nu^2}. \tag{3.66}$$

For the strain energy density (3.31), the relation (3.65) yields

$$\begin{aligned} W &= \frac{1}{2}\lambda \operatorname{tr}(E)^2 + \mu E : E \\ &= \frac{1}{2}\bar{\lambda}(E^1{}_1 + E^2{}_2)(E^1{}_1 + E^2{}_2 + E^3{}_3) + \mu E : E \\ &= \frac{1}{2}\bar{\lambda}(E^1{}_1 + E^2{}_2)^2 + \mu(E : E - E^{33}E_{33}) \\ &= \frac{1}{2}\bar{\lambda}(E^1{}_1 + E^2{}_2)^2 + \mu(E^{11}E_{11} + E^{22}E_{22} + E^{12}E_{12} + E^{21}E_{21}), \end{aligned} \tag{3.67}$$

since transverse shear components vanish in the model. The resulting expression does not depend on transverse components of the strain tensor. We can then introduce the in-plane elasticity tensor $\bar{K}$ with components

$$\bar{K}^{\alpha\beta\gamma\delta} = \bar{\lambda}A^{\alpha\beta}A^{\gamma\delta} + \mu(A^{\alpha\gamma}A^{\beta\delta} + A^{\alpha\delta}A^{\beta\gamma}) \tag{3.68}$$

and the energetically conjugate in-plane stress tensor $\bar{S} = \bar{K} : \bar{E}$. Assuming that Z is close to the identity tensor, i.e., $G \approx A$, the strain energy density corresponding to the in-plane strain and stress tensors is approximately equal to the one in (3.67), i.e.,

$$\bar{W} = \frac{1}{2}\bar{S} : \bar{E} = \frac{1}{2}\lambda \operatorname{tr}(\bar{E})^2 + \mu\bar{E} : \bar{E} \approx W. \tag{3.69}$$

Contractions of in-plane tensors are taken with respect to the surface metric tensor.

For thin shells with $|\zeta| \ll 1$, we can neglect higher-order terms in ζ and obtain

$$\bar{E} = \bar{E}^{\mathrm{m}} + \zeta\bar{E}^{\mathrm{b}} + \mathcal{O}(\zeta^2) \approx \bar{E}^{\mathrm{m}} + \zeta\bar{E}^{\mathrm{b}} \tag{3.70}$$

from (3.60) with the membrane and bending strain tensors

$$\bar{E}^{\mathrm{m}} = \frac{1}{2}(a - A), \quad \bar{E}^{\mathrm{b}} = -(b - B). \tag{3.71}$$

Pre-integration of the strain energy along the transverse direction then yields

$$\begin{aligned} \Psi_{\mathrm{int}} &= \int_B W \,\mathrm{dV} = \frac{1}{2}\int_A \int_{h^-}^{h^+} S : E \,\det(Z)\,\mathrm{d}\zeta\,\mathrm{dA} \approx \frac{1}{2}\int_A \int_{h^-}^{h^+} \bar{S} : \bar{E}\,\mathrm{d}\zeta\,\mathrm{dA} \\ &\approx \frac{1}{2}\int_A \int_{h^-}^{h^+} \bar{K}^{\alpha\beta\gamma\delta}\left(\bar{E}^{\mathrm{m}}_{\alpha\beta} + \zeta\bar{E}^{\mathrm{b}}_{\alpha\beta}\right)\left(\bar{E}^{\mathrm{m}}_{\gamma\delta} + \zeta\bar{E}^{\mathrm{b}}_{\gamma\delta}\right)\mathrm{d}\zeta\,\mathrm{dA} \\ &= \frac{1}{2}\int_A \int_{h^-}^{h^+} \bar{K}^{\alpha\beta\gamma\delta}\left(\bar{E}^{\mathrm{m}}_{\alpha\beta}\bar{E}^{\mathrm{m}}_{\gamma\delta} + \zeta\left(\bar{E}^{\mathrm{m}}_{\alpha\beta}\bar{E}^{\mathrm{b}}_{\gamma\delta} + \bar{E}^{\mathrm{b}}_{\alpha\beta}\bar{E}^{\mathrm{m}}_{\gamma\delta}\right) + \zeta^2\bar{E}^{\mathrm{b}}_{\alpha\beta}\bar{E}^{\mathrm{b}}_{\gamma\delta}\right)\mathrm{d}\zeta\,\mathrm{dA} \\ &= \frac{1}{2}\int_A \bar{K}^{\alpha\beta\gamma\delta}\left(h\bar{E}^{\mathrm{m}}_{\alpha\beta}\bar{E}^{\mathrm{m}}_{\gamma\delta} + \frac{h^3}{12}\bar{E}^{\mathrm{b}}_{\alpha\beta}\bar{E}^{\mathrm{b}}_{\gamma\delta}\right)\mathrm{dA} \\ &= \frac{1}{2}\int_A \left(\bar{S}^{\mathrm{m}} : \bar{E}^{\mathrm{m}} + \bar{S}^{\mathrm{b}} : \bar{E}^{\mathrm{b}}\right)\mathrm{dA}, \end{aligned} \tag{3.72}$$

where the effective stress resultants (membrane force and bending moment) are given by

$$\bar{S}^{\mathrm{m}} = h\bar{K} : \bar{E}^{\mathrm{m}}, \quad \bar{S}^{\mathrm{b}} = \frac{h^3}{12}\bar{K} : \bar{E}^{\mathrm{b}}. \tag{3.73}$$

The constant term in ζ integrates to

$$\int_{h^-}^{h^+} 1 \,\mathrm{d}\zeta = h^+ - h^- = h, \tag{3.74}$$

the linear term vanishes due to $h^- = -h^+$ and odd symmetry

$$\int_{h^-}^{h^+} \zeta \,\mathrm{d}\zeta = \frac{1}{2}(h^+)^2 - \frac{1}{2}(h^-)^2 = 0, \tag{3.75}$$

and for the quadratic term, we use that $h = 2h^+$ to obtain

$$\begin{aligned} \int_{h^-}^{h^+} \zeta^2 \,\mathrm{d}\zeta &= \frac{1}{3}(h^+)^3 - \frac{1}{3}(h^-)^3 = \frac{1}{3}(h^+ - h^-)((h^+)^2 + h^+h^- + (h^-)^2) \\ &= \frac{1}{3}h\left(\frac{1}{4}h^2 - \frac{1}{4}h^2 + \frac{1}{4}h^2\right) = \frac{h^3}{12}. \end{aligned} \tag{3.76}$$

Note that the effective stress resultants have no direct physical interpretation and need to be converted to true stress resultants in order to perform reliable stress analysis.

3.2.3 Boundary value problem of thin elastic shells

Common boundary conditions for shells in static equilibrium consist in a combination of structural supports, e.g., pinned, clamped, and roller supports, which correspond to fixing some components of the configuration and its derivatives at the boundary. For the sake of simplicity, we consider the case where the shell is clamped along the normal vector field at some part of the boundary.

Let the reference surface be connected with piecewise smooth boundary $\partial A = A_\mathrm{D} \cup A_\mathrm{N}$. The set of admissible surface configurations consistent with the boundary conditions reads

$$\mathfrak{A} = \left\{ \bar{\xi} \in \mathrm{Emb}(\overline{A}, \mathbb{E}^3) \;\middle|\; \bar{\xi} = \bar{\xi}_\mathrm{fix},\ \mathrm{T}\bar{\xi} \cdot \bar{n}_\mathrm{fix} = 0 \text{ on } A_\mathrm{D} \right\}, \tag{3.77}$$

where $\bar{\xi}_\mathrm{fix}$ is the prescribed deformation and $\bar{n}_\mathrm{fix}$ a corresponding normal vector field on the Dirichlet boundary A_D. Since the strain energy in (3.72) only depends on kinematic variables of the reference surface, we can define the shell strain energy functional as

$$\bar{\Psi}_\mathrm{int} \colon \mathfrak{A} \to \mathbb{R}, \quad \bar{\xi} \mapsto \frac{1}{2}\int_A \left(\bar{S}^\mathrm{m}(\bar{\xi}) : \bar{E}^\mathrm{m}(\bar{\xi}) + \bar{S}^\mathrm{b}(\bar{\xi}) : \bar{E}^\mathrm{b}(\bar{\xi}) \right) \mathrm{dA}. \tag{3.78}$$

For the mechanical work done by external forces, we assume that there is an external force $\bar{F}_\mathrm{ext}$ acting on the reference surface A and an external traction force $\bar{G}_\mathrm{ext}$ acting on the Neumann part A_N of the boundary curve ∂A, but no external moments for simplicity. The external energy functional is then given by

$$\bar{\Psi}_\mathrm{ext} \colon \mathfrak{A} \to \mathbb{R}, \quad \bar{\xi} \mapsto \int_A \bar{F}_\mathrm{ext} \cdot \bar{\xi} \,\mathrm{dA} + \int_{A_\mathrm{N}} \bar{G}_\mathrm{ext} \cdot \bar{\xi} \,\mathrm{dS}. \tag{3.79}$$

Similar to the derivation in (3.43), we can use the principle of virtual work to obtain the variational formulation for the non-linear Koiter shell model: Find an admissible surface configuration $\bar{\xi} \in \mathfrak{A}$ such that

$$\bar{a}(\bar{\xi}, \bar{\eta}) = \bar{b}(\bar{\eta}) \tag{3.80}$$

for all admissible shell variations $\bar{\eta} \in \mathrm{T}_{\bar{\xi}}\mathfrak{A}$, where

$$\bar{a}(\bar{\xi}, \bar{\eta}) = \bar{\Psi}'_{\mathrm{int}}(\bar{\xi})\bar{\eta} = \int_A \big(\bar{S}^{\mathrm{m}}(\bar{\xi}) : \bar{D}^{\mathrm{m}}(\bar{\xi}, \bar{\eta}) + \bar{S}^{\mathrm{b}}(\bar{\xi}) : \bar{D}^{\mathrm{b}}(\bar{\xi}, \bar{\eta})\big)\,\mathrm{dA}, \tag{3.81a}$$

$$\bar{b}(\bar{\eta}) = \bar{\Psi}'_{\mathrm{ext}}(\bar{\xi})\bar{\eta} = \int_A \bar{F}_{\mathrm{ext}} \cdot \bar{\eta}\,\mathrm{dA} + \int_{A_{\mathrm{N}}} \bar{G}_{\mathrm{ext}} \cdot \bar{\eta}\,\mathrm{dS}, \tag{3.81b}$$

with $\bar{D}^{\mathrm{m}}(\bar{\xi}, \bar{\eta}) = \delta\bar{E}^{\mathrm{m}}(\bar{\xi}, \bar{\eta})$ and $\bar{D}^{\mathrm{b}}(\bar{\xi}, \bar{\eta}) = \delta\bar{E}^{\mathrm{b}}(\bar{\xi}, \bar{\eta})$.

The procedure in Section 3.1.4 yields the linearized membrane and bending strain tensors

$$\varepsilon_{\mathrm{m}}(u) = \bar{D}^{\mathrm{m}}(\xi_0, u), \quad \varepsilon_{\mathrm{b}}(u) = \bar{D}^{\mathrm{b}}(\xi_0, u) \tag{3.82}$$

as well as the corresponding linearized effective stress resultants

$$\sigma_{\mathrm{m}}(u) = h\bar{K} : \varepsilon_{\mathrm{m}}(u), \quad \sigma_{\mathrm{b}}(u) = \frac{h^3}{12}\bar{K} : \varepsilon_{\mathrm{b}}(u). \tag{3.83}$$

From these, we obtain the displacement formulation for the linearized Koiter shell model: Find an admissible shell displacement field $u \in \mathfrak{G} = \mathrm{T}_{\xi_0}\mathfrak{A}$ such that

$$a(u, v) = b(v) \tag{3.84}$$

for all admissible shell variations $v \in \mathfrak{H} = \mathrm{T}_{\xi}\mathfrak{A}$, where

$$a(u, v) = \int_A \big(\sigma_{\mathrm{m}}(u) : \varepsilon_{\mathrm{m}}(v) + \sigma_{\mathrm{b}}(u) : \varepsilon_{\mathrm{b}}(v)\big)\,\mathrm{dA}, \tag{3.85a}$$

$$b(v) = \int_A F_{\mathrm{ext}} \cdot v\,\mathrm{dA} + \int_{A_{\mathrm{N}}} G_{\mathrm{ext}} \cdot v\,\mathrm{dS}. \tag{3.85b}$$

The corresponding linearized shell strain energy is given by

$$\psi_{\mathrm{int}} \colon \mathfrak{G} \to \mathbb{R}, \quad u \mapsto \frac{1}{2}\int_A \big(\sigma_{\mathrm{m}}(u) : \varepsilon_{\mathrm{m}}(u) + \sigma_{\mathrm{b}}(u) : \varepsilon_{\mathrm{b}}(u)\big)\,\mathrm{dA}. \tag{3.86}$$

Note that the bars above the variables have been omitted for visual clarity. The strain tensors and the linearized counterparts have the following components in local coordinates:

$$\begin{aligned} E^{\mathrm{m}}_{\alpha\beta} &= \frac{1}{2}(\partial_\alpha\gamma \cdot \partial_\beta\gamma - \partial_\alpha\gamma_0 \cdot \partial_\beta\gamma_0), \quad (\varepsilon_{\mathrm{m}})_{\alpha\beta} = \frac{1}{2}(\partial_\alpha u \cdot \partial_\beta\gamma_0 + \partial_\alpha\gamma_0 \cdot \partial_\beta u), \\ E^{\mathrm{b}}_{\alpha\beta} &= -(\partial_\alpha\partial_\beta\gamma \cdot n - \partial_\alpha\partial_\beta\gamma_0 \cdot n_0), \quad (\varepsilon_{\mathrm{b}})_{\alpha\beta} = -(\partial_\alpha\partial_\beta u \cdot n_0 + \partial_\alpha\partial_\beta\gamma_0 \cdot n'_0), \end{aligned} \tag{3.87}$$

where $n'_0 = m_0 - (n_0 \cdot m_0)n_0$ with

$$m_0 = \frac{\partial_1 u \times \partial_2\gamma_0 + \partial_1\gamma_0 \times \partial_2 u}{\|\partial_1\gamma_0 \times \partial_2\gamma_0\|} \tag{3.88}$$

is the first variation of the normal vector field.

For the weak formulation, we consider the closed subspace

$$\mathfrak{V} = \big\{v \in \mathrm{H}^1(A, \mathbb{R}^3) \;\big|\; \partial_\alpha\partial_\beta v \cdot n \in \mathrm{L}^2(A),\, v = \partial_\alpha v \cdot n = 0 \text{ on } A_{\mathrm{D}}\big\}, \tag{3.89}$$

which guarantees that the above integrals are well-defined if the surface configuration is sufficiently regular, e.g., of class $\mathrm{W}^{2,\infty}$, according to Blouza and Le Dret [48]. There is also a different formulation where the displacements are expressed in terms of contravariant coordinates instead of Cartesian coordinates. In this case, the normal component of the displacement field has to be twice weakly differentiable, while the tangential components can be assumed to only have first-order weak derivatives, in order for the integrals to exist. Existence and uniqueness results for linear shell models can be found in [48, 49, 68, 69], especially [48, Theorem 14] in our case, while the non-linear case is discussed in [70, 110].

3.2.4 Plate and beam models

If the initial undeformed configuration of the reference surface is planar and there are no membrane strains, one speaks of a plate instead of a shell. The displacement of the mid-surface from the initial configuration is then reduced to its vertical deflection perpendicular to the plane. For a Kirchhoff plate in the xy-plane, we start with the assumption that

$$\gamma_0(x, y) = (x, y, 0), \tag{3.90a}$$
$$\gamma(x, y) = (x, y, w(x, y)), \tag{3.90b}$$
$$u(x, y) = (0, 0, w(x, y)). \tag{3.90c}$$

In this case, the membrane part of the strain tensor vanishes and the bending term can be written in terms of the deflection w perpendicular to the plane:

$$s_{\mathrm{b}}(w) : e_{\mathrm{b}}(v) = D\left(\nu \Delta w \Delta v + (1-\nu)\nabla^2 w : \nabla^2 v\right), \tag{3.91}$$

where $v = \delta w$ is now the variation in vertical direction and the coefficient

$$D = \frac{Y h^3}{12(1-\nu^2)} \tag{3.92}$$

denotes the flexural rigidity of the plate. The weak formulation is then modified to

$$a(w, v) = \int_A D\left(\nu \Delta w \Delta v + (1-\nu)\nabla^2 w : \nabla^2 v\right) \,\mathrm{dA}, \tag{3.93a}$$
$$\ell(v) = \int_A f_{\mathrm{ext}}\, v \,\mathrm{dA} + \int_{\partial A} g_{\mathrm{ext}}\, v \,\mathrm{dS}, \tag{3.93b}$$

where f_{ext} and g_{ext} denote the vertical components of F_{ext} and G_{ext}, respectively.

In the one-dimensional case with $w = w(x)$, the bending term reduces further, which leads to a fourth-order differential equation for an Euler–Bernoulli beam when considering the strong formulation of the problem without boundary conditions:

$$\frac{\mathrm{d}^2}{\mathrm{d}x^2}\left(\tilde{D}\,\frac{\mathrm{d}^2 w}{\mathrm{d}x^2}\right) = f_{\mathrm{ext}}. \tag{3.94}$$

Here, $\tilde{D}$ is a flexural rigidity that depends on the cross-sectional geometry of the beam.

3.3 Mathematical model of Earth's lithosphere

In this work, the term "lithosphere" refers to the solid part of Earth's interior that responds elastically to applied mechanical loads on time scales of geologic duration. It encompasses Earth's outermost layer, the crust, and a portion of Earth's upper mantle (see Figure 9). This particular notion is called the elastic lithosphere in Melosh [177, Box 3.4] and should be distinguished from the other definitions. Since the mechanical behavior of a planet's interior depends on the rheology of the material of which it is composed and the duration of the loads under consideration, the location and size of the lithosphere are rather ill-defined. Nevertheless, the concept of an elastic lithosphere has proven useful for modeling purposes.

We treat the lithosphere as an elastic shell floating on the asthenosphere and subject to gravitational body forces. The asthenosphere comprises the mechanically weak and ductile region of Earth's upper mantle, which behaves like a viscous fluid on geologic time scales and exerts an outward buoyancy force on the lithosphere. The magnitude of the

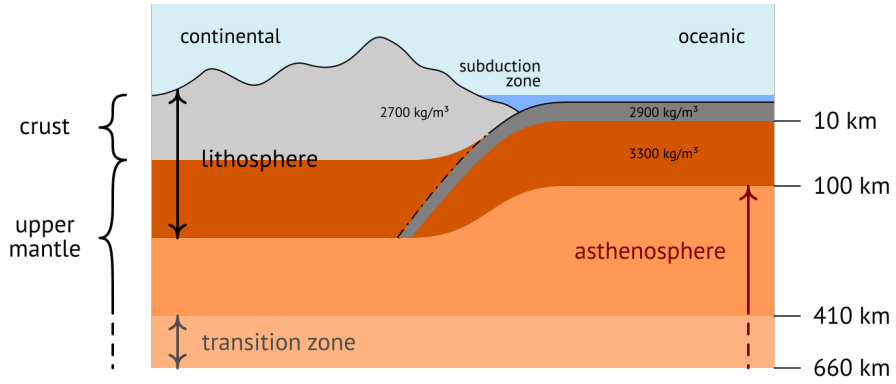

Figure 9: Top layers of the Earth (see Lowrie [169] and Rogers [217]).

force is proportional to the pressure difference between the fluid and the submerged body. According to Archimedes' principle, it is equal to the weight of the displaced fluid, which, in our case, depends on the depression of the lithosphere. The weight of topography is treated as a gravitational load, i.e., an inward force proportional to topographic elevation and rock density acts on the lithosphere, which causes its depression. Isostasy or isostatic equilibrium refers to the state of mechanical equilibrium between the lithosphere and the asthenosphere due to gravity and buoyancy (see Gutenberg [118] and Watts [274]).

3.3.1 Topographic loading and buoyancy

We model the lithosphere as a thin elastic plate of effective elastic thickness t floating on the asthenosphere and subject to gravitational forces. The initial depth of the mid-surface in the undeformed configuration corresponds to the theoretical depth relative to the mean sea level when there is no overlying mass. The actual mid-surface of the lithosphere does not have to coincide with the Mohorovičić surface, which is the boundary between the crust and the upper mantle of the Earth. However, we assume that they are close to each other and differ only by a constant vertical displacement.

Starting from the equilibrium equations for a Kirchhoff plate with external load f_{ext}, we split up the contributions from gravity and buoyancy: $f_{\text{ext}} = f_{\text{grav}} + f_{\text{buoy}}$.

Gravitational load is obtained by integrating all the weight above the mid-surface. The density of overlying air is considered to be negligible, so that the weight of topography ranges from Earth's surface down to the mid-surface. It is given by

$$f_{\text{grav}} = -\int_d^h \varrho g \, \mathrm{d}z, \tag{3.95}$$

where d is the depth of the mid-surface relative to the mean sea level, h is the topographic elevation, ϱ is the density of overlying mass, and g is the gravitational acceleration, which is assumed to be constant for the sake of simplicity.

The vertical displacement of the mid-surface from the initial depth is given by $w = d - d_0$. The buoyant force is equal to the weight of displaced asthenosphere, thus

$$f_{\text{buoy}} = \int_d^{d_0} \varrho_{\text{m}} g \, \mathrm{d}z = -\varrho_{\text{m}} g w, \tag{3.96}$$

assuming a constant upper mantle density ϱ_{m}.

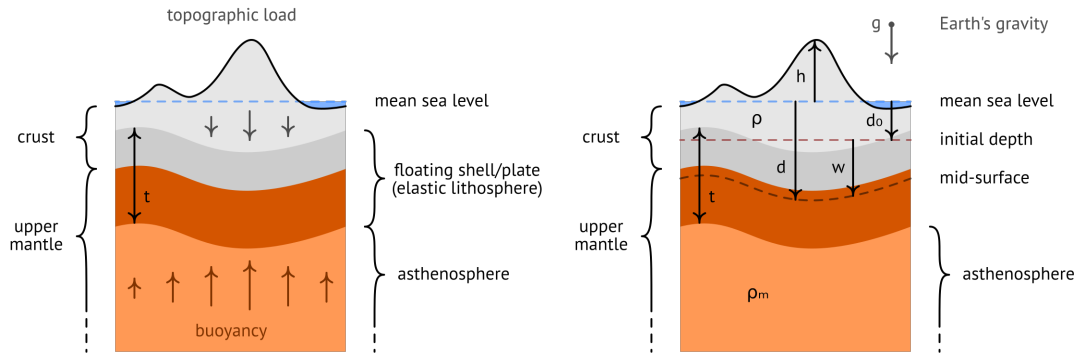

Figure 10: Left: Floating elastic lithosphere under topographic loading. Right: Relevant quantities for the mathematical model.

Instead of working with the actual topographic elevation, we use a mass representation r obtained by taking the mass above the mid-surface of the lithosphere and normalizing it by some depth-independent reference density ϱ_r. We choose the reference density as the mean rock density from the current depth of the mid-surface to its initial depth and assume that it is homogeneous in space, so that

$$\varrho_\mathrm{r} = \frac{1}{|w|}\int_d^{d_0} \varrho \,\mathrm{d}z, \quad r = \frac{1}{\varrho_\mathrm{r}}\int_{d_0}^{h} \varrho \,\mathrm{d}z. \tag{3.97}$$

Using the mass representation r, which corresponds to rock-equivalent topography, we can write the external load as

$$f_\mathrm{ext} = -(\varrho_\mathrm{m} - \varrho_\mathrm{r})gw - \varrho_\mathrm{r} g r. \tag{3.98}$$

Plugging this into the weak variational formulation for the plate model without external boundary forces yields $a(w,v) + b(w,v) = c(v)$ with the bilinear form (3.93a) and

$$b(w,v) = \int_A (\varrho_\mathrm{m} - \varrho_\mathrm{r}) g w v \,\mathrm{dA}, \quad c(v) = -\int_A \varrho_\mathrm{r} g r v \,\mathrm{dA}. \tag{3.99}$$

This is the Vening-Meinesz model of flexural isostasy used to explain regional compensation. See, e.g., Vening-Meinesz [265], Abd-Elmotaal [1], and Pelletier [205, Chapter 5].

In the case where there is no flexural rigidity, the Vening-Meinesz model reduces to the Airy–Heiskanen model of local isostasy [5], for which the well-known relation

$$\left(\frac{\varrho_\mathrm{m} - \varrho_\mathrm{r}}{\varrho_\mathrm{r}}\right)(d_0 - d) = r \tag{3.100}$$

holds. It states that the lithospheric depression relative to the initial depth is proportional to the mass representation of the topography with a scaling factor of $(\varrho_\mathrm{m} - \varrho_\mathrm{r})/\varrho_\mathrm{r}$. Using the above relation, we can determine the initial depth from some standard crustal thickness t_0 corresponding to a lithospheric plate in local isostasy when the topographic elevation is zero.

3.3.2 Isostatic boundary value problem

If we consider only a portion of Earth's lithosphere for the simulation, conditions on the boundary of the domain have to be prescribed to compensate for the missing information

outside of it. A natural choice is given by the full Neumann boundary condition, which corresponds to setting $g_{\text{ext}} = 0$ on the whole boundary. The resulting isostatic boundary value problem for a Kirchhoff–Love plate then reads: Find an admissible deflection w such that $a(w, v) + b(w, v) = c(v)$ for all admissible variations $v = \delta w$.

The Sobolev space $\mathrm{H}^2(A)$ is chosen as the space of admissible deflections for the boundary value problem. It consists of square-integrable functions on the reference surface with square-integrable weak derivatives up to second order. For the full Neumann problem, the variational problem is well-posed by the Lax–Milgram theorem [55, Chapter II], provided that $A \subset \mathbb{R}^2$ is a bounded Lipschitz domain and the coefficients $D(1 - \nu)$ and $(\varrho_{\text{m}} - \varrho_{\text{r}})g$ are bounded from below by a positive number. The H^2 coercivity of the bilinear form follows from the fact that the H^2 norm is equivalent to a similar one without the terms containing first-order derivatives [195, Theorem 1.8].

The above displacement formulation requires H^2 regularity, which implies global C^1 continuity for the trial and test functions. The difficulty of C^1 finite elements can be circumvented by considering isogeometric shape functions.

3.3.3 Spherical model of the lithosphere

Using the more general equations for thin elastic shells, it is possible to perform simulations of the lithosphere on the whole surface of the Earth. From a modeling point of view, the results may not reflect the physical reality, since the Earth consists of different regimes and tectonic plates that interact with each other in a complex manner. Moreover, due to the large scale of the simulation, the effects of flexural rigidity will usually not be visible. Nevertheless, we assume that the entire lithosphere can be modeled as a single spherical shell to showcase the capabilities of isogeometric analysis (IGA) in numerical simulations on curved domains, especially on a spherical domain. Note that it is also possible to model the surface of the Earth as an oblate spheroid or an irregular geoid instead of a sphere. For the sake of simplicity, we restrict ourselves to the spherical model.

Some considerations in Section 3.3.1 for lithospheric plates in isostatic equilibrium have to be adapted to the shell model. The buoyant force in three dimensions reads

$$b(u, v) = \int_A (\varrho_{\text{m}} - \varrho_{\text{r}}) g (n \cdot u)(n \cdot v) \,\mathrm{dA}, \tag{3.101}$$

where $(n \cdot u)$ and $(n \cdot v)$ are the radial part of the trial and test function, respectively, given by the orthogonal projection onto the unit normal n of the sphere. Similarly, the external load is given by a radial gravitational force

$$c(v) = -\int_A \varrho_{\text{r}} g r (n \cdot v) \,\mathrm{dA}. \tag{3.102}$$

With the above adjustments, the isostatic problem for a Koiter shell then reads: Find an admissible displacement u such that $a(u, v) + b(u, v) = c(v)$ for all admissible variations $v = \delta u$. We consider the vector-valued Sobolev space $\mathrm{H}^2(A, \mathbb{R}^3)$ for the displacements of the spherical shell, which is a subspace of (3.89) without boundary conditions.

4 Riemannian framework for shape spaces

In common usage, a shape refers to the form of a physical object, which can be represented by the boundary of the object and comprises topological as well as geometric information. Connections between parts of the object are specified by the topology, whereas relative arrangement of the parts within space is described by the geometry. A shape can thus be considered as a collection of points endowed with a topology and a geometry.

Mathematically, we can model shapes as certain subsets of some ambient topological space, also called the hold-all domain. A shape space refers to the set of admissible shapes within a given framework. The most general choice that can be made for a shape space is to consider all subsets of the ambient space as admissible shapes. However, such a power set contains too many objects, which makes the analysis of shapes within the ambient space generally hard. It is more viable to restrict the set of admissible shapes to an appropriate subset of the power set.

If the objective is to perform shape optimization with PDE constraints, where the domain of the PDE is determined by the shape, a certain regularity has to be imposed on the shapes to guarantee the existence and uniqueness of solutions to the PDE. A common choice is to consider bounded Lipschitz domains as the set of admissible shapes, which are also present in most industrial applications. In the framework presented hereafter, limits of smooth shapes corresponding to some Riemannian metric are considered instead.

We distinguish between three branches of shape optimization: parameter, geometry, and topology optimization [123, 122]. In the setting of parameter optimization, the problem is reduced to a set of parameters that are to be optimized. Examples of such parameters are sizing ones, e.g., lengths and thicknesses, or other kinds of features, e.g., curvature radii. This thesis is mainly concerned with geometry optimization, where the inherent geometry of a shape with fixed topology is considered as optimization variable instead of typical features of the shape. In contrast, topology optimization allows changes in both geometry and topology of the shape during the optimization process, such as generation and removal of holes in the shape, and is the most versatile among the three branches. It is not the subject of this thesis, since different techniques are usually required to handle topology optimization. Nevertheless, a very short and concise overview is provided in Section 4.1.3. For a thorough introduction to topology optimization, we refer to Bendsøe and Sigmund [36]. An overview is given by Sigmund and Maute [250].

In the statistical shape analysis community, the term “shape” often refers to “what is left when the differences which can be attributed to translations, rotations, and dilatations have been quotiented out” [152, Section 2, p. 82]. For the purpose of shape optimization, we do not generally adopt this notion of shape, since the above similarity transformations might still play a role in the value of the objective function, especially in structural optimization. What should always be quotiented out in this context, however, is the dependence of the problem on particular representations of the shape via some parametrization.

The use of the term “shape” in this thesis is also to be distinguished from Borsuk’s theory of shape in topology [50, 173] and other incompatible notions in unrelated fields.

4.1 Review of existing frameworks

Before we introduce the Riemannian framework for shape spaces, we provide a brief non-exhaustive overview of other existing frameworks in the context of shape optimization.

More details can be found in the main references: Pironneau [208], Sokołowski and Zolésio [253], Allaire [6], Haslinger and Mäkinen [123], Bendsøe and Sigmund [36], Delfour and Zolésio [85], Sigmund and Maute [250].

4.1.1 Perturbations of identity

In a construction due to Micheletti [179], shapes are identified with some quotient group of perturbations of identity that acts on the Euclidean space $\mathbb{E}^n$ and is endowed with the Courant metric that turns it into a complete metric space. A perturbation of identity of type $\mathcal{W}$ is a bijective transformation $\tau\colon \mathbb{E}^n \to \mathbb{E}^n$ of the form $\tau = \mathrm{id} + w$ for some $w \in \mathcal{W}$, whose inverse can be written in a similar way, i.e., it is an element of the set

$$\mathcal{T} = \big\{\tau\colon \mathbb{E}^n \to \mathbb{E}^n \;\big|\; \tau \text{ bijective}, \, \tau, \tau^{-1} \in \mathrm{id} + \mathcal{W}\big\}, \tag{4.1}$$

where $\mathcal{W}$ is a function space of mappings from $\mathbb{E}^n$ to $\mathbb{E}^n$ of a certain regularity. The set $\mathcal{T}$ together with the composition operator is a group under mild assumptions on $\mathcal{W}$. The original construction by Micheletti uses perturbations of identity of class C^k with vanishing derivatives at infinity. It has been extended to a larger family of Banach and Fréchet spaces of mappings in Delfour and Zolésio [85, Chapter 3, Section 2].

The corresponding shape space is defined as the set of images of some reference shape $\Omega_0 \subseteq \mathbb{E}^n$ under perturbations of identity, i.e.,

$$\mathcal{S} = \big\{\tau(\Omega_0) \subseteq \mathbb{E}^n \;\big|\; \tau \in \mathcal{T}\big\}, \tag{4.2}$$

which can be identified with the quotient group $\mathcal{T}/\mathcal{T}_0$, where

$$\mathcal{T}_0 = \big\{\tau \in \mathcal{T} \;\big|\; \tau(\Omega_0) = \Omega_0\big\} \tag{4.3}$$

is the closed subgroup of $\mathcal{T}$ that keeps the reference shape fixed. If $(\mathcal{W}, \|\cdot\|_{\mathcal{W}})$ is a Banach space of mappings from $\mathbb{E}^n$ to $\mathbb{E}^n$, the Courant metric is a distance function on $\mathcal{T}$ given by

$$\mathrm{dist}(\sigma, \tau) = \mathrm{dist}(\mathrm{id}, \tau \circ \sigma^{-1}), \tag{4.4}$$

for $\sigma, \tau \in \mathcal{T}$, where

$$\mathrm{dist}(\mathrm{id}, \tau) = \inf_{\substack{\tau = \tau_1 \circ \cdots \circ \tau_k \\ \tau_1, \ldots, \tau_k \in \mathcal{T}}} \sum_{i=1}^{k} \big(\|\tau_i - \mathrm{id}\|_{\mathcal{W}} + \|\tau_i^{-1} - \mathrm{id}\|_{\mathcal{W}}\big). \tag{4.5}$$

The infimum is taken over all finite factorizations of τ in $\mathcal{T}$, i.e., $\tau = \tau_1 \circ \cdots \circ \tau_k$ for some $k \in \mathbb{N}$ and $\tau_1, \ldots, \tau_k \in \mathcal{T}$. The resulting distance function is right-invariant and can thus be used for the shape space $\mathcal{S} \simeq \mathcal{T}/\mathcal{T}_0$. For the function spaces considered in Delfour and Zolésio [85, Chapter 3, Theorem 2.9], the shape space endowed with the distance function

$$\mathrm{dist}(\Omega_1, \Omega_2) = \inf\big\{\mathrm{dist}(\mathrm{id}, \tau) \;\big|\; \tau \in \mathcal{T}, \, \tau(\Omega_1) = \Omega_2\big\}, \tag{4.6}$$

for $\Omega_1, \Omega_2 \in \mathcal{S}$, is a complete metric space.

Another formula is given by the right-invariant pseudo-distance function

$$\underline{\mathrm{dist}}(\Omega_1, \Omega_2) = \inf\big\{\|\tau - \mathrm{id}\|_{\mathcal{W}} + \|\tau^{-1} - \mathrm{id}\|_{\mathcal{W}} \;\big|\; \tau \in \mathcal{T}, \, \tau(\Omega_1) = \Omega_2\big\}, \tag{4.7}$$

which satisfies all requirements of a distance function except for the triangle inequality. For perturbations of identity of class $\mathrm{W}^{r,\infty}$ with $r \in \mathbb{N}$, a distance function of the form

$$\mathrm{dist}(\Omega_1, \Omega_2) = \inf\{\underline{\mathrm{dist}}(\Omega_1, \Omega_2), c\}, \tag{4.8}$$

for some constant $c > 0$, can be constructed from the pseudo-distance function, according to Murat and Simon [187, Theorem 1]. A sequence of shapes $(\Omega_i)_{i\in\mathbb{N}}$ in $\mathcal{S}$ converges to Ω in $\mathcal{S}$, i.e.,

$$\lim_{i\to\infty} \operatorname{dist}(\Omega_i, \Omega) = 0, \tag{4.9}$$

if and only if there is a sequence of perturbations of identity $(\tau_i)_{i\in\mathbb{N}}$ in $\mathcal{T}$ and $\tau \in \mathcal{T}$ with $\tau_i(\Omega_0) = \Omega_i$ and $\tau(\Omega_0) = \Omega$ such that

$$\lim_{i\to\infty} \|\tau_i - \tau\|_{\mathcal{W}} = 0. \tag{4.10}$$

We refer to Murat and Simon [188, pp. II-29–II-30] for a proof.

Using the above identification, we can endow the shape space with a differential structure obtained from the topological vector space $\mathcal{W}$. A shape functional $F\colon \mathcal{S} \to \mathbb{R}$ is associated with the mapping

$$\tilde{F}\colon \mathrm{B}_\varepsilon(0) \to \mathbb{R}, \quad w \mapsto F((\mathrm{id} + w)(\Omega)), \tag{4.11}$$

defined on a neighborhood of the origin in $\mathcal{W}$. Shape differentiability of F at Ω is then attributed to differentiability of $\tilde{F}$ at 0, i.e., $\delta F(\Omega, w) = \delta\tilde{F}(0, w)$ with

$$\delta\tilde{F}(0, w) = \lim_{t\to 0^+} \frac{F((\mathrm{id} + tw)(\Omega)) - F(\Omega)}{t}. \tag{4.12}$$

4.1.2 Velocity method

Another approach is the velocity method [253, Section 2.9], which is based on prescribing a velocity vector field for deformations of the shape within the ambient space. Given a shape functional $F\colon \mathcal{S} \to \mathbb{R}$, the shape derivative of F at $\Omega \in \mathcal{S}$ in the direction of a continuous velocity vector field $v\colon [0, \varepsilon] \times \mathbb{E}^n \to \mathbb{E}^n$ is established via the Eulerian semi-derivative

$$\delta F(\Omega, v) = \lim_{t\to 0^+} \frac{F(\Omega_t) - F(\Omega)}{t}, \tag{4.13}$$

where $\Omega_t = \psi_t(\Omega)$ is a family of transformed shapes corresponding to the time-dependent flow $\psi\colon [0, \varepsilon] \times \mathbb{E}^n \to \mathbb{E}^n$ satisfying

$$\partial_t\psi(t, x) = v(t, \psi(t, x)), \quad \psi(t, x) = x, \tag{4.14}$$

for all $(t, x) \in [0, \varepsilon] \times \mathbb{E}^n$. The method of perturbations of identity is a special case of the velocity method that uses transformations of the form $\psi_t = \mathrm{id} + tw$ for some $w \in \mathcal{W}$. Both methods yield the same notion of first-order shape derivatives under suitable assumptions on the velocity vector field or family of transformations [84].

A stronger notion of differentiability for which all the rules of classical differential calculus remain available is Hadamard semi-differentiability [86]. The difference is that the limit in (4.13) is required to be independent of the choice of the continuous velocity vector field v with $v(0, x) = w(x)$, where $w \in \mathcal{W}$ is a mapping from $\mathbb{E}^n$ to $\mathbb{E}^n$ of a certain regularity. This ties to the manifold definition of derivatives and a shape space modeled on a topological vector space $\mathcal{W}$.

4.1.3 Topology optimization

Various approaches and techniques have emerged for topology optimization in the context of structural design since its advent in 1988 [250], initiated by the seminal work of Bendsøe and Kikuchi [35]. Most methods involve the use of densities [34, 248], phase fields [53, 272], and level sets [8, 9, 273] for material distribution, as well as the concept of topological derivatives [99, 252, 199]. Evolutionary approaches [282, 289] based on discrete binary design variables have also been developed for topology optimization.

A popular technique for compliance minimization using densities for material distribution is the solid isotropic material with penalization (SIMP) method [223, 224, 36]. The idea is to assign a relative density value $\varrho(x) \in [0,1]$ to each point x in the hold-all domain N, which determines whether there is material at the respective point or not. Intermediate density values correspond to regions with composite or porous material. If such regions are not desired, a penalization term is added to the stiffness of the material as a function of the density according to the power law

$$Y(\varrho) = Y_0 \varrho^p, \tag{4.15}$$

where Y_0 is the reference Young's modulus for a region filled with solid isotropic material. To suppress intermediate density values and facilitate binary solutions, the penalty factor $p > 1$ is usually chosen to be greater than or equal to 3 [36, Section 1.1.2].

A spatial discretization of the density distribution and the state variable is considered to solve the problem numerically, e.g., using the finite element method (FEM). Starting from an initial distribution, usually with $\varrho(x) = 1$ for all $x \in N$, the density field $\varrho\colon N \to [0,1]$ is updated in an iterative process based on sensitivity analysis of the objective function. This can be done using standard methods of optimal control theory [131, 260], since the shape variable has been reduced to some density parameter, which is just a scalar-valued quantity. A sensitivity filtering scheme is commonly used to establish some connectivity between neighboring elements and avoid checkerboard patterns in this way [248, 249].

Phase field methods are based on the minimization of a modified functional of the form

$$\tilde{F}(\varrho) = \alpha F(\varrho) + \int_N \left(\frac{1}{\varepsilon}(\omega \circ \varrho) + \frac{\varepsilon}{2} \|\nabla \varrho\|^2 \right) \mathrm{dV}, \tag{4.16}$$

with positive constants α, ε, and the phase field $\varrho\colon N \to \mathbb{R}$, where $F\colon \mathcal{S} \to \mathbb{R}$ denotes the original objective function that is to be minimized and $\mathcal{S}$ is some suitable function space for the phase field. They can be seen as a particular penalty method for the density approach. The penalty function $\omega\colon \mathbb{R} \to [0,\infty)$ is given by a double well potential with minima at 0 and 1, which serves to penalize intermediate density values. The functional derivative or L^2 gradient of (4.16) is given by

$$\operatorname{grad} \tilde{F}(\varrho) = \alpha \operatorname{grad} F(\varrho) + \frac{1}{\varepsilon}\omega'(\varrho) - \varepsilon \Delta \varrho \tag{4.17}$$

and the phase field $\varrho\colon [0,\varepsilon] \times N \to \mathbb{R}$ is evolved according to the Cahn–Hilliard equation

$$\partial_t \varrho = \operatorname{div}(D \operatorname{grad} \tilde{F}(\varrho)) \tag{4.18}$$

with some diffusion coefficient D [270].

For level set methods, the boundary of the shape $\Omega \in \mathcal{S} \subseteq \mathscr{P}(N)$ is described by the zero locus of some scalar-valued function $\phi\colon N \to \mathbb{R}$, i.e.,

$$\begin{aligned} \phi(x) > 0 \quad &\Leftrightarrow \quad x \in \operatorname{int}\Omega, \\ \phi(x) = 0 \quad &\Leftrightarrow \quad x \in \partial\Omega, \\ \phi(x) < 0 \quad &\Leftrightarrow \quad x \in \operatorname{ext}\Omega, \end{aligned} \tag{4.19}$$

where $\operatorname{int}\Omega$ and $\operatorname{ext}\Omega$ denote the interior and exterior of Ω, respectively. The evolution of $\phi\colon [0,\varepsilon] \times N \to \mathbb{R}$ along a normal velocity vector field $v = an$ is described by the transport equation

$$\partial_t \phi + a\|\partial_x \phi\| = 0. \tag{4.20}$$

Given an objective function $F\colon \mathcal{S} \to \mathbb{R}$, a descent direction can be obtained on the whole domain N by using the boundary representation of the shape derivative for each level set $\Phi(c) = \{x \in N \mid \phi(x) = c\}$ with $c \in \mathbb{R}$. See Allaire et al. [8, 9] for more information.

In Sokołowski and Zochowski [252], the topological derivative of a shape functional $F\colon \mathcal{S} \to \mathbb{R}$, defined on a collection $\mathcal{S} \subseteq \mathscr{P}(N)$ that contains every subset of the form $N \setminus K$ for some compact subset $K \subseteq \overline{N}$, is given by

$$\mathscr{D}F(x) = \lim_{r \to 0^+} \frac{F(N \setminus \overline{\mathrm{B}_r(x)}) - F(N)}{|\overline{\mathrm{B}_r(x)}|} \tag{4.21}$$

for $x \in N$, where $|\overline{\mathrm{B}_r(x)}|$ is the volume of a ball of radius r. It has formerly been called the bubble method by Eschenauer et al. [99]. The topological derivative $\mathscr{D}F(x)$ provides information on variations of the shape functional if an infinitesimal hole is created at x, which can be used to perform topology optimization based on the approaches described previously. Apart from spherical holes, different types of holes can be considered, which may lead to different kinds of topological derivatives [7, Section 4]. The computation of topological sensitivities generally requires more work than shape derivatives due to the mathematical difficulties involved in the concept [199].

4.1.4 Kendall's shape space

A different approach to modeling shapes using Riemannian geometry is due to Kendall [152], where configurations of a finite amount of landmarks that do not collapse to a single point are considered as variables. Such a configuration consists of a labeled set of k points in $\mathbb{E}^n$, which can be represented by a matrix of size $n \times k$ with real-valued entries. Kendall's shape space is then obtained by removing translations, dilatations, and rotations from the configurations.

Let $x = (x_1, \ldots, x_k) \in (\mathbb{E}^n)^k$ be a configuration of k landmarks and $x_0 \in \mathbb{E}^n$ be its centroid given by the Euclidean mean

$$x_0 = \frac{1}{k} \sum_{i=1}^{k} x_i. \tag{4.22}$$

The relative position of landmarks can be specified using displacement vectors $\bar{x}_i = x_i - x_0$ with respect to the centroid x_0 for $i = 1, \ldots, k$. Since the relation $\sum_{i=1}^{k} \bar{x}_i = 0$ holds by construction, a subset of $k-1$ displacement vectors is already sufficient to fully determine the relative configuration, i.e., one of the displacement vectors is redundant and can be

removed, e.g., using orthogonally transformed coordinates as described in [152, Section 2]. A translation-invariant measure of size for configurations is given by the Frobenius norm

$$\|\bar{x}\|_{\mathrm{F}} = \sqrt{\sum_{i=1}^{k} \|\bar{x}_i\|^2} \tag{4.23}$$

of the displacement matrix $\bar{x} = \begin{pmatrix} \bar{x}_1 & \cdots & \bar{x}_k \end{pmatrix} \in \mathbb{R}^{n \times k}$, which is non-zero if and only if the landmarks do not collapse to a single point. Effects of dilatations can be ignored by normalizing configurations using the above norm, i.e., a non-degenerate configuration x is identified with the feature $\bar{x}/\|\bar{x}\|_{\mathrm{F}}$. This results in the pre-shape space

$$\mathbb{S}_n^k = \left\{ \bar{x} \in \mathbb{R}^{n \times k} \;\middle|\; \sum_{i=1}^{k} \bar{x}_i = 0,\ \|\bar{x}\|_{\mathrm{F}} = 1 \right\}. \tag{4.24}$$

The rotation group $\mathrm{SO}(n)$ acts on $\mathbb{S}_n^k$ via left matrix multiplication. Identifying rotationally symmetric configurations with one another yields the shape space

$$\Sigma_n^k = \mathbb{S}_n^k / \mathrm{SO}(n), \tag{4.25}$$

which can be endowed with a so-called Procrustean distance function that is induced by the spherical distance function

$$\operatorname{dist}(\bar{x}, \bar{y}) = \arccos(\operatorname{tr}(\bar{x}^{\mathsf{T}} \bar{y})), \quad \bar{x}, \bar{y} \in \mathbb{S}_n^k, \tag{4.26}$$

corresponding to the Frobenius inner product. In the case $n = 2$, the quotient space Σ_2^k is a Riemannian manifold and the Procrustean distance corresponds to the Riemannian distance induced by a particular Fubini–Study metric [152, Theorem 1, p. 92].

4.2 Shape space of submanifolds of a fixed type

The aim of this section is to establish an appropriate mathematical model for the shape space of submanifolds of a fixed type, which consists of submanifolds of an ambient space diffeomorphic to some reference shape with fixed topology and diffeology. An elaborate treatment of infinite-dimensional differential geometry and manifolds of smooth mappings is given in the monograph by Kriegl and Michor [159], where manifolds modeled on so-called convenient vector spaces are considered. The underlying theory is based on the concept that smooth mappings between manifolds map smooth paths to smooth paths, from which many desirable properties follow, e.g., the chain rule and the exponential law. It provides a means to deal with spaces of compactly supported smooth functions on manifolds that are not compact. For smooth functions on compact manifolds, it is sufficient to consider Fréchet manifolds. See, e.g., Bruveris [59, Section 1.2].

4.2.1 Manifold of smooth mappings

We begin with the manifold structure of the space of smooth mappings and explain in which sense it can be considered an infinite-dimensional manifold. Let M be a compact manifold of dimension m and N be Riemannian manifold of dimension n with Riemannian metric $\bar{g}$. We additionally assume that M and N are connected and of positive dimension to exclude the case of discrete shapes.

Lemma 4.1

Let $(Y, \|\cdot\|_Y)$ be a Banach space. The function space $\mathrm{C}^\infty(M, Y)$ endowed with the countable family of (semi-)norms given by

$$\|u\|_{\mathrm{C}^r} = \sum_{|\alpha|\leq r} \|\partial^\alpha u\|_\infty = \sup_{p\in M} \sum_{|\alpha|\leq r} \|\partial^\alpha u(p)\|_Y, \quad u \in \mathrm{C}^\infty(M, Y),\, r \in \mathbb{N}_0, \tag{4.27}$$

is a Fréchet space. The topology induced by the translation-invariant metric

$$\mathrm{dist}_{\mathrm{C}^\infty}(v, w) = \sum_{r=0}^{\infty} 2^{-r} \frac{\|v - w\|_{\mathrm{C}^r}}{1 + \|v - w\|_{\mathrm{C}^r}}, \quad v, w \in \mathrm{C}^\infty(M, Y), \tag{4.28}$$

is the Whitney C^∞ topology.

Proof. We refer to Golubitsky and Guillemin [111, Proposition 1.9]. □

Remark 4.2

For $r \in \mathbb{N}_0$, the function space $\mathrm{C}^r(M, Y)$ can be endowed with the C^r norm, which turns it into the usual Banach space of r-times continuously differentiable functions. The topology induced by the C^r norm is the Whitney C^r topology.

Lemma 4.3

The space of smooth sections $\Gamma(\xi^*\mathrm{T}N)$ over $\xi \in \mathrm{C}^\infty(M, N)$ is a vector space and $\mathrm{C}^\infty(M)$-module under fiberwise vector addition and scalar multiplication. It can be endowed with the Whitney C^∞ topology, which turns it into an infinite-dimensional Fréchet space.

Proposition 4.4

The manifold of smooth mappings $\mathrm{C}^\infty(M, N)$ is an infinite-dimensional Fréchet manifold modeled on spaces of smooth sections $\Gamma(\xi^*\mathrm{T}N)$ endowed with the Whitney C^∞ topology.

Proof. A proof is given in Golubitsky and Guillemin [111, Theorem 1.11]. □

Remark 4.5

The tangent space $\mathrm{T}_\xi\mathrm{C}^\infty(M, N)$ at $\xi \in \mathrm{C}^\infty(M, N)$ can thus be identified with the space of smooth vector fields over ξ. See, e.g., Golubitsky and Guillemin [111, Proposition 1.13], Hamilton [120, Example 4.3.3], and Kriegl and Michor [159, Theorem 42.17]. The corresponding tangent bundle is a Fréchet bundle given by

$$\mathrm{TC}^\infty(M, N) \simeq \big\{(\xi, v) \,\big|\, \xi \in \mathrm{C}^\infty(M, N),\, v \in \Gamma(\xi^*\mathrm{T}N)\big\}. \tag{4.29}$$

4.2.2 Pre-shape space of smooth configurations

A subset of the ambient space N is an embedded submanifold of N diffeomorphic to the reference shape M if and only if it is the image of an embedding from M to N. To allow shapes with self-intersections, we can also consider immersed submanifolds of N. In this case, we have to restrict ourselves to free and proper immersions to ensure that the resulting shape space is a manifold rather than an orbifold. See Cervera et al. [63].

A smooth immersion $\xi \in \mathrm{Imm}(M, N)$ is called free if the smooth diffeomorphism group of M acts freely on it, i.e., if $\xi \circ \varphi = \xi$ for some $\varphi \in \mathrm{Diff}(M)$, then $\varphi = \mathrm{id}_M$. Moreover, it is called proper if the pre-image of compact subsets is compact, which is readily satisfied

for a compact domain M. The first property is required to show that the quotient space $\operatorname{Imm}(M,N)/\operatorname{Diff}(M)$ is a manifold. The second one is used to show that the resulting quotient manifold is Hausdorff.

An example of a non-free immersion of $\mathbb{S}_1$ in $\mathbb{E}^2$ is given by one that traverses a simple closed curve multiple times. It turns out that if there is a point in the image with only one pre-image, then the immersion is free [63, Lemma 1.4]. Injective immersions and especially embeddings, which are relevant in applications, are therefore free. Note that there are free immersions that has no point with only one pre-image, e.g., a figure eight that is traversed twice along the first petal and three times along the second one.

The space of smooth immersions $\operatorname{Imm}(M,N)$ is an open submanifold of the manifold of smooth mappings $\mathrm{C}^\infty(M,N)$. Furthermore, we have that

$$\operatorname{Emb}(M,N) \subseteq \operatorname{Imm}_{\text{free}}(M,N) \subseteq \operatorname{Imm}(M,N) \subseteq \mathrm{C}^\infty(M,N), \tag{4.30}$$

where the inclusions are all open. We refer to the configuration subspaces in (4.30) as the pre-shape space of smooth embeddings, free smooth immersions, and smooth immersions, respectively.

4.2.3 Shape space of immersed submanifolds

In the following, we restrict ourselves to the case of free smooth immersions and omit the subscript from $\operatorname{Imm}_{\text{free}}(M,N)$.

Lemma 4.6

The smooth diffeomorphism group $\operatorname{Diff}(M)$ *is an open submanifold of* $\mathrm{C}^\infty(M,M)$ *and a regular Fréchet Lie group acting on* $\mathrm{C}^\infty(M,N)$ *via composition from the right.*

Proof. A proof is given in Kriegl and Michor [159, Section 43.1]. □

Definition 4.7

The shape space of (unparametrized and free) smooth immersions is defined as the quotient space of $\operatorname{Imm}(M,N)$ under the action of $\operatorname{Diff}(M)$, i.e.,

$$\mathrm{B}(M,N) = \operatorname{Imm}(M,N)/\operatorname{Diff}(M). \tag{4.31}$$

It consists of smoothly immersed submanifolds of N of (fixed) type M.

Proposition 4.8

The pre-shape space of free smooth immersions $\operatorname{Imm}(M,N)$ *is the total space of a smooth principal fiber bundle with structure group* $\operatorname{Diff}(M)$ *and base manifold* $\mathrm{B}(M,N)$.

Proof. A proof in the case of smooth embeddings or free smooth immersions can be found in Kriegl and Michor [159, Section 44.1, Section 44.2]. For non-free immersions (leading to a shape orbifold instead of a shape manifold), we refer to Cervera et al. [63]. □

Remark 4.9

By definition, two configurations $\xi_1, \xi_2 \in \operatorname{Imm}(M,N)$ describe the same shape in $\mathrm{B}(M,N)$ if there is a diffeomorphism $\varphi \in \operatorname{Diff}(M)$ such that $\xi_1 \circ \varphi = \xi_2$. The set of images given by the collection of subsets

$$\mathrm{S}(M,N) = \big\{ \xi(M) \subseteq N \,\big|\, \xi \in \operatorname{Imm}(M,N) \big\} \subseteq \mathscr{P}(N) \tag{4.32}$$

can be identified with the shape space $\mathrm{B}(M, N)$ in the case of injective immersions, which is not necessarily true for more general immersions. Nevertheless, we write $\Omega \in \mathrm{B}(M, N)$ to refer to an element of the shape space and treat the element as a subset of the ambient space, even in the more general case where self-intersections are allowed and the shape as a subset may correspond to different immersed submanifolds.

4.3 Infinite-dimensional Riemannian geometry

Let S be a Fréchet manifold. We distinguish between weak and strong Riemannian metrics in the infinite-dimensional setting. A Riemannian metric G on S is called weak if it induces a weaker topology than the original topology on the tangent spaces and strong if the same topology is induced. Every Riemannian metric on a finite-dimensional manifold is strong and the only strong Riemannian manifolds are Hilbert manifolds [59, Section 2.2].

Many known properties of finite-dimensional manifolds do not generalize to the infinite-dimensional case. One should be cautious when employing standard tools of differential geometry. An example is given by the Hopf–Rinow theorem, which shows the relation between metric and geodesic completeness, as well as the existence of length minimizing geodesics between any two points in the same connected component. In the finite-dimensional case, metric completeness is equivalent to geodesic completeness and both imply the existence of length minimizing geodesics. However, this characterization fails in infinite dimensions [19] and the only implication that holds true is that metric completeness implies geodesic completeness in Hilbert manifolds [59, Section 3.1].

Another issue is that the cotangent bundle of an infinite-dimensional Riemannian manifold can generally not be identified with the tangent bundle. This is due to the fact that the dual bundle may be strictly larger than the original vector bundle. The bundle mapping $\flat\colon \mathrm{T}S \to \mathrm{T}^*S$ associated with a weak Riemannian metric is injective, but can never be surjective. This poses a difficulty when the inverse metric tensor is required in a formula. Weak Riemannian metrics are considered for shape spaces because the configuration space in the smooth setting cannot be made into a Hilbert manifold.

In the following, we discuss suitable choices of Riemannian metrics for the shape spaces introduced in Section 4.2.3.

4.3.1 Riemannian metrics on shape spaces

A $\mathrm{Diff}(M)$-invariant Riemannian metric on $\mathrm{Imm}(M, N)$ induces a Riemannian metric on the quotient space $\mathrm{B}(M, N)$. The tangent space $\mathrm{T}_\Omega\mathrm{B}(M, N)$ at some $\Omega \in \mathrm{B}(M, N)$ consists of smooth vector fields on Ω that are horizontal with respect to the Riemannian metric in certain cases considered in this thesis.

Proposition 4.10 (Quotient Riemannian metrics)

Given a $\mathrm{Diff}(M)$*-invariant Riemannian metric on* $\mathrm{Imm}(M, N)$*, there is a unique Riemannian metric on the quotient space* $\mathrm{B}(M, N) = \mathrm{Imm}(M, N)/\mathrm{Diff}(M)$ *such that the quotient mapping* $\pi\colon \mathrm{Imm}(M, N) \to \mathrm{B}(M, N)$ *is a Riemannian submersion.*

Proof. We refer to Bauer et al. [27, Section 4.7], Michor and Mumford [182, Section 3]. □

Definition 4.11 (Riemannian shape spaces)

A Riemannian shape space refers to a shape space endowed with the unique Riemannian

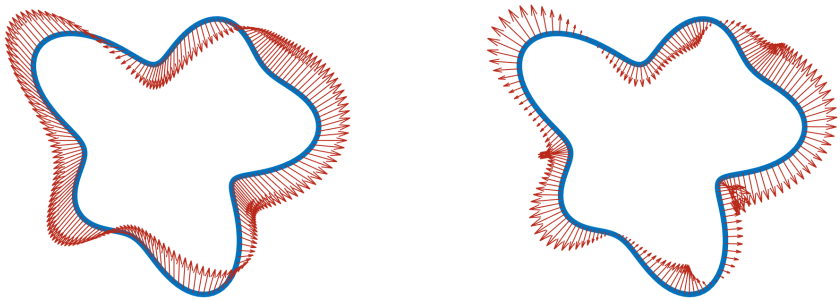

Figure 11: Left: A vector field over an embedding of the circle. Right: Tangent vectors of certain Riemannian shape spaces correspond to horizontal vector fields on the shape. Note that horizontal vector fields are, by definition, orthogonal to vertical ones with respect to the Riemannian metric, but not necessarily normal to the shape in the ambient space.

metric in Proposition 4.10. We write G for both Riemannian metrics on $\mathrm{Imm}(M, N)$ and $\mathrm{B}(M, N)$, respectively, since there will be no confusion with proper context.

Remark 4.12 (Limits of smooth shapes)

In practice—when numerical computations are involved—the resulting designs in the shape optimization process will not necessarily converge toward an element of the shape space $\mathrm{B}(M, N)$ even if all the computed designs are smooth. Therefore, suitable completions of the shape space are often considered. Two shapes in the same path-connected component can be assigned a distance corresponding to the Riemannian metric. Every path-connected component of the shape space can thus be made into a metric space using the geodesic distance. We write $\overline{\mathrm{B}(M, N)}$ for the corresponding metric completion of $\mathrm{B}(M, N)$.

For existence and uniqueness theorems, Sobolev completions of the pre-shape space are usually considered. See, e.g., Bauer et al. [27, Section 6.6].

Remark 4.13 (Vertical and horizontal vector fields)

Let $\xi \in \mathrm{Imm}(M, N)$. A vertical vector field over ξ is an element of the vertical subspace

$$\mathrm{V}_\xi \mathrm{Imm}(M, N) = \ker(\mathrm{T}_\xi \pi) \subseteq \mathrm{T}_\xi \mathrm{Imm}(M, N). \tag{4.33}$$

A Riemannian metric G on $\mathrm{Imm}(M, N)$ determines a horizontal subspace via

$$\mathrm{H}_\xi \mathrm{Imm}(M, N) = \big\{ w \in \mathrm{T}_\xi \mathrm{Imm}(M, N) \,\big|\, G_\xi(v, w) = 0 \text{ for all } v \in \mathrm{V}_\xi \mathrm{Imm}(M, N) \big\}. \tag{4.34}$$

The horizontal subspace on the shape space is not necessarily a complement of the vertical subspace if the Riemannian metric is weak. In the case where they are complementary, i.e.,

$$\mathrm{T}_\xi \mathrm{Imm}(M, N) = \mathrm{V}_\xi \mathrm{Imm}(M, N) \oplus \mathrm{H}_\xi \mathrm{Imm}(M, N), \tag{4.35}$$

horizontal vector fields over ξ correspond to tangent vectors of the shape space at $\pi(\xi)$. We write $v = v^{\mathrm{ver}} + v^{\mathrm{hor}}$ for the uniquely determined vertical and horizontal component of the vector field $v \in \mathrm{T}_\xi \mathrm{Imm}(M, N) \simeq \Gamma(\xi^* \mathrm{T}N)$.

Standard L^2 Riemannian metric

There are various Riemannian metrics that can be considered on pre-shape spaces. The simplest one is given by the standard L^2 Riemannian metric

$$G^{\mathrm{L}^2}(X, Y) = \int_M \bar{g}(X, Y) \operatorname{vol}(g) \tag{4.36}$$

for $X, Y \in \mathrm{TImm}(M, N)$, which corresponds to taking the inner product of the vector field values with respect to the ambient Riemannian metric $\bar{g}$ at each respective point on the shape and integrating the resulting scalar field over the shape. However, it turns out that this choice leads to vanishing geodesic distance [181], which is a purely infinite-dimensional phenomenon.

Weighted (almost local) L^2 Riemannian metrics

A remedy for the vanishing geodesic distance is given by weighted (also called almost local) L^2 Riemannian metrics, which contains some information on the curvature of the shape to regularize the metric [28]. For oriented hyper-surfaces M in $N = \mathbb{E}^n$, it is defined as

$$G^{\Phi}(X, Y) = \int_M \Phi(\mu, \kappa)\, \bar{g}(X, Y)\, \mathrm{vol}(g), \tag{4.37}$$

where $X, Y \in \mathrm{TImm}(M, N)$ and $\Phi(\mu, \kappa) \in \mathrm{C}^\infty(M)$ is a scalar field that depends on the oriented volume $\mu = \mathrm{Vol}(M)$ and the trace of the shape operator $\kappa = \mathrm{tr}(\mathcal{S})$. A particular example is given by $\Phi(\mu, \kappa) = 1 + c\,\kappa^2$, i.e.,

$$G^{1+c\,\kappa^2}(X, Y) = \int_M (1 + c\,\kappa^2)\, \bar{g}(X, Y)\, \mathrm{vol}(g), \tag{4.38}$$

which has been initially studied in Michor and Mumford [181].

Sobolev-type Riemannian metrics

The Riemannian metric considered in this work is a Sobolev-type Riemannian metric with a (fiberwise) positive and symmetric elliptic pseudo-differential operator

$$P \colon \mathrm{TImm}(M, N) \to \mathrm{TImm}(M, N), \tag{4.39}$$

which is associated with a technique called Sobolev smoothing or Sobolev preconditioning. It is given by

$$G^{P}(X, Y) = \int_M \bar{g}(PX, Y)\, \mathrm{vol}(g) \tag{4.40}$$

for $X, Y \in \mathrm{TImm}(M, N)$. In particular, we consider Sobolev–Riemannian metrics, where the differential operator is given by $P = 1 + c\,\Delta^r$ with some positive constant c and the Bochner–Laplace operator of order r, i.e.,

$$G^{1+c\,\Delta^r}(X, Y) = \int_M \bar{g}((1 + c\,\Delta^r)X, Y)\, \mathrm{vol}(g). \tag{4.41}$$

This kind of metrics has been extensively studied in Bauer et al. [27].

Inner and outer metrics

The above Riemannian metrics are referred to as inner metrics due to the sole dependence on the immersion of the shape in ambient space. Another type of Riemannian metric, which is not considered in this thesis, is given by outer metrics induced by the diffeomorphism group of the ambient space. They are used in the LDDMM framework (Large Deformation Diffeomorphic Mapping Method) for computational anatomy and shape analysis [33, 59]. We refer to Younes [283] for a thorough exposition.

4.3.2 Ambient covariant derivative

Let D be a manifold, $\xi \in \mathrm{C}^\infty(D, \mathrm{Imm}(M,N))$, and $s \in \Gamma(\xi^* \mathrm{TImm}(M,N))$ be a section over ξ. The Levi-Civita connection $\nabla^{\bar{g}}$ on the ambient space induces a covariant derivative on the pre-shape space of immersions $\mathrm{Imm}(M,N)$ via

$$\nabla^{\bar{g}}_X s = \left(\nabla^{\bar{g}}_{(X,0_M)} s^\vee\right)^\wedge \tag{4.42}$$

for $X \in \Gamma(\mathrm{T}D)$, where $0_M \in \Gamma(\mathrm{T}M)$ is the zero section, $s\colon D \to \mathrm{C}^\infty(M, \mathrm{T}N)$ is identified with $s^\vee\colon D \times M \to \mathrm{T}N$, and $\wedge\colon \mathrm{C}^\infty(D \times M, \mathrm{T}N) \to \mathrm{C}^\infty(D, \mathrm{C}^\infty(M, \mathrm{T}N))$ is the curry operator, which turns the resulting vector field back to a vector field over ξ. The resulting affine connection on $\mathrm{Imm}(M,N)$ is torsion-free and compatible with the ambient Riemannian metric, but not necessarily with the Riemannian metric G chosen for the pre-shape space [27, Section 4.2]. We omit the superscript from $\nabla^{\bar{g}}$ and use the ambient covariant derivative in subsequent sections. The geodesic equation introduced in Proposition 4.15 has a particular form with respect to this covariant derivative.

4.4 Geodesics in Riemannian shape spaces

Let S be a Fréchet manifold. In general, we distinguish between affine and metric geodesics.

Definition 4.14 (Affine and metric geodesics)

a) Given an affine connection ∇ on S, affine geodesics are smooth paths $\gamma\colon [t_0, t_1] \to S$ with a velocity vector field $\dot{\gamma}$ that is parallel with respect to the affine connection, i.e.,

$$\nabla_{\partial_t \dot{\gamma}} = 0. \tag{4.43}$$

b) Given a Riemannian metric G on S, metric geodesics are smooth paths $\gamma\colon [t_0, t_1] \to S$ that are locally length-minimizing with respect to the Riemannian distance induced by the metric. They are defined as stationary points of the energy functional

$$E(\gamma) = \frac{1}{2} \int_{t_0}^{t_1} G_{\gamma(t)}(\dot{\gamma}(t), \dot{\gamma}(t)) \,\mathrm{d}t. \tag{4.44}$$

Affine and metric geodesics coincide in a Riemannian manifold if the affine connection is compatible with the Riemannian metric. This is the case for the Levi-Civita connection. However, the affine connection ∇ on $\mathrm{Imm}(M,N)$ associated with the ambient covariant derivative in Section 4.3.2 is not necessarily compatible with the chosen Riemannian metric.

In the following, we use the metric definition for geodesics on $\mathrm{Imm}(M,N)$.

Proposition 4.15 (Geodesic equation on pre-shape space of immersions)

Stationary points of the energy functional are characterized by the geodesic equation

$$\nabla_{\partial_t \dot{\gamma}} = \frac{1}{2} A_\gamma(\dot{\gamma}, \dot{\gamma}) - B_\gamma(\dot{\gamma}, \dot{\gamma}), \tag{4.45}$$

where $A, B \in \Gamma(\mathrm{T}^{0,2}\mathrm{Imm}(M,N))$ are the metric gradients given by

$$\nabla_Z G_\gamma(X,Y) = G_\gamma(A_\gamma(X,Y), Z) = G_\gamma(B_\gamma(X,Z), Y) \tag{4.46}$$

for all $X, Y, Z \in \Gamma(\mathrm{TImm}(M,N))$.

Proof. We follow the proof in [27, Section 4.4]. Let $\gamma \in \mathrm{C}^\infty((-\varepsilon,\varepsilon)\times[t_0,t_1]\times M,N)$ be a smooth variation of paths of immersions with fixed end points. We have that

$$\begin{aligned}\partial_s(G_\gamma(\dot\gamma,\dot\gamma)) &= \nabla_{\partial_s}G_\gamma(\dot\gamma,\dot\gamma) + G_\gamma(\nabla_{\partial_s}\dot\gamma,\dot\gamma) + G_\gamma(\dot\gamma,\nabla_{\partial_s}\dot\gamma)\\ &= G_\gamma(A_\gamma(\dot\gamma,\dot\gamma),\eta) + 2(\partial_t(G_\gamma(\dot\gamma,\eta)) - \nabla_{\partial_t}G_\gamma(\dot\gamma,\eta) - G_\gamma(\nabla_{\partial_t}\dot\gamma,\eta))\\ &= G_\gamma(A_\gamma(\dot\gamma,\dot\gamma),\eta) + 2\partial_t(G_\gamma(\dot\gamma,\eta)) - 2G_\gamma(B_\gamma(\dot\gamma,\dot\gamma),\eta) - 2G_\gamma(\nabla_{\partial_t}\dot\gamma,\eta)\\ &= G_\gamma(A_\gamma(\dot\gamma,\dot\gamma) - 2B_\gamma(\dot\gamma,\dot\gamma) - 2\nabla_{\partial_t}\dot\gamma,\eta) + 2\partial_t(G_\gamma(\dot\gamma,\eta)).\end{aligned} \tag{4.47}$$

The integral of the last term

$$\int_{t_0}^{t_1}\partial_t(G_\gamma(\dot\gamma,\eta))\,\mathrm{d}t = G_\gamma(\dot\gamma,\eta)|_{t_0}^{t_1} = 0 \tag{4.48}$$

vanishes due to $\eta(t_0)=\eta(t_1)=0$. Thus

$$\delta E(\gamma,\eta) = \frac{1}{2}\int_{t_0}^{t_1}\partial_s(G_\gamma(\dot\gamma,\dot\gamma))\,\mathrm{d}t = \int_{t_0}^{t_1}G_\gamma(\tfrac{1}{2}A_\gamma(\dot\gamma,\dot\gamma) - B_\gamma(\dot\gamma,\dot\gamma) - \nabla_{\partial_t}\dot\gamma,\eta)\,\mathrm{d}t. \tag{4.49}$$

From $\delta E(\gamma,\eta)=0$ for all $\eta\in \mathrm{T}_\gamma\mathrm{Imm}(M,N)$, it follows that

$$\nabla_{\partial_t}\dot\gamma = \frac{1}{2}A_\gamma(\dot\gamma,\dot\gamma) - B_\gamma(\dot\gamma,\dot\gamma) \tag{4.50}$$

for stationary points of the energy functional. □

For the geodesic equation on the shape space $\mathrm{B}(M,N)$, we consider paths in $\mathrm{Imm}(M,N)$ that are horizontal with respect to the Riemannian metric, i.e., $\dot\gamma(t)\in \mathrm{H}_{\gamma(t)}\mathrm{Imm}(M,N)$ or

$$G_{\gamma(t)}(v(t),\dot\gamma(t)) = 0 \tag{4.51}$$

for all $t\in[t_0,t_1]$ and $v(t)\in \mathrm{V}_{\gamma(t)}\mathrm{Imm}(M,N)$. We refer to them as horizontal paths, which lead to the horizontal geodesic equation. Note that a horizontal geodesic path induces a geodesic path in shape space. See [27, Section 4.8] and [180, Section 26].

Proposition 4.16 (Geodesic equation on shape space of immersions)

Assuming that every path in $\mathrm{B}(M,N)$ *can be lifted to a horizontal path in* $\mathrm{Imm}(M,N)$*, the geodesic equation on shape space is characterized by*

$$\dot\gamma = \dot\gamma^{\mathrm{hor}}, \tag{4.52a}$$

$$(\nabla_{\partial_t}\dot\gamma)^{\mathrm{hor}} = \left(\frac{1}{2}A_\gamma(\dot\gamma,\dot\gamma) - B_\gamma(\dot\gamma,\dot\gamma)\right)^{\mathrm{hor}}. \tag{4.52b}$$

Proof. We refer to [27, Section 4.9]. □

Note that the horizontal lift on a Fréchet bundle may not exist or be unique because the usual existence and uniqueness theorems for ODEs do not generally hold for Fréchet spaces, see [120, p. 94]. However, paths in $\mathrm{B}(M,N)$ can be lifted to horizontal paths in $\mathrm{Imm}(M,N)$ with respect to Sobolev-type Riemannian metrics, according to [27, Section 6.9].

4.4.1 Hamiltonian formulation of the geodesic equation

The geodesic equation can be expressed in terms of the momentum, i.e., an element of the regular cotangent bundle

$$G(\mathrm{TImm}(M,N)) = \big\{(q, G_q(v,\,\cdot\,)) \,\big|\, v \in \mathrm{T}_\xi\mathrm{Imm}(M,N)\big\} \subseteq \mathrm{T}^*\mathrm{Imm}(M,N), \tag{4.53}$$

which is related to the Hamiltonian formulation of a Lagrangian system described by the stationarity of an action functional $E\colon \mathrm{C}^\infty([t_0,t_1],\mathrm{Imm}(M,N)) \to \mathbb{R}$ of the form

$$E(\gamma) = \int_{t_0}^{t_1} L(\gamma(t),\dot\gamma(t))\,\mathrm{d}t. \tag{4.54}$$

In our case, the Lagrangian $L\colon \mathrm{TImm}(M,N) \to \mathbb{R}$ is given by the path energy density

$$L(q,v) = \frac{1}{2}G_q(v,v) \tag{4.55}$$

for $(q,v) \in \mathrm{TImm}(M,N)$ and the corresponding Euler–Lagrange equation

$$\frac{\mathrm{d}}{\mathrm{d}t}\frac{\partial L}{\partial v}(\gamma,\dot\gamma) = \frac{\partial L}{\partial q}(\gamma,\dot\gamma) \tag{4.56}$$

is precisely the geodesic equation in Proposition 4.15 in the Riemannian setting.

The Hamiltonian of the system is given by the Legendre transformation of the Lagrangian, i.e.,

$$H\colon \mathrm{T}^*\mathrm{Imm}(M,N) \to \mathbb{R}, \quad H(q,p) = \sup\big\{pv - L(q,v) \,\big|\, v \in \mathrm{T}_q\mathrm{Imm}(M,N)\big\}. \tag{4.57}$$

Stationary points $\bar v \in \mathrm{T}_q\mathrm{Imm}(M,N)$ of the mapping $v \mapsto pv - L(q,v)$ are characterized by

$$p = \frac{\partial L}{\partial v}(q,\bar v) = G_q(\bar v,\,\cdot\,) \in G_q(\mathrm{T}_q\mathrm{Imm}(M,N)). \tag{4.58}$$

Taking the derivative of H with respect to p, where we view $\bar v$ as a function of (q,p), the above characterization yields

$$\begin{aligned}\frac{\partial H}{\partial p}(q,p) &= \frac{\partial}{\partial p}\big(p\bar v(q,p) - L(q,\bar v(q,p))\big)\\ &= \bar v(q,p) + p\frac{\partial \bar v}{\partial p}(q,p) - \frac{\partial L}{\partial v}(q,\bar v(q,p))\frac{\partial \bar v}{\partial p}(q,p)\\ &= \bar v(q,p).\end{aligned} \tag{4.59}$$

By defining the velocity $\dot q$ and the associated momentum p through

$$\dot q = \bar v(q,p) = \frac{\partial H}{\partial p}(q,p), \quad p = \frac{\partial L}{\partial v}(q,\dot q) = G_q(\dot q,\,\cdot\,), \tag{4.60}$$

we obtain Hamilton's equations of motion

$$\dot q = \frac{\partial H}{\partial p}(q,p), \quad \dot p = -\frac{\partial H}{\partial q}(q,p), \tag{4.61}$$

from the Euler–Lagrange equation (4.56), since we have that $H(q,p) = p\dot q - L(q,\dot q)$, thus

$$\frac{\partial H}{\partial q}(q,p) = -\frac{\partial L}{\partial q}(q,\dot q) = -\frac{\mathrm{d}}{\mathrm{d}t}\frac{\partial L}{\partial v}(q,\dot q) = -\frac{\mathrm{d}}{\mathrm{d}t}G_q(\dot q,\,\cdot\,) = -\dot p. \tag{4.62}$$

Solutions to (4.61) preserve the Hamiltonian energy

$$H(q,p) = p\dot{q} - L(q,\dot{q}) = G_q(\dot{q},\dot{q}) - \frac{1}{2}G_q(\dot{q},\dot{q}) = \frac{1}{2}G_q(\dot{q},\dot{q}) = L(q,\dot{q}) \tag{4.63}$$

in the sense that

$$\frac{\mathrm{d}}{\mathrm{d}t}H(q,p) = \frac{\partial H}{\partial q}(q,p)\,\dot{q} + \frac{\partial H}{\partial p}(q,p)\,\dot{p} = 0. \tag{4.64}$$

We write $H(t)$ for the energy of the system at time $t \in [t_0, t_1]$.

Using the metric gradient in Proposition 4.15, we obtain the following formulation for the geodesic equation on shape space:

Proposition 4.17 (Hamiltonian formulation of the horizontal geodesic equation)

Assuming that every path in $\mathrm{B}(M,N)$ *can be lifted to a horizontal path in* $\mathrm{Imm}(M,N)$*, the horizontal geodesic equation in* (4.52) *can be written in terms of the momentum:*

$$p = G_\gamma(\dot{\gamma},\,\cdot\,)^{\mathrm{hor}}, \tag{4.65a}$$

$$(\nabla_{\partial_t} p)^{\mathrm{hor}} = \frac{1}{2}G_\gamma(A_\gamma(\dot{\gamma},\dot{\gamma}),\,\cdot\,)^{\mathrm{hor}}. \tag{4.65b}$$

Proof. A proof is given in [27, Section 4.5]. See also [27, Section 4.10]. □

Conservation of energy along geodesic paths is important for the verification of numerical results related to the geodesic equation in Section 7.1. When the ambient space N is given by the Euclidean space $\mathbb{E}^n$ and the Riemannian metric on the pre-shape space is invariant under the action of the Euclidean group $\mathrm{E}(n)$ or the reparametrization group $\mathrm{Diff}(M)$, there are additional conserved quantities, such as the linear and angular momentum or the reparametrization momentum, respectively [183]. The latter, in particular, plays a role in the mesh quality during the optimization process.

4.4.2 Geodesic equation for Sobolev-type Riemannian metrics

In this section, we discuss an important class of Riemannian metrics defined on the pre-shape space of immersions through an elliptic operator. Under some suitable conditions, every path in the shape space endowed with this kind of Riemannian metric can be lifted to a horizontal path. Additionally, the reparametrization momentum is conserved.

Proposition 4.18 (Sobolev-type Riemannian metrics)

Let G^P *be a Sobolev-type Riemannian metric with a (fiberwise) elliptic pseudo-differential operator* $P\colon \mathrm{TImm}(M,N) \to \mathrm{TImm}(M,N)$ *that satisfies the following conditions:*

a) The restriction P_ξ *is symmetric and positive with respect to the standard* L^2 *Riemannian metric, i.e.,*

$$\int_M \bar{g}(P_\xi\eta,\zeta)\,\mathrm{vol}(g) = \int_M \bar{g}(\eta,P_\xi\zeta)\,\mathrm{vol}(g) \tag{4.66}$$

for all $\xi \in \mathrm{Imm}(M,N)$*,* $\eta,\zeta \in \mathrm{T}_\xi\mathrm{Imm}(M,N)$*, and*

$$\int_M \bar{g}(P_\xi\eta,\eta)\,\mathrm{vol}(g) > 0 \tag{4.67}$$

if and only if η *is not the zero vector field.*

b) The operator P is $\mathrm{Diff}(M)$*-invariant, i.e.,*

$$P_\xi(\eta)\circ\varphi = P_{\xi\circ\varphi}(\eta\circ\varphi) \tag{4.68}$$

for all $(\xi,\eta)\in \mathrm{TImm}(M,N)$ *and* $\varphi\in\mathrm{Diff}(M)$.

c) The covariant derivative ∇P *admits a smooth adjoint* $\mathrm{Adj}(\nabla P)$ *in the sense that*

$$\int_M \bar g((\nabla_Z P)X,Y)\operatorname{vol}(g) = \int_M \bar g(\mathrm{Adj}(\nabla P)(X,Y),Z)\operatorname{vol}(g) \tag{4.69}$$

for all $X,Y,Z\in\mathrm{TImm}(M,N)$.

Then the metric gradients corresponding to the Sobolev–Riemannian metric G^P *exist and are given by solutions to the following elliptic differential equations:*

$$PA(X,Y) = \mathrm{Adj}(\nabla P)(X,Y) - \mathrm{T}\xi\circ(\nabla\bar g(PX,Y))^\sharp - \bar g(PX,Y)\operatorname{tr}^g(\vec h), \tag{4.70a}$$
$$PB(X,Z) = (\nabla_Z P)X + \operatorname{tr}^g(\bar g(\mathrm{T}\xi,\nabla Z))PX. \tag{4.70b}$$

Proof. A proof can also be found in [27, Section 6.3]. Note that the first assumption a) together with the ellipticity condition (see Shubin [243] for more information on pseudo-differential operators) implies that the section

$$G^P\in\Gamma(\mathrm{T}^{0,2}\mathrm{Imm}(M,N)) \simeq \Gamma(\mathrm{TImm}(M,N))^*\otimes_{\mathrm{C}^\infty(\mathrm{Imm}(M,N))}\Gamma(\mathrm{TImm}(M,N))^* \tag{4.71}$$

(see (2.67) and (2.83) for the canonical isomorphisms) defined by

$$G^P(X,Y) = \int_M \bar g(PX,Y)\operatorname{vol}(g),\quad X,Y\in\mathrm{TImm}(M,N), \tag{4.72}$$

is indeed a Riemannian metric on $\mathrm{Imm}(M,N)$, which is also $\mathrm{Diff}(M)$-invariant due to the second assumption b).

For $X,Y,Z\in\mathrm{TImm}(M,N)$, we can calculate the covariant derivative

$$\begin{aligned}\nabla_Z G^P(X,Y) &= \int_M \Big(\bar g((\nabla_Z P)X,Y)\operatorname{vol}(g) + \bar g(PX,Y)\nabla_Z\operatorname{vol}(g)\Big)\\ &= \int_M \Big(\bar g((\nabla_Z P)X,Y) + \bar g(PX,Y)\operatorname{tr}^g(\bar g(\mathrm{T}\xi,\nabla Z))\Big)\operatorname{vol}(g)\\ &= \int_M \bar g((\nabla_Z P)X + \operatorname{tr}^g(\bar g(\mathrm{T}\xi,\nabla Z))PX,Y)\operatorname{vol}(g),\end{aligned} \tag{4.73}$$

which yields the second equation (4.70b). See Proposition 5.14 for the first variation of the volume form. Using the third assumption c) and the following calculations:

$$\begin{aligned}\bar g(PX,Y)\operatorname{tr}^g(\bar g(\mathrm{T}\xi,\nabla Z)) &= \bar g(PX,Y)\operatorname{tr}^g(\nabla\bar g(\mathrm{T}\xi,Z) - \bar g(\vec h,Z))\\ &= -\bar g(PX,Y)\nabla^*\bar g(\mathrm{T}\xi,Z) - \bar g(PX,Y)\operatorname{tr}^g(\bar g(\vec h,Z))\\ &= -g^{0,1}(\nabla\bar g(PX,Y),\bar g(\mathrm{T}\xi,Z)) - \bar g(PX,Y)\,\bar g(\operatorname{tr}^g(\vec h),Z)\\ &= -\bar g(\mathrm{T}\xi\circ(\nabla\bar g(PX,Y))^\sharp,Z) - \bar g(\bar g(PX,Y)\operatorname{tr}^g(\vec h),Z),\end{aligned} \tag{4.74}$$

we can further express the covariant derivative as

$$\nabla_Z G^P(X,Y) = \int_M \bar g(\mathrm{Adj}(\nabla P)(X,Y) - \mathrm{T}\xi\circ(\nabla\bar g(PX,Y))^\sharp - \bar g(PX,Y)\operatorname{tr}^g(\vec h),Z)\operatorname{vol}(g), \tag{4.75}$$

which results in the first equation (4.70a).

□

Proposition 4.19 (Horizontal lift)

Let $\mathrm{Imm}(M,N)$ *be endowed with a Sobolev–Riemannian metric satisfying the conditions in Proposition 4.18. Then the tangent bundle splits into a direct sum of the vertical and horizontal subbundle, i.e.,*

$$\mathrm{TImm}(M,N) = \mathrm{VImm}(M,N) \oplus_{\mathrm{Imm}(M,N)} \mathrm{HImm}(M,N). \tag{4.76}$$

This means that for each $w \in \mathrm{T}_\Omega \mathrm{B}(M,N)$*, there is a unique* $z \in \mathrm{H}_\xi \mathrm{Imm}(M,N)$ *such that* $\mathrm{T}_\xi \pi(z) = w$*, where* $\Omega \in \mathrm{B}(M,N)$ *and* $\xi \in \mathrm{Imm}(M,N)$ *with* $\pi(\xi) = \Omega$*.*

Furthermore, every smooth path in $\mathrm{B}(M,N)$ *can be uniquely lifted to a horizontal smooth path in* $\mathrm{Imm}(M,N)$ *corresponding to the Sobolev–Riemannian metric. In particular, we have that for any smooth path of immersions* $\tilde{\gamma}\colon [a,b] \times M \to N$*, there is a unique smooth path of diffeomorphisms* $\varphi\colon [a,b] \times M \to M$ *such that the smooth path of immersions* $\gamma\colon [a,b] \times M \to N$ *given by* $\gamma(t,p) = \tilde{\gamma}(t, \varphi(t,p))$ *for* $(t,p) \in [a,b] \times M$ *satisfies*

$$\bar{g}(P\dot{\gamma}, \mathrm{T}\gamma \circ X) = 0 \tag{4.77}$$

for all $X \in \Gamma(\mathrm{T}M)$*.*

Proof. We refer to [27, Section 6.8, Section 6.9]. □

Proposition 4.20 (Reparametrization momentum)

Let P *be a* $\mathrm{Diff}(M)$*-invariant elliptic pseudo-differential operator. Then the reparametrization momentum corresponding to the Sobolev–Riemannian metric* G^P *is conserved along any geodesic path* γ *in* $\mathrm{Imm}(M,N)$*, i.e., for all* $X \in \Gamma(\mathrm{T}M)$*, the quantity*

$$G^P_\gamma(\dot{\gamma}, \mathrm{T}\gamma \circ X) = \int_M \bar{g}(P\dot{\gamma}, \mathrm{T}\gamma \circ X) \operatorname{vol}(g) \tag{4.78}$$

is constant with respect to the time variable.

Proof. A proof is given in [183, Section 2.5]. See also [27, Section 6.7]. □

4.4.3 Geodesic equation on shape space of hyper-surfaces

The geodesic equation for Sobolev-type Riemannian metrics has been derived in its utmost generality in Bauer et al. [27]. In the following, we focus on the special case $P = 1 + c\,\Delta$ with $c > 0$ and the setting of hyper-surfaces in the Euclidean space $\mathbb{E}^n$ with $\bar{g} = \langle \cdot\,, \cdot \rangle$.

Lemma 4.21 (Horizontal path condition)

For a Sobolev-type Riemannian metric, the horizontal path condition is characterized by the elliptic differential equation $P\dot{\gamma} = an$*, where* a *is a scalar field, representing the scalar momentum, and* n *is a unit normal to the hyper-surface.*

Lemma 4.22 (Adjoint of the covariant derivative of an elliptic operator)

Let $P = 1 + c\,\Delta$*. The adjoint of the covariant derivative* ∇P *is given by*

$$\begin{aligned} \mathrm{Adj}(\nabla P)(X,Y) = \mathrm{T}\xi \circ \big(\nabla \bar{g}(PX,Y) - \bar{g}(PX, \nabla Y) - \bar{g}(\nabla X, PY)\big)^\sharp \\ + c\,\big(2\,\mathrm{tr}\big(g^{-1}\vec{h}\,g^{-1}\bar{g}(\nabla X, \nabla Y)\big) + \nabla^* \bar{g}(\nabla X, Y)\,\mathrm{tr}^g(\vec{h})\big). \end{aligned} \tag{4.79}$$

Proof. An expression for the general case has been derived in [27, Section 8.2]. The claim follows from the case $p = 1$ and the fact that the Riemann curvature tensor vanishes in a flat Riemannian manifold. □

Proposition 4.23 (Geodesic equation on shape space of hyper-surfaces)

The geodesic equation for a Sobolev-type Riemannian metric G^P on the shape space of hyper-surfaces in $\mathbb{E}^n$ is given by

$$P\dot{\gamma} = an, \tag{4.80a}$$

$$\partial_t\big(a \operatorname{vol}(g)\big) = \frac{1}{2}\big(\bar{g}\big(\operatorname{Adj}(\nabla P)(\dot{\gamma},\dot{\gamma}), n\big) - \kappa\, \bar{g}(P\dot{\gamma},\dot{\gamma})\big) \operatorname{vol}(g). \tag{4.80b}$$

In particular, the geodesic equation for the H^1 *Sobolev–Riemannian metric with* $P = 1 + c\,\Delta$ *reads*

$$(1 + c\,\Delta)\dot{\gamma} = an,$$
$$\partial_t\big(a \operatorname{vol}(g)\big) = \Big(c \operatorname{tr}\big(g^{-1} h\, g^{-1} \bar{g}(\nabla\dot{\gamma}, \nabla\dot{\gamma})\big) - \frac{\kappa}{2}\left(\bar{g}(\dot{\gamma},\dot{\gamma}) + c \operatorname{tr}\big(g^{-1}\bar{g}(\nabla\dot{\gamma},\nabla\dot{\gamma})\big)\right)\Big) \operatorname{vol}(g).$$

Proof. A proof is given in [27, Section 9.1]. □

Example 4.24 (Geodesic equation on shape space of planar curves)

In the case of closed planar curves, the shape space is denoted by $\mathrm{B}(\mathbb{S}_1, \mathbb{E}^2)$ and the H^1 Sobolev–Riemannian metric reads

$$G^{1+c\,\Delta}(X,Y) = \int_{\mathbb{S}_1} \langle (1 + c\,\Delta)X, Y\rangle \,\mathrm{dS} = \int_{\mathbb{S}_1} \Big(\langle X, Y\rangle + c\,\langle \mathrm{D}_s X, \mathrm{D}_s Y\rangle\Big) \|\partial_s\gamma\| \,\mathrm{d}s, \tag{4.81}$$

where $\mathrm{D}_s X = \|\partial_s\gamma\|^{-1}\partial_s X$ is the arc length derivative of X. The corresponding geodesic equation can be formulated in the following ways:

$$\partial_t((1 + c\,\Delta)\dot{\gamma}) = \frac{\kappa}{2}\big(c\,\|\mathrm{D}_s\dot{\gamma}\|^2 - \|\dot{\gamma}\|^2\big)n - a\langle v, \mathrm{D}_s\dot{\gamma}\rangle n - a\langle n, \mathrm{D}_s\dot{\gamma}\rangle v, \tag{4.82a}$$

$$\partial_t(an) = \partial_t a n + a\partial_t n = \partial_t a n - a\langle n, \mathrm{D}_s\dot{\gamma}\rangle v, \tag{4.82b}$$

$$\partial_t a = \frac{\kappa}{2}\big(c\,\|\mathrm{D}_s\dot{\gamma}\|^2 - \|\dot{\gamma}\|^2\big) - a\langle v, \mathrm{D}_s\dot{\gamma}\rangle, \tag{4.82c}$$

$$\partial_t(a \operatorname{vol}(g)) = \partial_t a \operatorname{vol}(g) + a\,\partial_t \operatorname{vol}(g) = \frac{\kappa}{2}\big(c\,\|\mathrm{D}_s\dot{\gamma}\|^2 - \|\dot{\gamma}\|^2\big) \operatorname{vol}(g), \tag{4.82d}$$

$$\partial_t(an \operatorname{vol}(g)) = \frac{\kappa}{2}\big(c\,\|\mathrm{D}_s\dot{\gamma}\|^2 - \|\dot{\gamma}\|^2\big)n - a\langle n, \mathrm{D}_s\dot{\gamma}\rangle v, \tag{4.82e}$$

where $v = \|\partial_s\gamma\|^{-1}\partial_s\gamma$ is the unit tangent vector and $n = (-v_2, v_1)$ is the corresponding unit normal vector of the planar curve.

4.4.4 Initial value problem for geodesics

The geodesic equation is a second-order ODE, which is also a Hamiltonian system. Given a set of initial conditions, we may ask for the well-posedness of the initial value problem. It has been shown in [27, Section 6.6] that, under some mild assumptions on the elliptic pseudo-differential operator P, which are satisfied for the H^1 Sobolev–Riemannian metric, the geodesic equation admits unique local solutions in the manifold of H^{k+2p} immersions, where $p \geq 1$ and $k > \dim(M)/2 + 1$.

For the purpose of gradient-based numerical shape optimization, it is important to devise suitable numerical time integration methods for the geodesic equation. Unfortunately, the Hamiltonian of the system is not separable, so there are no standard explicit symplectic integrators that can be applied to the system. There is also a highly non-linear dependence of the geodesic equation on the shape variable that suggests the use of implicit methods for reliable accuracy. However, such methods tend to be costly in terms of computational complexity. Despite this, numerical experiments for the geodesic equation in Section 7.1 indicate that standard explicit methods perform relatively well, i.e., the problem does not seem to be stiff in the case of the H^1 Sobolev–Riemannian metric with a sufficiently large regularization parameter $c > 0$.

4.4.5 Boundary value problem for geodesics

In many applications, e.g., statistical shape analysis or computer graphics, one is interested in finding a path of shapes that connects two given shapes. A geodesic path is a particular one that is natural in the sense that it minimizes the length locally. There are two common approaches for solving the geodesic boundary value problem numerically. The first one is the path straightening method, where we start with an admissible path that connects the two given shapes and minimize the horizontal path energy while fixing the ends of the path. The second one is the geodesic shooting method, where an initial value problem is solved with an initial guess that is adjusted until the terminal value is met.

For demonstration purpose, we will briefly cover these two topics and present a numerical example in Section 7.2 involving the interpolation of closed planar curves.

Path straightening method

Let $(t_0, ..., t_m)$ be a partition of the time interval $[a, b]$. In the path straightening method, we aim to minimize the time-discrete path energy given by

$$E_h(\gamma_0, \dots, \gamma_m) = \frac{1}{2} \sum_{i=1}^{m} \int_{t_{i-1}}^{t_i} G_h(\gamma_{i-1}, \gamma_i)(t) \, \mathrm{d}t, \tag{4.83}$$

where $\gamma_i \in \mathrm{Imm}(M, N)$ is a piecewise linear approximation of the path of configurations at time $t_i \in [a, b]$ for $i = 0, \dots, m$, i.e.,

$$G_h(\gamma_{i-1}, \gamma_i)(t) = G_{\gamma_h(t)}(\log(\gamma_{i-1}, \gamma_i), \log(\gamma_{i-1}, \gamma_i)) \approx G_{\gamma(t)}(\dot{\gamma}(t), \dot{\gamma}(t)) \tag{4.84}$$

with $\gamma_h \colon [a, b] \times M \to N$, $\gamma_h(t, p) = \exp(\gamma_{i-1}(p), t \log(\gamma_{i-1}(p), \gamma_i(p)))$ for $(t, p) \in (t_{i-1}, t_i) \times M$. Here, exp and log denote the Riemannian exponential and logarithmic mapping on the ambient space N, respectively. Instead of a piecewise linear approximation of the path, one can also consider spline approximations in time [127]. To evaluate (4.83) numerically, a suitable spatial discretization of the configurations should be chosen.

Starting from a feasible time-discrete path of configurations connecting the two endpoints of the sought geodesic $\gamma \colon [a, b] \times M \to N$, i.e., $\gamma_0 = \gamma(a)$ and $\gamma_m = \gamma(b)$, we update the configurations γ_i according to information on first-order derivatives of the time-discrete path energy for $i = 1, \dots, m - 1$ until a stationary point is found. To obtain a geodesic path in shape space, the path energy has to be replaced with the horizontal path energy by projecting the approximation of $\dot{\gamma}(t)$ onto the horizontal subspace. This has been done for the shape space of planar curves in Bauer et al. [29] using another approach. The more general setting is already a challenging problem from a computational point of view—even in the case of surfaces [32].

Geodesic shooting method

In the geodesic shooting method, the boundary value problem is addressed by iteratively solving an initial value problem. Starting from an initial guess for the initial velocity, the next guess is obtained from the adjoint sensitivity corresponding to the deviation of the configuration at the final time from the target configuration.

Let $\gamma\colon [t_0, t_1] \to \mathrm{Imm}(M, N)$ refer to a path in configuration space. The optimal control problem associated with the geodesic shooting method reads

$$\min \ \frac{1}{2} \operatorname{dist}(\gamma(t_1), \xi_1)^2, \tag{4.85a}$$

$$\text{s.t. } \nabla_{\partial_t} \dot{\gamma} = \frac{1}{2} A_\gamma(\dot{\gamma}, \dot{\gamma}) - B_\gamma(\dot{\gamma}, \dot{\gamma}), \tag{4.85b}$$

$$\gamma(t_0) = \xi_0, \quad \dot{\gamma}(t_0) = \eta, \tag{4.85c}$$

$$\eta \in \mathrm{T}_{\xi_0}\mathrm{Imm}(M, N), \tag{4.85d}$$

where $\xi_0 \in \mathrm{Imm}(M, N)$ and $\xi_1 \in \mathrm{Imm}(M, N)$ denote the initial and target configuration, respectively, which are assumed to be in the same path-connected component of the pre-shape space. The objective function is given by half of the squared geodesic distance from the end of the trial path $\gamma(t_1)$ to the target configuration ξ_1. We use the geodesic distance induced by a Riemannian metric on $\mathrm{Imm}(M, N)$. The first component is denoted by the mapping

$$f_\zeta\colon \mathrm{Imm}(M, N) \to \mathbb{R}, \quad \xi \mapsto \frac{1}{2} \operatorname{dist}(\xi, \zeta)^2 \tag{4.86}$$

for $\zeta \in \mathrm{Imm}(M, N)$. Its gradient is given by the negative of the Riemannian logarithmic mapping on $\mathrm{Imm}(M, N)$, i.e.,

$$\operatorname{grad} f_\zeta(\xi) = -\log(\xi, \zeta). \tag{4.87}$$

See, e.g., Afsari et al. [4], Bačák et al. [24], Bergmann and Gousenbourger [37].

Let $\gamma_k\colon [t_0, t_1] \to \mathrm{Imm}(M, N)$ be the solution to the state equation corresponding to the current guess $\eta_k \in \mathrm{T}_{\xi_0}\mathrm{Imm}(M, N)$ for the initial velocity, i.e., $\gamma_k(t_0) = \xi_0$ and $\dot{\gamma}_k(t_0) = \eta_k$. The next guess can be computed as

$$\eta_{k+1} = \eta_k + s_k \lambda(t_0), \tag{4.88}$$

where $s_k > 0$ is a step size and $\lambda\colon [t_0, t_1] \to \mathrm{TImm}(M, N)$ is a solution to the adjoint state equation associated with the problem and the terminal value $\lambda(t_1) = \log(\gamma_k(t_1), \xi_1)$. This corresponds to transporting the deviation at the final time back to the initial time and figuring out in which direction the initial velocity should be perturbed to cause a decrease in the objective function. A plain steepest descent method using the Riemannian gradient in (4.87) is employed, which results in the update formula (4.88). We refer to Sengupta et al. [239] and Arguillère et al. [18] for similar optimal control problems.

The calculation and backward integration of the adjoint state equation, which also requires the Riemannian logarithmic mapping on the pre-shape space for the terminal value, can be circumvented by considering a special kind of Riemannian metric. Note that for geodesic paths in shape space, the distance function has to be replaced with

$$\operatorname{dist}(\pi(\xi_1), \pi(\xi_2)) = \inf\bigl\{\operatorname{dist}(\xi_1 \circ \varphi, \xi_2) \bigm| \varphi \in \mathrm{Diff}(M)\bigr\} \tag{4.89}$$

for $\pi(\xi_1), \pi(\xi_2) \in \mathrm{B}(M, N)$. See, e.g., Bauer et al. [29].

4.4.6 Square root velocity field transform

There is a particular Riemannian metric on the shape space of closed planar parametrized curves modulo translations that allows for an efficient computation of the adjustments for the geodesic shooting method. It is based on the square root velocity field (SRVF) transform

$$R\colon \operatorname{Imm}(\mathbb{S}_1,\mathbb{E}^2)/\operatorname{Tra}(\mathbb{E}^2) \to \mathrm{C}^\infty(\mathbb{S}_1,\mathbb{R}^2\setminus\{0\}),\quad R(\gamma) = \frac{1}{\sqrt{\|\gamma'\|}}\gamma' = \sqrt{\|\gamma'\|}v, \tag{4.90}$$

introduced in Srivastava et al. [255]. The pullback of the L^2 metric in the ambient space under the SRVF transform induces a $\operatorname{Diff}(\mathbb{S}_1)$-invariant Riemannian metric on $\operatorname{Imm}(\mathbb{S}_1,\mathbb{E}^2)$ given by

$$\begin{aligned} G^R_\gamma(X,Y) &= G^{\mathrm{L}^2}_{R(\gamma)}(\mathrm{T}R(\gamma,X),\mathrm{T}R(\gamma,Y)) = \int_{\mathbb{S}_1}\langle \mathrm{T}R(\gamma,X),\mathrm{T}R(\gamma,Y)\rangle \,\mathrm{d}s \\ &= \int_{\mathbb{S}_1}\Big(\langle n,\mathrm{D}_sX\rangle\langle n,\mathrm{D}_sY\rangle + \frac{1}{4}\langle v,\mathrm{D}_sX\rangle\langle v,\mathrm{D}_sY\rangle\Big)\operatorname{vol}(g), \end{aligned} \tag{4.91}$$

called the elastic SRVF metric. The SRVF transform is invertible with the inversion formula

$$\gamma(t_1) = \gamma(t_0) + \int_{t_0}^{t_1}\|r\|r\,\mathrm{d}t, \tag{4.92}$$

since $r = R(\gamma)$ is equivalent to $\gamma' = \sqrt{\|\gamma'\|}r = \|r\|r$. Images of closed curves under the SRVF transform are characterized by

$$C(r) = \int_{\mathbb{S}_1}\|r\|r\,\mathrm{d}s = 0. \tag{4.93}$$

The Riemannian logarithm mapping in the image space of the SRVF transform is simply given by the projection of the pointwise Euclidean difference onto the tangent space of

$$\mathfrak{R} = \big\{r\in\mathrm{C}^\infty(\mathbb{S}_1,\mathbb{R}^2\setminus\{0\}) \,\big|\, C(r)=0\big\} \tag{4.94}$$

at the base point, i.e., for $r_0, r_1 \in \mathfrak{R}$, we have that

$$\log(r_0,r_1) = \operatorname{proj}(r_0, r_1 - r_0) \in \mathrm{T}_{r_0}\mathfrak{R}. \tag{4.95}$$

Starting with an initial and final closed planar curve γ_0 and γ_1, we consider their images r_0 and r_1 under the SRVF transform, respectively, and perform geodesic shooting in the image space $\mathfrak{R}$, where geodesics are simply given by pointwise linear interpolation in Euclidean space. The resulting solution to the original boundary value problem can then be obtained using the inversion formula. This is done in the numerical experiment in Section 7.2.

Let M be a two-dimensional manifold. The elastic SRVF metric can be transferred to the setting of parametrized surfaces in three-dimensional Euclidean space using the similar square root normal field (SRNF) transform

$$Q\colon \operatorname{Imm}(M,\mathbb{E}^3) \to \mathrm{C}^\infty(M,\mathbb{R}^3),\quad Q(\gamma) = \frac{\partial_1\gamma\times\partial_2\gamma}{\sqrt{\|\partial_1\gamma\times\partial_2\gamma\|}}, \tag{4.96}$$

introduced by Jermyn et al. [142]. However, the image space of the SRNF transform is not geodesically convex nor well understood. Furthermore, the pre-image of configurations under Q might not even exist or be unique [257].

5 PDE constrained shape optimization

The difference between shape optimization problems and standard optimization problems with PDE constraints is that the domain of the state space may change depending on the shape variable. In general, the set of admissible shapes $\mathcal{B}$ does not admit a vector space structure, which invalidates standard results in, e.g., Hinze et al. [131] and Tröltzsch [260]. There have been different attempts to cast shape optimization problems into a usable framework by considering appropriate subsets of $\mathscr{P}(N)$ for the set of admissible shapes. One of them is the perturbation of identity method [187, 188], which provides the shape space with a metric and also differential structure, so that a notion of distance between shapes and a notion of derivatives with respect to shape variables are available. Another attempt is given by the velocity method as described in [253]. It has similar ideas to the perturbation of identity method and yields the same notion of shape derivatives under some mild assumptions [84, 85]. A general framework for shape optimization that relies on a universal notion of convergence of shapes is given in Haslinger and Mäkinen [123].

5.1 General formulation of the problem

A general PDE constrained shape optimization problem (SOP) has the form

$$\min \ \mathcal{J}(\Omega, u), \tag{5.1a}$$

$$\text{s.t. } \mathcal{R}(\Omega, u) = 0, \tag{5.1b}$$

$$\Omega \in \mathcal{B},\ u \in \mathcal{U}(\Omega), \tag{5.1c}$$

where $\mathcal{B} \subseteq \mathscr{P}(N)$ is the set of admissible shapes, which usually consists of certain subsets of some ambient space N, and $(\mathcal{U}(\Omega))_{\Omega\in\mathcal{B}}$ is a family of function spaces for the solution to the state equation (5.1b) corresponding to the governing equations of the system. Functions in $\mathcal{U}(\Omega)$ are defined on the domain $\Omega \subseteq N$ and have values in some finite-dimensional vector space. The objective function $\mathcal{J}\colon \mathcal{U} \to \mathbb{R}$ is defined on the total space of a vector bundle

$$\mathcal{U} = \coprod_{\Omega\in\mathcal{B}} \mathcal{U}(\Omega) = \big\{(\Omega, u) \,\big|\, \Omega \in \mathcal{B},\ u \in \mathcal{U}(\Omega)\big\} \tag{5.2}$$

and depends on the shape variable $\Omega \in \mathcal{B}$ as well as the state variable $u \in \mathcal{U}(\Omega)$. The state equation operator $\mathcal{R}\colon \mathcal{U} \to \mathcal{V}^*$ is a bundle morphism with values in dual vector bundle

$$\mathcal{V}^* = \coprod_{\Omega\in\mathcal{B}} \mathcal{V}(\Omega)^* = \big\{(\Omega, w) \,\big|\, \Omega \in \mathcal{B},\ w \in \mathcal{V}(\Omega)^*\big\}, \tag{5.3}$$

where $(\mathcal{V}(\Omega))_{\Omega\in\mathcal{B}}$ is a family of function spaces and $\mathcal{V}(\Omega)^*$ is the dual space of $\mathcal{V}(\Omega)$. We refer to elements of $\mathcal{V}(\Omega)$ as test functions as opposed to trial functions in $\mathcal{U}(\Omega)$. Further, let $\mathcal{F} = \{(\Omega, u) \in \mathcal{U} \mid \mathcal{R}(\Omega, u) = 0\}$ denote the set of feasible solutions to (5.1).

The state equation operator is commonly given by the residual of the weak formulation of some variational problem, i.e.,

$$\langle \mathcal{R}(\Omega, u), v\rangle = b_\Omega(v) - a_\Omega(u, v), \quad u \in \mathcal{U}(\Omega),\ v \in \mathcal{V}(\Omega) \tag{5.4}$$

where $a\colon \mathcal{U} \times_{\mathcal{B}} \mathcal{V} \to \mathbb{R}$ is a fiberwise bilinear form and $b\colon \mathcal{V} \to \mathbb{R}$ is a fiberwise linear functional. In this case, we have that $(\Omega, u) \in \mathcal{F}$ if and only if

$$a_\Omega(u, v) = b_\Omega(v) \quad \forall\, v \in \mathcal{V}(\Omega). \tag{5.5}$$

In the following, we consider the Riemannian framework for PDE constrained shape optimization, which has been proposed by Schulz et al. [232, 234] in 2014 and makes use of the Riemannian shape spaces introduced in Section 4.

5.2 Riemannian vector bundle framework

Let the ambient space N be given by a Riemannian manifold of dimension n endowed with the Riemannian metric $\bar{g}$. We restrict ourselves to shapes that are immersed submanifolds of N diffeomorphic to some given reference shape M, which is assumed to be a smooth manifold of dimension m with boundary. Changes in the topology and the diffeology of the shapes are therefore not considered in the framework. The set of admissible shapes is then chosen as a subset of the shape space

$$\mathrm{B}(M, N) = \mathrm{Imm}(M, N)/\operatorname{Diff}(M). \tag{5.6}$$

See Section 4.2.3 for more details on shape spaces of immersions.

First, we want to establish that, given a suitable family of function spaces $(\mathcal{U}(\Omega))_{\Omega\in\mathcal{B}}$, the disjoint union of state spaces in (5.2) is indeed the total space of a vector bundle. Note that, in this framework, a function defined on a shape $\Omega \in \mathcal{B}$ is actually a section over an immersion $\xi \in \mathcal{G}$ corresponding to the shape, where $\mathcal{B} = \mathcal{G}/\operatorname{Diff}(M)$.

Proposition 5.1

Let (E, N, π_E) be a vector bundle of finite rank endowed with a linear connection. The set

$$\mathcal{E} = \big\{(\xi, s) \,\big|\, \xi \in \mathcal{G},\, s \in \Gamma(\xi^* E)\big\} \tag{5.7}$$

is the total space of a vector bundle with projection $\pi_{\mathcal{E}} \colon \mathcal{E} \to \mathcal{G}$, $(\xi, s) \mapsto \xi$.

Proof. The proof originates from a construction in Kriegl and Michor [159, Theorem 42.1, Theorem 42.17]. Let U be an open neighborhood of the zero section of $\mathrm{T}N$ such that

$$(\pi_{\mathrm{T}N}, \exp) \colon U \subseteq \mathrm{T}N \to N \times N, \quad (q, v) \mapsto (q, \exp_q(v)), \tag{5.8}$$

is a smooth diffeomorphism onto an open neighborhood V of the diagonal of $N \times N$, where exp denotes the Riemannian exponential mapping on N. For $f_0 \in \mathcal{G}$, consider the subset

$$W_{\xi_0} = \big\{\xi \in \mathcal{G} \,\big|\, (\xi_0(p), \xi(p)) \in V \text{ for all } p \in M\big\}, \tag{5.9}$$

which is open in $\mathcal{G}$, and the mapping

$$\varphi_{\xi_0} \colon \pi_E^{-1}(W_{\xi_0}) \to W_{\xi_0} \times \Gamma(\xi_0^* E), \quad (\xi, s) \mapsto (\xi, \mathrm{P}_{\xi,\xi_0}(s)), \tag{5.10}$$

where P_{ξ,ξ_0} is the parallel transport induced by the linear connection on E along geodesic paths connecting $\xi(p)$ and $\xi_0(p)$ for each $p \in M$. We may have to choose a smaller open neighborhood U to ensure that the parallel transports are all defined. The mapping φ_{ξ_0} is a fiberwise linear isomorphism. We can endow $\mathcal{E}$ with the coarsest topology such that all φ_{ξ_0} remain continuous, which turns $(\mathcal{E}, \mathcal{G}, \pi_{\mathcal{E}})$ into a vector bundle. Note that the resulting topology on the total space is Hausdorff if the topology on the base space and on each fiber is Hausdorff. □

The parallel transports in the above proof can be extended to fiberwise continuous linear isomorphisms between the Sobolev spaces $\mathrm{H}^k(\xi^* E)$ and $\mathrm{H}^k(\xi_0^* E)$ for $k \in \mathbb{N}_0$, since $\Gamma(\xi^* E)$ is dense in the Hilbert space $\mathrm{H}^k(\xi^* E)$ and

$$P_{\xi,\xi_0} \colon \Gamma(\xi^* E) \subseteq \mathrm{H}^k(\xi^* E) \to \mathrm{H}^k(\xi_0^* E) \tag{5.11}$$

is fiberwise continuous linear with respect to the H^k Sobolev norm. The resulting vector bundle becomes a Hilbert bundle. Furthermore, one can also consider Banach bundles.

5.2.1 Transformed optimization problem

Since we only consider submanifolds of the ambient space that are diffeomorphic to some reference shape, state equations posed on domains described by the shape variable can be transformed to a reference domain. In order to guarantee that the transformed problem is equivalent to the original one, the geometric transformations are required to have a certain regularity (see Section 2.2.5). This is not an issue in the smooth setting. However, less regular domains may occur in practice and it is generally a difficult task to represent smooth shapes adequately in the discretized setting. Isogeometric analysis offers a convenient way to raise the smoothness of finite-dimensional representations of the shape and solutions to the state equation within a single patch, but it suffers from the same or perhaps more difficulties as conventional finite element methods when it comes to multi-patch geometries.

Pulling back (5.1) to the reference manifold M yields the transformed problem

$$\min \ \hat{\mathcal{J}}(\xi, \hat{u}), \tag{5.12a}$$
$$\text{s.t. } \hat{\mathcal{R}}(\xi, \hat{u}) = 0, \tag{5.12b}$$
$$\xi \in \mathcal{G},\ \hat{u} \in \hat{\mathcal{U}}_\xi, \tag{5.12c}$$

where the objective function and the state equation operator are related to the original ones via the quotient mapping $\pi\colon \mathcal{G} \to \mathcal{B}$ and the pullback operator, i.e.,

$$\hat{\mathcal{J}}\colon \hat{\mathcal{U}} \to \mathbb{R}, \quad \hat{\mathcal{J}}(\xi, \hat{u}) = \mathcal{J}(\pi(\xi), \hat{u} \circ \xi^{-1}), \tag{5.13a}$$
$$\hat{\mathcal{R}}\colon \hat{\mathcal{U}} \to \hat{\mathcal{V}}^*, \quad \hat{\mathcal{R}}(\xi, \hat{u}) = \mathcal{R}(\pi(\xi), \hat{u} \circ \xi^{-1}). \tag{5.13b}$$

Thus $\hat{u} = u \circ \xi$ if $u \in \mathcal{U}(\Omega)$ is a function defined on the domain $\Omega = \xi(M)$, regarded as a subset of the ambient space N. In the vector bundle framework, the state spaces of trial and test functions consist of sections over ξ defined on the fixed reference domain M and generate the total spaces

$$\hat{\mathcal{U}} = \coprod_{\xi \in \mathcal{G}} \hat{\mathcal{U}}_\xi = \coprod_{\xi \in \mathcal{G}} \Gamma(\xi^* E) = \big\{(\xi, u) \,\big|\, \xi \in \mathcal{G},\ u \in \Gamma(\xi^* E)\big\}, \tag{5.14a}$$
$$\hat{\mathcal{V}} = \coprod_{\xi \in \mathcal{G}} \hat{\mathcal{V}}_\xi = \coprod_{\xi \in \mathcal{G}} \Gamma(\xi^* F) = \big\{(\xi, v) \,\big|\, \xi \in \mathcal{G},\ v \in \Gamma(\xi^* F)\big\}, \tag{5.14b}$$

according to Proposition 5.1. Here, (E, N, π_E) and (F, N, π_F) are vector bundles of finite rank, each endowed with a linear connection. Note that if ξ is not an injective immersion, it is not always possible to transform the problem back to the original one.

5.2.2 Existence of optimal shapes

The existence of optimal solutions to PDE constrained shape optimization problems can be shown under the following general set of conditions:

Assumption 5.2

(A1) The set of admissible shapes $\mathcal{B}$ is a non-empty, compact, and metrizable space.

(A2) For each $\Omega \in \mathcal{B}$, there is a unique solution $\mathcal{K}(\Omega) \in \mathcal{U}(\Omega)$ to the state equation (5.1b) that depends continuously on Ω, i.e., $\mathcal{K}\colon \mathcal{B} \to \mathcal{U}$ is a continuous solution operator.

(A3) The objective function $\mathcal{J}$ in (5.1a) is lower semi-continuous.

Lemma 5.3

Let X be a non-empty, compact, metrizable space. Furthermore, let $f\colon X \to \mathbb{R}$ be lower semi-continuous. Then there exists an $x_* \in X$ such that $f(x_*) \leq f(x)$ for all $x \in X$.

Proof. Let $(x_n)_{n\in\mathbb{N}} \subseteq X$ be an infimizing sequence with $\lim_{n\to\infty} f(x_n) = \inf_{x\in X} f(x)$. Since compactness is equivalent to sequential compactness in a metrizable space, there is a subsequence $(x_{n_k})_{k\in\mathbb{N}}$ that converges to some $x_* \in X$. Lower semi-continuity of f then yields

$$f(x_*) = f(\lim_{k\to\infty} x_{n_k}) \leq \liminf_{k\to\infty} f(x_{n_k}) = \lim_{n\to\infty} f(x_n) = \inf_{x\in X} f(x) \leq f(x_*), \tag{5.15}$$

thus $f(x_*) = \inf_{x\in X} f(x)$, i.e., the minimum is attained and $f(x_*) \leq f(x)$ for all $x \in X$. □

Lemma 5.4

Let $f\colon X \to Y$ be a surjective continuous mapping from a compact metrizable space X to a Hausdorff space Y. Then Y is compact and metrizable.

Proof. This lemma is a corollary of Urysohn's metrization theorem. A proof can be found in [280, Corollary 23.2]. □

Proposition 5.5 (Existence of optimal shapes)

Under Assumption 5.2, the shape optimization problem (5.1) *has an optimal solution, i.e., there exists some $(\Omega_*, u_*) \in \mathcal{F}$ such that $\mathcal{J}(\Omega_*, u_*) \leq \mathcal{J}(\Omega, u)$ for all $(\Omega, u) \in \mathcal{F}$.*

Proof. A proof is also given in Haslinger and Mäkinen [123, Theorem 2.8, Theorem 2.10].

Using Lemma 5.3, it remains to show that the graph

$$\mathcal{F} = \big\{(\Omega, u) \in \mathcal{U} \,\big|\, \mathcal{R}(\Omega, u) = 0\big\} = \big\{(\Omega, \mathcal{K}(\Omega)) \,\big|\, \Omega \in \mathcal{B}\big\} \subseteq \mathcal{U} \tag{5.16}$$

is non-empty, compact, and metrizable. Since $\mathcal{B}$ is non-empty and there is a solution to the state equation for each $\Omega \in \mathcal{B}$, the set of feasible solutions $\mathcal{F}$ is also non-empty. As continuous image of a compact and metrizable space in a Hausdorff space, it is also compact and metrizable, according to Lemma 5.4. □

Since compactness is a fairly strong requirement in the infinite-dimensional setting, the conditions in Assumption 5.2 may be replaced with the corresponding versions in the weak topology. See Hinze et al. [131, Theorem 1.45] for the case of reflexive Banach spaces.

5.2.3 Optimality conditions

Numerical methods for solving PDE constrained shape optimization problems are based on optimality conditions associated with the problem. Here, we introduce the variational inequality and state first-order necessary conditions for optimal solutions in the Banach space setting, followed by some considerations for optimization on shape spaces.

Lemma 5.6 (Variational inequality)

Let S be a convex subset of a Banach space X and $f\colon S \to \mathbb{R}$ be a function that is Gateaux differentiable in an open neighborhood around S.

a) If $x_* \in S$ is a solution to the minimization problem

$$\min f(x), \quad x \in S, \tag{5.17}$$

then it is a stationary point of f, i.e., x_* satisfies the variational inequality

$$\delta f(x_*, x - x_*) \geq 0 \tag{5.18}$$

for all $x \in S$.

b) The converse is true if f is additionally convex on S. Furthermore, if f is strictly convex on S, then there exists at most one solution to (5.17).

c) If x_* is an interior point of S, then the variational inequality (5.18) *is equivalent to*

$$\delta f(x_*, v) = 0 \tag{5.19}$$

for all $v \in X$, i.e., $f'(x_*) = 0$ if f is Fréchet differentiable.

Proof. We refer to Hinze et al. [131, Theorem 1.46] for a proof. □

A version of Lemma 5.6 for differentiable functions defined on geodesically convex subsets of a Riemannian manifold can be found in Boumal [52, Corollary 11.22, Exercise 11.26].

First-order optimality conditions can be derived via the method of Lagrange multipliers. Given an optimization problem of the form

$$\min \ \mathcal{J}(q, u), \tag{5.20a}$$
$$\text{s.t. } \mathcal{R}(q, u) = 0, \tag{5.20b}$$
$$q \in \mathcal{S},\ u \in \mathcal{U}, \tag{5.20c}$$

with $\mathcal{J}\colon \mathcal{Q} \times \mathcal{U} \to \mathbb{R}$ and $\mathcal{R}\colon \mathcal{Q} \times \mathcal{U} \to \mathcal{V}^*$, where $\mathcal{Q}$, $\mathcal{U}$, and $\mathcal{V}$ are Banach spaces and $\mathcal{S}$ is a subset of $\mathcal{Q}$, we can define the Lagrange function $\mathcal{L}\colon \mathcal{Q} \times \mathcal{U} \times \mathcal{V} \to \mathbb{R}$ by

$$\mathcal{L}(q, u, v) = \mathcal{J}(q, u) + \langle \mathcal{R}(q, u), v \rangle. \tag{5.21}$$

Let $\mathcal{F} = \{(q, u) \in \mathcal{Q} \times \mathcal{U} \mid \mathcal{R}(q, u) = 0\}$ denote the set of feasible solutions and consider the following assumptions:

Assumption 5.7

(B1) The subset $\mathcal{S} \subseteq \mathcal{Q}$ is non-empty, convex, and closed.

(B2) For each q in an open neighborhood $\mathcal{P} \subseteq \mathcal{Q}$ of $\mathcal{S}$, there is a unique solution $\mathcal{K}(q) \in \mathcal{U}$ to the state equation (5.20b), i.e., the solution operator $\mathcal{K}\colon \mathcal{P} \to \mathcal{U}$ is well-defined.

(B3) The objective function $\mathcal{J}$ and the state equation operator $\mathcal{R}$ are continuously differentiable. Furthermore, $\partial_u \mathcal{R}(q, \mathcal{K}(q))$ has a bounded inverse for all $q \in \mathcal{P}$.

Then the following statement holds:

Theorem 5.8 (First-order optimality conditions)

Let Assumption 5.7 be satisfied and $(q_*, u_*) \in \mathcal{F}$ be an optimal solution to (5.20). *Then there exists an adjoint state $v_* \in \mathcal{V}$ such that the Karush–Kuhn–Tucker (KKT) conditions*

$$\langle \partial_q \mathcal{L}(q_*, u_*, v_*), q - q_* \rangle \geq 0 \quad \forall\, q \in \mathcal{S} \qquad \textit{(design equation)}, \tag{5.22a}$$
$$\langle \partial_u \mathcal{L}(q_*, u_*, v_*), \delta u \rangle = 0 \quad \forall\, \delta u \in \mathcal{U} \quad \textit{(adjoint equation)}, \tag{5.22b}$$
$$\langle \partial_v \mathcal{L}(q_*, u_*, v_*), \delta v \rangle = 0 \quad \forall\, \delta v \in \mathcal{V} \qquad \textit{(state equation)}, \tag{5.22c}$$

with the partial derivatives

$$\partial_q \mathcal{L}(q,u,v) = \partial_q \mathcal{J}(q,u) + \langle \partial_q \mathcal{R}(q,u), v\rangle, \tag{5.23a}$$
$$\partial_u \mathcal{L}(q,u,v) = \partial_u \mathcal{J}(q,u) + \langle \partial_u \mathcal{R}(q,u), v\rangle, \tag{5.23b}$$
$$\partial_v \mathcal{L}(q,u,v) = \mathcal{R}(q,u), \tag{5.23c}$$

are fulfilled. We refer to $(q_*, u_*, v_*) \in \mathcal{Q} \times \mathcal{U} \times \mathcal{V}$ *as a solution to the* KKT *system* (5.22).

Proof. A proof is given in Hinze et al. [131, Section 1.7.2]. □

The optimality conditions motivate the adjoint approach for solving shape optimization problems numerically instead of the forward sensitivity approach and can be generalized to the smooth manifold setting [38]. However, some caution is required when dealing with the infinite-dimensional case, even in the case of Banach manifolds [39]. A satisfactory result that is applicable to the shape spaces considered in this thesis is difficult to obtain and—to our knowledge—not available in the literature yet.

5.2.4 Adjoint state method

Consider the reduced cost functional

$$\mathcal{I}\colon \mathcal{Q} \to \mathbb{R}, \quad \mathcal{I}(q) = \mathcal{J}(q, \mathcal{K}(q)), \tag{5.24}$$

and assume that $\mathcal{J}$, $\mathcal{R}$, and $\mathcal{K}$ are continuously differentiable. Gradient-based optimization methods require the evaluation of the derivative of $\mathcal{I}$ with respect to the design variables. A straightforward way is given by the formula

$$\mathrm{d}\mathcal{I}(q) = \partial_q \mathcal{J}(q, \mathcal{K}(q)) + \partial_u \mathcal{J}(q, \mathcal{K}(q)) \mathrm{D}\mathcal{K}(q), \tag{5.25}$$

which results from applying the chain rule to $\mathcal{I}(q) = \mathcal{J}(q, \mathcal{K}(q))$. However, evaluation of the last term $\mathrm{D}\mathcal{K}(q)$ requires a solution to the state equation for every variation δq, which is costly and not very efficient from a computational point of view. It is not advisable if there is a large number of design variables.

The adjoint state method takes advantage of the fact that $\mathcal{R}(q, \mathcal{K}(q)) = 0$ along solutions, i.e.,

$$\mathcal{I}(q) = \mathcal{J}(q, \mathcal{K}(q)) + \langle \mathcal{R}(q, \mathcal{K}(q)), v\rangle = \mathcal{L}(q, \mathcal{K}(q), v), \tag{5.26}$$

for all $q \in \mathcal{Q}$ and $v \in \mathcal{V}$. In this case, the total derivative of $\mathcal{I}$ can be written as

$$\mathrm{d}\mathcal{I}(q) = \mathrm{d}\mathcal{L}(q, \mathcal{K}(q), v) = \partial_q \mathcal{L}(q, \mathcal{K}(q), v) + \partial_u \mathcal{L}(q, \mathcal{K}(q), v) \mathrm{D}\mathcal{K}(q). \tag{5.27}$$

Given an admissible design $q_* \in \mathcal{Q}$ and a corresponding solution $u_* = \mathcal{K}(q_*)$ to the state equation, we can choose $v_* \in \mathcal{V}$ as a solution to the adjoint state equation

$$\partial_u \mathcal{L}(q_*, u_*, v_*) = \partial_u \mathcal{J}(q_*, u_*) + \langle \partial_u \mathcal{R}(q_*, u_*), v_*\rangle = 0 \tag{5.28}$$

such that the term vanishes in (5.27). The sought derivative is then computed as

$$\mathrm{d}\mathcal{I}(q_*) = \partial_q \mathcal{L}(q_*, u_*, v_*) = \partial_q \mathcal{J}(q_*, u_*) + \langle \partial_q \mathcal{R}(q_*, u_*), v_*\rangle, \tag{5.29}$$

which is considerably more efficient than the direct approach in (5.25). We refer to v_* as an adjoint state associated with (q_*, u_*). This approach also corresponds to solving the KKT system (5.22) in Theorem 5.8 and can be applied to shape optimization problems.

5.3 Methods for shape optimization

There are two approaches to numerical optimization for infinite-dimensional problems. The first one is the *first optimize–then discretize* (FOTD) approach, where the optimality conditions are considered in the infinite-dimensional setting and numerical discretizations are utilized to approximate relevant quantities. The second one is the *first discretize–then optimize* (FDTO) approach, where a finite-dimensional representation of the optimization variable is considered a priori and the optimality conditions are posed in the finite-dimensional case on some subset of the Euclidean space. In the context of PDE constrained optimization, the difference between the two approaches is that there is a choice for the discretization of the adjoint state space in the former. In the latter, it is already determined by the choice for the discrete state space [131, Chapter 3]. In the end, both approaches lead to a discretized finite-dimensional system that has to be solved numerically.

An iterative method for shape optimization is based on generating a sequence of design iterates for a shape from an initial design that is expected to converge toward a desirable result, e.g., a local optimizer of the shape optimization problem. Local optimizers are often satisfactory, since it is generally a difficult task to obtain a global optimizer for problems that are not convex. Probabilistic techniques, such as stochastic gradient descent methods and simulated annealing, can be applied to search the design space for a global solution in a more efficient manner than brute-force approaches that rely on trial and error using different initial guesses for the design. An exhaustive search is not feasible for problems with a large or infinite-dimensional design space, as is the case with shape optimization problems. We refer to Marti [175] for stochastic optimization methods.

Common methods for non-linear optimization include gradient-based descent methods, (quasi-)Newton methods, and trust-region methods. Projection methods, penalty methods, interior-point methods (IPM), and sequential quadratic programming (SQP) can be applied to handle equality and inequality constraints. In this thesis, the augmented Lagrangian method (ALM) is employed to impose additional constraints on the geometry of shapes. A standard reference on numerical methods for continuous optimization problems is given by Nocedal and Wright [198].

The above algorithms require information on first-order and, in some cases, higher-order derivatives of the objective and constraint functions, which can be obtained either analytically, semi-analytically, or numerically, e.g., using finite differences. The sensitivities can also be computed using symbolic and automatic differentiation if there are only finitely many optimization parameters [115, 191, 190]. One of the main challenges in shape optimization is to determine a correct and useful descent direction along which the shape can be evolved in order to reduce the objective value. Since the optimization variable is a shape, a suitable framework has to be chosen for the design space (see Section 4). In many cases, it is preferable to have an analytical expression for the shape sensitivities. However, they are often only available for simple problems. Complex problems may require tedious mathematical calculations that make the approach using analytical sensitivities intractable.

There are derivative-free methods that rely on evaluations of the objective function only [75]. However, currently existing algorithms are still only effective for small problems and thus not suitable for shape optimization problems that are inherently infinite-dimensional.

One of the most popular methods for structural shape optimization in the FDTO approach is the method of moving asymptotes (MMA) by Svanberg [258] and the globally convergent generalization based on conservative convex separable approximations (CCSA) [259]. It is

designed to be flexible, i.e., able to handle quite general types of optimization parameters and constraints, and is suitable for large scale problems. Another method for structural optimization based on nodal shape variables is the vertex-assigned morphing of optimal shape (VAMOS) [46, 134]. It has been successfully applied to problems of industrial scale, especially for optimization of thin-walled structures [15, 109, 229]. A connection of the vertex morphing method with Tikhonov regularization in the case of a linear least squares problem has been established by Rosandi and Simeon [220].

In the following, we focus on gradient-based descent methods in the setting of Riemannian manifolds. For the numerical implementation of shape optimization methods in the FOTD approach, the passage to finite-dimensional approximations of shape updates is discussed in Section 6.4.

5.3.1 Optimization on Riemannian manifolds

We are concerned with general optimization problems of the form

$$\min f(p), \quad p \in S, \tag{5.30}$$

where S is a Riemannian manifold and the objective function $f\colon S \to \mathbb{R}$ is continuously differentiable. Methods for unconstrained optimization extend to the Riemannian setting by replacing straight lines with geodesic paths. More generally, we can consider retractions, which are first-order approximations of the Riemannian exponential mapping.

Definition 5.9 (Retractions)

A retraction on S is a smooth mapping $R\colon \mathrm{T}S \to S$ that satisfies

a) $R_p(0) = p$,

b) $\mathrm{D}R_p(0) = \mathrm{id}_{\mathrm{T}_pS}$,

for all $p \in S$, where $R_p\colon \mathrm{T}_pS \to S$ denotes the restriction of R to p and the tangent space $\mathrm{T}_0(\mathrm{T}_pS)$ is identified with T_pS in the usual way for the identity mapping in b).

A retraction provides a way for moving along a specified direction on the manifold. The update formula reads

$$p_{k+1} = R(p_k, s_k v_k), \quad k \in \mathbb{N}_0, \tag{5.31}$$

which is a generalization of $p_{k+1} = p_k + s_k v_k$ in the linear setting, where p_k is the current design, p_{k+1} is the next design, $s_k > 0$ is the step size, and $v_k \in \mathrm{T}_{p_k}S$ is a given direction. An example of a retraction is given by the Riemannian exponential mapping itself, i.e.,

$$R(p, v) = \exp(p, v), \quad (p, v) \in \mathrm{T}S, \tag{5.32}$$

which is referred to as a geodesic retraction. See Absil et al. [2, Proposition 5.4.1] and the illustration in Figure 12.

A general descent method on Riemannian manifolds is given in Algorithm 1. The iteration is executed until a stopping condition is fulfilled, e.g., the norm of the objective gradient is below a given tolerance or there is no sufficient decrease in the objective value. Optimality conditions have to be checked to ensure that the method converges toward a feasible local minimizer. In the Hilbert manifold setting, we can choose

$$\Sigma\colon S \to [0, \infty), \quad \Sigma(p) = \|\mathrm{grad}\, f(p)\|_p, \tag{5.33}$$

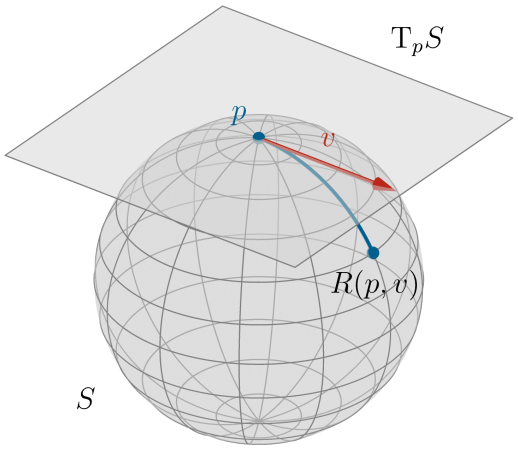

Figure 12: Geodesic retraction on a sphere as a generalization of straight paths.

Algorithm 1 General descent method on Riemannian manifolds

Input: Objective function $f\colon S \to \mathbb{R}$ and initial design $p_0 \in S$.
Output: Sequence of design iterates $(p_k)_{k\in\mathbb{N}_0}$ in S with $f(p_{k+1}) < f(p_k)$ for $k \in \mathbb{N}_0$.

1: **for** $k = 0, 1, 2, \ldots$ (until $\mathrm{d}f(p_k) = 0$ or a stopping condition is fulfilled) **do**
2: Choose a descent direction $v_k \in \mathrm{T}_{p_k}S$ with $\mathrm{d}f(p_k)[v_k] < 0$.
3: Choose a step size $s_k > 0$ with $f(R(p_k, s_k v_k)) < f(p_k)$.
4: Set $p_{k+1} \coloneqq R(p_k, s_k v_k)$.
5: **end**

as a stationarity measure, where $\|\cdot\|_p$ is the norm on the tangent space at $p \in S$ induced by the Riemannian metric G, i.e., $\|v\|_p = \sqrt{G_p(v, v)}$ for $v \in \mathrm{T}_pS$. The stopping condition then reads $\Sigma(p) < \varepsilon$ for some given tolerance $\varepsilon > 0$.

Let $p_k \in S$ be the current design in the k-th iteration of the optimization procedure and $v_k \in \mathrm{T}_{p_k}S$ be a descent direction with $\mathrm{d}f(p_k)[v_k] < 0$, which exists if p_k is not a stationary point. A line search algorithm is commonly applied to determine the step size $s_k > 0$. To facilitate a sufficient decrease in each iteration and guarantee the global convergence of the method, the descent directions are typically chosen to satisfy an angle condition (see, e.g., Hinze et al. [131, Section 2.2.1] and Absil et al. [2, Section 4.2]) and the Armijo–Goldstein condition is used for the step sizes:

$$f(p_{k+1}) \leq f(p_k) + c\, s_k\, \mathrm{d}f(p_k)[v_k], \tag{5.34}$$

where $c \in (0, 1)$ is some constant related to the desired decrease. A curvature condition can be imposed on the step size s_k in addition to (5.34), which is usually required for the analysis of quasi-Newton methods. Together they make up the so-called Wolfe conditions. A feasible step size that fulfills the Wolfe conditions can always be found under reasonable assumptions on the objective function [198, Lemma 3.1]. In practice, the Armijo–Goldstein condition is sufficient for most optimization algorithms [215, p. 9].

A backtracking line search can be applied to determine the step size efficiently. Starting from a relatively large estimate for the step size, we shrink it iteratively until the Armijo–Goldstein condition is fulfilled. Let $s_{k,0} > 0$ denote the first estimate and $\tau \in (0, 1)$ be the shrinking factor, i.e., $s_{k,m} = \tau^m s_{k,0}$ for $m \in \mathbb{N}_0$. The step size $s_k = s_{k,m_k}$ is chosen for the

k-th iteration, where m_k is the smallest non-negative integer such that s_{k,m_k} fulfills (5.34). This is referred to as the Armijo rule and the resulting s_k's are called Armijo step sizes.

The following result is available regarding the convergence of descent methods on finite-dimensional Riemannian manifolds:

Theorem 5.10

Let $f\colon S \to \mathbb{R}$ be continuously differentiable and $(p_k)_{k\in\mathbb{N}_0}$, $(v_k)_{k\in\mathbb{N}_0}$, $(s_k)_{k\in\mathbb{N}_0}$ be sequences generated by Algorithm 1. If $(v_k)_{k\in\mathbb{N}_0}$ is an admissible sequence of descent directions, i.e.,

$$\limsup_{l\to\infty} \langle \operatorname{grad} f(p_{k_l}), v_{k_l} \rangle < 0 \tag{5.35}$$

for any subsequence $(p_{k_l})_{l\in\mathbb{N}_0}$ that converges to a non-critical point of f, where $(v_{k_l})_{l\in\mathbb{N}_0}$ is bounded, and the step sizes $(s_k)_{k\in\mathbb{N}_0}$ satisfy the Armijo–Goldstein condition in (5.34)*, then every accumulation point of $(p_k)_{k\in\mathbb{N}_0}$ is a stationary point of f. Furthermore, if the level set $K = \{p \in S \mid f(p) \leq f(p_0)\}$ is compact, then*

$$\lim_{k\to\infty} \|\operatorname{grad} f(p_k)\|_{p_k} = 0. \tag{5.36}$$

Proof. A proof is given in Absil et al. [2, Theorem 4.3.1, Corollary 4.3.2]. □

We refer to Ring and Wirth [215] for the infinite-dimensional case, where the manifold is modeled on separable Hilbert spaces and assumed to be geodesically complete. Due to the difficulties involved with the more general setting, an adequate convergence analysis of descent methods on the shape spaces considered in this thesis is—to our knowledge—not available in the literature yet. This does not pose an issue for the numerical optimization algorithms considered in this thesis, which rely on finite-dimensional representations to approximate the shapes. However, it is interesting to investigate how the approximations are related to the true solution in the infinite-dimensional setting.

For a treatment of Newton-type methods on Riemannian shape spaces in the context of PDE constrained shape optimization, we refer to Schulz et al. [232, 234]. Main references on optimization in the setting of smooth manifolds include Absil et al. [2], Bergmann and Herzog [38], Bergmann et al. [39], and Boumal [52].

5.3.2 Augmented Lagrangian method for equality constraints

If equality constraints are present, the optimization problem (5.30) is modified to

$$\begin{aligned} \min\ & f(p), && \text{(5.37a)}\\ \text{s.t.}\ & g(p) = 0, && \text{(5.37b)}\\ & p \in S. && \text{(5.37c)} \end{aligned}$$

Here, $g\colon S \to \mathbb{R}^m$ is a constraint function corresponding to m equality constraints, which is assumed to be continuously differentiable. Penalty methods treat constrained optimization problems by solving a sequence of unconstrained subproblems that incorporate additional terms associated with the constraints into the objective function. Large penalty parameters correspond to stronger enforcement of the constraints. Solutions to the subproblems with increasing penalty parameters are then expected to converge toward a feasible solution to the original problem.

Algorithm 2 Augmented Lagrangian method for equality constraints

Input: Initial design $p_0 \in S$, Lagrange multiplier $\lambda_0 \in \mathbb{R}^m$, and penalty parameter $\mu_0 > 0$.
Output: Sequence of design iterates $(p_k)_{k\in\mathbb{N}_0}$ in S.

1: **for** $k = 0, 1, 2, \ldots$ (until a stopping condition is fulfilled) **do**
2: Compute an approximate local minimizer $\bar{p}_k \in S$ of $L(\,\cdot\,, \lambda_k, \mu_k)$ using an iterative method for unconstrained optimization with p_k as a starting point.
3: Set $\lambda_{k+1} \coloneqq \lambda_k - \mu_k g(\bar{p}_k)$.
4: Choose $\mu_{k+1} \geq \mu_k$.
5: Set $p_{k+1} \coloneqq \bar{p}_k$.
6: **end**

A common penalty term is given by the sum of squares of each component of the constraint function scaled by the parameter $\mu > 0$. This results in a quadratic penalty function

$$f_\mu(p) = f(p) + \frac{\mu}{2} \sum_{j=1}^{m} g_j(p)^2. \tag{5.38}$$

In the finite-dimensional Euclidean setting, e.g., $S = \mathbb{R}^n$, the Hessian matrix of f_μ at p is poorly conditioned if μ is large, $m < n$, and p is close to the minimizer of f_μ. To avoid the ill-conditioning, the augmented Lagrangian function

$$L(p, \lambda, \mu) = f(p) - \sum_{i=1}^{m} \lambda_i g_i(p) + \frac{\mu}{2} \sum_{j=1}^{m} g_j(p)^2 \tag{5.39}$$

is usually considered instead of (5.38), where $\lambda = (\lambda_1, \ldots, \lambda_m) \in \mathbb{R}^m$ denotes the Lagrange multipliers. Similar to penalty methods, the augmented Lagrangian method (ALM) solves a sequence of unconstrained subproblems to compute a feasible solution to the original problem with constraints. During the optimization process, the penalty parameter and the Lagrange multipliers are updated according to Algorithm 2.

Standard penalty and augmented Lagrangian methods in Euclidean space are discussed in more detail in Nocedal and Wright [198, Chapter 17]. Extensions of the methods to Banach spaces [146] and finite-dimensional Riemannian manifolds [167] are possible. However, as mentioned in Section 5.3.1, the case of infinite-dimensional shape spaces remains an open area of research. Some effort has been made on stochastic augmented Lagrangian methods in the context of Riemannian shape spaces [108]. In this thesis, constrained optimization is mainly required to enforce the fixed area constraint for the shell optimization problem in Section 5.4.2, which is a single equality constraint.

5.4 Shape differential calculus

In the following, we consider mappings $F\colon \operatorname{Imm}(M, N) \to Z$ from the pre-shape space of smooth immersions to some Fréchet space Z. The notation $\mathrm{D}_{(\xi,\eta)}F$ refers to the derivative of F at $\xi \in \operatorname{Imm}(M, N)$ in the direction of $\eta \in \mathrm{T}_\xi \operatorname{Imm}(M, N)$ given by

$$\mathrm{D}_{(\xi,\eta)}F = \mathrm{D}F(\xi)[\eta] = \partial_t (F \circ \gamma)(0) = \lim_{t\to 0} \frac{F(\gamma(t)) - F(\gamma(0))}{t}, \tag{5.40}$$

where $\gamma\colon (-\varepsilon, \varepsilon) \to \operatorname{Imm}(M, N)$ is a smooth path of immersions that satisfies $\gamma(0) = \xi$ and $\dot{\gamma}(0) = \eta$. This can be put in connection with the shape derivative via the identification

$$\mathrm{B}(M, N) = \operatorname{Imm}(M, N) / \operatorname{Diff}(M) \tag{5.41}$$

and a choice of Riemannian metric on the shape space.

5.4.1 Shape derivative and variational formulas

Let $\mathrm{B}(M,N)$ denote the shape space of smooth immersions endowed with a Riemannian metric G. It consists of immersed submanifolds of the ambient Riemannian manifold N diffeomorphic to the reference shape M and can be identified with the collection of subsets

$$\mathrm{S}(M,N) = \big\{\xi(M) \subseteq N \,\big|\, \xi \in \mathrm{Imm}(M,N)\big\} \subseteq \mathscr{P}(N) \tag{5.42}$$

in the case of injective immersions. We assume that the horizontal lift corresponding to the Riemannian metric is well-defined, which is true for Sobolev-type Riemannian metrics (see Proposition 4.19).

Definition 5.11 (Riemannian shape derivative)

Let $F\colon \mathrm{B}(M,N) \to Z$ be a shape functional with values in the Fréchet space Z. It induces a mapping $\tilde{F} = F \circ \pi\colon \mathrm{Imm}(M,N) \to Z$ on the pre-shape space of smooth immersions via the Riemannian submersion $\pi\colon \mathrm{Imm}(M,N) \to \mathrm{B}(M,N)$. The shape derivative of F at $\Omega \in \mathrm{B}(M,N)$ in the direction of $\delta\Omega \in \mathrm{T}_\Omega\mathrm{B}(M,N)$ is defined as

$$\mathrm{D}F(\Omega)[\delta\Omega] = \mathrm{D}\tilde{F}(\xi)[\eta], \tag{5.43}$$

where $(\xi,\eta) \in \mathrm{TImm}(M,N)$ is the unique horizontal vector field with $\mathrm{T}\pi(\xi,\eta) = (\Omega,\delta\Omega)$. Thus, shape differentiability of F is attributed to the differentiability of $\tilde{F}$. The notions of differentiation used for topological vector spaces can be found in Section 2.1.3.

Without the assumption on the horizontal lift, the derivative on the right-hand side of (5.43) may differ depending on the choice of vector field in $\mathrm{TImm}(M,N)$. For equivariant tensor fields, the tangential difference is related to the Lie derivative. See Bauer et al. [27, Section 5.4].

Lemma 5.12 (Tangential variation of equivariant tensor fields)

Let $F\colon \mathrm{Imm}(M,N) \to \Gamma(\mathrm{T}^{r,s}M)$ be a mapping with values in the space of tensor fields on M. If F is equivariant with respect to pullbacks by diffeomorphisms of M, i.e.,

$$F(\xi) = (\varphi^* F)(\xi) = \varphi^*\Big(F\big((\varphi^{-1})^*\xi\big)\Big) \tag{5.44}$$

for all $\xi \in \mathrm{Imm}(M,N)$ and $\varphi \in \mathrm{Diff}(M)$, then the tangential variation of F is given by the Lie derivative

$$\mathrm{D}_{(\mathrm{T}\xi\circ X)}F = \mathcal{L}_X\big(F(\xi)\big), \tag{5.45}$$

where $X \in \Gamma(\mathrm{T}M)$.

Proof. We refer to Kolář et al. [158, Section 6.17]. □

In the following, we provide some variational formulas of first order that are important for deriving shape derivatives of common shape functionals. Let $\bar{g}$ denote the Riemannian metric on the ambient space N.

Proposition 5.13 (First variation of the pullback metric)

The mapping

$$g\colon \mathrm{Imm}(M,N) \to \Gamma(\mathrm{T}^{0,2}M), \quad \xi \mapsto \xi^*\bar{g}, \tag{5.46}$$

is differentiable with

$$\mathrm{D}_{(\xi,\eta)}g = 2\,\mathrm{sym}\big(\bar{g}(\mathrm{T}\xi, \nabla\eta)\big) \tag{5.47}$$

for $(\xi,\eta) \in \mathrm{TImm}(M,N)$.

Proof. A proof can be found in Bauer et al. [27, Section 5.5]. □

Proposition 5.14 (First variation of the volume form)
The mapping

$$\mathrm{vol}\colon \mathrm{Imm}(M,N) \to \Gamma(\mathrm{T}^{0,m}M), \quad \xi \mapsto \mathrm{vol}(\xi^*\bar{g}), \tag{5.48}$$

is differentiable with

$$\begin{aligned} \mathrm{D}_{(\xi,\eta)}\mathrm{vol} &= \frac{1}{2}\,\mathrm{tr}\big(g^{-1}\mathrm{D}_{(\xi,\eta)}g\big)\,\mathrm{vol}(g) = \mathrm{tr}^g\big(\bar{g}(\mathrm{T}\xi, \nabla\eta)\big)\,\mathrm{vol}(g) \\ &= \Big(\mathrm{div}(\eta^{\parallel}) - \bar{g}(\mathrm{tr}^g(\vec{h}), \eta^{\perp})\Big)\,\mathrm{vol}(g) \end{aligned} \tag{5.49}$$

for $(\xi,\eta) \in \mathrm{TImm}(M,N)$.

Proof. See Bauer et al. [27, Section 5.7] for a proof. □

Proposition 5.15 (First variation of a scalar field)
Let $f\colon N \to \mathbb{R}$ *with* $f|_\Omega \in \mathrm{W}^{1,1}(\Omega)$ *for all* $\Omega \in \mathrm{B}(M,N)$. *Then the mapping*

$$\mathrm{Imm}(M,N) \to \mathrm{W}^{1,1}(M), \quad \xi \mapsto (f \circ \xi), \tag{5.50}$$

is well-defined and differentiable with

$$\mathrm{D}_{(\xi,\eta)}(f\circ\xi) = \mathrm{d}f \circ (\xi,\eta) = \bar{g}(\mathrm{grad}\, f \circ \xi, \eta) \in \mathrm{L}^1(M) \tag{5.51}$$

for $(\xi,\eta) \in \mathrm{TImm}(M,N)$.

Proof. A proof is given in Murat and Simon [188, Theorem 4.2, pp. IV-24–IV-25] in the setting of perturbations of identity. □

In many applications, the shape functional is given by the integral of a function on the ambient space restricted to the shape.

Corollary 5.16 (First variation of a shape functional)
Let $f\colon N \to \mathbb{R}$ *with* $f|_\Omega \in \mathrm{W}^{1,1}(\Omega)$ *for all* $\Omega \in \mathrm{B}(M,N)$. *Then the mapping*

$$F\colon \mathrm{Imm}(M,N) \to \mathbb{R}, \quad \xi \mapsto \int_\Omega f\,\mathrm{d}\lambda = \int_M (f\circ\xi)\,\mathrm{vol}(\xi^*\bar{g}), \tag{5.52}$$

is $\mathrm{Diff}(M,N)$*-invariant and differentiable with*

$$\mathrm{d}F(\xi)[\eta] = \int_M \Big(\bar{g}(\mathrm{grad}\, f\circ\xi, \eta) + (f\circ\xi)\,\mathrm{tr}^g\big(\bar{g}(\mathrm{T}\xi, \nabla\eta)\big)\Big)\,\mathrm{vol}(g) \tag{5.53}$$

for $(\xi,\eta) \in \mathrm{TImm}(M,N)$.

Proof. The reparametrization invariance is a standard result in vector calculus. The first variation formula (5.53) follows directly from Proposition 5.14, Proposition 5.15, and an application of the chain and product rule. □

In the case of a bounded open submanifold M of N with Lipschitz boundary, the shape derivative has a particular boundary representation, called the Hadamard form, which can be obtained via the divergence theorem. More generally, the Hadamard structure theorem states that the shape derivative is a distribution on the boundary of the domain that only depends on normal perturbations of the boundary [253, 85].

Theorem 5.17 (Hadamard structure theorem)

Let M be a bounded open submanifold of N with Lipschitz boundary and $F\colon \mathrm{B}(M,N) \to \mathbb{R}$ be the shape functional in (5.52)*, given by the domain integral*

$$F(\Omega) = \int_\Omega f \,\mathrm{d}\lambda \tag{5.54}$$

for some $f\colon N \to \mathbb{R}$ with $f|_\Omega \in \mathrm{W}^{1,1}(\Omega)$ for all $\Omega \in \mathrm{B}(M,N)$. The shape derivative of F at Ω in the direction of $\delta\Omega$ can be expressed as a surface integral

$$\mathrm{d}F(\Omega)[\delta\Omega] = \int_\Omega \operatorname{div}(f\delta\Omega)\,\mathrm{d}\lambda = \int_{\partial\Omega} f\,\bar{g}(n,\delta\Omega)\,\mathrm{d}\sigma, \tag{5.55}$$

where n is the unit outward-pointing normal vector field on $\partial\Omega$. Note that the restriction $f|_{\partial\Omega} \in \mathrm{L}^1(\partial\Omega)$ is well-defined by the trace theorem [20, Theorem 6.3.10].

Proof. We refer to Sokołowski and Zolésio [253, Theorem 2.27] and Delfour and Zolésio [85, Chapter 9, Theorem 3.6]. □

In the following, we derive the sensitivities that are required for the optimization problems discussed in this thesis.

5.4.2 Compliance minimization of thin elastic shells

The shape of a thin elastic shell is determined by an embedding of the reference surface in three-dimensional Euclidean space. Let (B, A, π) be a shell. The set of admissible initial surface configurations $\mathcal{G} \subseteq \operatorname{Emb}(A, \mathbb{E}^3)$ of the shell is a subset of the pre-shape space of embeddings of a certain regularity. The corresponding set of admissible shapes is denoted by $\mathcal{B} = \mathcal{G}/\operatorname{Diff}(A)$ and can be identified with the collection of subsets

$$\mathcal{S} = \big\{\xi(A) \subseteq \mathbb{E}^3 \,\big|\, \xi \in \mathcal{G}\big\}. \tag{5.56}$$

We formulate the compliance minimization problem in terms of the spatial and material picture. The latter is more convenient to work with, since the function spaces involved are defined on a fixed reference domain in our framework.

Formulation in spatial picture

We consider the shape optimization problem (SOP)

$$\begin{aligned} &\min\ b_\Omega(u), && \text{(5.57a)}\\ &\text{s.t. } a_\Omega(u,v) = b_\Omega(v) \quad \forall\, v \in \mathcal{V}(\Omega), && \text{(5.57b)}\\ &\qquad \Omega \in \mathcal{B},\ u \in \mathcal{U}(\Omega), && \text{(5.57c)} \end{aligned}$$

where the fiberwise linear functional $b\colon \mathcal{U} \to \mathbb{R}$ defined by

$$b_\Omega(u) = \int_\Omega (f \cdot u)\,\mathrm{d}\lambda, \quad \Omega \in \mathcal{B},\ u \in \mathcal{U}(\Omega), \tag{5.58}$$

is the compliance corresponding to an external load $f\colon N \to \mathbb{R}^3$ with $f|_\Omega \in \mathrm{H}^1(\Omega, \mathbb{R}^3)$ for all $\Omega \in \mathcal{B}$ and

$$a_\Omega(u,v) = \int_\Omega \big(\sigma_\mathrm{m}(u) : \varepsilon_\mathrm{m}(v) + \sigma_\mathrm{b}(u) : \varepsilon_\mathrm{b}(v)\big)\,\mathrm{d}\lambda, \quad \Omega \in \mathcal{B},\ u \in \mathcal{U}(\Omega),\ v \in \mathcal{V}(\Omega), \tag{5.59}$$

is the fiberwise bilinear form $a\colon \mathcal{U} \times_\Omega \mathcal{V} \to \mathbb{R}$ associated with the linear Koiter shell model in Section 3.2.3. External forces acting on the boundary curve ∂A have been omitted for the sake of simplicity. The objective function $\mathcal{J}\colon \mathcal{U} \to \mathbb{R}$ reads

$$\mathcal{J}(\Omega, u) = b_\Omega(u), \tag{5.60}$$

and the state equation operator $\mathcal{R}\colon \mathcal{U} \to \mathcal{V}^*$ is given by the residuum

$$\langle \mathcal{R}(\Omega, u), v\rangle = b_\Omega(v) - a_\Omega(u,v). \tag{5.61}$$

We choose $\mathcal{U}(\Omega)$ as a closed subspace of

$$\mathfrak{U}(\Omega) = \big\{u \in \mathrm{H}^1(\Omega, \mathbb{R}^3) \,\big|\, \partial_\alpha \partial_\beta u \cdot n \in \mathrm{L}^2(\Omega)\big\} \tag{5.62}$$

consistent with the boundary conditions, and $\mathcal{V}(\Omega)$ as its tangent space.

Formulation in material picture

Pulling back (5.57) to the reference surface $A \subset B$ yields the equivalent problem

$$\min\ \hat{b}_\xi(\hat{u}), \tag{5.63a}$$

$$\text{s.t. } \hat{a}_\xi(\hat{u}, \hat{v}) = \hat{b}_\xi(\hat{v}) \quad \forall\, \hat{v} \in \hat{\mathcal{V}}_\xi, \tag{5.63b}$$

$$\xi \in \mathcal{G},\ \hat{u} \in \hat{\mathcal{U}}_\xi, \tag{5.63c}$$

where the set of admissible shapes $\mathcal{B}$ is replaced by the set of admissible configurations $\mathcal{G}$ (see Section 5.2.1 for the transformation). The associated objective function $\hat{\mathcal{J}}\colon \hat{\mathcal{U}} \to \mathbb{R}$ and state equation operator $\hat{\mathcal{R}}\colon \hat{\mathcal{U}} \to \hat{\mathcal{V}}^*$ are given by

$$\begin{aligned} \hat{\mathcal{J}}(\xi, \hat{u}) = \hat{b}_\xi(\hat{u}) &= \int_A (\hat{f} \cdot \hat{u})\,\mathrm{vol}(g), \\ \langle \hat{\mathcal{R}}(\xi, \hat{u}), \hat{v}\rangle = \hat{b}_\xi(\hat{v}) - \hat{a}_\xi(\hat{u}, \hat{v}) &= \int_A \big((\hat{f} \cdot \hat{v}) - \sigma_\mathrm{m}(\hat{u}) : \varepsilon_\mathrm{m}(\hat{v}) - \sigma_\mathrm{b}(\hat{u}) : \varepsilon_\mathrm{b}(\hat{v})\big)\,\mathrm{vol}(g), \end{aligned} \tag{5.64}$$

where $\Omega = \xi(A)$, $\hat{u} = u \circ \xi$, $\hat{v} = v \circ \xi$, and $\hat{f} = f \circ \xi$. The corresponding state space $\hat{\mathcal{U}}_\xi$ is chosen as a closed subspace of

$$\hat{\mathfrak{U}}_\xi = \big\{\hat{u} \in \mathrm{H}^1(A, \mathbb{R}^3) \,\big|\, \partial_\alpha \partial_\beta \hat{u} \cdot \hat{n} \in \mathrm{L}^2(A)\big\} \tag{5.65}$$

consistent with the boundary conditions and $\hat{\mathcal{V}}_\xi$ denotes its tangent space.

In the following, we derive the sensitivities required for numerical shape optimization.

Shape sensitivity analysis

Under certain conditions, the elastostatic BVP for linear Koiter shells is well-posed (see Section 3.2.3). Let $\hat{u}_*\colon \mathcal{G} \to \hat{\mathcal{U}}$ denote the solution operator to the state equation (5.63b). The reduced cost functional is given by

$$\hat{\mathcal{I}}\colon \mathcal{G} \to \mathbb{R}, \quad \xi \mapsto \hat{\mathcal{J}}(\xi, \hat{u}_*(\xi)). \tag{5.66}$$

According to Section 5.2.4 on the adjoint state method, the derivative of $\hat{\mathcal{I}}$ at $\xi \in \mathcal{G}$ in the direction of $\eta \in \mathrm{T}_\xi\mathcal{G}$ can be obtained using the formula

$$\mathrm{d}\hat{\mathcal{I}}(\xi)[\eta] = \partial_\xi \hat{\mathcal{L}}(\xi, \hat{u}_*(\xi), \hat{v}_*(\xi))[\eta] = \partial_\xi \hat{\mathcal{J}}(\xi, \hat{u}_*(\xi))[\eta] + \langle \partial_\xi \hat{\mathcal{R}}(\xi, \hat{u}_*(\xi))[\eta], \hat{v}_*(\xi)\rangle, \quad (5.67)$$

where $\hat{v}_*(\xi) \in \hat{\mathcal{V}}$ is a solution to the adjoint state equation corresponding to $\hat{u}_*(\xi) \in \hat{\mathcal{U}}$, i.e.,

$$\partial_{\hat{u}} \hat{\mathcal{L}}(\xi, \hat{u}_*(\xi), \hat{v}_*(\xi)) = \partial_{\hat{u}} \hat{\mathcal{J}}(\xi, \hat{u}_*(\xi)) + \langle \partial_{\hat{u}} \hat{\mathcal{R}}(\xi, \hat{u}_*(\xi)), \hat{v}_*(\xi)\rangle = 0. \quad (5.68)$$

It turns out that the compliance minimization problem (5.63) is self-adjoint, since

$$\hat{b}_\xi(\delta\hat{u}) - \hat{a}_\xi(\delta\hat{u}, \hat{v}_*(\xi)) = 0 \quad \forall\, \delta\hat{u} \in \hat{\mathcal{U}} \quad (5.69)$$

follows from (5.68), which implies $\hat{v}_*(\xi) = \hat{u}_*(\xi)$ due to symmetry of the bilinear form $\hat{a}_\xi$ and the characterization of solutions to the state equation (5.63b).

Proposition 5.18

The derivative of the reduced cost functional (5.66) *in material picture is given by*

$$\mathrm{d}\hat{\mathcal{I}}(\xi)[\eta] = \int_A \Big(\big(\mathrm{grad}(f \cdot u) \circ \xi\big) \cdot \eta + \big((f \cdot u) \circ \xi\big) \,\mathrm{tr}^g\big(\bar{g}(\mathrm{T}\xi, \nabla\eta)\big)\Big) \,\mathrm{vol}(g) \quad (5.70)$$

for $(\xi, \eta) \in \mathrm{T}\mathcal{G}$*. In spatial picture, the shape derivative reads*

$$\mathrm{d}\mathcal{I}(\Omega)[\delta\Omega] = \int_\Omega \Big(\mathrm{grad}(f \cdot u) \cdot \delta\Omega + (f \cdot u)\big(\mathrm{div}(\delta\Omega^{\parallel}) - \kappa\, \delta\Omega^{\perp}\big)\Big) \,\mathrm{d}\lambda, \quad (5.71)$$

where $(\Omega, \delta\Omega) \in \mathrm{T}\mathcal{B}$ *and* $\kappa = \kappa_1 + \kappa_2$ *is the sum of principal curvatures of the surface.*

Proof. The claim follows directly from Corollary 5.16. Change of variables along with the alternative form in Proposition 5.14 yields the derivative in spatial picture. □

The formulas in the above proposition require information on the derivative of the external load to compute the gradient

$$\mathrm{grad}(f \cdot u) = (\mathrm{J}f)^{\mathsf{T}} u + (\mathrm{J}u)^{\mathsf{T}} f. \quad (5.72)$$

To circumvent this, one can minimize the linear shell strain energy ψ_{int} in (3.86) instead of the compliance. Solutions to the state equation (5.63b) satisfy

$$\hat{\mathcal{J}}(\xi, \hat{u}_*(\xi)) = \hat{b}_\xi(\hat{u}_*(\xi)) = \hat{a}_\xi(\hat{u}_*(\xi), \hat{u}_*(\xi)) = 2\,\psi_{\mathrm{int}}(\hat{u}_*(\xi)), \quad (5.73)$$

so that both problems are equivalent up to a factor of two and yield the same minimizers.

Proposition 5.19

The derivative of the reduced cost functional (5.66) *has the alternative form*

$$\begin{aligned} \mathrm{d}\hat{\mathcal{I}}(\xi)[\eta] = 2 \int_A \Big(\sigma_{\mathrm{m}}(\hat{u}) : \mathrm{D}_{(\xi,\eta)}\varepsilon_{\mathrm{m}}(\hat{u}) + \sigma_{\mathrm{b}}(\hat{u}) : \mathrm{D}_{(\xi,\eta)}\varepsilon_{\mathrm{b}}(\hat{u})\Big) \,\mathrm{vol}(g) \\ + \int_A \Big(\sigma_{\mathrm{m}}(\hat{u}) : \varepsilon_{\mathrm{m}}(\hat{u}) + \sigma_{\mathrm{b}}(\hat{u}) : \varepsilon_{\mathrm{b}}(\hat{u})\Big) \,\mathrm{tr}^g\big(\bar{g}(\mathrm{T}\xi, \nabla\eta)\big) \,\mathrm{vol}(g) \end{aligned} \quad (5.74)$$

for $(\xi, \eta) \in \mathrm{T}\mathcal{G}$*. The first variation of the membrane strain tensor is given by*

$$\mathrm{D}_{(\xi,\eta)}\varepsilon_{\mathrm{m}}(\hat{u}) = \mathrm{sym}\big(\bar{g}(\nabla\hat{u}, \nabla\eta)\big), \quad (5.75)$$

while the first variation of the bending strain tensor reads

$$\mathrm{D}_{(\xi,\eta)}\varepsilon_{\mathrm{b}}(\hat{u}) = -\bar{g}\big(\mathrm{D}_{(\xi,\eta)}\hat{n}, \nabla^2\hat{u}\big) - \bar{g}\big(\mathrm{D}_{(\xi,\hat{u})}\hat{n}, \nabla^2\eta\big) - \bar{g}\big(\mathrm{D}_{(\xi,\eta)}\mathrm{D}_{(\xi,\hat{u})}\hat{n}, \nabla\mathrm{T}\xi\big). \quad (5.76)$$

Proof. Similar to Proposition 5.18, we can apply Corollary 5.52. To show (5.75) and (5.76), it suffices to recall that the membrane and bending strain tensors are given by

$$\varepsilon_{\mathrm{m}}(\hat{u}) = \operatorname{sym}\big(\bar{g}(\nabla\hat{u}, \mathrm{T}\xi)\big), \tag{5.77a}$$

$$\varepsilon_{\mathrm{b}}(\hat{u}) = -\bar{g}\big(\hat{n}, \nabla^2\hat{u}\big) - \bar{g}\big(\mathrm{D}_{(\xi,\hat{u})}\hat{n}, \nabla\mathrm{T}\xi\big). \tag{5.77b}$$

See the local coordinate expressions (3.87) in Section 3.2.3. □

To impose the fixed area constraint, we add the condition

$$\int_\Omega 1 \,\mathrm{d}\lambda = \int_A \operatorname{vol}(g) = c_0 \tag{5.78}$$

to the problem, where $c_0 > 0$ denotes the initial surface area. The constraint function then reads

$$c(\Omega) = \int_\Omega 1 \,\mathrm{d}\lambda - c_0, \quad \hat{c}(\xi) = \int_A \operatorname{vol}(\xi^*\bar{g}) - c_0 \tag{5.79}$$

in spatial and material picture, respectively. The (shape) derivative of (5.79) is given by

$$\mathrm{d}c(\Omega)[\delta\Omega] = \int_\Omega \big(\operatorname{div}(\delta\Omega^{\parallel}) - \kappa\,\delta\Omega^{\perp}\big)\,\mathrm{d}\lambda, \tag{5.80a}$$

$$\mathrm{d}\hat{c}(\xi)[\eta] = \int_A \operatorname{tr}^g\big(\bar{g}(\mathrm{T}\xi, \nabla\eta)\big)\operatorname{vol}(g). \tag{5.80b}$$

This follows directly from Corollary 5.16 and the alternative form in Proposition 5.14.

5.4.3 Parameter identification from observed data

In this section, we describe a method to identify parameters of the plate model for Earth's lithosphere in Section 3.3 that are most plausible to explain the observed depths for the Mohorovičić surface. The quantities we are interested in are the effective elastic thickness, the reference density, and the topographic load that acts on the lithosphere. To determine the spatial distribution of those quantities, we perform PDE constrained optimization with a tracking-type objective function, e.g., a quadratic loss function. This corresponds to a so-called indirect inversion method, where the forward problem is solved iteratively until an adequate choice of parameter is found. Another method involves the direct inversion of spectral measures. See Kirby [155] for more information on that subject.

Tracking-type optimization problem

A common tracking-type objective function is given by the integrated squared error

$$\mathcal{J}(q, w) = \frac{1}{2}\int_A (w - w_{\mathrm{d}})^2 \,\mathrm{dA}, \tag{5.81}$$

which corresponds to the method of least squares and gauges the deviation of w from the observed data w_{d}. The state equation of the isostatic problem in weak formulation reads

$$\langle \mathcal{R}(q, w), z\rangle = c_r(z) - a_q(w, z) - b_p(w, z) = 0 \tag{5.82}$$

for all variations z, where the bilinear forms and linear functional are given by

$$\begin{aligned} a_q(w, z) &= \int_A q\,(\nu\Delta w\Delta z + (1-\nu)\nabla^2 w : \nabla^2 z)\,\mathrm{dA}, \\ b_p(w, z) &= \int_A pwz\,\mathrm{dA}, \quad c_r(z) = -\int_A rz\,\mathrm{dA}, \end{aligned} \tag{5.83}$$

with the flexural parameter q, the crustal depth-to-height ratio p, and the rock-equivalent topography r given by

$$q = \frac{D}{\varrho_{\mathrm{r}} g} = \frac{Et^3}{12(1-\nu^2)\varrho_{\mathrm{r}} g}, \quad p = \frac{\varrho_{\mathrm{m}} - \varrho_{\mathrm{r}}}{\varrho_{\mathrm{r}}}, \quad r = \frac{1}{\varrho_{\mathrm{r}}} \int_{d_0}^{h} \varrho \, \mathrm{d}z, \tag{5.84}$$

respectively. To ensure that the parameters are feasible from a physical point of view, we impose a minimum value on them using box constraints in the optimization process.

Adjoint sensitivity analysis

The adjoint state equation for the isostatic BVP with the integrated squared error (5.81) as objective function reads

$$a_q(\delta w, z) + b_p(\delta w, z) = \int_A (w - w_{\mathrm{d}}) \, \delta w \, \mathrm{dA} \tag{5.85}$$

for all variations δw. Given a solution z to the adjoint state equation (5.85) corresponding to the flexural parameter q as design variable and the state w, the derivative of the reduced cost functional at q in the direction of δq can be computed via

$$\mathrm{d}\mathcal{I}(q)[\delta q] = -a_{\delta q}(w, z). \tag{5.86}$$

Similarly, we have for the other parameters p and r that

$$\mathrm{d}\mathcal{I}(p)[\delta p] = -b_{\delta p}(w, z), \tag{5.87a}$$
$$\mathrm{d}\mathcal{I}(r)[\delta r] = c_{\delta r}(z), \tag{5.87b}$$

where the adjoint state equation (5.85) remains the same. The first-order sensitivities can be used for gradient-based optimization. Since this is a standard optimization problem with PDE constraints, we can apply the usual methods for numerical optimization without taking account of the considerations made for shape spaces.

6 Isogeometric finite element analysis

The finite element method (FEM) has been widely used to approximate solutions to PDEs numerically. In standard FEM, the computational domain is subdivided into parts that are images of elementary geometric shapes, called finite elements, on which a number of shape functions are defined. Usually, the shape functions are polynomial functions determined by interpolation conditions on some reference element. Joining together all the elements along with the shape functions yields a finite element space in which a numerical solution to the problem is sought. It is constructed by finding a linear combination of the shape functions on each element that best approximates the exact solution [57, 55, 288].

Globally C^1 finite element spaces are necessary for a conforming discretization of higher-order problems, such as the shell and plate problems considered in this work. In general, the construction of such spaces is computationally expensive and requires a lot of degrees of freedom per element. This has led to various methods for solving the shell and plate equations more efficiently. An example is the non-conforming mixed formulation given by the classical discrete Kirchhoff triangular (DKT) elements [26], where the C^1 condition is imposed only at the nodes of the mesh. Other examples include the use of rotation-free (RF) elements [204], discontinuous Galerkin (DG) methods [97], assumed natural deviatoric strain (ANDES) elements [186], and the Hellan–Herrmann–Johnson (HHJ) method [194]. Another way to address the problem is to apply isogeometric finite element methods. See Kiendl et al. [153], Apostolatos et al. [16], Goyal and Simeon [112], Verhelst et al. [266].

Isogeometric analysis (IGA) is a computational paradigm for solving PDEs that employs the same shape functions used to describe the domain of the problem to construct finite element approximations of solutions to the problem. It allows the integration of finite element analysis (FEA) with technologies from computer-aided design (CAD). The concept of isogeometric analysis has first been presented in the seminal work by Hughes et al. [138] in 2005. Standard references on the subject include Cottrell et al. [79], Buffa and Sangalli [60], Lyche et al. [170], Jüttler and Simeon [145], and van Brummelen et al. [263].

This section introduces the notions required for the numerical discretization of elliptic boundary value problems using isogeometric analysis. We begin with the definition of B-splines and NURBS. A more elaborate treatment of NURBS with numerical algorithms is available in Rogers [216], Cohen et al. [72], de Boor [81], Schneider [230], and the NURBS book by Piegl and Tiller [207].

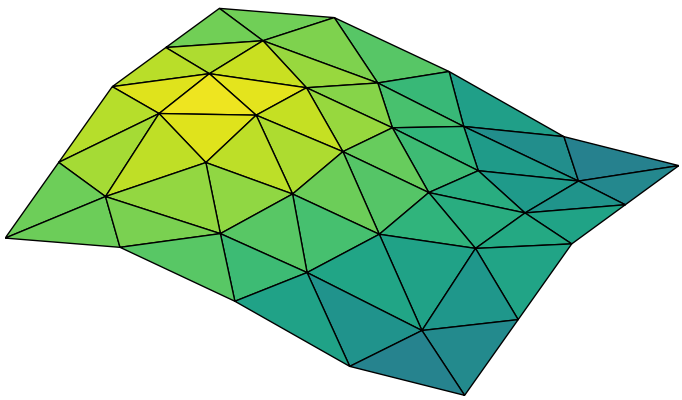

Figure 13: Finite element discretization of a surface.

6.1 B-spline and NURBS functions

Let $\vartheta_0 \leq \cdots \leq \vartheta_m$ be a finite sequence of non-decreasing real numbers. A spline of degree p is a piecewise polynomial function $f\colon [\vartheta_0, \vartheta_m] \to \mathbb{R}$ with the property that the restriction to each subinterval $[\vartheta_{i-1}, \vartheta_i)$ for $i = 1, \ldots, m$ is a polynomial function of maximum degree p. The tuple $\Theta = (\vartheta_0, \ldots, \vartheta_m)$ is called a knot sequence for the spline with knot values ϑ_i and the term "breakpoint" is used to refer to a distinct knot value. The half-open interval $[\vartheta_{i-1}, \vartheta_i)$ is called the i-th knot span, which can be empty.

The maximum order of continuity that a spline of degree p can attain at the breakpoints is $p - 1$. We refer to such splines as smooth splines. A lower order of continuity can be obtained by placing multiple knots in the same location. Each additional knot reduces the order of continuity by one until the resulting spline is discontinuous at the breakpoint.

The type of a spline is completely characterized by its degree and the knot sequence. Let $\mathcal{S}(\Theta, p)$ denote the space of splines of degree p with knot sequence Θ. It is a vector space of dimension $m - p$. By introducing the numbers $\widetilde{m} = m + 1$, $\widetilde{p} = p + 1$, and $\widetilde{n} = n + 1$, where $\widetilde{m}$ is the number of knots, $\widetilde{p}$ is the order of the spline, and $\widetilde{n}$ is the dimension of $\mathcal{S}(\Theta, p)$, we can write $\widetilde{n} = \widetilde{m} - \widetilde{p}$ or, equivalently, $m = n + p + 1$.

In the following, we consider splines on the unit interval $[0, 1]$ with an open knot sequence, i.e., the first and last knot values have multiplicity $p + 1$, to enable interpolatory control points at the boundary. Then the knot sequence has the form

$$\Theta = (\underbrace{0, \ldots, 0}_{(p+1)\text{-times}}, \vartheta_{p+1}, \ldots, \vartheta_n, \underbrace{1, \ldots, 1}_{(p+1)\text{-times}}) \tag{6.1}$$

with the knot values $\vartheta_0 = \cdots = \vartheta_p = 0$, $\vartheta_{n+1} = \cdots = \vartheta_{n+p+1} = 1$, and $\vartheta_i \in (0, 1)$ for $i = p + 1, \ldots, n$.

6.1.1 B-spline basis functions

A particular basis for the spline space $\mathcal{S}(\Theta, p)$ is given by the B-splines (basis splines). They have minimal support and allow for quick evaluation of the splines using de Boor's algorithm, which is convenient for isogeometric analysis. The B-splines of degree p are recursively defined via the Cox–de Boor formula

$$B_{k,p}(\vartheta) = \frac{\vartheta - \vartheta_k}{\vartheta_{k+p} - \vartheta_k} B_{k,p-1}(\vartheta) + \frac{\vartheta_{k+1+p} - \vartheta}{\vartheta_{k+1+p} - \vartheta_{k+1}} B_{k+1,p-1}(\vartheta) \tag{6.2}$$

with $\vartheta \in [0, 1]$, $k = 0, \ldots, n$, and

$$B_{k,0}(\vartheta) = \begin{cases} 1 & \text{for } \vartheta \in [\vartheta_k, \vartheta_{k+1}), \\ 0 & \text{otherwise,} \end{cases} \tag{6.3}$$

for $k = 0, \ldots, n + p$, where the convention $0/0 = 0$ is used if the knot values in the denominator coincide. We refer to $B_{k,p}$ as the k-th B-spline basis function of degree p.

Given a finite sequence of control points $c_0, \ldots, c_n \in \mathbb{R}^r$ in the physical space of dimension r, we can construct a B-spline curve of degree p through a linear combination of the form

$$\gamma\colon [0, 1] \to \mathbb{R}^r, \quad \gamma(\vartheta) = \sum_{k=0}^{n} c_k B_{k,p}(\vartheta). \tag{6.4}$$

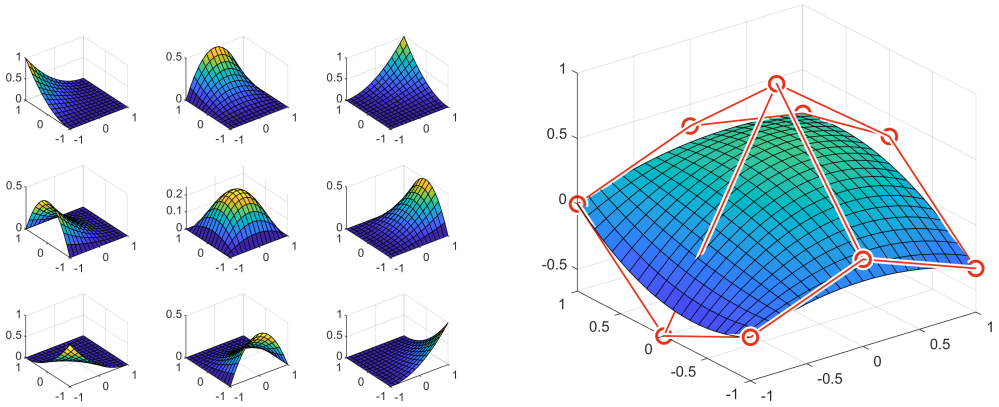

Figure 14: Left: Isogeometric shape functions on a bivariate quadratic B-spline patch. Right: A linear combination of the isogeometric shape functions and corresponding mesh of control points (red).

B-spline curves are commonly used to represent shapes in computer-aided design (CAD). The description using control points allows for intuitive local manipulation of free-form shapes. In isogeometric analysis, the control points additionally serve as degrees of freedom for the unknowns in a discretized system of equations.

If the domain of the problem is two- or three-dimensional, B-spline surfaces or volumes are used to describe its geometry. Multivariate spline spaces are constructed via the tensor product of univariate spline spaces. Instead of a single knot sequence and a single spline degree, we have a family of knot sequences $\Theta = (\Theta^{(1)}, \dots, \Theta^{(d)})$ along with a tuple of spline degrees $p = (p_1, \dots, p_d)$ corresponding to each parametric dimension. The B-spline basis functions of the spline space $\mathcal{S}_d(\Theta, p) = \mathcal{S}(\Theta^{(1)}, p_1) \otimes \cdots \otimes \mathcal{S}(\Theta^{(d)}, p_d)$ are given by

$$B_{k,p}(\vartheta) = B^{(1)}_{k_1,p_1}(\vartheta^1) \cdots B^{(d)}_{k_d,p_d}(\vartheta^d) \tag{6.5}$$

for $\vartheta = (\vartheta^1, \dots, \vartheta^d) \in [0,1]^d$ in the multivariate setting. The B-splines $B^{(j)}_{0,p_j}, \dots, B^{(j)}_{n_j,p_j}$ form a basis for $\mathcal{S}(\Theta^{(j)}, p_j)$ and $k = (k_1, \dots, k_d)$ is a multi-index with $k_j = 0, \dots, n_j$ for $j = 1, \dots, d$. We order the basis functions lexicographically, so that $B_{k,p}$ corresponds to the k-th basis function when using an integer index $k = 0, \dots, n$ instead of a multi-index.

A d-variate B-spline patch corresponding to the control points $c_0, \dots, c_n \in \mathbb{R}^r$ refers to a parametrization of the form

$$\gamma\colon [0,1]^d \to \mathbb{R}^r, \quad \gamma(\vartheta) = \sum_{k=0}^{n} c_k B_{k,p}(\vartheta). \tag{6.6}$$

We refer to the image of γ also as a B-spline patch and write $\mathcal{S}_{d,r}(\Theta, p)$ for the space of d-variate B-spline patches in $\mathbb{R}^r$.

6.1.2 NURBS basis functions

B-splines can be generalized to include rational functions in addition to polynomial ones by assigning a weight to each control point. This greatly increases the design capabilities of free-form shapes, e.g., conic sections can be exactly represented by rational B-splines with weighted control points as opposed to non-rational ones. The term “non-uniform”

in the acronym NURBS stresses the fact that the distribution of knot values in the knot sequence is not necessarily uniform.

Given a B-spline basis $B_{0,p}, \dots, B_{n,p}$ for the spline space $\mathcal{S}(\Theta, p)$ and a tuple of positive weights $\omega = (\omega_0, \dots, \omega_n)$, the NURBS space $\mathcal{S}^\omega(\Theta, p)$ is generated by rational functions of the form

$$N^\omega_{k,p}(\vartheta) = \frac{\omega_k B_{k,p}(\vartheta)}{\omega(\vartheta)}, \quad k = 0, \dots, n, \tag{6.7}$$

with $\vartheta \in [0, 1]$. The weight function in the denominator is a weighted sum of the B-spline basis functions

$$\omega(\vartheta) = \sum_{k=0}^{n} \omega_k B_{k,p}(\vartheta). \tag{6.8}$$

Note that the original spline space is a particular case of the NURBS space with constant weights. For the multivariate case, we proceed similarly to the non-rational B-splines and define the NURBS basis functions as

$$N^\omega_{k,p}(\vartheta) = \frac{\prod_{j=1}^{d} \omega^{(j)}_{k_j} B^{(j)}_{k_j,p_j}(\vartheta^j)}{\omega(\vartheta)}, \quad k = 0, \dots, n, \tag{6.9}$$

for $\vartheta = (\vartheta^1, \dots, \vartheta^d) \in [0, 1]^d$. The multivariate weight function reads

$$\omega(\vartheta) = \sum_{k_1=0}^{n_1} \cdots \sum_{k_d=0}^{n_d} \omega^{(1)}_{k_1} B^{(1)}_{k_1,p_1}(\vartheta^1) \cdots \omega^{(d)}_{k_d} B^{(d)}_{k_d,p_d}(\vartheta^d), \tag{6.10}$$

where $\omega = (\omega^{(1)}, \dots, \omega^{(d)})$ is a family of weight tuples corresponding to each parametric dimension. Contrary to the non-rational B-splines, the resulting multivariate NURBS space $\mathcal{S}^\omega_d(\Theta, p)$ is no longer a tensor product space because of the weight function ω. Nevertheless, it is called tensor-product-like, following the terminology in isogeometric analysis.

A d-variate NURBS patch corresponding to the control points $c_0, \dots, c_n \in \mathbb{R}^r$ refers to a parametrization of the form

$$\gamma \colon [0, 1]^d \to \mathbb{R}^r, \quad \gamma(\vartheta) = \sum_{k=0}^{n} c_k N^\omega_{k,p}(\vartheta). \tag{6.11}$$

We refer to the image of γ also as a NURBS patch and write $\mathcal{S}^\omega_{d,r}(\Theta, p)$ for the space of d-variate NURBS patches in $\mathbb{R}^r$.

To shorten the notation, we omit the superscript ω and the subscript p from the NURBS basis functions and introduce the double index $\alpha = (k, l)$, ranging from $(0, 1)$ to (n, r), so that a NURBS patch can be written as

$$\gamma = \sum_{k=0}^{n} \sum_{l=1}^{r} c_{k,l} N_k e_l = \sum_{k=0}^{n} \sum_{l=1}^{r} c_{k,l} N_{k,l} = \sum_{\alpha \in \mathcal{A}} c_\alpha N_\alpha, \tag{6.12}$$

where $\mathcal{A} = \big\{(k, l) \in \mathbb{N}_0^2 \mid 0 \le k \le n, 1 \le l \le r\big\}$ is the index set with $(n + 1) \cdot r$ elements, $c_\alpha = c_{k,l}$ denotes the l-th component of the k-th control point, and $N_\alpha = N_{k,l} = N_k e_l$ is the α-th vector-valued NURBS basis function.

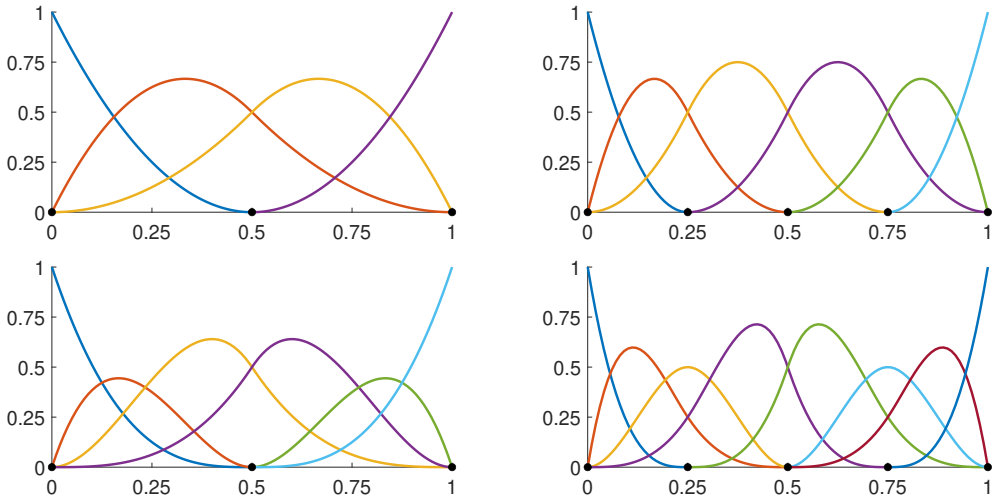

Figure 15: Initial isogeometric shape functions given by quadratic B-splines (top-left) and the shape functions that result from h-refinement (top-right), p-refinement (bottom-left), and k-refinement (bottom-right).

6.1.3 Refinement methods

In order to get better approximation results for the numerical solutions, the NURBS space used for the discretization of the problem has to be refined. There are two refinement methods that increase the number of shape functions and preserve the global smoothness of the NURBS space. The first method is called knot insertion (also known as h-refinement), where a finer NURBS space is constructed by adding new breakpoints to the knot sequence. The second one is order elevation (p-refinement), which raises the order of the NURBS space without changing the knot spans. Performing order elevation followed by knot insertion results in a so-called k-refinement. See Figure 15 for an illustration of the methods.

For the multivariate case, inserting a breakpoint to a knot sequence will affect all elements along the transverse direction due to the tensor-product-like structure. To enable local refinement, several methods can be considered. In our work, we employ hierarchical B-splines as described in Vuong et al. [267]. Adaptive local refinement can then be performed if an error estimator for the numerical solution to the problem is available [107, 61].

6.2 Finite element discretization

Given a weak formulation of the variational problem, a numerical solution can be obtained by considering a projection onto some finite-dimensional subspace of the solution space. This is generally referred to as a Galerkin projection. Finite element methods are based on subdividing the domain of the problem into finitely many elements on which a number of shape functions are defined. The finite element space is then constructed from linear combinations of the shape functions on each element, which satisfy certain interpolation conditions.

Isoparametric finite elements enable the solution of problems on domains with curved boundaries by using the same shape functions for the numerical approximation of solutions to describe the geometry of the domain. They serve as a basis for the isogeometric paradigm, where we consider domains that can be represented by some NURBS geometry and use refinements of the corresponding NURBS space to construct approximations of solutions to

the problem.

An isogeometric mesh consists of NURBS patches, each of which can be refined to increase the accuracy of the numerical approximation. As opposed to a standard finite element mesh, the smoothness of shape functions within each patch can be preserved without much effort when the mesh is subdivided into smaller elements. This greatly reduces the number of degrees of freedom compared to classical C^1 finite elements, which is useful when working with shell and plate equations that require global C^1 continuity.

We first consider domains that can be exactly represented by a single NURBS patch. The main idea is to transform the problem posed on the patch to a fixed parameter domain, approximate the solution with a linear combination of NURBS functions that result from refinements of the NURBS space associated with the geometry function, and transform the numerical solution back to the physical domain.

6.2.1 Domain transformation

Let $\Omega \subset \mathbb{R}^r$ denote the physical domain described by the geometry function

$$\gamma\colon \hat{\Omega} \to \Omega, \quad \gamma(\vartheta) = \sum_{k=0}^{n} \sum_{l=1}^{r} \gamma_{k,l} N_{k,l}(\vartheta), \tag{6.13}$$

with control points $\gamma_0, \dots, \gamma_n \in \mathbb{R}^r$ and the parameter domain $\hat{\Omega} = [0,1]^d$. To ensure that the domain is suitable for isogeometric analysis, we require that the geometry function is at least a bi-Lipschitz transformation. Thus, it is important to impose conditions on the control points of the geometry such that this requirement is fulfilled.

The weak formulation of a variational problem posed on the physical domain can be transformed to the parameter domain by pulling back functions in the solution space $\mathcal{V}(\Omega)$ to the parameter domain using the geometry function. By doing so, we obtain an equivalent weak formulation of the problem on the parameter domain: Find $\hat{u} \in \hat{\mathcal{V}}(\hat{\Omega})$ such that $\hat{a}(\hat{u}, \hat{v}) = \hat{b}(\hat{v})$ for all $\hat{v} \in \hat{\mathcal{V}}(\hat{\Omega})$ with $\hat{\mathcal{V}}(\hat{\Omega}) = \{v \circ \gamma_0 \mid v \in \mathcal{V}(\Omega)\}$ and

$$\hat{a}(\hat{u}, \hat{v}) = a(\hat{u} \circ \gamma_0^{-1}, \hat{v} \circ \gamma_0^{-1}), \quad \hat{b}(\hat{v}) = b(\hat{v} \circ \gamma_0^{-1}). \tag{6.14}$$

6.2.2 Ritz–Galerkin method

To discretize the transformed weak formulation, we consider isogeometric shape functions that result from refinements of the NURBS space associated with the geometry function. We choose $\hat{\mathcal{V}}_{h,p} = \mathcal{S}^{\omega}_{d,s}(\Theta_h, p) \cap \hat{\mathcal{V}}(\hat{\Omega})$ for the finite-dimensional subspace, where h is a discretization parameter corresponding to the diameter of elements and s is the number of components of functions in the solution space. Galerkin projection then yields a family of finite-dimensional problems of the form: Find $\hat{u}_{h,p} \in \hat{\mathcal{V}}_{h,p}$ such that $\hat{a}(\hat{u}_{h,p}, \hat{v}_{h,p}) = \hat{b}(\hat{v}_{h,p})$ for all $\hat{v}_{h,p} \in \hat{\mathcal{V}}_{h,p}$.

The trial and test functions are given by linear combinations of the basis functions, i.e.,

$$\hat{u}_{h,p} = \sum_{k=0}^{n} \sum_{l=1}^{s} u_{k,l} N_{k,l}, \quad \hat{v}_{h,p} = \sum_{k=0}^{n} \sum_{l=1}^{s} v_{k,l} N_{k,l}, \tag{6.15}$$

with control points $u_0, \dots, u_n \in \mathbb{R}^s$ and $v_0, \dots, v_n \in \mathbb{R}^s$, respectively. The coordinates of the control points are organized in a single column vector so that the Galerkin equation can be written in matrix-vector form. The problem then reduces to solving a system of

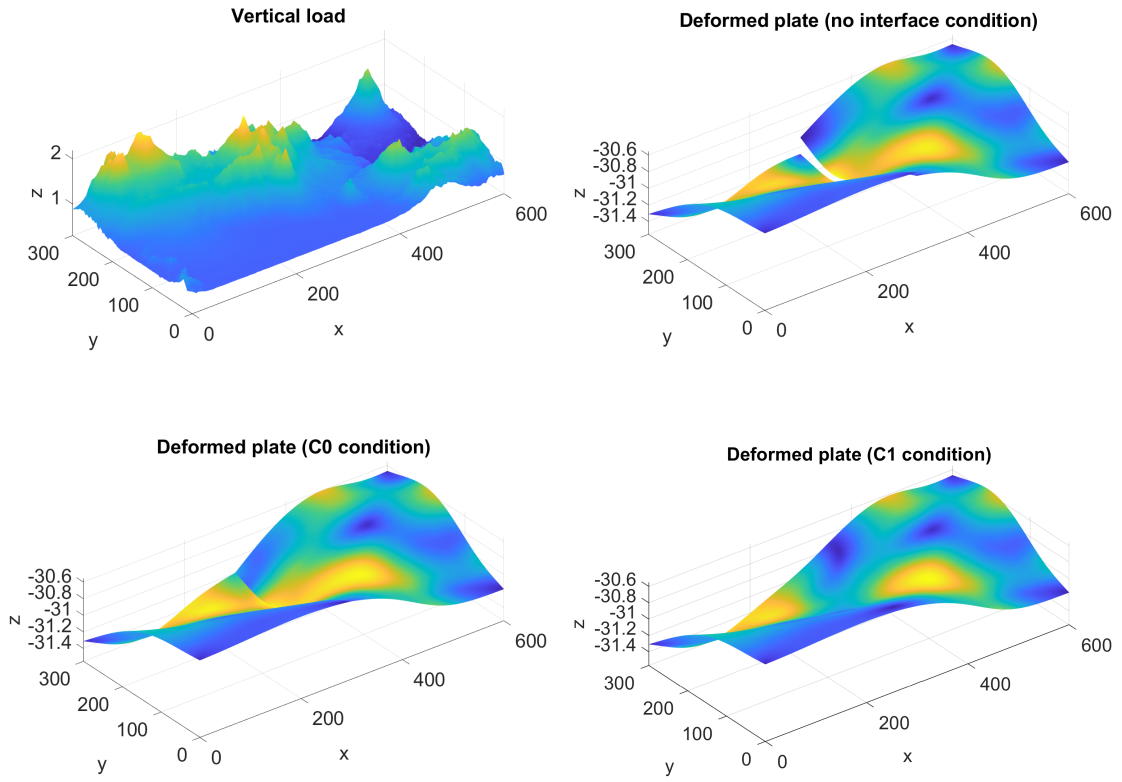

Figure 16: Coupling of two rectangular lithospheric plates in isostatic equilibrium.

linear equations of the form $A^\intercal u = b$ with the coefficient matrix $A_{\alpha\beta} = \hat{a}(N_\alpha, N_\beta)$ and the right-hand side $b_\beta = \hat{b}(N_\beta)$, where α and β are double indices in some specified order, ranging from $(0, 1)$ to (n, s). Numerical integration using Gaussian quadrature is used to compute the entries of A and b when exact expressions are not available.

The solution vector $u \in \mathbb{R}^{(n+1)s}$ contains the coordinates of the control points associated with the trial function $\hat{u}_{h,p}$ and is referred to as the vector of degrees of freedom in the fully unconstrained solution space. When boundary or interface conditions are present, it is restricted to a subspace fulfilling those conditions.

6.3 Multi-patch C^1 coupling

In the case where the domain consists of multiple NURBS patches, the subproblems on each patch have to be coupled in a way that retains the global C^1 continuity of solutions. There are various methods that can be employed to achieve this in the context of isogeometric analysis of plates and shells. Penalty methods [154, 76, 77], Nitsche methods [17, 197, 117], and mortar methods [92, 51, 135] fall into the category of weak coupling methods that use a modified variational formulation to establish the C^1 continuity weakly across multiple patches. Strong coupling methods, on the other hand, are based on the construction of globally C^1 shape functions, which are then used for a C^1 conforming discretization of the variational formulation.

Multi-patch C^1 isogeometric spline spaces can be constructed by replacing shape functions that influence the derivative of solutions at patch interfaces with C^1 shape functions that

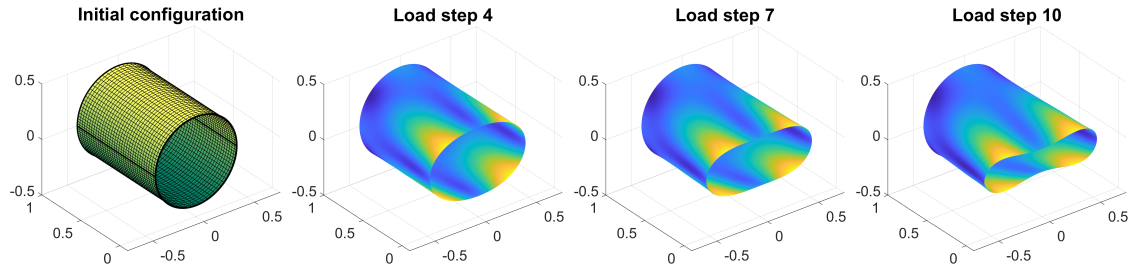

Figure 17: Numerical simulation of a two-patch cylindrical shell with 10 load steps.

span over multiple patches (see Kapl et al. [148, 149]). This has been extended from the case of planar multi-patch domains to multi-patch surfaces in Farahat et al. [101, 102]. Another approach to stitch shape functions at patch interfaces together is to impose the C^1 condition at some collocation points [64] or weakly via the constraint matrix

$$C_{\alpha\beta} = \int_\Gamma [\![n \cdot \nabla N_\alpha]\!] [\![n \cdot \nabla N_\beta]\!] \, \mathrm{dS}, \tag{6.16}$$

where n is a unit normal at the patch interface Γ and $[\![\cdot]\!]$ denotes the jump of a function between the patches [73]. The latter yields an approximately C^1 isogeometric spline space on a multi-patch geometry [276] and has been used for the numerical experiments in this work. The method is straightforward to implement but has the drawback that the resulting system of linear equations will lose its sparse structure if the basis functions for the null space of the constraint matrix C are not carefully chosen to be locally supported. Note that contiguous patches are assumed to share the same interpolatory control points at the interfaces to enforce the C^0 continuity in our implementation.

An example is given in Figure 16 to demonstrate the multi-patch coupling method in the case of the isostatic boundary value problem for the plate model of Earth's lithosphere (see Section 3.3). For multi-patch surfaces, we simulate the pinching of a two-patch cylindrical shell in Figure 17 using the Koiter shell model in Section 3.2.3 with multiple load steps.

The construction of multi-patch C^1 isogeometric spline spaces with optimal approximation properties is a challenging problem for more complex geometries. A so-called C^1 locking might occur for G^1 multi-patch parametrizations that are not analysis-suitable [73].

6.4 Isogeometric shape optimization

A common procedure in isogeometric shape optimization is to use a NURBS description of the geometry and consider a subset of control point coordinates as design variables. This corresponds to the FDTO approach and has been conventionally used in a wide range of applications, e.g., Wall et al. [269], Nguyen et al. [196], Bletzinger et al. [45], López et al. [171], and Weeger [275]. The use of B-splines for optimal shape design in this manner dates back to Braibant and Fleury [56]. While it is a fairly straightforward way to perform shape optimization in the context of isogeometric finite element analysis, the results will typically depend on the particular representation of the geometry, since the problem is reduced to a finite-dimensional one that often disregards the inherent geometric structure of shapes. On the other hand, the FOTD approach attempts to provide approximations of solutions to some underlying infinite-dimensional problem. It has been discussed in, e.g., Blanchard et al. [42], Azegami et al. [23], Fußeder et al. [105], Rosandi and Simeon [221], for isogeometric shape optimization.

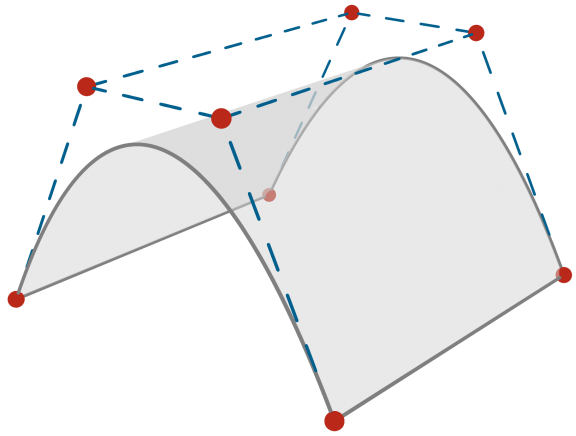

Figure 18: NURBS representation of the geometry of a surface.

Methods based on spline or more general representations of geometry from computer-aided design rely on control point coordinates or other design parameters to generate an explicit parametrization of the shape. The advantage of such an approach is that the number of design variables required to resolve the problem to sufficient accuracy is usually much smaller than the number of nodal variables required for the same accuracy in node-based shape optimization. However, it suffers from the same deficiency as other FDTO approaches if the design parameters are treated independently of each other. Another critical issue is that the parametrization generated for the geometry may become degenerate, e.g., non-injective, during the optimization process. These are difficulties that need to be resolved when devising a robust shape optimization method. Some efforts in mesh parametrization have been made for isogeometric finite element analysis [241, 240] and isogeometric shape optimization [166].

6.4.1 Shape optimization loop

Starting from an initial design $\Omega_0 \in \mathcal{B}$, a general gradient-based PDE constrained shape optimization loop using the adjoint state method consists of the following steps:

1) Solve the state equation
$$\mathcal{R}(\Omega_k, u_k) = 0 \tag{6.17}$$
for the state variable $u_k \in \mathcal{U}(\Omega_k)$.

2) Solve the adjoint state equation
$$\partial_u \mathcal{J}(\Omega_k, u_k) + \langle \partial_u \mathcal{R}(\Omega_k, u_k), v_k \rangle = 0 \tag{6.18}$$
for the adjoint state variable $v_k \in \mathcal{V}(\Omega_k)$.

3) Use the shape derivative
$$\mathrm{d}\mathcal{I}(\Omega_k) = \partial_\Omega \mathcal{J}(\Omega_k, u_k) + \langle \partial_\Omega \mathcal{R}(\Omega_k, u_k), v_k \rangle \tag{6.19}$$
to compute the shape gradient $\operatorname{grad} \mathcal{I}(\Omega_k) \in \mathrm{T}_{\Omega_k}\mathcal{B}$ according to
$$G_{\Omega_k}(\operatorname{grad} \mathcal{I}(\Omega_k), \delta\Omega_k) = \mathrm{d}\mathcal{I}(\Omega_k)[\delta\Omega_k] \quad \forall\, \delta\Omega_k \in \mathrm{T}_{\Omega_k}\mathcal{B}, \tag{6.20}$$
where G is a chosen Riemannian metric on $\mathcal{B}$.

4) Compute the next design $\Omega_{k+1} \in \mathcal{B}$ using information on the shape gradient at Ω_k.

The loop results in a sequence of design iterates $(\Omega_k)_{k\in\mathbb{N}_0}$ in $\mathcal{B}$ and can be executed until a stopping condition is fulfilled, e.g., according to the criterion in Section 5.3.1.

The shape gradient in the FOTD approach is independent of the choice of configuration in the pre-shape space $\mathcal{G}$ if the Riemannian metric is reparametrization invariant. This allows for remeshing as long as the shape $\Omega \in \mathcal{B}$ remains the same, i.e., $\gamma \in \mathcal{G}$ with $\Omega = \gamma(\hat{\Omega})$.

In isogeometric shape optimization, we choose a finite-dimensional NURBS representation of the design and state variables to compute numerical approximations of solutions using Galerkin methods. Let $\gamma_h \in \mathcal{G}_h = \mathcal{S}^{\omega}_{d,r}(\Theta_h, p) \cap \mathcal{G}$ be the geometry function in the current step and

$$\hat{\mathcal{U}}_h = \mathcal{S}^{\omega_u}_{d,s_u}(\Theta_{h_u}, p_u) \cap \hat{\mathcal{U}}(\hat{\Omega}), \quad \hat{\mathcal{V}}_h = \mathcal{V}^{\omega_v}_{d,s_v}(\Theta_{h_v}, p_v) \cap \hat{\mathcal{V}}(\hat{\Omega}) \tag{6.21}$$

be refinements of the NURBS space $\mathcal{S}^{\omega}_d(\Theta_h, p)$ compatible with the original function spaces. Here, we omit the dependence of the discretization parameters on the particular refinements and simply use the subscript h to denote discrete quantities. For state equation operators of the form

$$\langle \mathcal{R}(\Omega, u), v\rangle = b_\Omega(v) - a_\Omega(u, v), \quad u \in \mathcal{U}(\Omega),\ v \in \mathcal{V}(\Omega), \tag{6.22}$$

where $a_\Omega \colon \mathcal{U}(\Omega) \times \mathcal{V}(\Omega) \to \mathbb{R}$ is a bilinear form and $b_\Omega \colon \mathcal{V}(\Omega) \to \mathbb{R}$ is a linear functional, we pull back the problem to the parameter domain $\hat{\Omega}$ akin to (6.14) and set up the Galerkin equation

$$\hat{a}_{\gamma_h}(\hat{u}_h, \hat{v}_h) = \hat{b}_{\gamma_h}(\hat{v}_h) \quad \forall\, \hat{v} \in \hat{\mathcal{V}}_h \tag{6.23}$$

to solve for the state variable $\hat{u} \in \hat{\mathcal{U}}_h$. We proceed similarly for the adjoint state equation.

After the first two steps of the optimization loop, we can use the numerical approximations of the state and adjoint state variable to compute the shape derivatives $\mathrm{d}\hat{\mathcal{I}}(N_\beta)$ for each shape function N_β in $\mathcal{S}^{\omega}_{d,r}(\Theta_h, p)$. The shape differential calculus developed in Section 5.4 is used to derive an analytical expression for the shape derivative, which is then approximated using numerical integration. The discrete shape gradient is obtained from the sensitivities by solving another Galerkin equation

$$\hat{G}_{\gamma_h}(\operatorname{grad}\hat{\mathcal{I}}_h(\gamma_h), N_\beta) = \mathrm{d}\hat{\mathcal{I}}(\gamma_h)[N_\beta] \quad \forall\, N_\beta \in \mathcal{S}^{\omega}_{d,r}(\Theta_h, p). \tag{6.24}$$

It describes a vector field over γ_h and—depending on the regularity of the model space for $\mathcal{G}$—can be seen as an element of $\mathcal{H}_h = \mathcal{S}^{\omega}_{d,r}(\Theta_h, p) \cap \mathrm{T}_{\gamma_h}\mathcal{G}$.

In the case of a shape space of hyper-surfaces endowed with a Sobolev-type Riemannian metric, the horizontal shape gradient is a solution to an elliptic PDE of the form

$$P\operatorname{grad}\hat{\mathcal{I}}(\gamma) = an, \tag{6.25}$$

where P is an elliptic pseudo-differential operator explained in Section 4.4.2, a is a scalar field corresponding to the momentum of the system, and n is a unit normal vector field over γ. Instead of solving for the shape gradient, we can solve for the scalar field a, which is a relevant quantity that appears in the geodesic equation. In the end, a solution to the elliptic PDE is still required for numerical time integration of the geodesic equation.

To compute a numerical approximation of the scalar momentum, one can either use the characterization

$$\begin{aligned} \hat{G}_\gamma(\operatorname{grad}\hat{\mathcal{I}}(\gamma), \delta\gamma) &= \int_{\hat{\Omega}} \langle P\operatorname{grad}\hat{\mathcal{I}}(\gamma), \delta\gamma\rangle \operatorname{vol}(g) \\ &= \int_{\hat{\Omega}} a\, \delta\gamma^{\perp} \operatorname{vol}(g) = \mathrm{d}\hat{\mathcal{I}}(\gamma)[\delta\gamma^{\perp} n] \quad \forall\, \delta\gamma \in \mathrm{T}_\gamma\mathcal{G}, \end{aligned} \tag{6.26}$$

where $\delta\gamma^\perp = \langle n, \delta\gamma\rangle$ denotes the normal component of the variation $\delta\gamma \in \mathrm{T}_\gamma\mathcal{G}$, or an L^2 projection to first obtain the right-hand side of the PDE in (6.25), followed by a projection onto the normal of the hyper-surface. We opt for the second approach.

For multi-patch geometries, we proceed similarly to Section 6.3. The last step of the shape optimization loop is discussed in the next section.

6.4.2 Discrete shape update

A descent direction can be obtained using information on first-order derivatives. For the steepest descent method in the Riemannian setting, the negative of the Riemannian shape gradient is usually chosen for the descent direction. Conjugate gradient and quasi-Newton methods additionally alter the shape gradient to achieve faster convergence rates. Note that there are other frameworks, such as the $\mathrm{W}^{1,\infty}$ approach by Deckelnick et al. [82, 83], where the direction of steepest descent cannot just be determined by computing the shape gradient, since such an object may not even exist in the more general setting.

Let $\eta_h = \sum_{\alpha\in\mathcal{A}} \eta_\alpha N_\alpha$ be the chosen discrete descent direction. In the FDTO approach, the components η_α are either directly given by the shape sensitivities $\mathrm{d}\hat{\mathcal{I}}(N_\alpha)$ for $\alpha \in \mathcal{A}$ or by a modification of the values according to some ad hoc filtering or smoothing scheme. In contrast, the FOTD approach treats η_h as an approximation of some vector field in $\mathrm{T}_{\gamma_h}\mathcal{G}$.

The simplest method is to modify the components of the discrete geometry function γ_h linearly in the direction of η_h, which corresponds to the update rule

$$(\gamma_h)_{k+1} = (\gamma_h)_k + s_k(\eta_h)_k, \quad k \in \mathbb{N}_0. \tag{6.27}$$

The step size $s_k > 0$ is determined using a line search algorithm along the path traced by the update rule, which can be done efficiently in this case due to the simple evaluation of (6.27). This method is referred to as (control pointwise) linear extrapolation in this thesis, which is associated with a retraction on the shape space $\mathcal{B}$.

A natural retraction is obtained by solving the geodesic equation on the Riemannian shape space. For a Sobolev-type Riemannian metric on the shape space of hyper-surfaces in $\mathbb{E}^n$, the dependent variables can be expressed in terms of the configuration γ and the scalar momentum a. The vertical method of lines is employed to discretize the time-dependent system, which results in the following semi-discretized ODE system at first:

$$P\dot{\gamma}_h = a_h n_h, \tag{6.28a}$$
$$\dot{a}_h = F(\gamma_h, a_h), \tag{6.28b}$$

where the right-hand side of the second equation is given by

$$F(\gamma_h, a_h) = \frac{1}{2}\Big(\bar{g}_h\big(\mathrm{Adj}(\nabla P)(\dot{\gamma}_h, \dot{\gamma}_h), n_h\big) - \kappa_h\, \bar{g}_h(P\dot{\gamma}_h, \dot{\gamma}_h)\Big) - a_h\, \mathrm{tr}(g_h^{-1}\bar{g}(\mathrm{T}\gamma_h, \nabla\dot{\gamma}_h)), \tag{6.29}$$

according to Proposition 4.23. Note that the discrete quantities n_h, g_h, and κ_h depend on the geometry function γ_h. A time integration method of choice can be applied to compute the evolution of the shape along the geodesic path in the direction of $\dot{\gamma}_h = \eta_h$.

For example, the forward Euler method yields the following scheme for time integration:

$$\gamma_h^{(i+1)} = \gamma_h^{(i)} + (t^{(i+1)} - t^{(i)})P^{-1}(a_h^{(i)} n_h^{(i)}), \tag{6.30a}$$
$$a_h^{(i+1)} = a_h^{(i)} + (t^{(i+1)} - t^{(i)})F(\gamma_h^{(i)}, a_h^{(i)}), \tag{6.30b}$$

Algorithm 3 Discrete geodesic backtracking line search

Input: Objective function $f\colon \mathcal{G}_h \to \mathbb{R}$, current design $\gamma_0 \in \mathcal{G}_h$, descent direction $\eta_0 \in \mathcal{H}_h$, initial step size $s_0 > 0$, and decrease factor $\sigma \in (0,1)$.

Output: Next design $\gamma_1 \in \mathcal{G}_h$ corresponding to the step size $s_1 > 0$.

1: Set $s_0^{(0)} \coloneqq s_0$.
2: **for** $j = 0, 1, 2, \ldots$ (until values for γ_1 and s_1 are returned) **do**
3: Compute a numerical solution $(\gamma_j^{(0)}, \ldots, \gamma_j^{(m)})$ to the geodesic initial value problem (6.28) corresponding to $\gamma_h(0) = \gamma_0$, $\dot{\gamma}_h(0) = \eta_0$, and a partition $(t_j^{(0)}, \ldots, t_j^{(m)})$ of the interval $[0, s_0^{(j)}]$.
4: Set $l \coloneqq m$.
5: **do**
6: **if** $f(\gamma_j^{(l)}) - f(\gamma_0) \leq \sigma t_j^{(l)} \mathrm{d}f(\gamma_0)[\eta_0]$ **then**
7: Return $\gamma_1 \coloneqq \gamma_j^{(l)}$ and $s_1 \coloneqq t_j^{(l)}$.
8: **else**
9: Choose $\lambda \in \{1, \ldots, l-1\}$.
10: Set $l \coloneqq \lambda$.
11: **end**
12: **while** $l > 1$
13: Set $s_0^{(j+1)} \coloneqq t_j^{(1)}$.
14: **end**

for $i = 0, \ldots, m$, where $\gamma_h^{(0)} = (\gamma_h)_k$, $a_h^{(0)} = (a_h)_k$, and $(t^{(0)}, \ldots, t^{(m)})$ is a partition of the interval $[0, s_k]$. The initial momentum $(a_h)_k$ can be obtained from the descent direction $(\eta_h)_k$ via (6.28a). The result at the final time is then used for the next design, i.e.,

$$(\gamma_h)_{k+1} = R((\gamma_h)_k, s_k(\eta_h)_k) = \gamma_h^{(m)}, \tag{6.31}$$

which is an approximation of the geodesic retraction $\exp((\gamma_h)_k, s_k(\eta_h)_k)$. If only one step of the forward Euler method is executed, i.e., $m = 1$, this approach coincides with linear extrapolation, since

$$(\gamma_h)_{k+1} = \gamma_h^{(1)} = \gamma_h^{(0)} + (t^{(1)} - t^{(0)}) P^{-1}(a_h^{(0)} n_h^{(0)}) = (\gamma_h)_k + s_k(\eta_h)_k. \tag{6.32}$$

The momentum equation (6.28b) does not play a role in this particular case.

If the step size is to be determined using a line search method, the geodesic initial value problem has to be solved for different points in time. In order to do this more efficiently—since some design updates are already available through numerical time integration of the geodesic equation—we propose the backtracking line search in Algorithm 3. For the choice of λ in Line 9 of the algorithm, one can either take the median, e.g., $\lambda = \lceil l/2 \rceil$, or a step size that satisfies $t_j^{(\lambda)} \leq \tau t_j^{(l)}$, where $\tau \in (0,1)$ is an interval shrinking factor. Alternatively, one can also directly take a minimizer

$$\lambda \in \operatorname{argmin}\Big\{ f(\gamma_h^{(l)}) \;\Big|\; l = 1, \ldots, l-1 \Big\}. \tag{6.33}$$

However, this requires objective function evaluations at all interior nodes of the partition and is therefore not very efficient.

An adequate partition of the time integration interval can be obtained using an adaptive ODE solver with step size control, e.g., embedded explicit Runge–Kutta methods, such as the Bogacki–Shampine, Dormand–Prince, and Fehlberg methods [119].

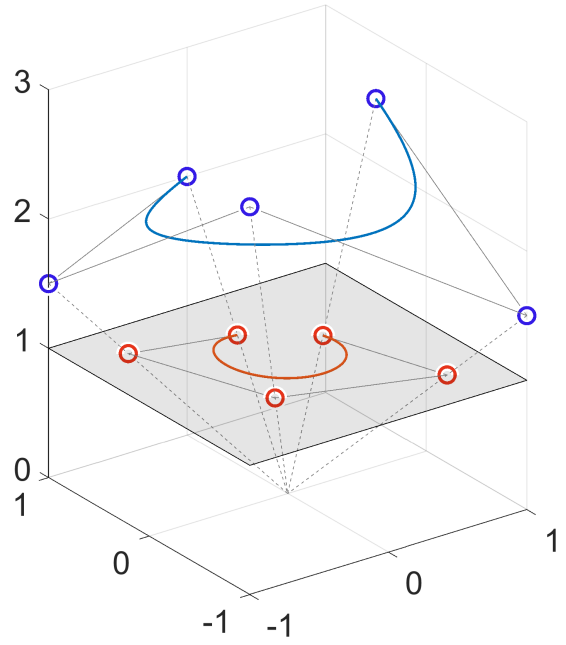

Figure 19: NURBS curve (red) as B-spline curve (blue) in the real projective space.

We conclude Section 6 with a brief discussion on how NURBS weights can be incorporated into the optimization routine.

6.4.3 Incorporation of NURBS weights

To incorporate NURBS weights into the shape optimization routine, NURBS patches can be represented as B-spline patches in the real projective space (see Figure 19). The perspective projection $H\colon \{(z_0, z_1, \dots, z_r) \in \mathbb{R}^{r+1} \mid z_0 > 0\} \to \mathbb{R}^r$ given by

$$H(z_0, z_1, \dots, z_r) = \left(\frac{z_1}{z_0}, \dots, \frac{z_r}{z_0}\right) \tag{6.34}$$

maps homogeneous coordinates to their representatives in the physical space $\mathbb{R}^r$, where $z_0 > 0$ corresponds to the weight of some control point. The homogeneous coordinate space can be endowed with a scale-invariant Riemannian metric

$$\tilde{g}_z(v, w) = \frac{\bar{g}(v, w)}{\bar{g}(z, z)} \tag{6.35}$$

for $z \in \{(z_0, z_1, \dots, z_r) \in \mathbb{R}^{r+1} \mid z_0 > 0\}$ and $v, w \in \mathrm{T}_z\mathbb{R}^{r+1} \simeq \mathbb{R}^{r+1}$, which also induces a Riemannian metric on the real projective space. Here, $\bar{g}$ denotes the inner product on the Euclidean space $\mathbb{R}^{r+1}$.

Sensitivities for the projected coordinates at z in the direction of $w = (w_0, \tilde{w})$ have been calculated by Qian [211] in the context of isogeometric shape optimization and are given by

$$\mathrm{D}_{(z,w)}H = \frac{1}{z_0}\big(\tilde{w} - w_0 H(z)\big). \tag{6.36}$$

They can be used to evaluate the discrete shape derivative in the free-weight NURBS space. See also Fußeder et al. [105] in this regard.

7 Numerical results and discussion

We demonstrate our proposed approach and numerical methods on several examples. The GeoPDEs package [268] has been used for isogeometric finite element analysis in MATLAB, extended by the computation of shape sensitivities and Riemannian shape optimization methods. We first discuss the numerical computation of geodesics in Riemannian shape spaces and shape optimization without PDE constraints, before presenting the main results on Riemannian shape optimization of thin elastic shells using isogeometric analysis.

7.1 Geodesics in shape spaces of planar curves and surfaces

In this section, we present the numerical treatment of the geodesic initial value problem corresponding to the family of H^1 Sobolev–Riemannian metrics $G^{1+c\,\Delta}$ on the shape space of planar curves and surfaces. Two different methods are considered for the spatial discretization of planar curves: the finite difference method (FDM) and the isogeometric finite element method (IGM), while only the latter is used for surfaces. The former method uses a polygonal chain to represent the curve at certain points and computes numerical approximations of relevant quantities based on finite differences, e.g., the relative position of vertices. For the isogeometric method, the curve is represented by a collection of B-spline or NURBS segments that are joined at the ends in a G^1 fashion. Approximations of relevant quantities are then obtained using numerical integration of isogeometric shape functions according to Section 6. Similarly, we use B-spline or NURBS patches to represent surfaces.

Central differences have been used to numerically approximate the first- and second-order spatial derivatives for the finite difference method. The discrete curvature at the i-th vertex of the polygonal chain is computed using the formula

$$\kappa_i = \langle N_i, T_{i,i+1} - T_{i-1,i} \rangle \tag{7.1}$$

given by the component of the difference of incident unit tangent vectors $T_{i-1,i}$ and $T_{i,i+1}$ along the unit angle bisector N_i. There are other notions of discrete curvatures that differ from (7.1) and preserve various properties of the smooth counterpart. However, no single choice fits all relevant properties and use cases [80].

For numerical time integration with adaptive step size control, we use the embedded explicit Runge–Kutta method `ode45` from the MATLAB ODE suite [242] based on the Dormand–Prince pair [91]. It performs generally well without much restriction to the step size if the regularization parameter c is not chosen too small. The Implicit Differential-Algebraic (IDA) equations systems solver [128], which is part of SUNDIALS [129], has been used to numerically solve the geodesic initial value problem by Bauer et al. [27]. It is mentioned there that explicit methods are probably much better adapted to the problem and that the implementation of an adequate explicit solver is a subject of further research.

7.1.1 Straight line segment

As a first example, we simulate the evolution of a straight line segment along a geodesic path with a sinusoidal initial momentum, where both ends of the curve are fixed in place (see Figure 20). To show the differences between a coarser and finer discretization, the curve is subdivided into 10, 18, and 100 segments for the finite difference method, while a cubic B-spline with 4, 8, and 16 elements is used for the isogeometric method, respectively. Mesh refinement yields numerical approximations that are more accurate and converge toward a

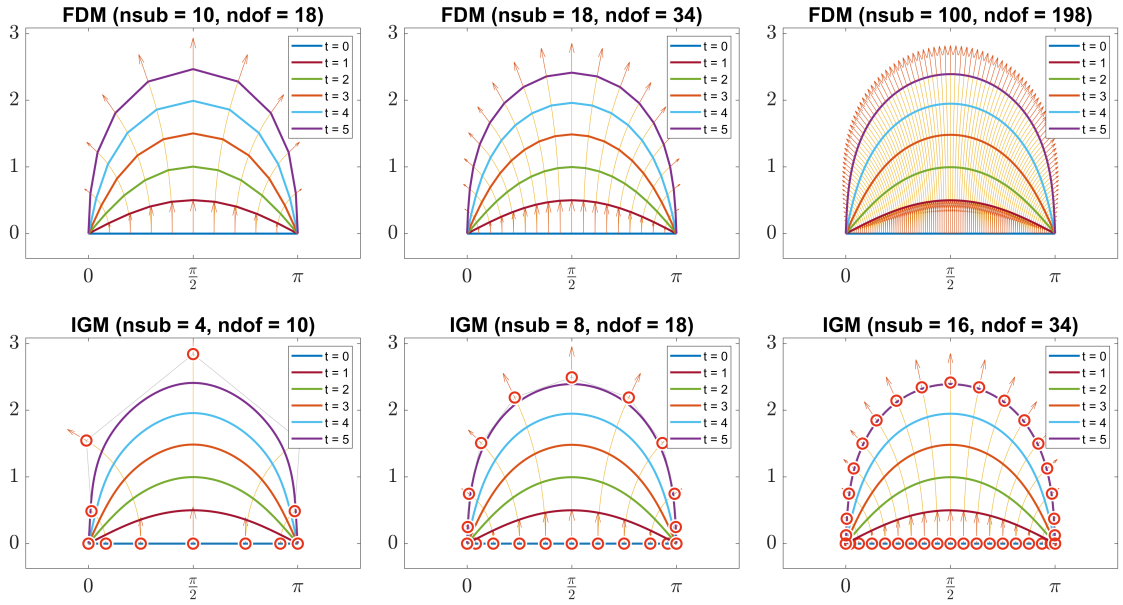

Figure 20: Numerical simulations of a geodesic path for an initially straight line segment of length π with fixed ends corresponding to the H^1 Sobolev–Riemannian metric $G^{1+c\Delta}$ with $c = 1$ and a sinusoidal initial momentum $a(x) = \sin(x)$ for $x \in [0, \pi]$. Red arrows depict velocity vectors for the initial and final curve. Yellow curves depict the path taken by each vertex or control point (marked with red circles). Top: Finite difference method with `nsub` segments. Bottom: Isogeometric method with a cubic B-spline and `nsub` elements.

limiting path of curves. This indicates that the numerical implementation effectively solves an underlying infinite-dimensional problem that depends on the shape of the curve.

The cubic B-spline representation of the curve with 8 elements is determined by 11 control points. Since the control points at the boundary are fixed, the total number of degrees of freedom is $2 \times 9 = 18$, which is the same amount that results from a subdivision into 10 piecewise linear segments. The numerical solution in Figure 20 (bottom middle) is already visually indistinguishable from the solution using finite differences with 100 segments in Figure 20 (top right). This illustrates the higher accuracy per degree of freedom (`ndof`) when using isogeometric analysis.

Replacing the zero displacement boundary conditions with natural ones at both ends and imposing a constant initial momentum yields a geodesic path along which the straight line segment moves at a constant speed in a direction normal to the tangent line.

7.1.2 Closed planar curves

Another simple case of a geodesic path is given by one through concentric circles, which can be obtained by choosing a circle as initial curve together with a constant initial momentum (see Figure 21b). For the isogeometric method, we represent the curve using 4 coupled NURBS segments. The coarsest representation of a unit circle using quadratic NURBS with weights $(1, 1/\sqrt{2}, 1)$ for the control points is shown in Figure 21a. According to a similar observation in [182, Section 5.1] for a weighted (almost local) L^2 Riemannian metric, the circles expand indefinitely with decreasing speed over time for the outward geodesic path, while the circles along the inward geodesic path shrink to a point in finite time. This is

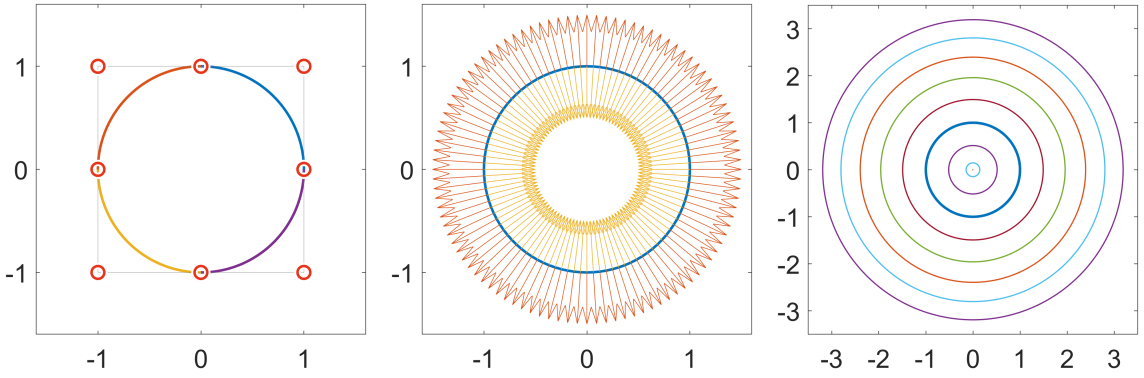

(a) Circle from NURBS segments (shown in 4 different colors).

(b) Initial curve and velocities (outward- and inward-pointing).

(c) Geodesic through concentric circles at unit time intervals.

Figure 21: Geodesic path for a circle corresponding to the H^1 Sobolev–Riemannian metric $G^{1+c\,\Delta}$ with $c = 1$ and a constant initial momentum $a(\theta) = \pm 1$ for $\theta \in [0, 2\pi)$.

supported by the numerical results in Figure 21c for the H^1 Sobolev–Riemannian metric.

We investigate two other geodesic paths with the unit circle as initial curve. The first one corresponds to an initial momentum of $a(\theta) = \cos(\theta)$, where $\theta \in [0, 2\pi)$ is the angle with respect to the x-axis, which is used to parametrize the circle at the origin. This choice leads to a movement of the curve to the right, which, however, does not preserve the shape of the circle and results in a bean-shaped curve at time $t = 5$ (see Figure 22a). The second initial momentum is given by $a(\theta) = \sin(5\theta)$, which turns the circle into a star-shaped curve. Note that a geodesic path in shape space will not necessarily avoid self-intersections, which may occur after a certain amount of time (see Figure 22b).

7.1.3 Surface patch

For the two-dimensional example, we choose an initially flat surface of size $\pi \times \pi$ with fixed boundaries and evolve it along the geodesic path corresponding to the initial momentum $a(x, y) = \sin(x)\sin(y)$ for $x, y \in [0, \pi]$. This example has been considered in [27, Section 11] using finite differences for spatial discretization. The results in Figure 23 are similar to the ones provided in the aforementioned paper. A cubic B-spline patch with 8×8 elements is used to represent the surface in the discrete setting. Dirichlet boundary conditions are configurable for each side of the surface patch in our implementation, which allows for a variety of numerical experiments.

7.1.4 Conservation of energy

To verify the implementation and the numerical results, we inspect the evolution of energy along geodesic paths. The methods used for integration in time are not energy-preserving, but subsequent energy values should nevertheless not deviate much from the initial energy if a sufficiently accurate solver is used.

The total energy of the Hamiltonian system corresponding to the geodesic equation on the shape space of planar curves $\mathrm{B}(M, \mathbb{E}^2)$ with Riemannian metric $G^{1+c\,\Delta}$ at time t reads

$$H(t) = \frac{1}{2} G^{1+c\,\Delta}_{\gamma(t)}(\dot\gamma(t), \dot\gamma(t)) = \frac{1}{2} \int_M \langle (1 + c\,\Delta)\dot\gamma(t), \dot\gamma(t) \rangle \operatorname{vol}(g) = \frac{1}{2} \int_M \langle an, \dot\gamma(t) \rangle \operatorname{vol}(g)$$

due to the horizontal path condition $(1 + c\,\Delta)\dot\gamma = an$.

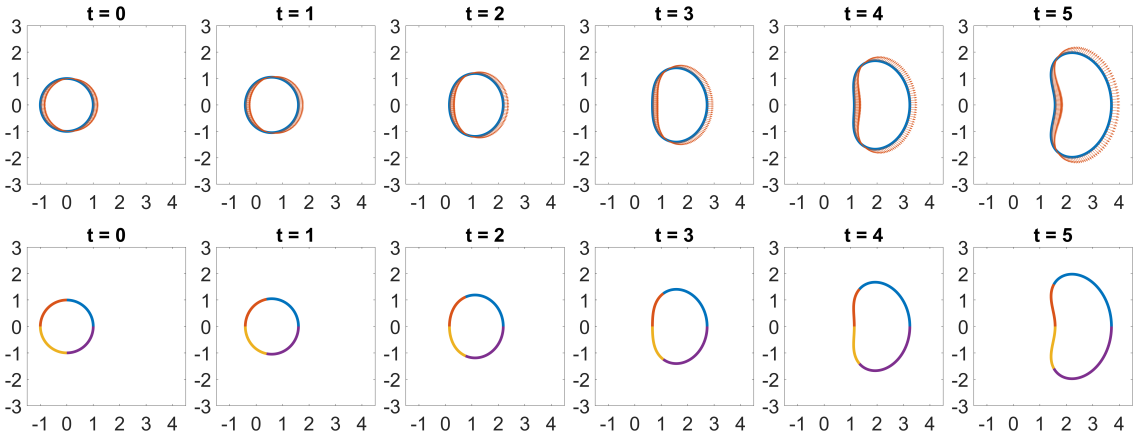

(a) The initial momentum is given by $a(\theta) = \cos(\theta)$ for $\theta \in [0, 2\pi)$. Top: Finite difference method with 200 segments. Red arrows depict velocity vectors at each vertex. Bottom: Isogeometric finite element method with 4 cubic NURBS segments and 16 elements each.

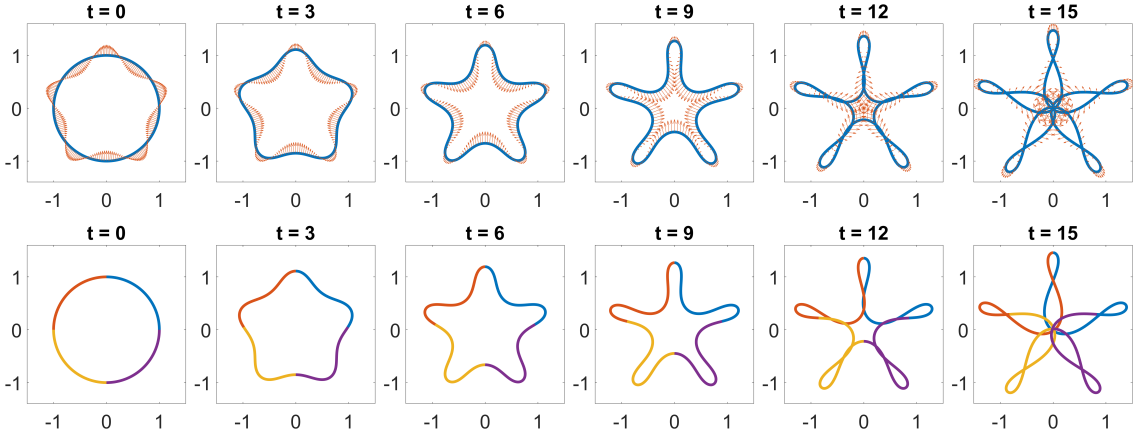

(b) The initial momentum is given by $a(\theta) = \sin(5\theta)$ for $\theta \in [0, 2\pi)$. Top: Finite difference method with 200 segments. Red arrows depict velocity vectors at each vertex. Bottom: Isogeometric finite element method with 4 cubic NURBS segments and 16 elements each.

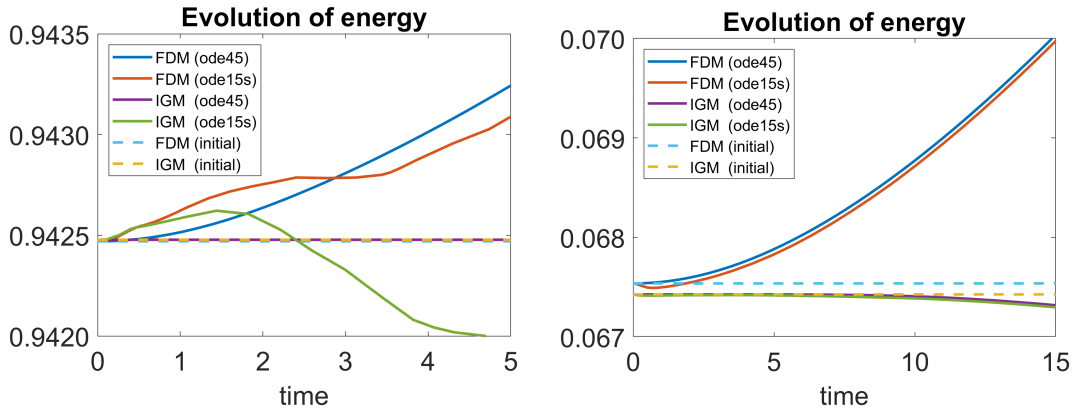

(c) Comparison of numerical discretization methods based on conservation of energy. Left: Energy corresponding to the geodesic path in Figure 22a. Right: Energy corresponding to the geodesic path in Figure 22b.

Figure 22: Geodesic path for a circle corresponding to the H^1 Sobolev–Riemannian metric $G^{1+c\Delta}$ with $c = 1$ and different initial momenta.

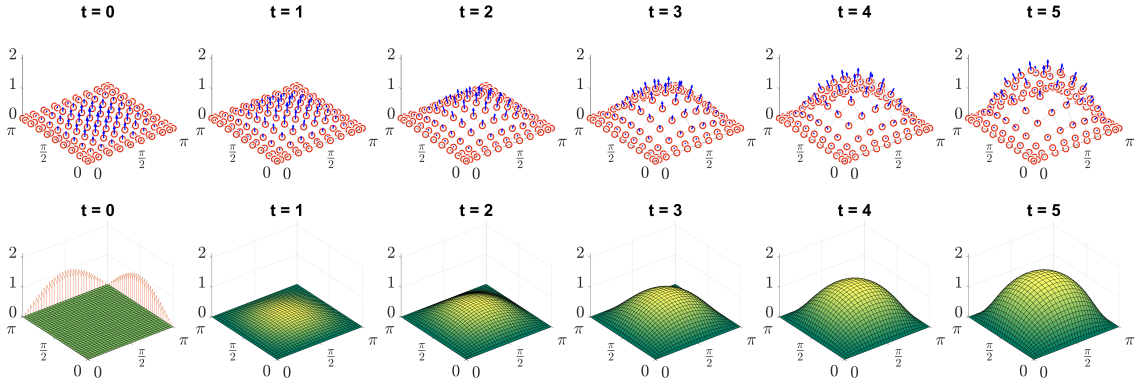

Figure 23: Geodesic path for an initially flat surface of size $\pi \times \pi$ with fixed boundaries corresponding to the H^1 Sobolev–Riemannian metric $G^{1+c\,\Delta}$ with $c = 1$ and the initial momentum $a(x, y) = \sin(x)\sin(y)$ for $x, y \in [0, \pi]$, which is indicated by red arrows in the bottom left image. Top: Control mesh (red circles) for a cubic B-spline surface with 8×8 elements and corresponding velocity vectors (blue arrows) at unit time intervals. Bottom: Resulting shape evolution of the B-spline surface.

For the straight line segment in Figure 20, a sinusoidal initial momentum $a(x) = \sin(x)$ for $x \in [0, \pi]$ yields the following initial energy:

$$H(0) = \frac{1}{2}\int_0^\pi \sin(x)\langle n, \dot\gamma(0)\rangle \,\mathrm{d}x = \frac{1}{2}\int_0^\pi \frac{\sin(x)^2}{1+c}\,\mathrm{d}x = \frac{\pi}{4(1+c)}. \tag{7.2}$$

The normal component of the initial velocity $y = \langle n, \dot\gamma(0)\rangle$ is given by the solution to the second-order differential equation

$$(1 + c\,\Delta)y(x) = y(x) - cy''(x) = \sin(x) \tag{7.3}$$

with zero boundary conditions, i.e., $y(x) = \sin(x)/(1 + c)$.

For a constant initial momentum a, the initial energy on the unit circle $\mathbb{S}_1$ is given by

$$H(0) = \frac{1}{2}\int_{\mathbb{S}_1} \left\langle an, \frac{a}{1+c}n \right\rangle \mathrm{vol}(g) = \frac{a^2\,\mathrm{Vol}(\mathbb{S}_1)}{2(1+c)} = \frac{\pi a^2}{1+c}, \tag{7.4}$$

since the initial velocity vector field must be of the form $\dot\gamma(0) = bn$ for some constant b due to rotational symmetry. Note that $\Delta n = n$ on $\mathbb{S}_1$, thus

$$an = (1 + c\,\Delta)\dot\gamma(0) = (1 + c)bn, \tag{7.5}$$

and therefore $b = a/(1 + c)$.

For the square in Figure 23 with initial momentum $a(x, y) = \sin(x)\sin(y)$ for $x, y \in [0, \pi]$, the initial energy on the shape space of surfaces $\mathrm{B}(M, \mathbb{E}^3)$ endowed with the Riemannian metric $G^{1+c\,\Delta}$ is given by

$$H(0) = \frac{1}{2}G^{1+c\,\Delta}_{\gamma(0)}(\dot\gamma(0), \dot\gamma(0)) = \frac{\pi^2}{8(1+2c)}, \tag{7.6}$$

according to [27, Figure 2 in Section 11].

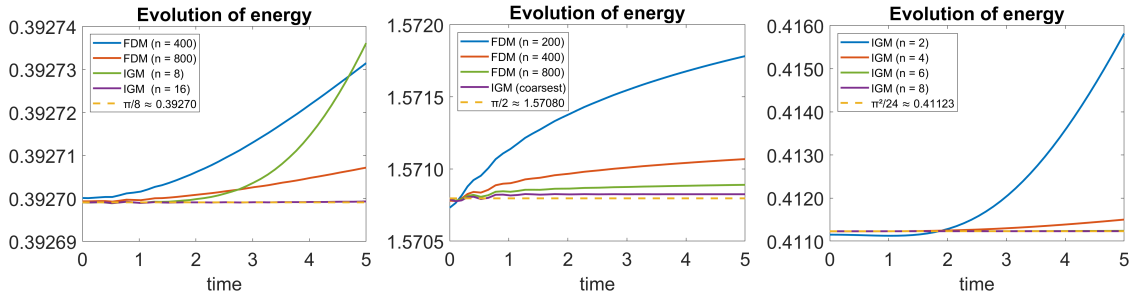

Figure 24: Comparison of the evolution of energy for the straight line segment (left), the outward geodesic path through concentric circles (middle), and the surface patch (right) corresponding to different spatial discretizations. The number of segments for the finite difference method and elements for the isogeometric method in each parametric direction is denoted by n. The Dormand–Prince method from the MATLAB ODE suite (`ode45`) with a maximum step size of $\Delta t = 0.125$ has been used for integration in time.

We compare the energy evolution for the straight line segment, the outward geodesic path through concentric circles, and the surface patch using different spatial discretizations (see Figure 24). In the case of concentric circles, even the coarsest discretization in Figure 21a is able to capture the energy to sufficient accuracy if the geometry can be exactly represented by the NURBS curve, which elucidates the importance of exact geometry representations in numerical simulations. If an exact representation is not available, just a few refinements of the NURBS space can significantly improve the results in terms of conservation of energy.

7.2 Interpolation of closed planar parametrized curves

In this section, we demonstrate the use of the square root velocity field (SRVF) transform to solve the geodesic boundary value problem using geodesic shooting for interpolation of closed planar parametrized curves that are translation-invariant (see Section 4.4.6). For the case of unparametrized curves, we refer to Bauer et al. [29].

To solve the shape interpolation problem numerically, we consider time-discrete paths in shape space and use finite differences or a spline discretization to approximate the curves spatially. Numerical time integration is carried out using the RATTLE algorithm [14], which is a velocity version of the SHAKE algorithm [226], commonly used to integrate constrained Hamiltonian systems [165]. This is required to enforce the constraint for closed curves in (4.93).

The results are compared with a simple pointwise linear interpolation (LERP) of the initial and target shape (see Figure 25). There is a point in time $0.2 \leq t \leq 0.4$ where the shape undergoes a self-intersection when using LERP. This does not occur for the interpolation using the elastic SRVF metric in this specific case. Instead, the creases are smoothed out and the shape seems to decrease in size before unfolding into the star-shaped target curve. The proposed method generates an interpolating geodesic path in $\mathrm{Imm}(\mathbb{S}_1, \mathbb{E}^2)/\operatorname{Tra}(\mathbb{E}^2)$, i.e., self-intersections may occur in other instances, since their avoidance is not a feature of the method.

7.3 Curve shortening flow and minimal surfaces

As simple examples of shape optimization problems without PDE constraints, we consider the curve shortening flow for planar curves and the mean curvature flow for surfaces. They

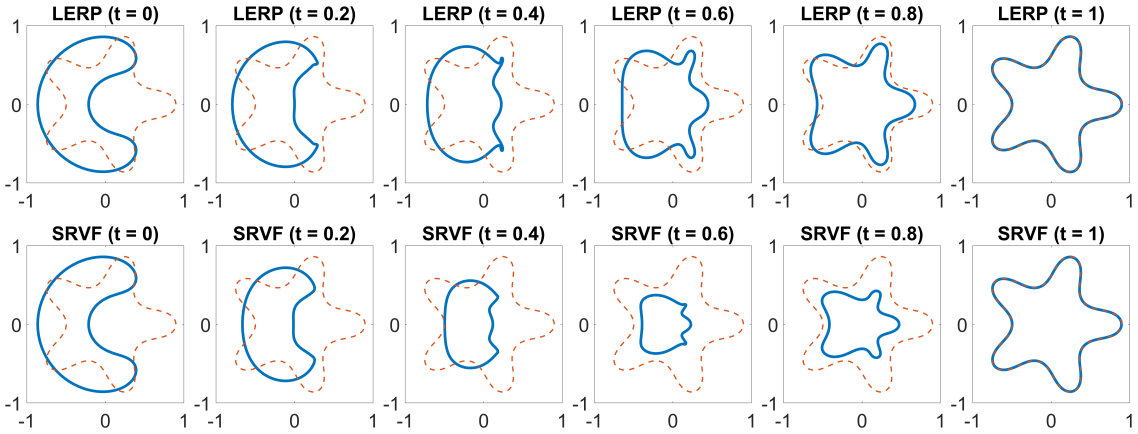

Figure 25: Interpolation of closed planar parametrized curves. Top: Pointwise linear interpolation (LERP). Bottom: Interpolating geodesic path in $\mathrm{Imm}(\mathbb{S}_1, \mathbb{E}^2)/\mathrm{Tra}(\mathbb{E}^2)$ corresponding to the elastic SRVF metric obtained via geodesic shooting. The target curve is shown by the red dashed curve.

are gradient flows corresponding to the length and area functional, respectively. Stationary points of the length functional are locally length-minimizing curves, i.e., geodesic curves in Euclidean space, while stationary points of the area functional are referred to as minimal surfaces. Both examples also play a role in enforcing geometry constraints, such as fixed length and fixed area constraints, for the problems in subsequent sections.

7.3.1 Curve shortening flow

Figure 26 (left) shows a numerical simulation of the gradient flow for the length functional corresponding to the H^1 Sobolev–Riemannian metric $G^{1+c\,\Delta}$ with $c = 1$ using an isogeometric spatial discretization and the Dormand–Prince method (`ode45`) for time integration. The initial curve is given by a parabolic arc described by the control points of a quadratic Bézier segment, which is fixed at both ends and has been refined into 8 cubic elements. The results approach the straight line segment connecting both ends, which is the solution to the length minimization problem. The evolution of length for different regularization parameters is depicted in Figure 26 (middle). Larger values for c cause slower convergence toward the solution. From an optimization point of view, small regularization parameters are thus preferred. However, they lead to numerical instabilities, especially in the case of the L^2 gradient flow, i.e., $c = 0$.

A gradient descent method differs from a numerical approximation of the gradient flow. Instead of moving along an integral path of the gradient field, the shape is evolved along a path corresponding to a retraction and some descent direction at the initial configuration until a sufficient decrease in the objective function is obtained. In the limiting case, if the step size at each descent approaches zero, the iterates will approximate an integral path. However, larger step sizes should be taken for an efficient optimization method to reduce the amount of function evaluations. This inevitably lead to different progressions of the optimization process.

For the descent path, one can either choose a geodesic retraction corresponding to the Riemannian exponential mapping or a simpler one that can be evaluated more efficiently. In the case of shape spaces with a Euclidean ambient space, a valid retraction is given by

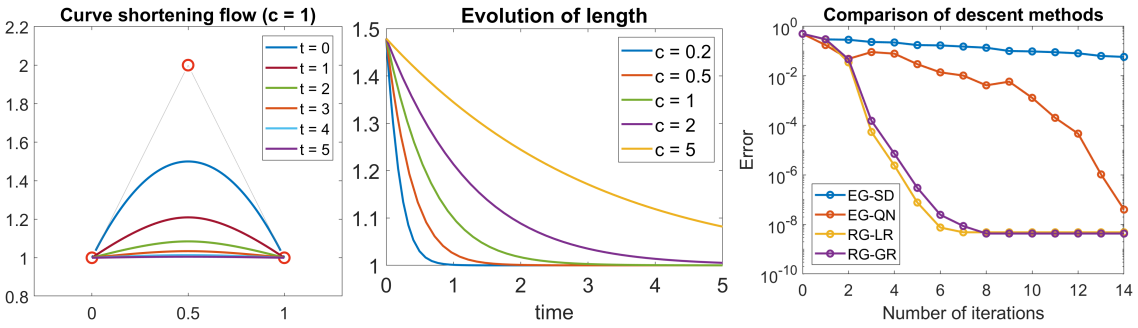

Figure 26: Left: Numerical simulation of the curve shortening flow for a parabolic arc. Middle: Evolution of length for different regularization parameters. Right: Comparison of descent methods for the length minimization problem with $c = 1$.

the pointwise linear extrapolation of vector fields. The obvious advantage of using such a linear retraction is the straightforward computation of shapes along the descent path, which is useful for an efficient line search. In contrast, a geodesic retraction requires a numerical solution to the geodesic initial value problem, which involves significant additional efforts. Nevertheless, we compare the following methods for the length minimization problem:

a) The *first discretize–then optimize* (FDTO) approach, where control point coordinates are treated as independent design variables in the Euclidean space and the standard Euclidean gradient is used for the steepest descent method with backtracking line search (EG-SD) and the BFGS quasi-Newton method (EG-QN).

b) The Riemannian gradient descent method according to the *first optimize–then discretize* (FOTD) approach on the shape space of planar curves using a linear retraction with backtracking line search (RG-LR) and a geodesic retraction with the line search strategy in Algorithm 3 (RG-GR).

To illustrate the difference between the FDTO approach using the Euclidean gradient and the Riemannian gradient descent method on the shape space of planar curves, we compare both approaches and summarize the results in Figure 26 (right). The slow convergence of the descent methods based on the Euclidean gradient is due to poor design updates that do not take the connectivity of control points into account. The BFGS method eventually approaches the solution after several iterations, while the Riemannian gradient descent methods are able to reach the limit of computational accuracy in less iterations. The rate of convergence can presumably be accelerated further by applying a Riemannian BFGS method instead, which has not been considered in this work.

Results using a geodesic retraction generally do not differ much from the ones that use a linear retraction. However, during the first few steps of the optimization procedure, where large step sizes may be taken, evolution along the geodesic path can yield vastly different design iterates. When the method is about to converge, it is advisable to switch to a linear retraction, since small step sizes are usually taken and there are no significant benefits to fully integrating the geodesic equation.

7.3.2 Minimal surfaces

For the two-dimensional case, we consider the numerical computation of a minimal surface of revolution constrained by two coaxial rings. Depending on the ratio of the distance l between the rings and the diameter d, local minimizers of the area functional are either

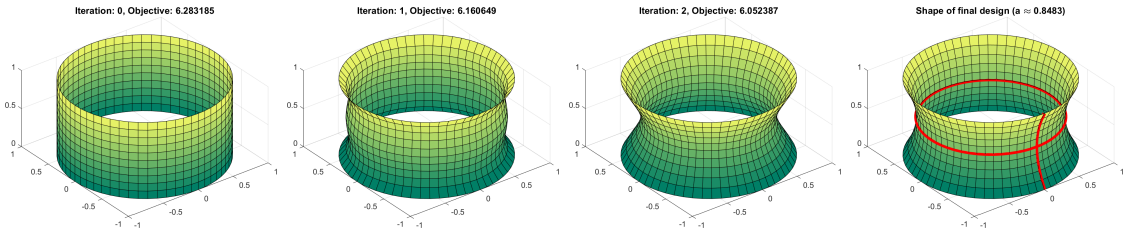

(a) First design iterations and shape of final design for the Riemannian gradient descent method. The resulting minimal surface constrained by two coaxial rings is a catenoid with $a \approx 0.8483$.

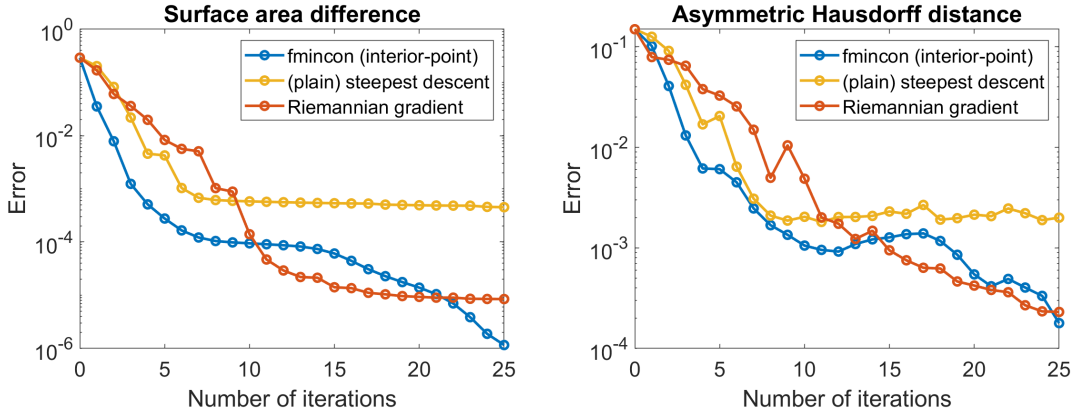

(b) Comparison of the surface area difference and the asymmetric Hausdorff distance to the exact solution during the optimization process for different algorithms.

Figure 27: Minimization of surface area with prescribed boundary conditions.

given by a catenoid corresponding to some catenary parameter a satisfying the condition

$$a \cosh\left(\frac{l}{2a}\right) = \frac{d}{2} \tag{7.7}$$

or by a so-called Goldschmidt solution, i.e., the surface breaks into two circular disks filling the two rings with minimal area. If the ratio l/d is larger than the Laplace limit constant $\lambda \approx 0.6627$, then only the latter case can occur. For more information on minimal surfaces and the mathematics of soap films, we refer to Isenberg [140], Oprea [203], and Dierkes et al. [88], as well as the Wolfram MathWorld entry by Weisstein [277].

The numerical results corresponding to a cylindrical initial surface are shown in Figure 27a. The geometry consists of a single globally C^0 cubic NURBS patch that is glued together at the seam by identifying coincident control points with each other. A Riemannian gradient descent method on the shape space of surfaces corresponding to the H^1 Sobolev–Riemannian metric $G^{1+c\,\Delta}$ with $c = 1$ and a linear retraction has been used. The method converges toward a catenoid with catenary parameter $a \approx 0.8483$, which is a solution to (7.7) with $l = 1$ and $d = 2$. Convergence plots for different optimization algorithms are provided in Figure 27b. The difference in surface area between the numerical approximation $\Omega \subseteq \mathbb{R}^3$ and the exact solution $\Omega_* \subseteq \mathbb{R}^3$ as well as the asymmetric Hausdorff distance

$$\operatorname{dist}_{\mathrm{A}}(\Omega, \Omega_*) = \sup_{x \in \Omega} \operatorname{dist}(x, \Omega_*) = \sup_{x \in \Omega} \inf_{y \in \Omega_*} \|x - y\| \tag{7.8}$$

have been used to measure the approximation error. An adequate sampling of Ω has to be chosen to evaluate (7.8) in the discrete setting. The minimal distance from each sample to

Ω_* can be computed using root-finding methods, since a parametrization of the optimal shape is known:

$$\gamma_*\colon [0,2\pi]\times[-l/2,l/2]\to\Omega_*,\quad (\theta,z)\mapsto\begin{pmatrix}\cos(\theta) & -\sin(\theta) & 0\\ \sin(\theta) & \cos(\theta) & 0\\ 0 & 0 & 1\end{pmatrix}\begin{pmatrix}a\cosh(z/a)\\ 0\\ z\end{pmatrix}. \quad (7.9)$$

The surface area of the catenoid is given by $\mathrm{Vol}(\Omega_*)=\pi a^2(\sinh(l/a)+(l/a))$.

7.4 Compliance minimization of a half-cylindrical shell

We consider the compliance minimization of a half-cylindrical shell of width $w=10$ and radius $r=10$ under static load and fixed area constraint. One end of the shell is pinned at the base, while only vertical displacements have been restricted for the other end. A homogeneous downwards gravitational body force of magnitude $F=0.05$ acts on the shell. We assume a shell thickness of $h=0.1$, a Young's modulus of $Y=7\cdot10^5$, and a Poisson's ratio of $\nu=0.33$. Shape sensitivities for the problem have been derived in Section 5.4.2 (see Proposition 5.19). For the surface area, we refer to Proposition 5.14 and (5.80).

The goal of the optimization procedure is to modify the initial shape design of the shell so that it resists most deformation in response to the prescribed load. The geometry is fixed at both ends of the shell, and the total surface area is not allowed to change. The former is achieved numerically by not including the degrees of freedom corresponding to the fixed part of the boundary in the optimization process for the FDTO approach and by imposing Dirichlet boundary conditions when computing the shape gradient using a Galerkin method for the FOTD approach. An augmented Lagrangian method is used to impose the fixed area constraint on the geometry (see Section 5.3.2).

We compare the following methods to assess the performance of the Riemannian shape optimization method: the interior-point method in MATLAB's `fmincon` applied to coordinates of variable control points of the geometry function, a plain steepest descent method using a backtracking line search based on the Armijo–Goldstein condition applied to the same coordinates, and a Riemannian gradient descent method using an H^1 Sobolev–Riemannian metric with $c=1$ and a linear retraction in the shape space of surfaces. The domain is discretized into 8×4 isogeometric elements using cubic splines, which results in a total of 252 degrees of freedom. Variable NURBS weights are not considered in the comparison.

The proposed method, which is a modification of the steepest descent method in Euclidean space, performs slightly better than the interior-point method in this particular example and yields designs that are qualitatively different. It allows curved arcs to form along the boundary of the half-cylindrical shell instead of vertical stiffeners (see Figure 28a–28c).

A comparison of final designs corresponding to different discretization levels using the H^1 Sobolev–Riemannian gradient descent method is shown in Figure 28d. The results depend highly on the chosen optimization parameters and the discretization level, which indicates that the discretized problem has many local minimizers. It is also not known whether the continuous problem is well-posed. Fine discretizations lead to the formation of wrinkles and microstructures in the designs. Choosing a coarse discretization or a large coefficient c for the H^1 Sobolev–Riemannian metric can be seen as a means to regularize the problem. The resulting designs tend to be smoother and have less details. Although they may be far from an optimal solution to the continuous problem—if one even exists—from a practical point of view, the proposed methods yield eligible designs that have better objective values than the initial design and are potentially useful in industrial applications.

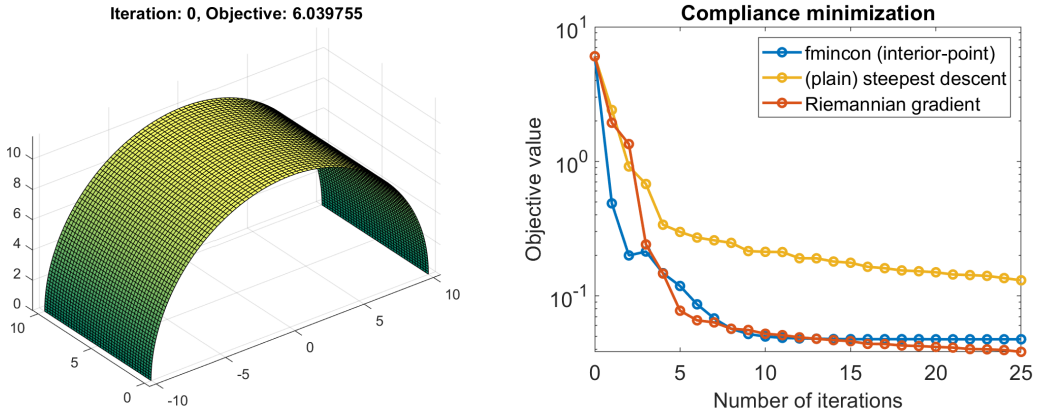

(a) Left: Initial design of the half-cylindrical shell. Right: Comparison of objective values during the optimization process.

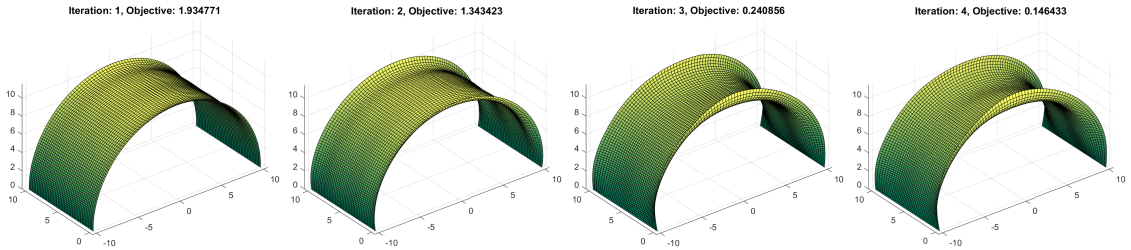

(b) First design iterations when using a Riemannian gradient descent method in the shape space of surfaces corresponding to the H^1 Sobolev–Riemannian metric. The domain has been subdivided into 8×4 cubic elements.

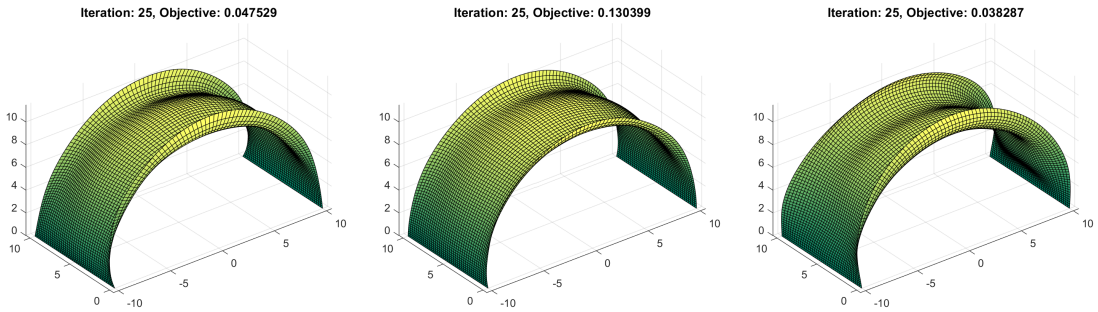

(c) Designs after 25 iterations. Left: Interior-point method (MATLAB's `fmincon`). Middle: Plain steepest descent method. Right: Riemannian gradient descent method.

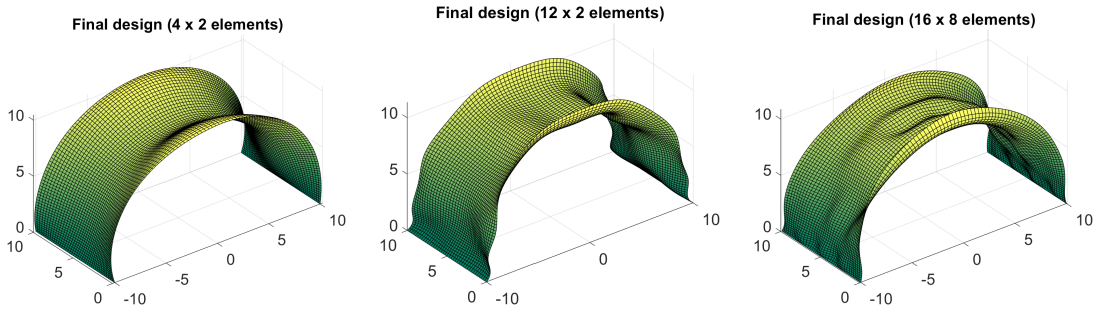

(d) Final designs corresponding to different discretization levels for the Riemannian gradient descent method.

Figure 28: Compliance minimization of a half-cylindrical thin elastic shell.

7.5 Isogeometric analysis of Earth's lithosphere

We conduct numerical experiments on various geographic locations using the global topography data from Earth2014 [133]. A Mohorovičić depth map is available for the European Plate [113], which is used to verify the results. Information about the ground truth additionally allows us to estimate unknown parameters of the model via least-squares methods constrained by the governing equations. This is applied to identify the spatial distribution of the effective elastic thickness, the density of overlying rock, and the topographic load that are most plausible to explain the measured data for the Mohorovičić depth.

The isostatic boundary value problem for a plate (see Section 3.3.2) is solved numerically using methods of isogeometric finite element analysis (see Section 6). Spectral methods [200], finite difference methods [279], and standard finite element methods [172] have been commonly used to simulate the lithospheric flexure. The advantage of using isogeometric finite elements lies in the simple construction of smooth shape functions.

The following geographic locations have been considered in this thesis: Central Java, the Java Island, the Indonesian Archipelago, the Hawaiian Islands, the Himalayan Mountain Range, and the European Plate. The corresponding geographic coordinates in decimal degrees are shown in Table 1.

The Earth2014 data [133] contain rock-equivalent topography that can be converted into topographic load by using the reference density and the gravitational acceleration in Table 2. For Central Java, we consider both a single-patch and multi-patch parametrization of the domain to show the capabilities of multi-patch isogeometric analysis when the data required for the simulation are only available on certain parts of Earth's surface. The results can be compared with the Mohorovičić depth data obtained using inversion of receiver functions from the work of Amukti et al. [13]. A Mohorovičić depth map is available for the European Plate [113], which is also used to estimate model parameters in Section 7.5.2.

7.5.1 Simulation of the lithospheric depression

In this subsection, we compare the results obtained from the simple Airy–Heiskanen model of local isostasy with the regional model of flexural isostasy by Vening-Meinesz to simulate the lithospheric depression due to topographic loading and buoyancy. Isogeometric analysis is used to solve the isostatic boundary value problem for the flexural model numerically. We choose the physical parameters in Table 2, which are assumed to be constant over the simulation domain. The mesh is subdivided into 16×16 elements and a spline degree of $(4, 4)$ is chosen for the isogeometric spline space.

Location	Longitude	Latitude
Central Java	109.5° to 111.75°	-8.5° to -6.25°
Java Island	105° to 115°	-10° to -5°
Indonesia	90° to 150°	-15° to 15°
Hawaii	-165° to -150°	13° to 28°
Himalaya	60° to 120°	20° to 50°
Europe	-25° to 25°	28° to 78°

Table 1: Geographic coordinates of locations of interest.

Parameter	Value
Young's modulus E	65 GPa
Poisson's ratio ν	0.25
reference rock density ϱ_{r}	$2.67\,\mathrm{g\,cm^{-3}}$
upper mantle density ϱ_{m}	$3.33\,\mathrm{g\,cm^{-3}}$
gravitational acceleration g	$9.81\,\mathrm{m\,s^{-2}}$
effective elastic thickness t	16 km
standard crustal thickness t_0	30 km
Earth radius R_{E}	6371 km

Table 2: Physical parameters for the numerical simulations.

Figure 29a (left) shows a contour plot of the bedrock topography of Central Java. The corresponding topographic load, expressed through rock-equivalent topography, is shown in Figure 29a (right), which also contains a multi-patch geometry of the domain of interest.

The computed lithospheric depression for a single-patch domain is shown in Figure 29b (right). Compared to the Airy–Heiskanen model in Figure 29b (left) and the available depth data [13, Figure 6], the topographic loading in the Vening-Meinesz model is additionally compensated by flexural rigidity. This leads to less local variations. High-frequency details are strongly attenuated and the mid-surface only reaches a depth of less than 32 km as opposed to the Airy–Heiskanen model that predicts Mohorovičić depths up to 42 km below the mean sea level when using the same physical parameters.

The result of the multi-patch simulation is depicted in Figure 29c (left). It differs from the single-patch result due to the missing data outside of the simulation domain that are replaced by zero Neumann boundary conditions. Augmenting the multi-patch domain with additional patches that cover the whole rectangular single-patch domain yields a result that is close to the single-patch solution (see Figure 29c, right). Both solutions appear continuously differentiable at the interfaces. Isogeometric finite element methods require less computational effort and degrees of freedom than classical approaches for solving the plate equation, provided that multiple patches are used sparingly.

Numerical experiments for the other geographic locations have been done to observe the effect of different scales and varying load distributions (see, e.g., Figure 32). Large scale simulations require more degrees of freedom to resolve details of the solution. Uniform refinement of the mesh leads to a rapid increase in computational effort, which may not be necessary for regions that are already resolved to sufficient accuracy. In order to reduce the computational effort by only adding degrees of freedom to regions that require more accuracy, we consider adaptive local refinement using hierarchical B-splines and a multi-level estimator with the maximum strategy [107]. For the European Plate, we compare the results of using a uniform mesh with 16×16 elements and a hierarchical mesh arising from adaptive local refinement in Figure 30b (right) and Figure 30c, respectively.

7.5.2 Parameter identification from observed data

The following model parameters have been estimated using the sensitivities in Section 5.4.3 and available Mohorovičić depth map of Europe: effective elastic thickness of the lithosphere, rock density in the crust, and existing topographic load. The depth data stem from the

work of Grad et al. [113] and can be seen in Figure 30a (right). A homogeneous effective elastic thickness of 16 km and a homogeneous reference density of $2.67\,\mathrm{g\,cm^{-3}}$ are assumed, when they are not subject to estimation. These default values are furthermore used as initial values for the estimation process.

We use the Earth2014 data by Hirt and Rexer [133] for the topographic load in Europe (see Figure 30a, left). When topographic load is the sought parameter, the initial value for the corresponding rock-equivalent topography is set to 1 km everywhere. The lithospheric depression that results from the default values and the topographic data are depicted in Figure 30b (right). It differs from the available Mohorovičić depth data due to simplified assumptions and missing information on position-dependent parameters of the model.

The estimated effective elastic thickness does not differ much from the initial distribution (see Figure 31a, left). There are particular spots scattered around the Mediterranean Sea and west of the British Isles that exhibit a slightly higher and lower thickness. A change in the effective elastic thickness of this magnitude does not significantly alter the resulting lithospheric depression (see Figure 31a, right, and Figure 30b, right). Overall, the result is not compatible with the spatial distributions found in Pérez-Gussinyé and Watts [210]. According to Forsyth [104], the flexural rigidity inferred from topographic loading is likely to be underestimated if there is significant internal loading due to subsurface variations, which has been disregarded in our simplified model.

The parameter estimation predicts a higher reference density in the Baltic Shield and a lower reference density around oceans, especially in the Norwegian Sea (see Figure 31b, left). The resulting lithospheric depression (Figure 31b, right) is similar to the Mohorovičić depth map in Figure 30a (right). A density distribution like the estimated one can explain the observed Mohorovičić depth data well.

The lithospheric depression that results from topographic load estimation is similar to the one that results from density estimation (see Figure 31b, right, and Figure 31c, right). Since the effective elastic thickness and the rock density of the lithosphere are constant, the estimated topographic load appears to mimic the contours of the Mohorovičić depth map (see Figure 31c, left).

7.5.3 Spherical model of the lithosphere

For the discretization of the variational problem in Section 3.3.3, we use a C^1 multi-patch parametrization from a quad sphere projection (see Figure 33b). The parametrization is not analysis-suitable G^1 continuous. However, a similar one that is analysis-suitable can be constructed from it, according to Kapl et al. [150]. The result will not necessarily represent the same geometry as before. Nevertheless, it can be used to obtain an analysis-suitable G^1 multi-patch parametrization of a surface that is close to a sphere.

Effective elastic thicknesses of 16 km and 1000 km are chosen for the spherical lithosphere. The latter serves to demonstrate the effects of flexural rigidity on a spherical shell under internal pressure, since the effects are negligible if the thickness is extremely small relative to the scale of the Earth. The Earth2014 data by Hirt and Rexer [133] are mapped to the sphere using a reverse geographic projection (see Figure 33a). The resulting deformation of the lithosphere in isostatic equilibrium is shown in Figures 33c and 33d, where elevation refers to the radial displacement relative to the reference sphere when a spherical Earth of constant radius is assumed. Note that the scale of the coordinate system is normalized to the radius of the Earth, which is specified in Table 2.

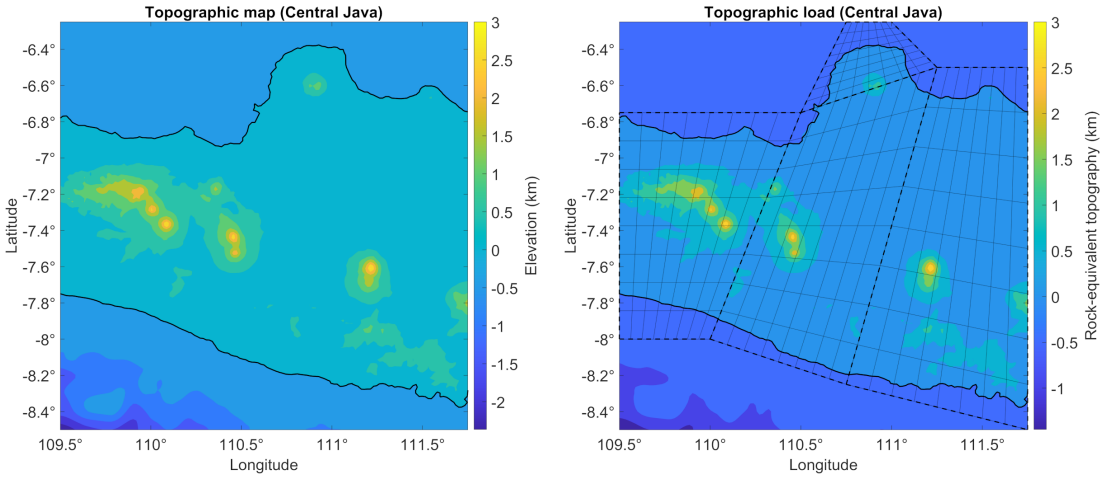

(a) Topographic map (left), corresponding load (right), and a multi-patch geometry (grid lines).

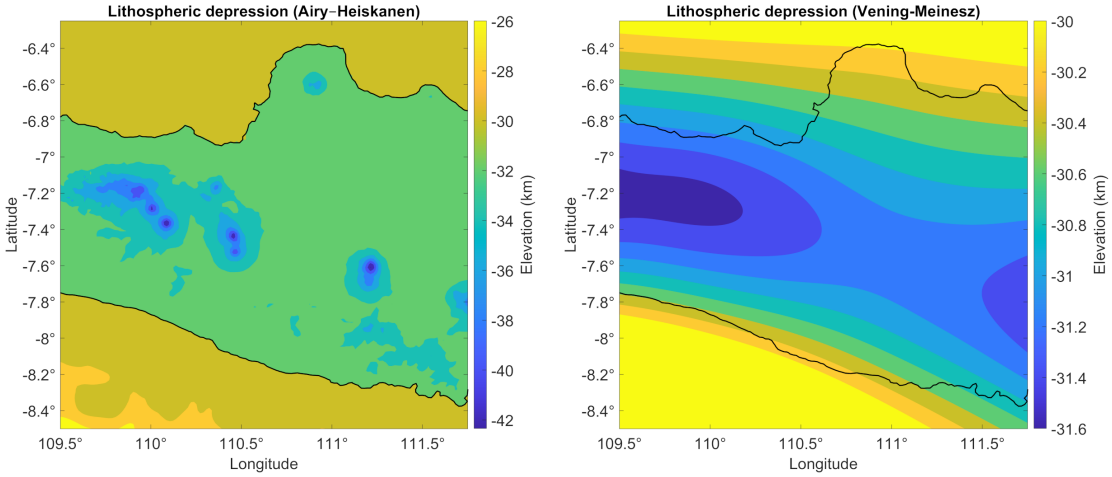

(b) Lithospheric depression according to the Airy–Heiskanen (left) and Vening-Meinesz (right) model of isostasy.

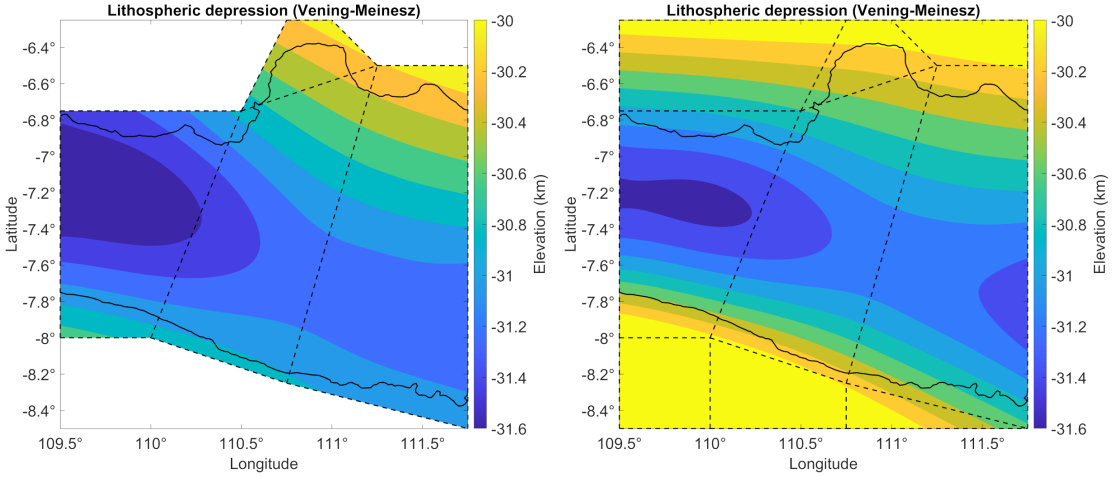

(c) Comparison between the partial (left) and the full (right) multi-patch parametrization.

Figure 29: Numerical simulations of the lithosphere in Central Java.

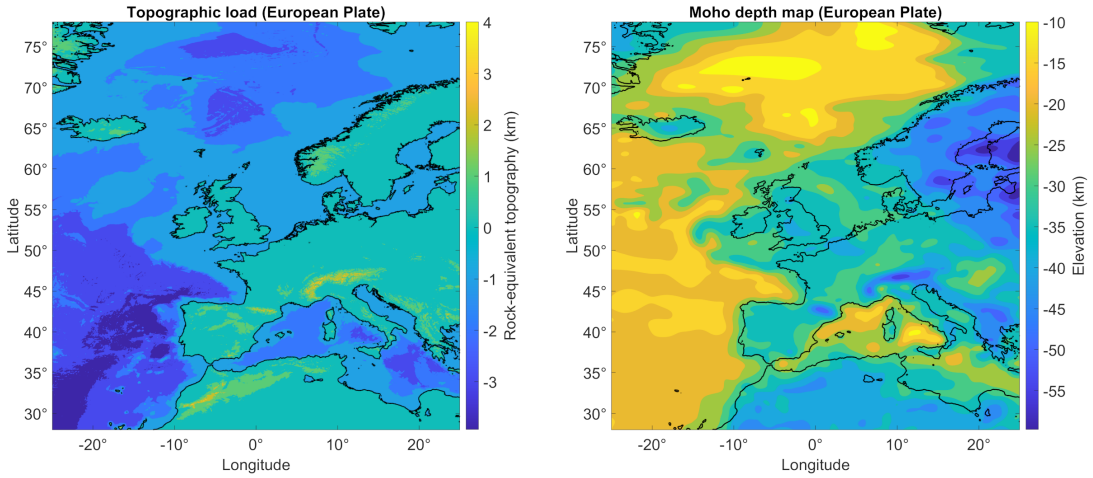

(a) Topographic load (left) and Mohorovičić depth map (right) of Europe.

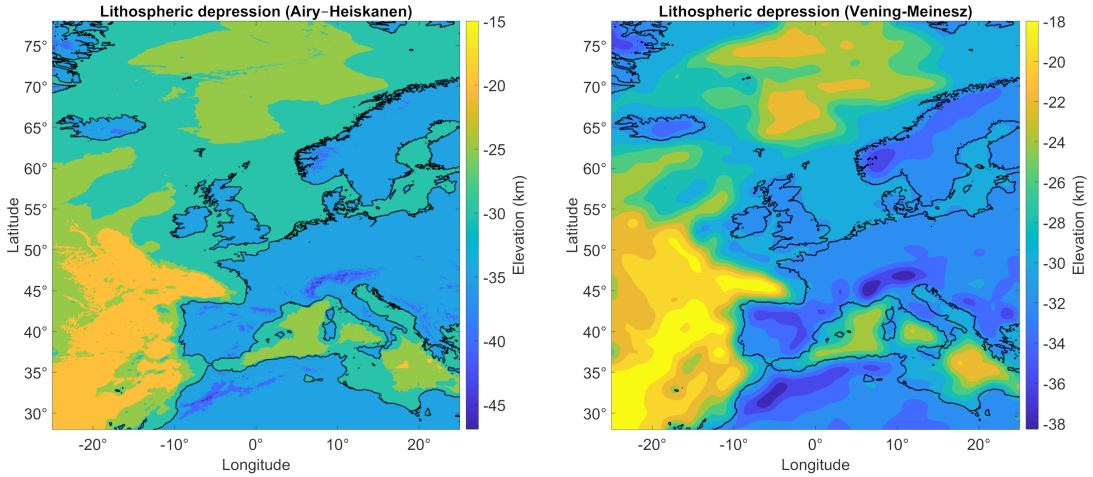

(b) Lithospheric depression according to the Airy–Heiskanen (left) and Vening-Meinesz (right) model of isostasy.

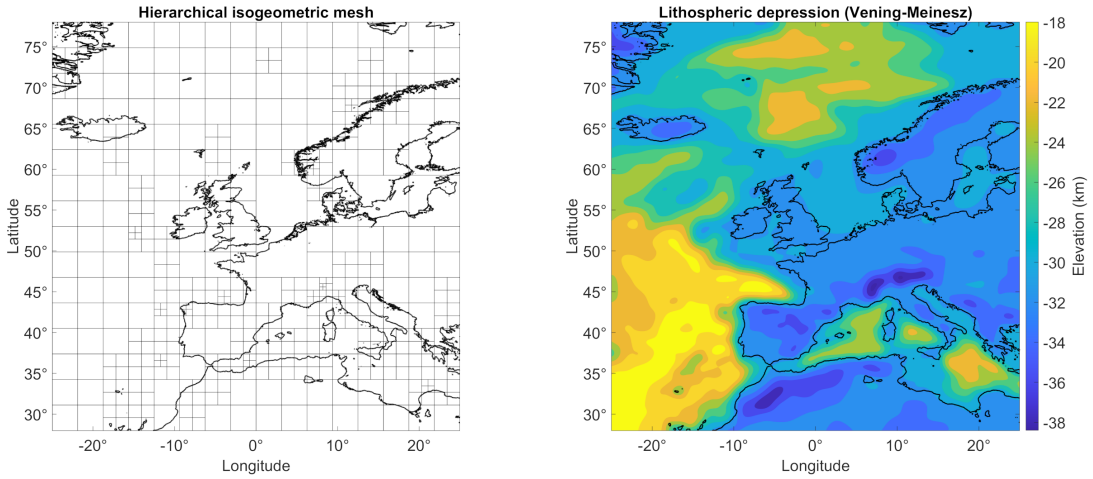

(c) Adaptive local refinement of the isogeometric mesh (left) and corresponding lithospheric depression (right).

Figure 30: Numerical simulations of the lithosphere in Europe.

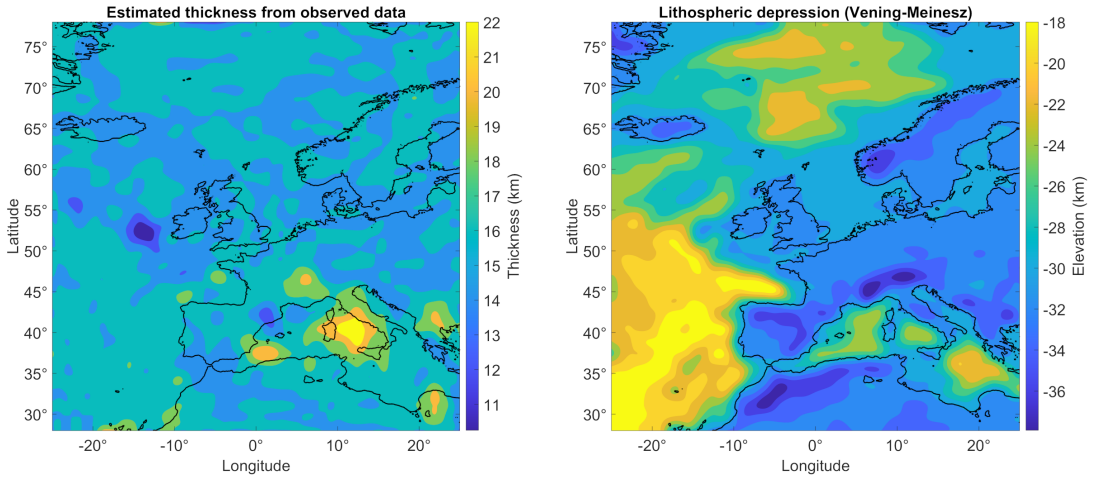

(a) Estimated effective elastic thickness (left) and corresponding lithospheric depression (right).

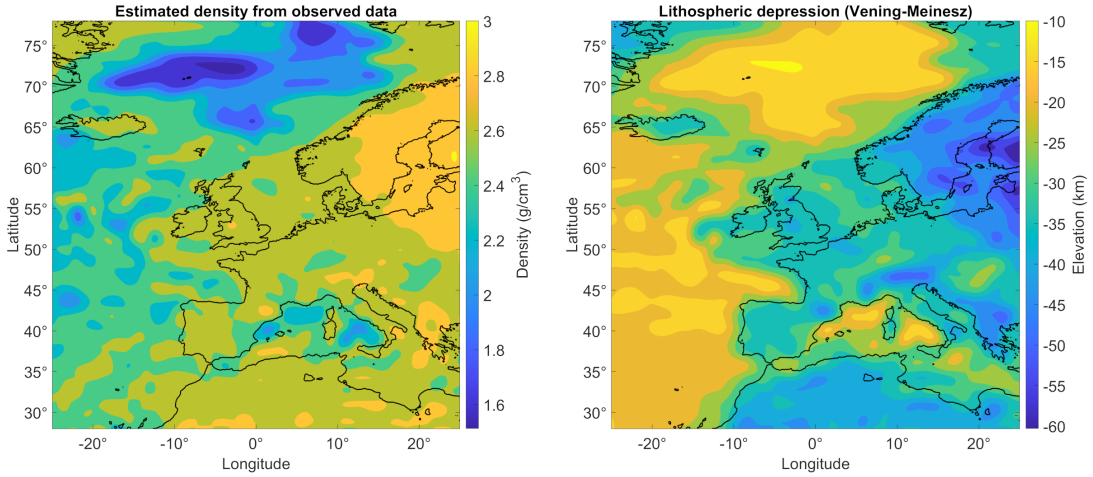

(b) Estimated reference rock density (left) and corresponding lithospheric depression (right).

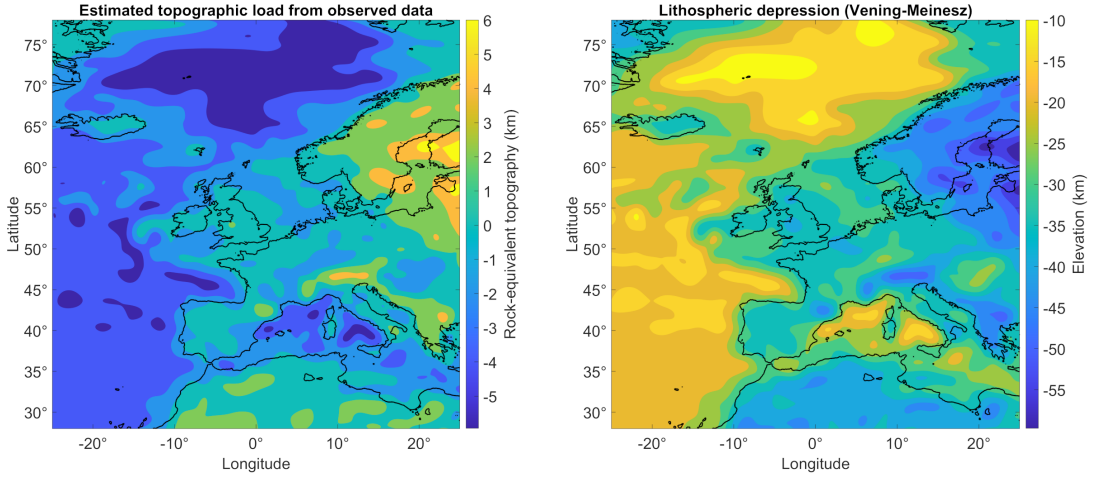

(c) Estimated topographic load (left) and corresponding lithospheric depression (right).

Figure 31: Parameter estimation of the effective elastic thickness, reference rock density, and topographic load in Europe.

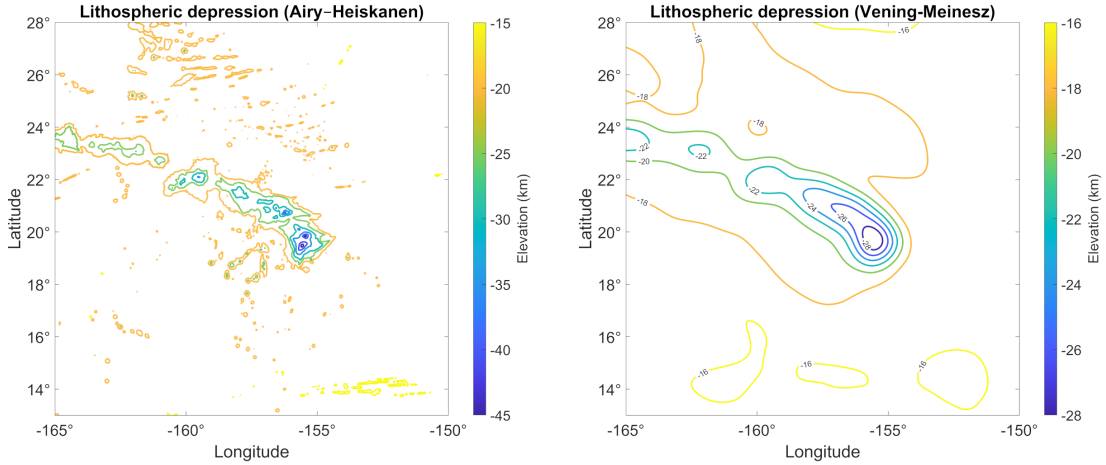

Figure 32: Lithospheric depression in the Hawaiian Islands according to the Airy–Heiskanen model of local isostasy (left) and the Vening-Meinesz model of flexural isostasy (right).

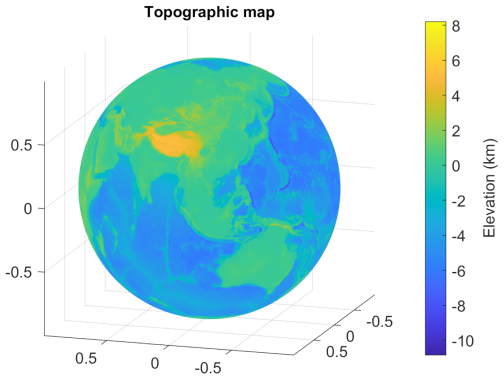

(a) Topographic map of the spherical Earth.

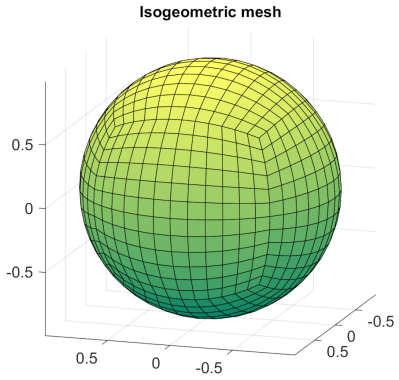

(b) Isogeometric mesh of the spherical domain.

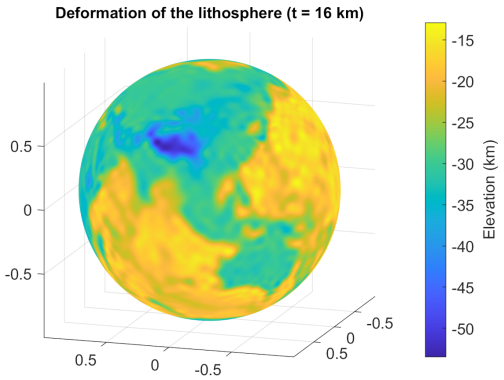

(c) Deformation of the lithosphere with an effective elastic thickness of 16 km.

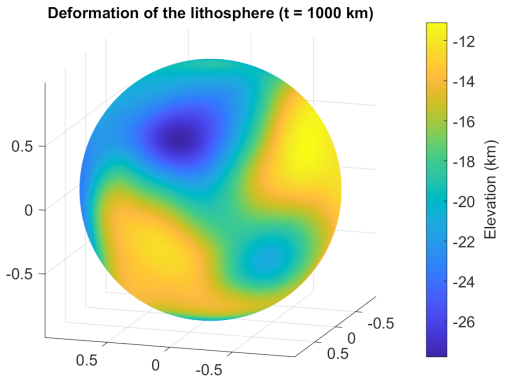

(d) Deformation of the lithosphere with an effective elastic thickness of 1000 km.

Figure 33: Global numerical simulations of Earth's lithosphere modeled as a thin elastic spherical shell using a multi-patch parametrization from a quad sphere projection.

8 Conclusion

Finally, we conclude the thesis with a summary of the main contents, the results achieved, and an outlook on future research work.

Summary

This thesis deals with the Riemannian framework for PDE constrained shape optimization and its application to problems involving planar curves and surfaces, especially thin elastic shells based on a linear Koiter model in structural mechanics. The aim is to develop and implement numerical methods that take the inherent geometric structure of shapes into account. Isogeometric finite element analysis has been used for numerical approximations of the geometry and the solutions to the governing equations, which is motivated by the simple construction of smooth shape functions on a single patch required for a conforming discretization of higher-order problems, such as the shell and plate problems considered in this work. Apart from structural optimization, the identification of parameters for a plate model of Earth's lithosphere using standard optimization with a tracking-type objective function and PDE constraints has also been considered.

Some effort has been put into providing a comprehensive theoretical foundation for the mathematical models used in this work from the ground up. The boundary value problem for thin elastic shells and plates in static equilibrium has been derived from the theory of three-dimensional elasticity and applied to the problem of isostasy. Frameworks for shape spaces have been discussed—with a focus on Riemannian shape spaces of submanifolds of a fixed type, which are commonly used in statistical shape analysis, but not yet prevalent in the field of PDE constrained shape optimization. The geodesic equation on shape space of hyper-surfaces endowed with an H^1 Sobolev–Riemannian metric has been presented in order to investigate the use of geodesic retractions over linear extrapolation. Some aspects of optimization with PDE constraints in combination with the Riemannian vector bundle framework have been addressed. However, the mathematical groundwork for Riemannian optimization on infinite-dimensional shape spaces is still far from complete and requires further development.

The implementation of numerical methods for solving the geodesic equation and for shape optimization in the Riemannian setting using isogeometric analysis has been explained and demonstrated on several examples involving planar curves and surface patches. Geodesic paths have been numerically computed and verified by the conservation of energy. Furthermore, the reparametrization momentum is conserved, which leads to shapes that roughly preserve the initial parametrization along horizontal geodesic paths corresponding to the chosen Riemannian metric. Although this sounds promising for the preservation of mesh quality during shape updates, in practice, it only has a substantial effect if very large step sizes are taken in the line search procedure. This may not be desirable if a local solution close to the initial shape is sought. If overshooting is not a concern, our suggestion is to use a geodesic retraction for the first few steps of the optimization process to facilitate large step sizes without impairing the mesh quality and switch to a linear retraction when the method is about to converge in order to reduce the computational effort.

The proposed Riemannian gradient descent method performs relatively well compared to the steepest descent method using the Euclidean gradient. There are instances where it can compete with a plain application of MATLAB's `fmincon` to control point coordinates. The combination of the Riemannian framework with isogeometric finite element analysis is

a promising approach for numerical PDE constrained shape optimization, also due to the capability of isogeometric shape functions to represent smooth shapes within a single patch. However, a considerable amount of work has still to be undertaken to make the method usable and sufficiently robust for industrial applications, especially because problems of practical relevance usually consist of geometries that are more complex and not necessarily suitable for analysis. Furthermore, numerical integration of the geodesic equation can be expected to be prohibitively expensive for large-scale problems.

Outlook

To further investigate the fitness of the proposed methods, it is essential to compare them to state-of-the-art methods for numerical shape optimization and consider extensions to methods with faster convergence rates, e.g., quasi-Newton methods such as the Riemannian (L-)BFGS method. A systematic study of the mesh preservation properties for the evolution of shapes along geodesic paths using suitable measures of mesh quality is also a subject of further research. The Riemannian framework for shape optimization is not limited to isogeometric discretizations. A comparison with other discretization approaches may reveal further advantages and disadvantages of using isogeometric finite element analysis over existing methods for the discretization and numerical optimization of shells and plates.

Although multi-patch geometries and adaptive local refinement have been used for the numerical simulation of selected problems considered in this thesis, the current implementation of the shape optimization pipeline is limited to single-patch geometries without the use of hierarchical meshes. A major overhaul of the software architecture is required for a seamless integration of all the components in order to enable a combination of the features. Additional challenges and difficulties may arise from this, which warrants further work on the realization of a versatile software for isogeometric shape optimization.

So far, only the elastostatic equilibrium for a Koiter shell and a Kirchhoff plate with a St.-Venant–Kirchhoff material has been considered for the state equation. It may be worth to explore other material models, possibly with inhomogeneities, as well as simultaneous shape and topology optimization [124, 286]. Thick shells and one-dimensional models of rods are possible extensions of this research. In addition to stationary problems in solid mechanics, time-dependent problems in the broader field of continuum mechanics are also prevalent in industrial applications. A particular challenging but interesting topic is shape optimization for fluid–structure interaction (FSI) problems [125].

The H^1 Sobolev–Riemannian metric has been considered in this work for simplicity. While it is commonly used for the shape space of planar curves, a higher-order metric may be more suitable for surfaces in three-dimensional Euclidean space. First-order metrics can still be too weak and lead to singularities in the case of surfaces [121]. An investigation of higher-order Sobolev-type metrics and other kinds of metrics on shape spaces is thus a natural direction of further research. Moreover, the smooth setting does not quite fit with shapes that are less regular and may occur in practice. This necessitates the study of rectifiable sets in geometric measure theory, techniques from geometric analysis, and mathematical optimization in the non-smooth setting.

Lastly, a thorough analysis of the shell optimization problem is of utmost importance to explain the numerical results obtained. The compliance minimization problem for thin elastic shells under fixed area constraint may be ill-posed, which should be investigated. If that is the case, one can attempt to identify additional constraints and regularization terms that are sufficient to make the problem well-posed and suitable for applications.

Bibliography

[1] H. A. Abd-Elmotaal. Theoretical background of the Vening-Meinesz isostatic model. In *Gravity and Geoid*, volume 113 of *International Association of Geodesy Symposia*. Springer, 1995.

[2] P.-A. Absil, R. Mahony, and R. Sepulchre. *Optimization Algorithms on Matrix Manifolds*. Princeton University Press, 2008.

[3] R. A. Adams and J. J. F. Fournier. *Sobolev Spaces*. Pure and Applied Mathematics. Academic Press, 2003.

[4] B. Afsari, R. Tron, and R. Vidal. On the convergence of gradient descent for finding the Riemannian center of mass. *SIAM Journal on Control and Optimization*, 51(3), 2013.

[5] G. B. Airy. On the computation of the effect of the attraction of mountain-masses, as disturbing the apparent astronomical latitude of stations in geodetic surveys. *Philosophical Transactions of the Royal Society of London*, 145:101–104, 1855.

[6] G. Allaire. *Shape Optimization by the Homogenization Method*, volume 146 of *Applied Mathematical Sciences*. Springer, 2002.

[7] G. Allaire and F. Jouve. Coupling the level set method and the topological gradient in structural optimization. In M. P. Bendsøe, N. Olhoff, and O. Sigmund, editors, *IUTAM Symposium on Topological Design Optimization of Structures, Machines and Materials*, volume 137 of *Solid Mechanics and Its Applications*. Springer, 2006.

[8] G. Allaire, F. Jouve, and A.-M. Toader. A level-set method for shape optimization. *Comptes Rendus Mathematique*, 334(12):1125–1130, 2002.

[9] G. Allaire, F. Jouve, and A.-M. Toader. Structural optimization using sensitivity analysis and a level-set method. *Journal of Computational Physics*, 194:363–393, 2005.

[10] G. Allaire, C. Dapogny, and F. Jouve. Shape and topology optimization. In A. Bonito and R. H. Nochetto, editors, *Geometric Partial Differential Equations – Part II*, volume 22 of *Handbook of Numerical Analysis*, pages 1–132. Elsevier, 2021.

[11] H. W. Alt. *Lineare Funktionalanalysis: Eine anwendungsorientierte Einführung*. Masterclass. Springer, 2012.

[12] A. Ambrosetti and G. Prodi. *A Primer of Nonlinear Analysis*. Cambridge Studies in Advanced Mathematics. Cambridge University Press, 1993.

[13] R. Amukti, A. Yunartha, A. Anggraini, W. Suryanto, and N. Achid. Modeling of the Earth's crust and upper mantle beneath central part of Java Island using receiver function data. In *AIP Conference Proceedings*, volume 2194, 2019.

[14] H. C. Andersen. RATTLE: A "velocity" version of the SHAKE algorithm for molecular dynamics calculations. *Journal of Computational Physics*, 52(1):24–34, 1983.

[15] I. Antonau, S. Warnakulasuriya, K.-U. Bletzinger, F. M. Bluhm, M. Hojjat, and R. Wüchner. Latest developments in node-based shape optimization using Vertex Morphing parameterization. *Structural and Multidisciplinary Optimization*, 65(198):1–19, 2022.

[16] A. Apostolatos, M. Breitenberger, R. Wüchner, and K.-U. Bletzinger. Domain decomposition methods and Kirchhoff–Love shell multipatch coupling in isogeometric analysis. In B. Jüttler and B. Simeon, editors, *Isogeometric Analysis and Applications 2014*, volume 107 of *Lecture Notes in Computational Science and Engineering*, pages 73–101. Springer, 2015.

[17] A. Apostolatos, R. Schmidt, R. Wüchner, and K.-U. Bletzinger. A Nitsche-type formulation and comparison of the most common domain decomposition methods in isogeometric analysis. *International Journal for Numerical Methods in Engineering*, 97(7):473–504, 2014.

[18] S. Arguillère, E. Trélat, A. Trouvé, and L. Younes. Shape deformation analysis from the optimal control viewpoint. *Journal de Mathématiques Pures et Appliquées*, 104:139–178, 2015.

[19] C. J. Atkin. The Hopf–Rinow theorem is false in infinite dimensions. *The Bulletin of the London Mathematical Society*, 7(3):261–266, 1975.

[20] K. Atkinson and W. Han. *Theoretical Numerical Analysis: A Functional Analysis Framework*. Texts in Applied Mathematics. Springer, 2007.

[21] H. Azegami and D. Murai. Error analysis of the H1 gradient method for shape-optimization problems of continua. *JSIAM Letters*, 5:29–32, 2013.

[22] H. Azegami and K. Takeuchi. A smoothing method for shape optimization: Traction method using the robin condition. *International Journal of Computational Methods*, 3(1):21–33, 2006.

[23] H. Azegami, S. Fukumoto, and T. Aoyama. Shape optimization of continua using NURBS as basis functions. *Structural and Multidisciplinary Optimization*, 47:247–258, 2013.

[24] M. Bačák, R. Bergmann, G. Steidl, and A. Weinmann. A second order nonsmooth variational model for restoring manifold-valued images. *Methods and Algorithms for Scientific Computing*, 38(1), 2016.

[25] J. M. Ball. Convexity conditions and existence theorems in nonlinear elasticity. *Archive for Rational Mechanics and Analysis*, 63:337–403, 1976.

[26] J.-L. Batoz, K.-J. Bathe, and L.-W. Ho. A study of three-node triangular plate bending elements. *International Journal for Numerical Methods in Engineering*, 15(12):1771–1812, 1980.

[27] M. Bauer, P. Harms, and P. W. Michor. Sobolev metrics on shape space of surfaces. *Journal of Geometric Mechanics*, 3(4):389–438, 2011.

[28] M. Bauer, P. Harms, and P. W. Michor. Almost local metrics on shape space of hypersurfaces in n-space. *SIAM Journal on Imaging Sciences*, 5(1):244–310, 2012.

[29] M. Bauer, M. Bruveris, S. Marsland, and P. W. Michor. Constructing reparametrization invariant metrics on spaces of plane curves. *Differential Geometry and its Applications*, 34: 139–165, 2014.

[30] M. Bauer, M. Bruveris, and P. W. Michor. Why use Sobolev metrics on the space of curves. In P. K. Turaga and A. Srivastava, editors, *Riemannian Computing in Computer Vision*, International Series of Numerical Mathematics, pages 233–255. Springer, 2016.

[31] M. Bauer, M. Bruveris, P. Harms, and J. Møller-Andersen. A numerical framework for Sobolev metrics on the space of curves. *SIAM Journal on Imaging Sciences*, 10(1):47–73, 2017.

[32] M. Bauer, N. Charon, P. Harms, and H.-W. Hsieh. A numerical framework for elastic surface matching, comparison, and interpolation. *International Journal of Computer Vision*, 129: 2425–2444, 2021.

[33] M. F. Beg, M. I. Miller, A. Trouvé, and L. Younes. Computing large deformation metric mappings via geodesic flows of diffeomorphisms. *International Journal of Computer Vision*, 61(2):139–157, 2005.

[34] M. P. Bendsøe. Optimal shape design as a material distribution problem. *Structural Optimization*, 1:193–202, 1989.

[35] M. P. Bendsøe and N. Kikuchi. Generating optimal topologies in structural design using a homogenization method. *Computer Methods in Applied Mechanics and Engineering*, 71: 197–224, 1988.

[36] M. P. Bendsøe and O. Sigmund. *Topology Optimization: Theory, Methods and Applications*. Springer, 2004.

[37] R. Bergmann and P.-Y. Gousenbourger. A variational model for data fitting on manifolds by minimizing the acceleration of a Bézier curve. *Frontiers in Applied Mathematics and Statistics*, 4:59(1–16), 2018. doi: 10.3389/fams.2018.00059.

[38] R. Bergmann and R. Herzog. Intrinsic formulation of KKT conditions and constraint qualifications on smooth manifolds. *SIAM Journal on Optimization*, 29(4):2423–2444, 2019.

[39] R. Bergmann, R. Herzog, J. O. López, and A. Schiela. First- and second-order analysis for optimization problems with manifold-valued constraints. *Journal of Optimization Theory and Applications*, 195:596–623, 2022.

[40] A. L. Besse. *Einstein Manifolds*. Classics in Mathematics. Springer, 1987.

[41] M. Bischoff, K.-U. Bletzinger, W. A. Wall, and E. Ramm. Models and finite elements for thin-walled structures. In *Encyclopedia of Computational Mechanics*, pages 59–137. Wiley, 2004.

[42] L. Blanchard, R. Duvigneau, A. Vuong, and B. Simeon. Shape gradient for isogeometric structural design. *Journal of Optimization Theory and Applications*, 161(2):1–7, 2013.

[43] S. Blauth. Nonlinear conjugate gradient methods for PDE constrained shape optimization based on Steklov–Poincaré-type metrics. *SIAM Journal on Optimization*, 31(3):1658–1689, 2021.

[44] S. Blauth, C. Leithäuser, and R. Pinnau. Shape sensitivity analysis for a microchannel cooling system. *Journal of Mathematical Analysis and Applications*, 492:124476, 2020.

[45] K.-U. Bletzinger, J. Kiendl, R. Schmidt, and R. Wüchner. Isogeometric shape optimization of shells using semi-analytical sensitivity analysis and sensitivity weighting. *Computer Methods in Applied Mechanics and Engineering*, 274:148–167, 2014.

[46] K.-U. Bletzinger. A consistent frame for sensitivity filtering and the vertex assigned morphing of optimal shape. *Structural and Multidisciplinary Optimization*, 49:873–895, 2014.

[47] K.-U. Bletzinger. Shape optimization. In E. Stein, R. de Borst, and T. J. R. Hughes, editors, *Encyclopedia of Computational Mechanics*. Wiley, 2017.

[48] A. Blouza and H. Le Dret. Existence and uniqueness for the linear Koiter model for shells with little regularity. *Quarterly of Applied Mathematics*, 57(2):317–337, 1999.

[49] A. Blouza and H. Le Dret. Naghdi's shell model: Existence, uniqueness and continuous dependence on the midsurface. *Journal of Elasticity*, 64:199–216, 2001.

[50] K. Borsuk. *Theory of Shape*, volume 59 of *Monografie Matematyczne*. Polish Scientific Publishers, 1975.

[51] R. Bouclier, J.-C. Passieux, and M. Salaün. Development of a new, more regular, mortar method for the coupling of NURBS subdomains within a NURBS patch: Application to a non-intrusive local enrichment of NURBS patches. *Computer Methods in Applied Mechanics and Engineering*, 316:123–150, 2017.

[52] N. Boumal. *An Introduction to Optimization on Smooth Manifolds*. Cambridge University Press, 2022.

[53] B. Bourdin and A. Chambolle. Design-dependent loads in topology optimization. *ESAIM: Control, Optimisation and Calculus of Variations*, 9:19–48, 2003.

[54] C. Bracco, A. Farahat, C. Giannelli, M. Kapl, and R. Vázquez. Adaptive methods with C^1 splines for multi-patch surfaces and shells. *Computer Methods in Applied Mechanics and Engineering*, 431:117287, 2024.

[55] D. Braess. *Finite Elements: Theory, Fast Solvers, and Applications in Solid Mechanics*. Cambridge University Press, 2007.

[56] V. Braibant and C. Fleury. Shape optimal design using B-splines. *Computer Methods in Applied Mechanics and Engineering*, 44:247–267, 1984.

[57] S. C. Brenner and L. R. Scott. *The Mathematical Theory of Finite Element Methods*. Texts in Applied Mathematics. Springer, 1994.

[58] H. Brezis. *Functional Analysis, Sobolev Spaces and Partial Differential Equations*. Universitext. Springer, 2011.

[59] M. Bruveris. Riemannian geometry for shape analysis and computational anatomy. In *Mathematics of Shapes and Applications*, pages 15–44. National University of Singapore, 2019.

[60] A. Buffa and G. Sangalli. *IsoGeometric Analysis: A New Paradigm in the Numerical Approximation of PDEs*. Lecture Notes in Mathematics, C.I.M.E. Foundation Subseries. Springer, 2016.

[61] A. Buffa, G. Gantner, C. Giannelli, D. Praetorius, and R. Vázquez. Mathematical foundations of adaptive isogeometric analysis. *Archives of Computational Methods in Engineering*, 29(7): 4479–4555, 2022.

[62] E. Bängtsson, D. Noreland, and M. Berggren. Shape optimization of an acoustic horn. *Computer Methods in Applied Mechanics and Engineering*, 192:1533–1571, 2003.

[63] V. Cervera, F. Mascaró, and P. W. Michor. The action of the diffeomorphism group on the space of immersions. *Differential Geometry and its Applications*, 1(4):391–401, 1991.

[64] C. L. Chan, C. Anitescu, and T. Rabczuk. Isogeometric analysis with strong multipatch C^1-coupling. *Computer Aided Geometric Design*, 62:294–310, 2018.

[65] T. F. Chan and L. A. Vese. Active contours without edges. *IEEE Transactions on Image Processing*, 10(2):266–277, 2001.

[66] P. G. Ciarlet. *Mathematical Elasticity, Volume I: Three-Dimensional Elasticity*. Studies in Mathematics and its Applications. North-Holland, 1988.

[67] P. G. Ciarlet. *Mathematical Elasticity, Volume II: Theory of Plates*. Studies in Mathematics and its Applications. North-Holland, 1997.

[68] P. G. Ciarlet. *Mathematical Elasticity, Volume III: Theory of Shells*. Studies in Mathematics and its Applications. North-Holland, 2000.

[69] P. G. Ciarlet. An introduction to differential geometry with applications to elasticity. *Journal of Elasticity*, 78:1–215, 2005.

[70] P. G. Ciarlet and C. Mardare. A nonlinear shell model of koiter's type. *Comptes Rendus de l'Académie des Sciences Paris, Series I*, 356:227–234, 2018.

[71] F. Cirak, M. J. Scott, E. K. Antonsson, M. Ortiz, and P. Schröder. Integrated modeling, finite-element analysis, and engineering design for thin-shell structures using subdivision. *Computer-Aided Design*, 34:137–148, 2002.

[72] E. Cohen, R. F. Riesenfeld, and G. Elber. *Geometric Modeling With Splines: An Introduction*. CRC Press, 2001.

[73] A. Collin, G. Sangalli, and T. Takacs. Analysis-suitable G^1 multi-patch parametrizations for C^1 isogeometric spaces. *Computer Aided Geometric Design*, 47:93–113, 2016.

[74] L. Conlon. *Differentiable Manifolds*. Modern Birkhäuser Classics. Birkhäuser, 2001.

[75] A. R. Conn, K. Scheinberg, and L. N. Vicente. *Introduction to Derivative-Free Optimization*. MPS-SIAM Series on Optimization. Society for Industrial and Applied Mathematics, 2009.

[76] L. Coradello, L. Gabriele, and A. Buffa. A projected super-penalty method for the C^1-coupling of multi-patch isogeometric Kirchhoff plates. *Computational Mechanics*, 67:1133–1153, 2021.

[77] L. Coradello, J. Kiendl, and A. Buffa. Coupling of non-conforming trimmed isogeometric Kirchhoff–Love shells via a projected super-penalty approach. *Computational Methods in Applied Mechanics and Engineering*, 387:114187, 2021.

[78] E. Cosserat and F. Cosserat. Théorie des corps déformables. In O. D. Chwolson, editor, *Traité de Physique*. A. Hermann et Fils, 1909.

[79] J. A. Cottrell, T. J. R. Hughes, and Y. Bazilevs. *Isogeometric Analysis: Toward Integration of CAD and FEA*. Wiley, 2009.

[80] K. Crane and M. Wardetzky. A glimpse into discrete differential geometry. *Notices of the American Mathematical Society*, 64(10):1153–1159, 2017.

[81] C. de Boor. *A Practical Guide to Splines*, volume 27 of *Applied Mathematical Sciences*. Springer, 1978.

[82] K. Deckelnick, P. J. Herbert, and M. Hinze. A novel $W^{1,\infty}$ approach to shape optimization with Lipschitz domains. *ESAIM: Control, Optimisation and Calculus of Variations*, 28(2): 1–29, 2022.

[83] K. Deckelnick, P. J. Herbert, and M. Hinze. PDE-constrained shape optimization with first-order and Newton-type methods in the $W^{1,\infty}$ topology. *Optimization Methods and Software*, pages 1–27, 2024.

[84] M. C. Delfour and J. P. Zolésio. Structure of shape derivatives for nonsmooth domains. *Journal of Functional Analysis*, 104(1):1–33, 1992.

[85] M. C. Delfour and J. P. Zolésio. *Shapes and Geometries: Metrics, Analysis, Differential Calculus, and Optimization*. Advances in Design and Control. Society for Industrial and Applied Mathematics, 2011.

[86] M. C. Delfour. Hadamard semidifferential, oriented distance function, and some applications. *Communications on Pure and Applied Analysis*, 21(6):1917–1951, 2022.

[87] M. Desbrun, M. Meyer, P. Schröder, and A. H. Barr. Implicit fairing of irregular meshes using diffusion and curvature flow. In *Proceedings of the 26th Annual Conference on Computer Graphics and Interactive Techniques*, SIGGRAPH '99, pages 317–324. ACM Press/Addison–Wesley, 1999.

[88] U. Dierkes, S. Hildebrandt, and F. Sauvigny. *Minimal Surfaces*. Springer, 2010.

[89] M. P. do Carmo. *Differential Geometry of Curves and Surfaces*. Prentice Hall, 1976.

[90] M. P. do Carmo. *Riemannian Geometry*. Mathematics: Theory & Applications. Birkhäuser, 1992.

[91] J. R. Dormand and P. J. Prince. A family of embedded Runge–Kutta formulae. *Journal of Computational and Applied Mathematics*, 6(1):19–26, 1980.

[92] W. Dornisch, G. Vitucci, and S. Klinkel. The weak substitution method — an application of the mortar method for patch coupling in NURBS-based isogeometric analysis. *International Journal for Numerical Methods in Engineering*, 103:205–234, 2015.

[93] X.-B. Duan, Y.-C. Ma, and R. Zhang. Shape-topology optimization for Navier–Stokes problem using variational level set method. *Journal of Computational and Applied Mathematics*, 222:487–499, 2008.

[94] I. Eckstein, J.-P. Pons, Y. Tong, C.-C. J. Kuo, and M. Desbrun. Generalized surface flows for mesh processing. In A. Belyaev and M. Garland, editors, *Geometry Processing*. The Eurographics Association, 2007.

[95] J. Eichhorn. The manifold structure of maps between open manifolds. *Annals of Global Analysis and Geometry*, 3:253–300, 1993.

[96] J. Eichhorn. *Global Analysis on Open Manifolds*. Nova Science Publishers, 2007.

[97] G. Engel, K. R. Garikipati, T. J. R. Hughes, M. G. Larson, L. Mazzei, and R. L. Taylor. Continuous/discontinuous finite element approximations of fourth-order elliptic problems in structural and continuum mechanics with applications to thin beams and plates, and strain gradient elasticity. *Computer Methods in Applied Mechanics and Engineering*, 191(34): 3669–3750, 2002.

[98] G. Eriksson and V. Stiernström. Acoustic shape optimization using energy stable curvilinear finite differences. *Journal of Computational Physics*, 517:113347, 2024.

[99] H. A. Eschenauer, V. V. Kobelev, and A. Schumacher. Bubble method for topology and shape optimization of structures. *Structural Optimization*, 8:42–51, 1994.

[100] L. C. Evans. *Partial Differential Equations*. Graduate Studies in Mathematics. American Mathematical Society, 1998.

[101] A. Farahat, B. Jüttler, M. Kapl, and T. Takacs. Isogeometric analysis with C^1-smooth functions over multi-patch surfaces. *Computer Methods in Applied Mechanics and Engineering*, 403:115706, 2023.

[102] A. Farahat, H. M. Verhelst, J. Kiendl, and M. Kapl. Isogeometric analysis for multi-patch structured Kirchhoff–Love shells. *Computer Methods in Applied Mechanics and Engineering*, 411:116060, 2023.

[103] G. B. Folland. *Real Analysis: Modern Techniques and Their Applications*. Pure and Applied Mathematics. Wiley, 1999.

[104] D. W. Forsyth. Subsurface loading and estimates of the flexural rigidity of continental lithosphere. *Journal of Geophysical Research*, 90(B14):12623–12632, 1985.

[105] D. Fußeder, B. Simeon, and A.-V. Vuong. Fundamental aspects of shape optimization in the context of isogeometric analysis. *Computer Methods in Applied Mechanics and Engineering*, 286:313–331, 2015.

[106] P. Gangl, U. Langer, A. Laurain, H. Meftahi, and K. Sturm. Shape optimization of an electric motor subject to nonlinear magnetostatics. *SIAM Journal on Scientific Computing*, 37(6): B1002–B1025, 2015.

[107] E. M. Garau and R. Vázquez. Algorithms for the implementation of adaptive isogeometric methods using hierarchical B-splines. *Applied Numerical Mathematics*, 123:57–78, 2018.

[108] C. Geiersbach, T. Suchan, and K. Welker. Stochastic augmented lagrangian method in riemannian shape manifolds. *Journal of Optimization Theory and Applications*, 203:165–195, 2024.

[109] A. Geiser, D. Schmölz, D. Baumgärtner, and K.-U. Bletzinger. Discretization-independent node-based shape optimization with the Vertex Morphing method using design variable scaling. *Structural and Multidisciplinary Optimization*, 67(191), 2024.

[110] T. H. Giang and C. Mardare. Existence theorems for nonlinear shell models of Koiter's type. *Mathematics and Mechanics of Solids*, 29(1):191–216, 2023.

[111] M. Golubitsky and V. Guillemin. *Stable Mappings and Their Singularities*. Graduate Texts in Mathematics. Springer, 1973.

[112] A. Goyal and B. Simeon. On penalty-free formulations for multipatch isogeometric Kirchhoff–Love shells. *Mathematics and Computers in Simulation*, 136:78–103, 2017.

[113] M. Grad, T. Tiira, and E. W. Group. The Moho depth map of the European Plate. *Geophysical Journal International*, 176(1):279–292, 2009.

[114] A. E. Green, P. M. Naghdi, and W. L. Wainwright. A general theory of a Cosserat surface. *Archive for Rational Mechanics and Analysis*, 20:287–308, 1965.

[115] A. Griewank and A. Walther. *Evaluating Derivatives: Principles and Techniques of Algorithmic Differentiation*, volume 105 of *Other Titles in Applied Mathematics*. Society for Industrial and Applied Mathematics, 2008.

[116] A. Grothendieck. *Topological Vector Spaces*. Notes on Mathematics and its Applications. Gordon and Breach, 1973.

[117] Y. Guo and M. Ruess. Nitsche's method for a coupling of isogeometric thin shells and blended shell structures. *Computer Methods in Applied Mechanics and Engineering*, 284:881–905, 2015.

[118] B. Gutenberg. Isostasy and its meaning. *Tellus*, 1(3):1–5, 1949.

[119] E. Hairer, G. Wanner, and S. P. Nørsett. *Solving Ordinary Differential Equations I: Nonstiff Problems*, volume 8 of *Springer Series in Computational Mathematics*. Springer, 1993.

[120] R. S. Hamilton. The inverse function theorem of Nash and Moser. *Bulletin of the American Mathematical Society*, 7(1):65–222, 1982.

[121] E. Hartman, Y. Sukurdeep, E. Klassen, N. Charon, and M. Bauer. Elastic shape analysis of surfaces with second-order Sobolev metrics: A comprehensive numerical framework. *International Journal of Computer Vision*, 131:1183–1209, 2023.

[122] L. Harzheim. *Strukturoptimierung: Grundlagen und Anwendungen*. Wissenschaftlicher Verlag Harri Deutsch GmbH, 2008.

[123] J. Haslinger and R. A. E. Mäkinen. *Introduction to Shape Optimization: Theory, Approximation, and Computation*. Advances in Design and Control. Society for Industrial and Applied Mathematics, 2003.

[124] B. Hassani, S. M. Tavakkoli, and H. Ghasemnejad. Simultaneous shape and topology optimization of shell structures. *Structural and Multidisciplinary Optimization*, 48:221–233, 2013.

[125] J. Haubner and M. Ulbrich. Numerical methods for shape optimal design of fluid–structure interaction problems. *Computer Methods in Applied Mechanics and Engineering*, 432:117352, 2024.

[126] E. Hebey. *Sobolev Spaces on Riemannian Manifolds*. Lecture Notes in Mathematics. Springer, 1996.

[127] B. Heeren, M. Rumpf, P. Schröder, M. Wardetzky, and B. Wirth. Splines in the space of shells. *Eurographics Symposium on Geometry Processing 2016*, 35(5):111–120, 2016.

[128] A. C. Hindmarsh. The PVODE and IDA algorithms. Technical Report UCRL-ID-141558, Lawrence Livermore National Laboratory, 2000.

[129] A. C. Hindmarsh, P. N. Brown, K. E. Grant, S. L. Lee, R. Serban, D. E. Shumaker, and C. S. Woodward. SUNDIALS: Suite of nonlinear and differential/algebraic equation solvers. *ACM Transactions on Mathematical Software*, 31(3):363–396, 2005.

[130] M. Hintermüller and W. Ring. A second order shape optimization approach for image segmentation. *SIAM Journal on Applied Mathematics*, 64(2):442–467, 2003.

[131] M. Hinze, R. Pinnau, M. Ulbrich, and S. Ulbrich. *Optimization with PDE Constraints*. Mathematical Modelling: Theory and Applications. Springer, 2009.

[132] M. W. Hirsch. *Differential Topology*. Graduate Texts in Mathematics. Springer, 1976.

[133] C. Hirt and M. Rexer. Earth2014: 1 arc-min shape, topography, bedrock and ice-sheet models – available as gridded data and degree-10,800 spherical harmonics. *International Journal of Applied Earth Observation and Geoinformation*, 39:103–112, 2015.

[134] M. Hojjat, E. Stavropoulou, and K.-U. Bletzinger. The Vertex Morphing method for node-based shape optimization. *Computer Methods in Applied Mechanics and Engineering*, 268:494–513, 2014.

[135] T. Horger, A. Reali, B. Wohlmuth, and L. Wunderlich. A hybrid isogeometric approach on multi-patches with applications to Kirchhoff plates and eigenvalue problems. *Computer Methods in Applied Mechanics and Engineering*, 348:396–408, 2019.

[136] L. L. Howell, S. P. Magleby, and B. M. Olsen. *Handbook of Compliant Mechanisms*. Wiley, 2013.

[137] Y.-L. Hsu. A review of structural shape optimization. *Computers in Industry*, 25(1):3–13, 1994.

[138] T. J. R. Hughes, J. A. Cottrell, and Y. Bazilevs. Isogeometric analysis: CAD, finite elements, NURBS, exact geometry and mesh refinement. *Computer Methods in Applied Mechanics and Engineering*, 194(39–41):4135–4195, 2005.

[139] D. Husemoller. *Fibre Bundles*. Graduate Texts in Mathematics. Springer, 1994.

[140] C. Isenberg. *The Science of Soap Films and Soap Bubbles*. Dover Publications, 1992.

[141] A. Jameson. Aerodynamic design via control theory. *Journal of Scientific Computing*, 3(3): 233–260, 1988.

[142] I. H. Jermyn, S. Kurtek, E. Klassen, and A. Srivastava. Elastic shape matching of parameterized surfaces using square root normal fields. In A. Fitzgibbon, S. Lazebnik, P. Perona, Y. Sato, and C. Schmid, editors, *Computer Vision– ECCV 2012*, pages 804–817. Springer, 2012.

[143] J. Jost. *Riemannian Geometry and Geometric Analysis*. Universitext. Springer, 2017.

[144] K. Jänich. *Vektoranalysis*. Springer-Lehrbuch. Springer, 2005.

[145] B. Jüttler and B. Simeon, editors. *Isogeometric Analysis and Applications 2014*. Lecture Notes in Computational Science and Engineering. Springer, 2015.

[146] C. Kanzow, D. Steck, and D. Wachsmuth. An augmented lagrangian method for optimization problems in banach spaces. *SIAM Journal on Control and Optimization*, 56(1):272–291, 2018.

[147] M. Kapl, V. Vitrih, B. Jüttler, and K. Birner. Isogeometric analysis with geometrically continuous functions on two-patch geometries. *Computers and Mathematics with Applications*, 70:1518–1538, 2015.

[148] M. Kapl, F. Buchegger, M. Bercovier, and B. Jüttler. Isogeometric analysis with geometrically continuous functions on planar multi-patch geometries. *Computer Methods in Applied Mechanics and Engineering*, 316:209–234, 2017.

[149] M. Kapl, G. Sangalli, and T. Takacs. Dimension and basis construction for analysis-suitable G^1 two-patch parametrizations. *Computer Aided Geometric Design*, 52–53:75–89, 2017.

[150] M. Kapl, G. Sangalli, and T. Takacs. Construction of analysis-suitable G^1 planar multi-patch parameterizations. *Computer-Aided Design*, 97:41–55, 2018.

[151] J. Karátson and L. Lóczi. Sobolev gradient preconditioning for the electrostatic potential equation. *Computers and Mathematics with Applications*, 50:1093–1104, 2005.

[152] D. G. Kendall. Shape manifolds, procrustean metrics, and complex projective spaces. *Bulletin of the London Mathematical Society*, 16:81–121, 1984.

[153] J. Kiendl, K.-U. Bletzinger, J. Linhard, and R. Wüchner. Isogeometric shell analysis with Kirchhoff–Love elements. *Computer Methods in Applied Mechanics and Engineering*, 198 (49–52):3902–3914, 2009.

[154] J. Kiendl, Y. Bazilevs, M.-C. Hsu, R. Wüchner, and K.-U. Bletzinger. The bending strip method for isogeometric analysis of Kirchhoff–Love shell structures comprised of multiple patches. *Computer Methods in Applied Mechanics and Engineering*, 199(37–40):2403–2416, 2010.

[155] J. Kirby. *Spectral Methods for the Estimation of the Effective Elastic Thickness of the Lithosphere*. Advances in Geophysical and Environmental Mechanics and Mathematics. Springer, 2022.

[156] W. T. Koiter. On the nonlinear theory of thin elastic shells. *Proc. Kon. Ned. Akad. Wet.*, B 69:1–54, 1966.

[157] W. T. Koiter. On the foundations of the linear theory of thin elastic shells. *Proc. Kon. Ned. Akad. Wet.*, B 73:169–195, 1970.

[158] I. Kolář, J. Slovák, and P. W. Michor. *Natural Operations in Differential Geometry*. Springer, 1993.

[159] A. Kriegl and P. W. Michor. *The Convenient Setting of Global Analysis*. Mathematical Surveys and Monographs. American Mathematical Society, 1997.

[160] S. Lang. *Fundamentals of Differential Geometry*. Graduate Texts in Mathematics. Springer, 1999.

[161] C. Le, T. Bruns, and D. Tortorelli. A gradient-based, parameter-free approach to shape optimization. *Computer Methods in Applied Mechanics and Engineering*, 200:985–996, 2011.

[162] J. M. Lee. *Manifolds and Differential Geometry*. Graduate Studies in Mathematics. American Mathematical Society, 2009.

[163] J. M. Lee. *Introduction to Smooth Manifolds*. Graduate Texts in Mathematics. Springer, 2012.

[164] J. M. Lee. *Introduction to Riemannian Manifolds*. Graduate Texts in Mathematics. Springer, 2018.

[165] B. Leimkuhler and S. Reich. *Simulating Hamiltonian Dynamics*. Cambridge Monographs on Applied and Computational Mathematics. Cambridge University Press, 2004.

[166] A. Limkilde, A. Evgrafov, J. Gravesen, and A. Mantzaflaris. Practical isogeometric shape optimization: Parametrization by means of regularization. *Journal of Computational Design and Engineering*, 8(2):547–558, 2021.

[167] C. Liu and N. Boumal. Simple algorithms for optimization on riemannian manifolds with constraints. *Applied Mathematics and Optimization*, 82:949–981, 2020.

[168] A. E. H. Love. The small free vibrations and deformation of a thin elastic shell. *Philosophical Transactions of the Royal Society of London A*, 179:491–546, 1888.

[169] W. Lowrie. *Fundamentals of Geophysics*. Cambridge University Press, 1997.

[170] T. Lyche, C. Manni, and H. Speleers, editors. *Splines and PDEs: From Approximation Theory to Numerical Linear Algebra*. Springer, 2018.

[171] J. López, C. Anitescu, and T. Rabczuk. Isogeometric structural shape optimization using automatic sensitivity analysis. *Applied Mathematical Modelling*, 89:1004–1024, 2021.

[172] P. Manríquez, E. Contreras-Reyes, and A. Osses. Lithospheric 3-D flexure modelling of the oceanic plate seaward of the trench using variable elastic thickness. *Geophysical Journal International*, 196(2):681–693, 2014.

[173] S. Mardešić. Thirty years of shape theory. *Mathematical Communications*, 2:1–12, 1997.

[174] J. E. Marsden and T. J. R. Hughes. *Mathematical Foundations of Elasticity*. Civil, Mechanical, and Other Engineering. Dover Publications, 1994.

[175] K. Marti. *Stochastic Optimization Methods: Applications in Engineering and Operations Research*. Springer, 2015.

[176] J. R. R. A. Martins. Aerodynamic design optimization: Challenges and perspectives. *Computers and Fluids*, 239:105391, 2022.

[177] H. J. Melosh. *Planetary Surface Processes*. Cambridge Planetary Science, 2011.

[178] N. G. Meyers and J. Serrin. H = W. *Proceedings of the National Academy of Sciences*, 51 (6):1055–1056, 1964.

[179] A. M. Micheletti. Metrica per famiglie di domini limitati e proprietà generiche degli autovalori. *Annali della Scuola Normale Superiore di Pisa*, 26(3):683–694, 1972.

[180] P. W. Michor. *Topics in Differential Geometry*. Graduate Studies in Mathematics. American Mathematical Society, 2008.

[181] P. W. Michor and D. Mumford. Vanishing geodesic distance on spaces of submanifolds and diffeomorphisms. *Documenta Mathematica*, 10:217–245, 2005.

[182] P. W. Michor and D. Mumford. Riemannian geometries on spaces of plane curves. *Journal of the European Mathematical Society*, 8:1–48, 2006.

[183] P. W. Michor and D. Mumford. An overview of the Riemannian metrics on spaces of curves using the Hamiltonian approach. *Applied and Computational Harmonic Analysis*, 23(1): 74–113, 2007.

[184] J. W. Milnor. *Topology: From the Differentiable Viewpoint*. Princeton Landmarks in Mathematics. Princeton University Press, 1997.

[185] B. Mohammadi and O. Pironneau. *Applied Shape Optimization for Fluids*. Oxford University Press, 2009.

[186] M. Mostafa, M. V. Sivaselvan, and C. A. Felippa. A solid-shell corotational element based on ANDES, ANS and EAS for geometrically nonlinear structural analysis. *International Journal for Numerical Methods in Engineering*, 95(2):145–180, 2013.

[187] F. Murat and J. Simon. Étude de problèmes d'optimal design. In *IFIP Technical Conference on Optimization Techniques*, pages 54–62. Springer, 1975.

[188] F. Murat and J. Simon. Sur le contrôle par un domaine géométrique. Technical Report 76015, Laboratoire d'Analyse Numérique, Université Pierre et Marie Curie (Paris VI), 1976.

[189] P. M. Naghdi. The theory of shells and plates. In S. Flügge and C. Truesdell, editors, *Handbuch der Physik VI-a/2: Mechanics of Solids II*. Springer, 1972.

[190] U. Naumann. *The Art of Differentiating Computer Programs: An Introduction to Algorithmic Differentiation*. Software, Environments, and Tools. Society for Industrial and Applied Mathematics, 2011.

[191] R. D. Neidinger. Introduction to Automatic Differentiation and MATLAB Object-Oriented Programming. *SIAM Review*, 52(3):545–563, 2010.

[192] J. W. Neuberger. *Sobolev Gradients and Differential Equations*. Lecture Notes in Mathematics. Springer, 2010.

[193] J. W. Neuberger and R. J. Renka. Minimal surfaces and Sobolev gradients. *SIAM Journal on Scientific Computing*, 16(6):1412–1427, 1995.

[194] M. Neunteufel and J. Schöberl. The Hellan–Herrmann–Johnson method for nonlinear shells. *Computers & Structures*, 225:106109, 2019.

[195] J. Nečas. *Direct Methods in the Theory of Elliptic Equations*. Springer Monographs in Mathematics. Springer, 2012.

[196] D. M. Nguyen, A. Evgrafov, and J. Gravesen. Isogeometric shape optimization for electromagnetic scattering problems. *Progress In Electromagnetics Research B*, 45:117–146, 2012.

[197] V. P. Nguyen, P. Kerfriden, M. Brino, S. P. A. Bordas, and E. Bonisoli. Nitsche's method for two and three dimensional NURBS patch coupling. *Computational Mechanics*, 53:1163–1182, 2014.

[198] J. Nocedal and S. J. Wright. *Numerical Optimization*. Springer, 2006.

[199] A. A. Novotny, R. A. Feijóo, E. Taroco, and C. Padra. Topological sensitivity analysis. *Computer Methods in Applied Mechanics and Engineering*, 192:803–829, 2003.

[200] J. A. Nunn and J. R. Aires. Gravity anomalies and flexure of the lithosphere at the middle amazon basin, brazil. *Journal of Geophysical Research*, 93(B1):415–428, 1988.

[201] N. Olhoff and J. E. Taylor. On structural optimization. *Journal of Applied Mechanics*, 50 (4b):1139–1151, 1983.

[202] B. O'Neill. *Elementary Differential Geometry*. Academic Press, 2006.

[203] J. Oprea. *The Mathematics of Soap Films: Explorations with Maple*, volume 10 of *Student Mathematical Library*. American Mathematical Society, 2000.

[204] E. Oñate and F. Zárate. Rotation-free triangular plate and shell elements. *International Journal for Numerical Methods in Engineering*, 47:557–603, 2000.

[205] J. D. Pelletier. *Quantitative Modeling of Earth Surface Processes*. Cambridge University Press, 2008.

[206] P. Petersen. *Riemannian Geometry*. Graduate Texts in Mathematics. Springer, 2016.

[207] L. Piegl and W. Tiller. *The NURBS Book*. Springer, 1995.

[208] O. Pironneau. *Optimal Shape Design for Elliptic Systems*. Springer Series in Computational Physics. Springer, 1984.

[209] L. Pryymak, T. Suchan, and K. Welker. A product shape manifold approach for optimizing piecewise-smooth shapes. In F. Nielsen and F. Barbaresco, editors, *Geometric Science of Information*, volume 14071 of *Lecture Notes in Computer Science*, pages 21–30. Springer, 2023.

[210] M. Pérez-Gussinyé and A. B. Watts. The long-term strength of europe and its implications for plate-forming processes. *Nature*, 436:381–384, 2005.

[211] X. Qian. Full analytical sensitivities in NURBS based isogeometric shape optimization. *Computer Methods in Applied Mechanics and Engineering*, 199:2059–2071, 2010.

[212] J. N. Reddy. *Theory and Analysis of Elastic Plates and Shells*. CRC Press, 2007.

[213] W. B. Richardson, Jr. Steepest descent using smoothed gradients. *Applied Mathematics and Computation*, 112:241–254, 2000.

[214] W. B. Richardson, Jr. High-order Sobolev preconditioning. *Nonlinear Analysis*, 63: e1779–e1787, 2005.

[215] W. Ring and B. Wirth. Optimization methods on Riemannian manifolds and their application to shape space. *SIAM Journal on Optimization*, 22:596–627, 2012.

[216] D. F. Rogers. *An Introduction to NURBS With Historical Perspective*. Morgan Kaufmann Publishers, 2001.

[217] N. Rogers, editor. *An Introduction to Our Dynamic Planet*. Cambridge University Press, 2008.

[218] R. Rosandi. rozanxt/igalith: Igalith (version 1.0.0), 2024. URL `https://doi.org/10.5281/zenodo.10950313`.

[219] R. Rosandi. rozanxt/shellopt: ShellOpt (version 0.1.0), 2024. URL `https://doi.org/10.5281/zenodo.11403572`.

[220] R. Rosandi and B. Simeon. A Hilbert space framework for sensitivity filtering and vertex morphing. *Proceedings in Applied Mathematics and Mechanics*, 21(S1):e202100258, 2021. doi: 10.1002/pamm.202100258.

[221] R. Rosandi and B. Simeon. Riemannian shape optimization of thin shells using isogeometric analysis. *Proceedings in Applied Mathematics and Mechanics*, 25(1):e202400204, 2025. doi: 10.1002/pamm.202400204.

[222] R. Rosandi, Y. Rosandi, and B. Simeon. Isogeometric analysis of the lithosphere under topographic loading: Igalith v1.0.0. *EGUsphere [preprint, to be published in Geoscientific Model Development]*, 2024. doi: 10.5194/egusphere-2024-1093.

[223] G. I. N. Rozvany and M. Zhou. The COC algorithm, part II: Topological, geometrical and generalized shape optimization. *Computer Methods in Applied Mechanics and Engineering*, 89:309–336, 1991.

[224] G. I. N. Rozvany, M. Zhou, and T. Birker. Generalized shape optimization without homogenization. *Structural Optimization*, 4:250–252, 1992.

[225] W. Rudin. *Functional Analysis*. International Series in Pure and Applied Mathematics. McGraw-Hill, Inc., 1991.

[226] J. P. Ryckaert, G. Ciccotti, and H. J. C. Berendsen. Numerical integration of the Cartesian equations of motion of a system with constraints: Molecular dynamics of n-alkanes. *Journal of Computational Physics*, 23(3):327–341, 1977.

[227] R. L. Schilling. *Maß und Integral*. De Gruyter Studium. De Gruyter, 2015.

[228] S. Schmidt, C. Ilic, V. Schulz, and N. R. Gauger. Three-dimensional large-scale aerodynamic shape optimization based on shape calculus. *AIAA Journal*, 51(11):2615–2627, 2013.

[229] D. Schmölz, B. Devresse, A. Geiser, and K.-U. Bletzinger. Simultaneous node-based shape and thickness optimization of thin-walled structures using the explicit Vertex Morphing method. *Structural and Multidisciplinary Optimization*, 68(37), 2025.

[230] P. J. Schneider. NURB curves: A guide for the uninitiated. *develop*, 25:48–74, 1996.

[231] V. Schulz and M. Siebenborn. Computational comparison of surface metrics for PDE constrained shape optimization. *Computational Methods in Applied Mathematics*, 16(3): 485–496, 2016.

[232] V. H. Schulz. A Riemannian view on shape optimization. *Foundations of Computational Mathematics*, 14:483–501, 2014.

[233] V. H. Schulz, M. Siebenborn, and K. Welker. Structured inverse modeling in parabolic diffusion problems. *SIAM Journal on Control and Optimization*, 53(6):3319–3338, 2015.

[234] V. H. Schulz, M. Siebenborn, and K. Welker. PDE constrained shape optimization as optimization on shape manifolds. In F. Nielsen and F. Barbaresco, editors, *Geometric Science of Information*, volume 9389 of *Lecture Notes in Computer Science*, pages 499–508. Springer, 2015.

[235] V. H. Schulz, M. Siebenborn, and K. Welker. Efficient PDE constrained shape optimization based on Steklov–Poincaré-type metrics. *SIAM Journal on Optimization*, 26(4):2800–2819, 2016.

[236] H. Schumacher. On H^2-gradient flows for the Willmore energy, 2017. arXiv:1703.06469.

[237] M. Schuster, C. Vollmann, and V. Schulz. Shape optimization for interface identification in nonlocal models. *Computational Optimization and Applications*, 88:963–997, 2024.

[238] S. Schuß, M. Dittmann, B. Wohlmuth, S. Klinkel, and C. Hesch. Multi-patch isogeometric analysis for Kirchhoff–Love shell elements. *Computer methods in applied mechanics and engineering*, 349:91–116, 2019.

[239] B. Sengupta, K. J. Friston, and W. D. Penny. Efficient gradient computation for dynamical models. *NeuroImage*, 98:521–527, 2014.

[240] A. Shamanskiy and B. Simeon. Mesh moving techniques in fluid-structure interaction: robustness, accumulated distortion and computational efficiency. *Computational Mechanics*, 67:583–600, 2021.

[241] A. Shamanskiy, M. H. Gfrerer, J. Hinz, and B. Simeon. Isogeometric parametrization inspired by large elastic deformation. *Computer Methods in Applied Mechanics and Engineering*, 363: 112920, 2020.

[242] L. F. Shampine and M. W. Reichelt. The MATLAB ODE suite. *SIAM Journal on Scientific Computing*, 18(1):1–22, 1997.

[243] M. A. Shubin. *Pseudodifferential Operators and Spectral Theory*. Springer, 2001.

[244] M. Siebenborn. A shape optimization algorithm for interface identification allowing topological changes. *Journal of Optimization Theory and Applications*, 177:306–328, 2018.

[245] O. Sigmund and J. Petersson. Numerical instabilities in topology optimization: A survey on procedures dealing with checkerboards, mesh-dependencies and local minima. *Structural Optimization*, 16:68–75, 1998.

[246] O. Sigmund. *Design of material structures using topology optimization*. PhD thesis, Technical University of Denmark, 1994.

[247] O. Sigmund. On the design of compliant mechanisms using topology optimization. *Mechanics of Structures and Machines*, 25(4):493–524, 1997.

[248] O. Sigmund. A 99 line topology optimization code written in Matlab. *Structural and Multidisciplinary Optimization*, 21:120–127, 2001.

[249] O. Sigmund and K. Maute. Sensitivity filtering from a continuum mechanics perspective. *Structural and Multidisciplinary Optimization*, 46(4):471–475, 2012.

[250] O. Sigmund and K. Maute. Topology optimization approaches: A comparative review. *Structural and Multidisciplinary Optimization*, 48:1031–1055, 2013.

[251] J. C. Simo and D. D. Fox. On a stress resultant geometrically exact shell model. Part I: Formulation and optimal parametrization. *Computer Methods in Applied Mechanics and Engineering*, 72(3):267–304, 1989.

[252] J. Sokołowski and A. Zochowski. On the topological derivative in shape optimization. *SIAM Journal on Control and Optimization*, 37(4):1251–1272, 1999.

[253] J. Sokołowski and J. P. Zolésio. *Introduction to Shape Optimization: Shape Sensitivity Analysis*. Springer Series in Computational Mathematics. Springer, 1992.

[254] M. Spivak. *Calculus on Manifolds: A Modern Approach to Classical Theorems of Advanced Calculus*. Addison–Wesley, 1965.

[255] A. Srivastava, E. Klassen, S. Joshi, and I. Jermyn. Shape analysis of elastic curves in Euclidean spaces. *IEEE Transactions on Pattern Analysis and Machine Intelligence*, 33(7): 1415–1428, 2011.

[256] D. Steigmann. Koiter's shell theory from the perspective of three-dimensional nonlinear elasticity. *Journal of Elasticity*, 111(1):91–107, 2013.

[257] Z. Su, M. Bauer, S. C. Preston, H. Laga, and E. Klassen. Shape analysis of surfaces using general elastic metrics. *Journal of Mathematical Imaging and Vision*, 62:1087–1106, 2020.

[258] K. Svanberg. The method of moving asymptotes—a new method for structural optimization. *International Journal for Numerical Methods in Engineering*, 24(2):359–373, 1987.

[259] K. Svanberg. A class of globally convergent optimization methods based on conservative convex separable approximations. *SIAM Journal on Optimization*, 12(2):555–573, 2002.

[260] F. Tröltzsch. *Optimal Control of Partial Differential Equations: Theory, Methods and Applications*. American Mathematical Society, 2010.

[261] L. W. Tu. *An Introduction to Manifolds*. Universitext. Springer, 2011.

[262] R. Udawalpola and M. Berggren. Optimization of an acoustic horn with respect to efficiency and directivity. *International Journal for Numerical Methods in Engineering*, 73(11):1571–1606, 2008.

[263] H. van Brummelen, C. Vuik, M. Möller, C. Verhoosel, B. Simeon, and B. Jüttler, editors. *Isogeometric Analysis and Applications 2018*. Lecture Notes in Computational Science and Engineering. Springer, 2021.

[264] D. E. Varberg. Change of variables in multiple integrals. *The American Mathematical Monthly*, 78(1):42–45, 1971.

[265] F. A. Vening-Meinesz. Une nouvelle méthode pour la réduction isostatique régionale de l'intensité de la pesanteur. *Bulletin Géodésique*, 29:33–51, 1931.

[266] H. M. Verhelst, M. Möller, J. H. Den Besten, A. Mantzaflaris, and M. L. Kaminski. Stretch-based hyperelastic material formulations for isogeometric Kirchhoff–Love shells with application to wrinkling. *Computer-Aided Design*, 139:103075, 2021.

[267] A.-V. Vuong, C. Giannelli, B. Jüttler, and B. Simeon. A hierarchical approach to adaptive local refinement in isogeometric analysis. *Computer Methods in Applied Mechanics and Engineering*, 200(49–52):3554–3567, 2011.

[268] R. Vázquez. A new design for the implementation of isogeometric analysis in Octave and Matlab: GeoPDEs 3.0. *Computers and Mathematics with Applications*, 72(3):523–554, 2016.

[269] W. Wall, M. Frenzel, and C. Cyron. Isogeometric structural shape optimization. *Computer Methods in Applied Mechanics and Engineering*, 197(33–40):2976–2988, 2008.

[270] M. Wallin, M. Ristinmaa, and H. Askfelt. Optimal topologies derived from a phase-field method. *Structural and Multidisciplinary Optimization*, 45:171–183, 2012.

[271] C. C. Wang and C. Truesdell. *Introduction to Rational Elasticity*. Mechanics of Continua. Springer, 1973.

[272] M. Y. Wang and S. Zhou. Phase field: A variational method for structural topology optimization. *Computer Modeling in Engineering and Sciences*, 6(6):547–566, 2004.

[273] M. Y. Wang, X. Wang, and D. Guo. A level set method for structural topology optimization. *Computer Methods in Applied Mechanics and Engineering*, 192(1–2):227–246, 2003.

[274] A. B. Watts. *Isostasy and Flexure of the Lithosphere*. Cambridge University Press, 2001.

[275] O. Weeger. Isogeometric sizing and shape optimization of 3D beams and lattice structures at large deformations. *Structural and Multidisciplinary Optimization*, 65(43), 2022.

[276] P. Weinmüller and T. Takacs. An approximate C^1 multi-patch space for isogeometric analysis with a comparison to nitsche's method. *Computer Methods in Applied Mechanics and Engineering*, 401:115592, 2022.

[277] E. W. Weisstein. Minimal surface of revolution. URL `https://mathworld.wolfram.com/MinimalSurfaceofRevolution.html`. From MathWorld–A Wolfram Web Resource.

[278] K. Welker. Suitable spaces for shape optimization. *Applied Mathematics and Optimization*, 84:869–902, 2021.

[279] A. D. Wickert. Open-source modular solutions for flexural isostasy: gFlex v1.0. *Geoscientific Model Development*, 9(3):997–1017, 2016.

[280] S. Willard. *General Topology*. Addison–Wesley Series in Mathematics. Addison–Wesley, 1970.

[281] R. Winkler. Geometrically exact shell theory from a hierarchical perspective. *Acta Mechanica*, 230:4077–4107, 2019.

[282] Y. M. Xie and G. P. Steven. A simple evolutionary procedure for structural optimization. *Computers & Structures*, 49(5):885–896, 1993.

[283] L. Younes. *Shapes and Diffeomorphisms*, volume 171 of *Applied Mathematical Sciences*. Springer, 2019.

[284] C. Yu, C. Brakensiek, H. Schumacher, and K. Crane. Repulsive surfaces. *ACM Transactions on Graphics*, 40(6):268(1–19), 2021.

[285] C. Yu, H. Schumacher, and K. Crane. Repulsive curves. *ACM Transactions on Graphics*, 40 (2):10(1–21), 2021.

[286] Z. Zhang, H. Yu, H. Wu, and Q. Chen. A simultaneous shape and topology optimization approach of shell structures based on isogeometric analysis and density distribution field. *Computers and Structures*, 305:107550, 2024.

[287] B. Zhu, X. Zhang, H. Zhang, J. Liang, H. Zang, H. Li, and R. Wang. Design of compliant mechanisms using continuum topology optimization: A review. *Mechanism and Machine Theory*, 143:103622, 2020.

[288] O. C. Zienkiewicz, R. L. Taylor, and J. Z. Zhu. *The Finite Element Method: Its Basis and Fundamentals*. Butterworth–Heinemann, 2013.

[289] Z. H. Zuo, Y. M. Xie, and X. Huang. Evolutionary topology optimization of structures with multiple displacement and frequency constraints. *Advances in Structural Engineering*, 15(2): 359–372, 2012.

Academic curriculum vitae

Rozan Irsyadulfawaz Rosandi

Since 2020:	Doctoral research and teaching associate *University of Kaiserslautern-Landau (RPTU)*
2018–2020:	Master of Science in Industrial Mathematics *Technical University of Kaiserslautern*
2015–2018:	Bachelor of Science in Mathematics with subsidiary subject Physics *Technical University of Kaiserslautern*
2014–2015:	Assessment examination for admission to study at German universities *International Preparatory and Language Center* *of the Johannes Gutenberg University Mainz*
2012–2014:	Ijazah Sekolah Menengah Atas (High School Diploma in Indonesia) *Sekolah Menengah Atas Negeri 24 Bandung*
2007–2012:	School for the Highly Gifted / International School (hbf/is) *Heinrich-Heine-Gymnasium Kaiserslautern*

Wissenschaftlicher Werdegang

Rozan Irsyadulfawaz Rosandi

Since 2020:	Wissenschaftlicher Mitarbeiter in der Forschung und Lehre *Rheinland-Pfälzische Technische Universität Kaiserslautern-Landau*
2018–2020:	Master im Studiengang Technomathematik *Technische Universität Kaiserslautern*
2015–2018:	Bachelor im Studiengang Mathematik mit Anwendungsfach Physik *Technische Universität Kaiserslautern*
2014–2015:	Feststellungsprüfung für die Hochschulzugangsberechtigung *Internationales Studien- und Sprachenkolleg (ISSK)* *der Johannes-Gutenberg-Universität Mainz*
2012–2014:	Ijazah Sekolah Menengah Atas (Abschluss der Oberschule in Indonesien) *Sekolah Menengah Atas Negeri 24 Bandung*
2007–2012:	Schule für Hochbegabtenförderung / Internationale Schule (hbf/is) *Heinrich-Heine-Gymnasium Kaiserslautern*